UNIVERSITY OF BIRMINGHAM

MULTIPHASE CARDIOVASCULAR HAEMODYNAMICS: IMPACT OF SURFACE ROUGHNESS AND PLATELET ACTIVATION

by

DAVID GWYN OWEN

A thesis submitted to the
University of Birmingham for the degree of
DOCTOR OF PHILOSOPHY

Biomedical Engineering Research Group
Department of Mechanical Engineering
School of Engineering
University of Birmingham
November 2021

ABSTRACT

With cardiovascular diseases (CVD) being the leading cause of death worldwide, computational fluid dynamics can be used to provide insight into the onset and progression of CVD and to improve the design of medical devices. This thesis develops novel cardiovascular simulations to evaluate how the multiphase rheology of blood impacts CVD and the activation of platelets, with an assessment of haemodialysis catheter design. To date all cardiovascular models assume a smooth artery wall, despite microscopic surface roughness being linked to CVD. A simulation of artery roughness showed a greater range in haemodynamic parameters associated with CVD, compared to a smooth wall, with increased residence time in an ultra low-shear environment (<25 s^{-1}). Stenosed coronary bifurcations were found to exhibit non-Newtonian and multiphase phenomena, with red blood cell residence time in aggregatory low-shear conditions found distal to stenosis. Increased levels of platelet activation and subsequent residence near the plaque highlight the mechanisms of atherothrombosis. Haemodialysis catheters were found to have improved performance with side-holes, however, to ensure long-term patency and reduce the chance of blood clots; the side-holes should be oval shaped, correctly scaled for body diameter, and with an angle-cut profile for optimal surface texture to reduce bio-fouling. Multiphase rheological blood models can be developed to better predict phenomena associated with CVD, yet require additional physical laws governing red blood cell aggregation and near-wall adhesion.

We're just monkeys in shoes

ACKNOWLEDGEMENTS

Dr Daniel Espino and Prof Duncan Shepherd for years of supervision, advice, quick chats, knowledge, patience, long chats, opportunities, help and most of all the support to make this possible.

The Biomedical Engineering Department – Only the best of friends can make a basement feel so welcoming.

My family – You've been there as long as I can remember, and I wouldn't have it any other way.

Everyone who I've known and no longer know; from the friends I've made, to the friends I just can't get rid of – You all have abysmally poor judgement of character.

The saints who post complex solutions to obscure CFD problems on ancient forums.

Old Joe.

La Fromagerie Des Belleville's Raclette au lait cru et charcuteries.

The Engineering and Physical Sciences Research Council (EPSRC) for funding my doctoral research [Grant no. EP/N509590/1].

KIMAL PLC and the EPSRC Impact Acceleration Account: IAA 2017 (601018) #20520 for funding the haemodialysis catheter research.

NOVEL CONTRIBUTIONS

Principal Author

Owen DG, Schenkel T, Shepherd DET, Espino DM. (2020) *Assessment of surface roughness and blood rheology on local coronary haemodynamics: a multi-scale computational fluid dynamics study*. J. R. Soc. Interface 17: 20200327. http://doi.org/10.1098/rsif.2020.0327

Owen DG, de Oliveira DC, Qian S, Green NC, Shepherd DET, Espino DM (2020) *Impact of side-hole geometry on the performance of hemodialysis catheter tips: A computational fluid dynamics assessment*. PLoS ONE 15(8): e0236946. https://doi.org/10.1371/journal.pone.0236946

Owen DG, Diana C. de Oliveira, Emma K. Neale, Duncan E.T. Shepherd, Daniel M. Espino (2021) *Numerical modelling of blood rheology and platelet activation through a stenosed left coronary artery bifurcation*. PLoS ONE 16(11): e0259196 https://doi.org/10.1371/journal.pone.0259196

NOVEL CONTRIBUTIONS

Second Author

de Oliveira DC, Owen DG, Qian S, Green NC, Espino DM, et al. (2021) *Computational fluid dynamics of the right atrium: Assessment of modelling criteria for the evaluation of dialysis catheters.* PLOS ONE 16(2): e0247438. https://doi.org/10.1371/journal.pone.0247438

Oral Presentations

Owen DG, Yan K, Kirkpatrick A, Rajagopal V, Mynard J, Espino DM (2019) *Assessing smoothed particle hydrodynamics for left ventricular diastolic models.* European Society of Biomechanics – Vienna 2019

Owen DG, de Oliveira DC, Qian S, Green NC, Shepherd DET, Espino DM (2021) *Optimising haemodialysis catheter designs with CFD: Do side-holes improve performance?* IMechE Technical Lecture 2021

TABLE OF CONTENTS

LIST OF FIGURES

LIST OF TABLES

LIST OF ABBREVIATIONS

AATAWSS	Area-averaged time-averaged wall shear stress
AFM	Atomic force microscopy
AVF	Arteriovenous fistula
CFD	Computational fluid dynamics
CKD	Chronic kidney disease
CVD	Cardiovascular disease
DVI	Diseased vorticity index
FV	Finite-volume
GFR	Glomerular filtration rate
HD	Haemodialysis
HPC	High performance computing
LAD	Left anterior descending (artery)
LCx	Left circumflex (artery)
LDL	Low-density lipoproteins
LMCA	Left main coronary artery
LOA	Level of activation
MI	Myocardial infarction
MKM5	Modified Krieger model 5-parameters
MPI	Message passing interface

NHS	National health service
NNIF	non-Newtonian importance factor
NS	Navier-Stokes
OSI	Oscillatory shear index
PDE	Partial differential equations
PLI	Platelet lysis index
RA	Right atrium
RBC	Red blood cells
RCA	Right coronary artery
RRT	Relative residence time
SIMPLE	Semi-implicit method for pressure linked equations
SEM	Scanning electron microscopy
SVC	Superior vena cava
TAWSS	Time-averaged wall shear stress
vWF	von Willebrand factor
WSS	Wall shear stress

1 | INTRODUCTION

Cardiovascular diseases (CVD) were responsible for an estimated 18.8 million deaths worldwide in 2017 (Roth *et al.*, 2018), with 27% of deaths in the UK caused by heart or circulatory diseases costing the UK economy an estimated £19 billion each year (BHF, 2019). Computational fluid dynamics (CFD) can be used to study the impact of CVD on haemodynamics, allowing for both increased understanding of disease progression, but also the development of more effective medical devices/treatment options.

This thesis aims to determine the relationship between blood rheology and coronary haemodynamics associated with progression of CVD in two novel scenarios:

- Assessing the impact of microscopic artery surface roughness in CFD models of the coronary artery;
- Investigating the effects of rheology on stenosed coronary bifurcations and associated platelet activation.

In addition to the theoretical considerations above, the thesis will then apply the knowledge and understanding gained from these studies to the improvement in design and performance of haemodialysis catheters, including analysis of platelet activation and potential for bio-film blockages.

The surface roughness of arteries has been associated with the early formation of atherosclerosis (Schmidt-Trucksäss *et al.*, 2003), yet to date no CFD model has incorporated this roughness in a three-dimensional multi-scale model both due to computational restraints and surface properties only recently being classified in porcine arteries (Burton, Freij and Espino, 2017).

The range of haemodynamics in stenosed coronary bifurcations lead to regions of low wall shear stress (WSS) which are associated with CVD, with the rheology of blood playing a crucial role in the health of the near-wall region (Malek and Alper, 2007). Fluctuations in fluid shear rate, haematocrit and residence time in these regions all result in increased morbidity and can impact platelet activation and transport (Govindarajan *et al.*, 2016).

Haemodialysis catheters are commonly used to provide treatment for chronic kidney disease (CKD), with a wide range of designs incorporating many different fundamental approaches to blood filtration commercially available (Owen, Oliveira, *et al.*, 2020). However, these lack a comprehensive and quantitative evaluation of their design features, including the effects on both absolute performance and long-term patency.

Chapter two provides a thorough background of the relevant anatomy of the cardiovascular system, including the key clinical considerations. This is then linked to the current applications of CFD models, including a detailed breakdown of the rheological properties of blood and how it is represented mathematically in CFD simulations.

Chapter three describes the methods of creating a realistic microscopic surface roughness model of the coronary artery, including a detailed assessment of current rheological models and their suitability at modelling the multi-scale artery. Haemodynamic parameters associated with atherosclerosis are then evaluated and discussed for rough/smooth arteries for each model.

Chapter four further evaluates the rheological models from chapter three, in a more complicated and clinically relevant stenosed coronary bifurcation. The trajectories and potential activation of platelets within the artery were also evaluated to determine both likely regions for thrombus (clot) formation, but also to study red blood cell (RBC) residence time in the disturbed, low-shear region around the bifurcation/stenosis.

Chapter five is a detailed study on the impact of side-holes on the performance of haemodialysis catheters. Generic designs were systematically evaluated to allow for direct comparisons of different side-hole shapes/sizes/numbers to determine their effects on key performance metrics (flow rate and velocity) and long-term patency (fibrin formation and platelet lysis).

Chapter six is a general discussion which summarises the key findings from each chapter and discusses their impact on both clinical/computational research. Potential future continuations and applications of the methods/results presented in this thesis are considered as closing sentiment.

2 | BACKGROUND

2.1 Overview

In order to create accurate simulations of blood flow relevant to the cardiovascular system, a clear understanding of the underlying physiology is essential. This chapter introduces key parts of the cardiovascular anatomy and their function, including typical physiological dimensions for reference wherever possible. This is followed by a comprehensive description of the composition and rheology of blood, and how they relate to haemodynamics. The current approaches to computational modelling of the cardiovascular system are then critically reviewed, including theoretical definitions of relevant numerical techniques and methods for the research in this thesis.

2.2 Cardiovascular anatomy

2.2.1 Introduction

The cardiovascular system is responsible for many key functions: supplying oxygen and nutrients throughout the entire body, transporting waste products from organs and protecting against trauma and infection through platelets and antibodies, respectively. It spans throughout the entire body, connecting all organs through an interconnected network of arteries, veins and capillaries. The arteries are thick-walled blood vessels

responsible for carrying oxygenated blood away from the heart, and veins are thinner walled, often wider vessels returning blood to the heart. Capillaries are micro-vessels with walls approximately one cell thick, allowing for the diffusion of oxygen/nutrients from the blood stream into cells/tissue.

2.2.2 Heart

The heart is responsible for pumping blood throughout the cardiovascular system. The typical healthy heart rate for adults is around 60 - 90 beats per minute (Avram *et al.*, 2019), corresponding to an average cardiac cycle length between 0.675 - 1 s. The heart is separated into 4 distinct chambers: the left and right atria, and the left and right ventricles (Figure 2.1), with the right side pumping deoxygenated blood from the circulatory system to the lungs, and the left side pumping freshly oxygenated blood from the lungs through the cardiovascular system. Cardiac muscle is used to expand/contract the chambers, generating the required pressure to pump blood throughout the cardiovascular system, with a normal adult arterial blood pressure during diastole and systole being 69 and 114 mmHg (9199 and 15199 Pa), respectively (Mattace-Raso *et al.*, 2010). Comparatively the pressure in the venous system is approximately 10× lower, between 6-8 mmHg (1066 Pa) (Tansey *et al.*, 2019).

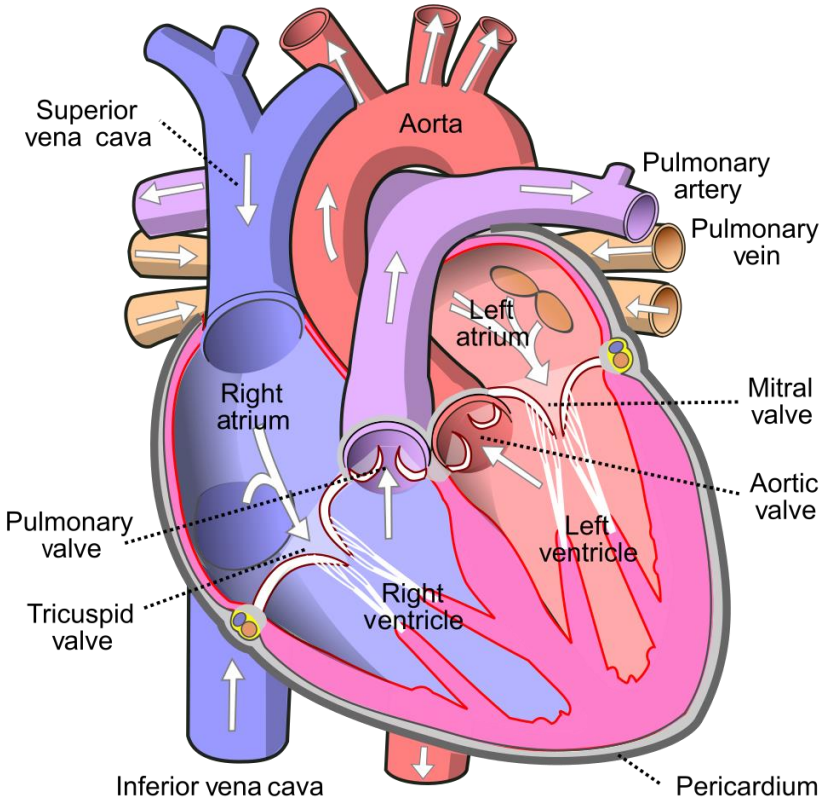

Figure 2.1: Labelled diagram of heart showing ventricles and connected veins/arteries (Created by Wapcaplet, reproduced under CC-BY 3.0: https://creativecommons.org/licenses/by-sa/3.0/deed.en)

2.2.3 Coronary arteries

The coronary arteries supply oxygenated blood to the cardiac muscles, originating from the ascending aorta and lying on the surface of the heart (Figure 2.2A). Similar to the atria/ventricles, the coronary arteries are classified as the left/right coronary arteries (LCA and RCA, respectively) depending on which portion of the heart they supply. Both the LCA and RCA typically begin with internal lumen diameters around 3.5 – 4.5 mm (Dodge *et al.*, 1992), which then bifurcate into multiple smaller branches. The reduction in lumen diameter at a bifurcation typically follows Murray's law (Murray,

1931), where the cube of the parent radii is equal to the sum of the cubed radii's in the daughter branches in blood vessels (Kassab and Fung, 1995). The mean of peak blood velocity taken at rest in 59 subjects for the LCA was 0.32 ± 17 ms^{-1} (Anderson *et al.*, 2000), with variations in blood velocity and trajectory arising due to anatomical features including: vessel curvature, lumen cross-sectional area, bifurcations and lumen surface texture (Anderson *et al.*, 2000; Zhu *et al.*, 2009; Oviedo *et al.*, 2010; Burton, Freij and Espino, 2017).

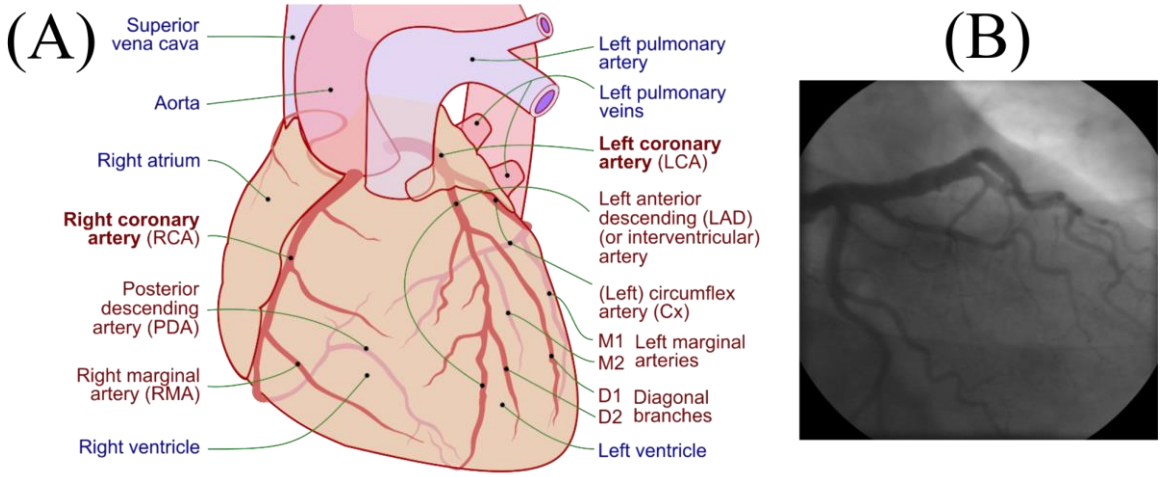

Figure 2.2: (A) – Labelled anatomical diagram of the coronary artery tree (Created by Mikael Häggström, M.D., reproduced under CC-BY 3.0 https://creativecommons.org/licenses/by-sa/3.0/deed.en), (B) – Angiogram of branching in male coronary artery (Created by Thomasjst, reproduced under CC-BY 3.0 https://creativecommons.org/licenses/by-sa/3.0/deed.en)

The artery wall is composed of three separate layers, connected through elastic membranes. These layers are the adventia, media and intima with the most relevant to this thesis being the intima (Figure 2.3). The intima thickness varies significantly in healthy human populations, but is around 0.25 mm thick in coronary arteries (Holzapfel

et al., 2005). It is coated in endothelial cells which line the inner wall of the artery (lumen).

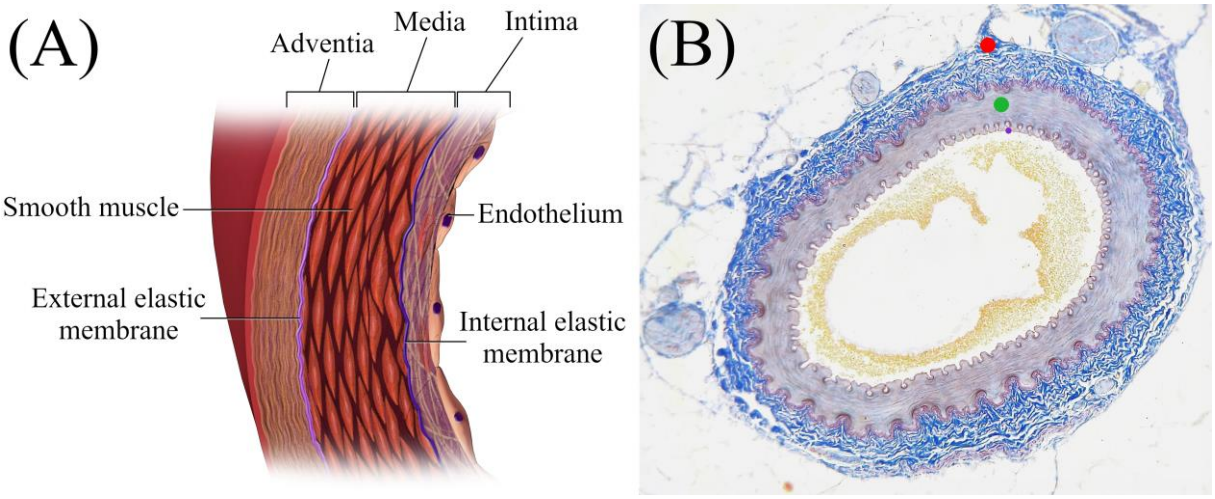

Figure 2.3: (A) – Labelled diagram of artery layers (Created by BruceBlaus, reproduced under CC-BY 3.0 https://creativecommons.org/licenses/by/3.0/deed.en, label text modified), (B) – Cross section of artery layers taken using microscopy with coloured dots used as labels (Red – Adventia, Green – Media and Purple – Intima)

2.3 Blood

2.3.1 Composition

Blood is formed from a concentrated suspension of cells within a plasma continuum. Over 99% of the cellular volume fraction within blood is comprised of erythrocytes (Picart *et al.*, 1998) called red blood cells (RBC), with a breakdown of all the cells shown in Table 2.1. As Leucocytes represent ~1% of the cellular volume fraction, their sizes are reported as a range over the entire group of leucocytes.

Table 2.1: Cell types and properties in blood (Reproduced with permission of the Licensor through PLSclear from p159 of '*The mechanics of the circulation 2nd Edition*' by Caro *et al.*, © Cambridge University Press 2012 (Caro *et al.*, 2011b))

Cell type	Number per mm^3	Unstressed shape and dimensions (µm)	Volume concentration in blood (%)
Erythrocytes (Red blood cell)	$4\text{-}6 \times 10^6$	Biconcave disc 8 × 1-3	45
Leucocytes	$4\text{-}11 \times 10^3$	Roughly spherical 7-22	1
Total			
Granulocytes			
Neutrophils	$1.5\text{-}7.5 \times 10^3$		
Eosinophil	$0\text{-}4 \times 10^2$		
Basophil	$0\text{-}2 \times 10^2$		
Lymphocytes	$1\text{-}1.45 \times 10^3$		
Monocytes	$0\text{-}8 \times 10^2$		
Platelets	$250\text{-}500 \times 10^3$	Rounded or Oval 2-4	

The main function of RBC is the transport of oxygen throughout the body, which is stored in an iron-based protein within the cell called haemoglobin. Individual RBC are elastic and deformable, and whilst the healthy adult range of haematocrit (volume concentration of RBC) is around 40-45%, it varies with age/gender/altitude and can vary from 10-70% in diseased cases (Hall and Guyton, 2020). It is the rheological

properties of the RBC which are the dominant factor in whole blood's rheology and will be described in further detail in subsequent sections.

Platelets are one of the key participants in the blood clotting process, where platelets adhere to damaged/wounded parts of the endothelium and release chemicals to further increase the adhesion of additional platelets to prevent bleeding (Gorbet and Sefton, 2004). Plasma is comprised predominantly of water, containing a mixture of dissolved nutrients/proteins and is conventionally considered to be a Newtonian fluid, with constant viscosity (Chien *et al.*, 1966).

2.3.2 Viscosity fundamentals

Viscosity (μ) is a measure of a fluid's internal resistance to deformation. It can be visualised on a small continuum scale shown in Figure 2.4, where two adjacent layers of fluid are moving past one another. Fluids with higher viscosities require greater forces to allow these layers to slide past each other and hence have higher resistance to flow.

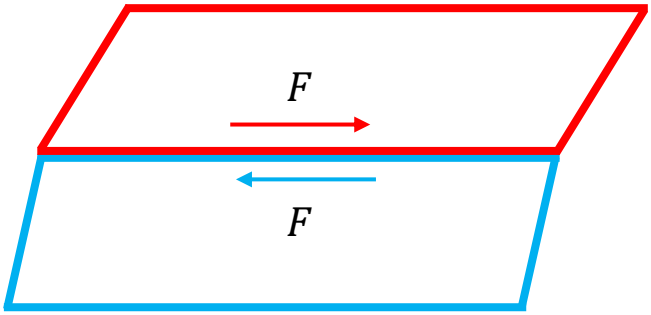

Figure 2.4: Diagram of two continuum fluid elements showing the effect viscosity has on fluid flow (F represents the shearing force acting on the continuum fluid element)

Non-Newtonian fluids have a varying viscosity which is typically a function of the shear rate of the fluid. Shear rate, $\dot{\gamma}$, can be visualised as the difference in velocity between the two adjacent layers of fluid above (Figure 2.4), or mathematically as the derivative of velocity with respect to radial distance. If the viscosity of the fluid increases when a shear force is applied it is referred to as 'shear-thickening' (e.g. Oobleck or fully saturated sand), and if the viscosity decreases when a shear force is applied it is referred to as 'shear-thinning' (e.g. Ketchup or blood).

The stress exerted as a result of the shear forces (outlined above) is described in Equation 2.1, which exists everywhere throughout the fluid domain, but is usually defined at the boundary between the fluid and the solid wall and is hence called wall shear stress (WSS).

$$\tau_w = \mu\dot{\gamma} = \mu \left.\frac{du_t}{dn}\right|_{wall} \qquad (2.1)$$

where τ_w is the WSS, u_t is the tangential wall velocity, μ is viscosity and n is the unit direction vector perpendicular to the wall.

2.3.3 non-Newtonian properties

Previous *in vivo* and *in vitro* studies on the properties of blood have shown significant non-Newtonian behaviour in both physiological and pathological cases (Fahraeus, 1929; Chien *et al.*, 1966; Brooks, Goodwin and Seaman, 1970). The three main factors affecting the non-Newtonian behaviour of blood are: Haematocrit, shear rate and RBC aggregation (Bishop *et al.*, 2001). As haematocrit increases, blood becomes mostly a conglomeration of RBC, past a critical threshold in which blood no longer behaves as a fluid (with experiments showing this value to be >0.98 (Chien *et al.*, 1966)). The dependence of blood viscosity on haematocrit as measured by Brooks *et al.* (Brooks, Goodwin and Seaman, 1970) is shown for a wide range of shear rates in Figure 2.5, with typical shear rates in arteries ranging from 300-800 s^{-1} (Gogia and Neelamegham, 2015).

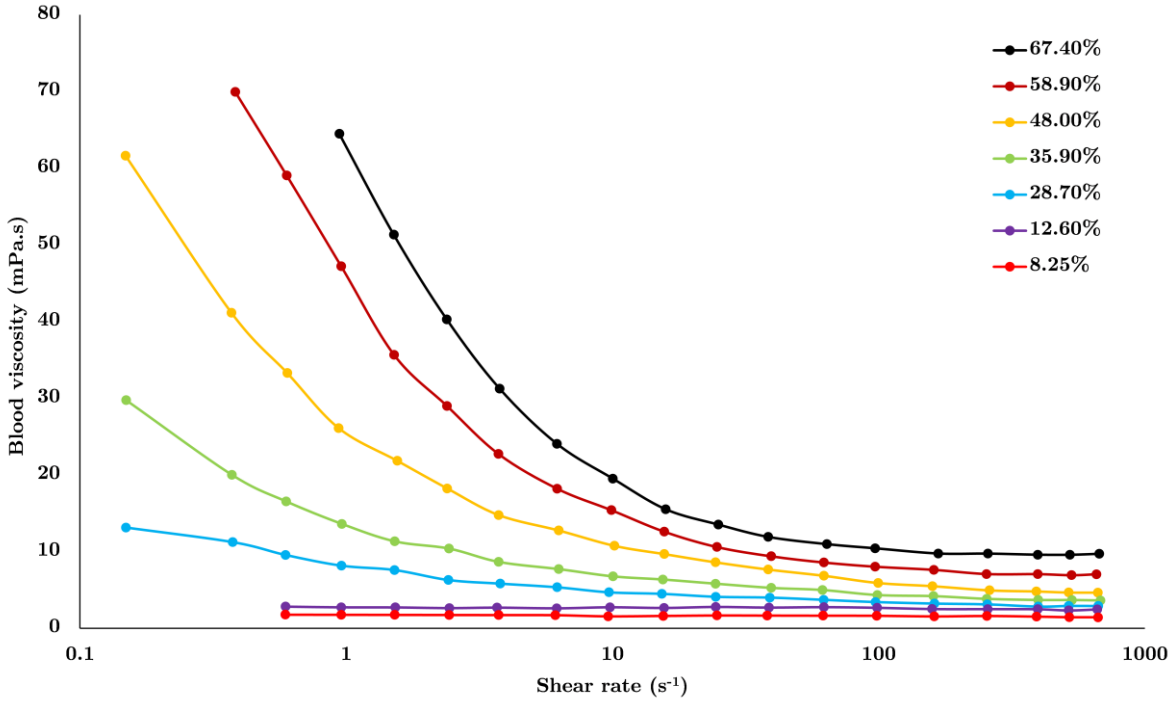

Figure 2.5: Variation of whole blood viscosity for a wide range of physiological haematocrits and shear rates (Data from the Brooks *et al.* dataset (Brooks, Goodwin and Seaman, 1970))

Blood is commonly referred to as a shear-thinning fluid, where increasing shear rate, decreases the viscosity of the fluid. Only at low shear rates (approximately <100 s^{-1}) are the non-Newtonian effects likely to be significant (Carty, Chatpun and Espino, 2016), with the viscosity of whole blood trending asymptotically towards a fixed value of around 3 - 5.5 mPa.s depending on individual physiology and haematocrit levels (Galidi *et al.*, 2008), hence the prevalent assumption in many cardiovascular models for Newtonian blood rheology due to higher shear rates in the bulk cardiovascular flow (Cho and Kensey, 1991).

Critically however, the dominant factor in blood's non-Newtonian behaviour is the aggregation of RBC, where RBC align and become grouped together in a process called *Rouleaux* formation (Bishop *et al.*, 2001).

2.3.4 RBC aggregation

When exposed to prolonged levels of low shear (>1.5 s), the deformability and elasticity of RBC results in the aggregation of individual RBC into a stacked group (rouleaux) which significantly alters the rheology of blood. These stacked columns can then become interconnected, hence forming larger and more dense aggregates which further increase the viscosity of blood. Examples of such formations in healthy human blood can be found using a Rheoscope and are shown in Figure 2.6.

The exact thresholds of shear rate and exposure time required for RBC to form aggregates is still unclear, being limited to *in vitro* studies of mechanically sheared blood (often RBC suspensions) or testing *ex vivo* samples of pathologic blood for aggregate concentrations (Schmid-Schönbein *et al.*, 1975; Bishop *et al.*, 2001). Significant aggregate formation has been found with exposure to shear rates <50 s^{-1} (Goldstone, Schmid-Schönbein and Wells, 1970), with estimated minimal exposure times around 1.5 s (Arzani, 2018) for aggregate formation.

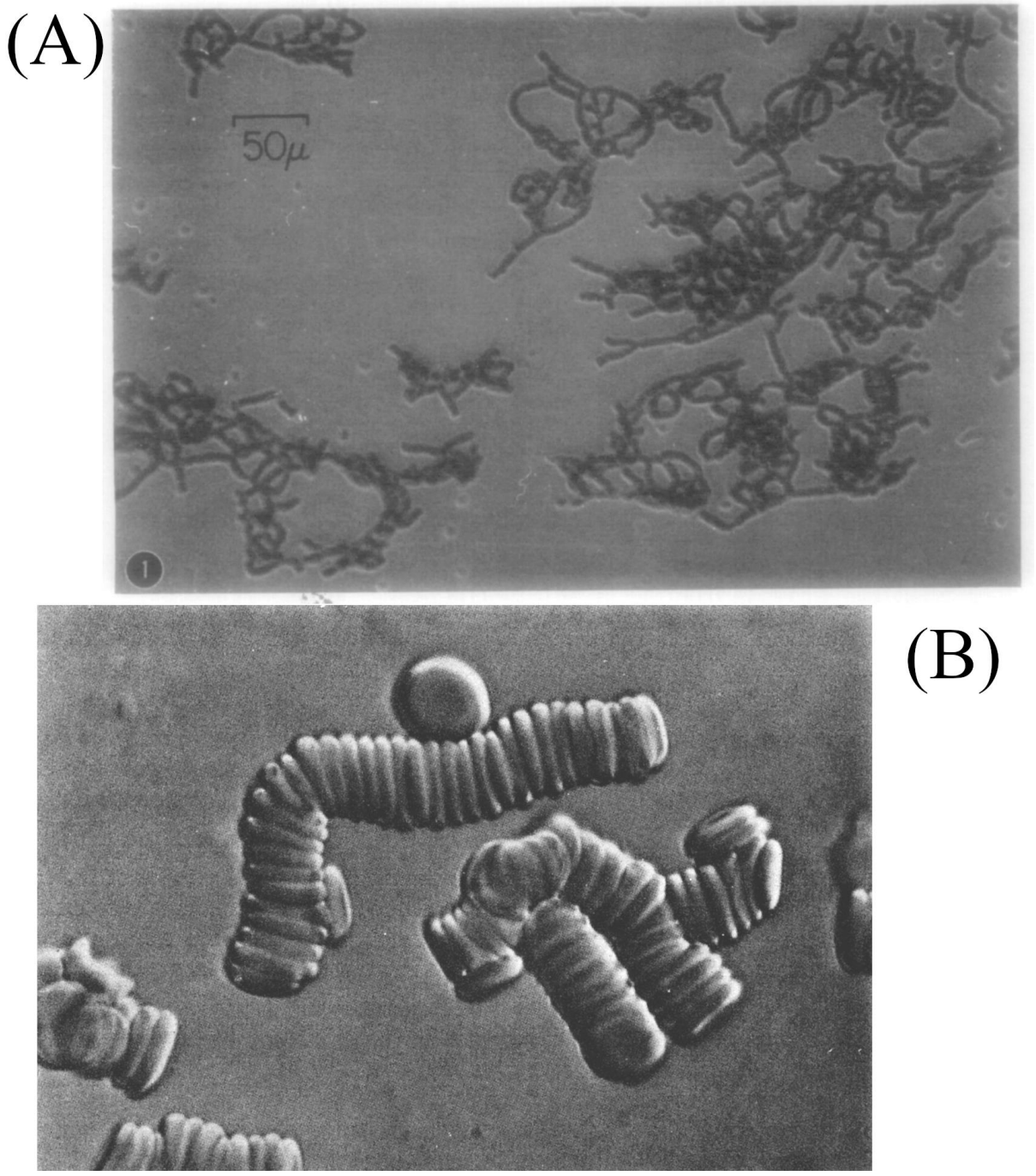

Figure 2.6: (A) - Photograph of physiological rouleaux formation with reduced haematocrit of 25% for clarity, sheared at 11.5 s^{-1}. (Reprinted from Microvascular Research, Vol 2 – Issue 3, Goldstone *et al.* (Goldstone, Schmid-Schönbein and Wells, 1970), *The rheology of red blood cell aggregates*, Copyright 1970, with permission from Elsevier Inc), (B) – Profile view of erythrocytes forming rouleaux (Reproduced with permission of the Licensor through PLSclear from p164 of '*The mechanics of the circulation 2nd Edition*' by Caro *et al.*, © Cambridge University Press 2012 (Caro *et al.*, 2011b))

Despite the impact aggregation has on the rheology of blood, it is a common occurrence within the cardiovascular system as in disease-free healthy vessels increased shear rates can easily disaggregate the RBC from their rouleaux formation and return to normal without any impact on their function (Galidi *et al.*, 2008). Similarly to aggregation, the level of shear required to disaggregate the RBC can vary significantly between studies and in pathologic cases has been found to exceed 450 s^{-1} (Goldstone, Schmid-Schönbein and Wells, 1970). With large regions of low-shear occurring with many CVD, bigger and more dense aggregates can form, which when coupled with increased residence time requires higher shear rates to disaggregate.

An additional factor in the formation of RBC aggregates are the concentrations of dissolved proteins within the blood – notably the concentration of fibrinogen. Fibrinogen is fibrous protein which is involved in thrombus/clot formation (Chien *et al.*, 1966; Bishop *et al.*, 2001), but also increases the strength of RBC aggregates by grouping multiple rouleaux together as shown using scanning electron microscopy (SEM) in Figure 2.7 (Wohner *et al.*, 2011).

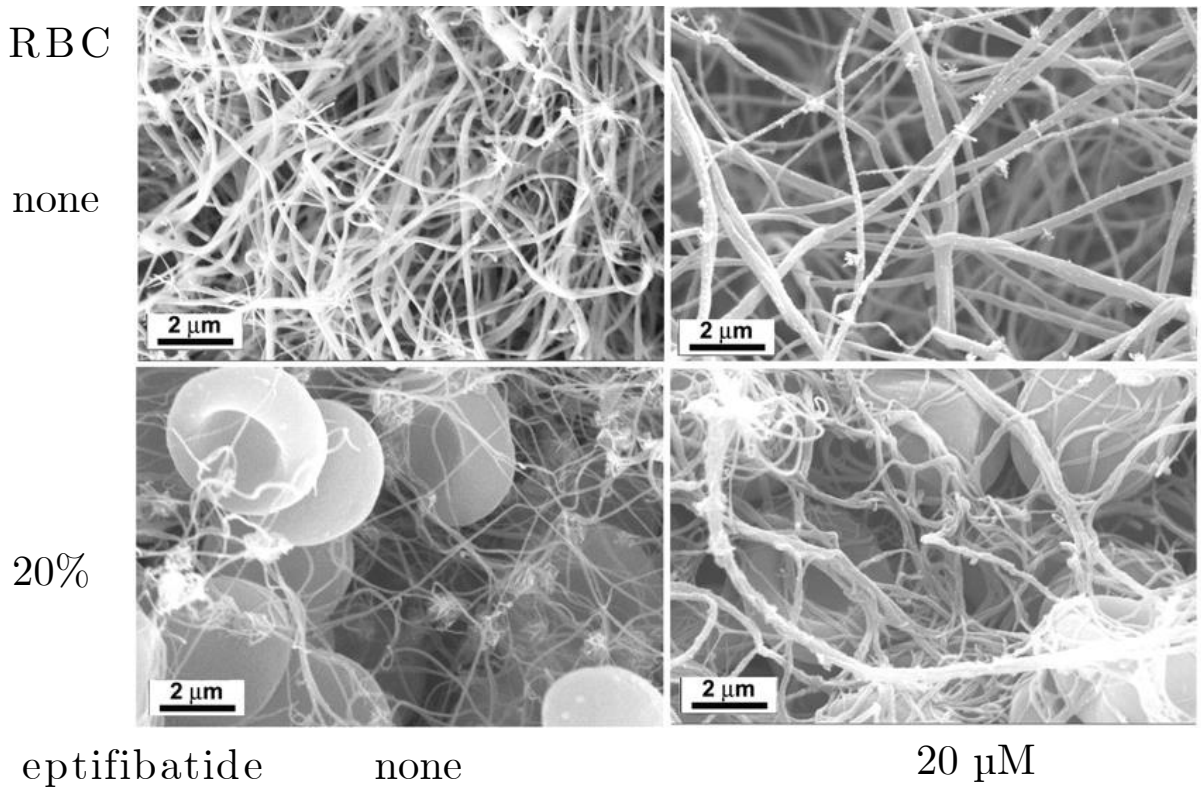

Figure 2.7: SEM image of fibrin network around RBC at 0% and 20% haematocrit, Eptifibatide is a glycoprotein which is used to inhibit clotting/fibrin formation, but its effects are not evaluated in this this work. (Reprinted from Arteriosclerosis, Thrombosis, and Vascular Biology, Vol 31 – Issue 10, Wohner *et al.* (Wohner *et al.*, 2011), *Lytic Resistance of Fibrin Containing Red Blood Cells,* © 2011, with permission from Wolters Kluwer Health)

2.3.5 Platelet activation

Platelet activation refers to the bio-physical process in which individual platelets become grouped together and adhere to surfaces such as endothelium or biomaterials in medical devices. Platelet activation can be broadly categorized into two distinct methods: bio-chemical induced activation via exposure to agonists or the mechanical

activation of platelets due to prolonged exposure to high shear stresses (Gorbet and Sefton, 2004).

The detailed sequence of chemical reactions leading to the coagulation of platelets has been studied extensively both *in vivo* and *in vitro* (Maxwell *et al.*, 2007; Nording, Seizer and Langer, 2015). Briefly, ruptured/damaged endothelial cells release von Willebrand factor (vWF) which causes a reaction between the exposed collagen in the endothelium and the platelet membrane, creating a bridge-like tether. The platelets themselves then release additional chemicals which trigger other platelets to activate, and the group then becomes bound together by fibrinogen/vWF and spreads out to create a plug/thrombus shown in Figure 2.8 (Simmonds *et al.*, 2018). This dense formation then becomes strongly tethered to the surface and prevents further bleeding. The process is often called a 'cascade' due to several catalytic processes happening simultaneously to cause the resulting platelet aggregation.

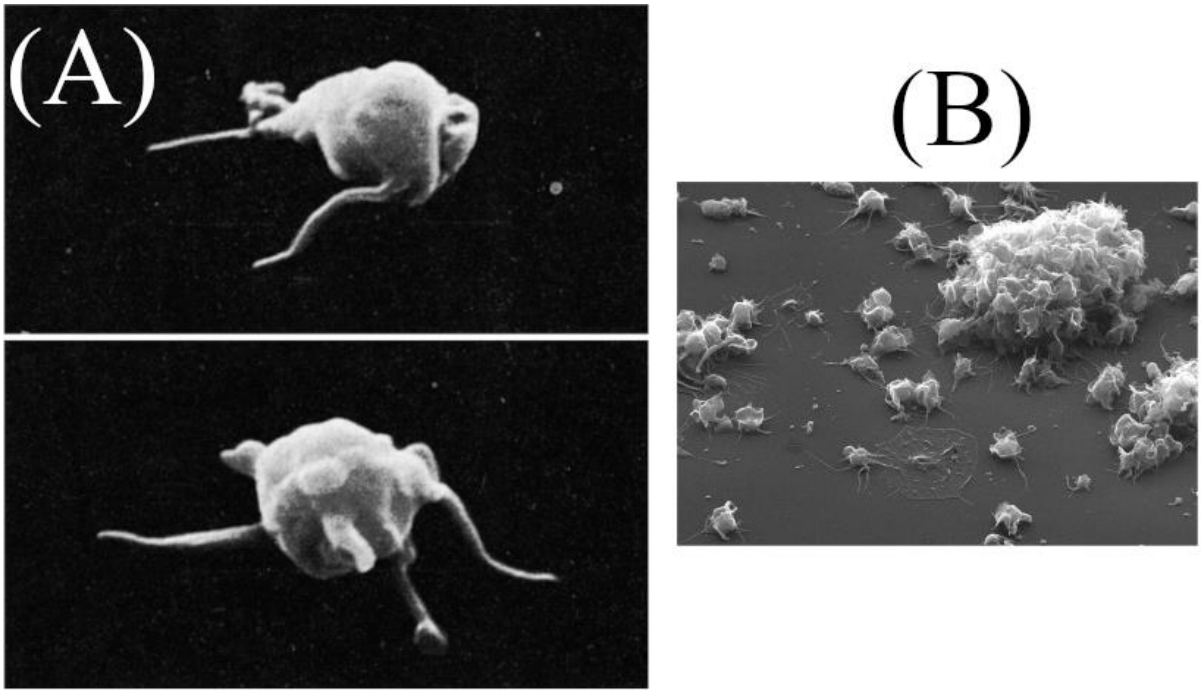

Figure 2.8: (A) – SEM image of activated platelets with large pseudopodia (Platelet diameter is approximately 2µm) (Reproduced with permission of the Licensor through PLSclear from p167 of '*The mechanics of the circulation 2nd Edition*' by Caro *et al.*, © Cambridge University Press 2012 (Caro *et al.*, 2011b)), (B) - SEM image of aggregated platelets on precoated silicone surfaces (Reprinted from Mechanical Circulatory and Respiratory Support, Chapter 19, Simmonds *et al.* (Simmonds *et al.*, 2018), *Blood-device interaction*, © 2018, with permission from Elsevier Inc.)

The haemodynamics of blood flow also play an important role in platelet transport/activation and thrombus (clot) formation. Thrombi typically form on the walls of arteries and veins, from the aggregation of RBC/platelets/proteins/cells into a dense clot. They can restrict blood flow, but also when dislodged (embolus) travel through the circulatory system and cause strokes/myocardial infarction in the brain or cardiovascular system respectively (Mustard and Packham, 1974). The shear rate within blood has been shown to affect the rate of platelet activation/adhesion, size of aggregates and the concentration of agonists (Anand, Rajagopal and Rajagopal, 2003;

AlMomani *et al.*, 2008; Anand and Rajagopal, 2017). Higher shear rates have been shown to deform specific platelet membranes which inhibit adhesion (Hellums *et al.*, 1987), uncoil vWF proteins so they protrude into the flow >7× longer (Yazdani *et al.*, 2017) and cause spontaneous aggregation between platelets at sufficiently high shear rates >10000 s^{-1} (Ruggeri *et al.*, 2006) in stenotic/pathologic arteries.

There is a well-documented trend of increased platelet concentration in the near-wall region (Cadroy and Hanson, 1990). This is thought to occur due to collisions with individual RBC (Skorczewski, Erickson and Fogelson, 2013), with migration increasing significantly with haematocrit levels in *in vitro* experiments (Turitto and Weiss, 1980). As platelets have also been associated with the coagulation of blood (Wagner, Steffen and Svetina, 2013), rouleaux formation and the role of RBC/platelet interaction has many clinical implications yet is both difficult to study *in vivo* and these interactions are limited to micro/meso-scale geometries (Skorczewski, Erickson and Fogelson, 2013).

2.4 Cardiovascular diseases

As the cardiovascular system is crucial to the supply and transport of oxygen/nutrients to all organs within the body, conditions which impact the cardiovascular system can have severe impacts on a patient's health. For several years, cardiovascular diseases (CVD) have been the leading cause of death worldwide, accounting for an estimated 31% of deaths worldwide in 2016 (*World Health Organisation - CVD Facts*, 2017). Given the important role of the coronary arteries in supplying oxygen to the heart, the impact of CVD is often directly related to conditions which affect these arteries in particular (Chatzizisis *et al.*, 2007).

In addition to the increase in morbidity associated with CVD, the healthcare treatment costs associated with CVD is £9 billion per year in the UK alone (BHF, 2019). As dietary risk factors are the largest contributors to CVD mortality, and with 24% of men and 26% of women in the UK being obese (Wilkins *et al.*, 2017), CVD related conditions place a significant strain on the National Health Service (NHS).

2.4.1 Atherosclerosis

Atherosclerosis begins as an inflammatory disease, affecting the endothelial surface of arteries/veins within the circulatory system (Chappell *et al.*, 1998). It causes a reduction in the artery diameter with the build-up of atherosclerotic plaques, which are an excessive build-up of low-density lipoproteins (LDL) in the arterial wall (Wentzel *et al.*, 2012).

The causes, progression, manifestation and associated conditions with atherosclerosis have been extensively studied *in vivo* (Caro, Fitz-Gerald and Schroter, 1971; Langille and O'Donnell, 1986; Malek and Alper, 2007). Atherosclerosis can be broadly categorised into three distinct stages (Figure 2.9):

- Inflammation of the endothelium resulting in increased intimal thickness (Desk, Williams and Health, 1992);
- Accumulation of small quantities of low-density lipoproteins and cholesterol within the intimal layer (fatty streak) (Stary *et al.*, 1994);
- Build-up of lipids, lipoproteins, fibrinogen and collagen within the 'core' of the plaque resulting in a significant reduction in lumen diameter (vascular remodelling) (Stary *et al.*, 1995).

Whilst coronary blood flow can remain relatively unaffected for mild stenosis (20-40% reduction in diameter), blood flow decreases significantly at around 70% stenosis and is clinically considered to be the 'critical burden' for which the most severe outcomes are likely (Stone, Coskun, Yeghiazarians, *et al.*, 2003; Stone *et al.*, 2011). There are several well established clinical risk factors for atherosclerosis, including: high cholesterol (Tall and Yvan-Charvet, 2015), high blood pressure (Berenson *et al.*, 1998), sedentary lifestyle (Mayer-Davis *et al.*, 1998) and smoking (Howard *et al.*, 1998). Unsurprisingly, atherosclerosis is often attributed to being the leading cause of death worldwide (Malek and Alper, 2007; Alberti *et al.*, 2009; Wentzel *et al.*, 2012).

The main cause of fatalities linked to atherosclerosis typically involve the deterioration of the plaque/lesion (Roberts, 1989), with two of the most significant complications being myocardial infarction (MI) and stroke (Mustard and Packham, 1974; Swirski and Nahrendorf, 2013), which are directly related with the rupture of the plaque (Bentzon *et al.*, 2014).

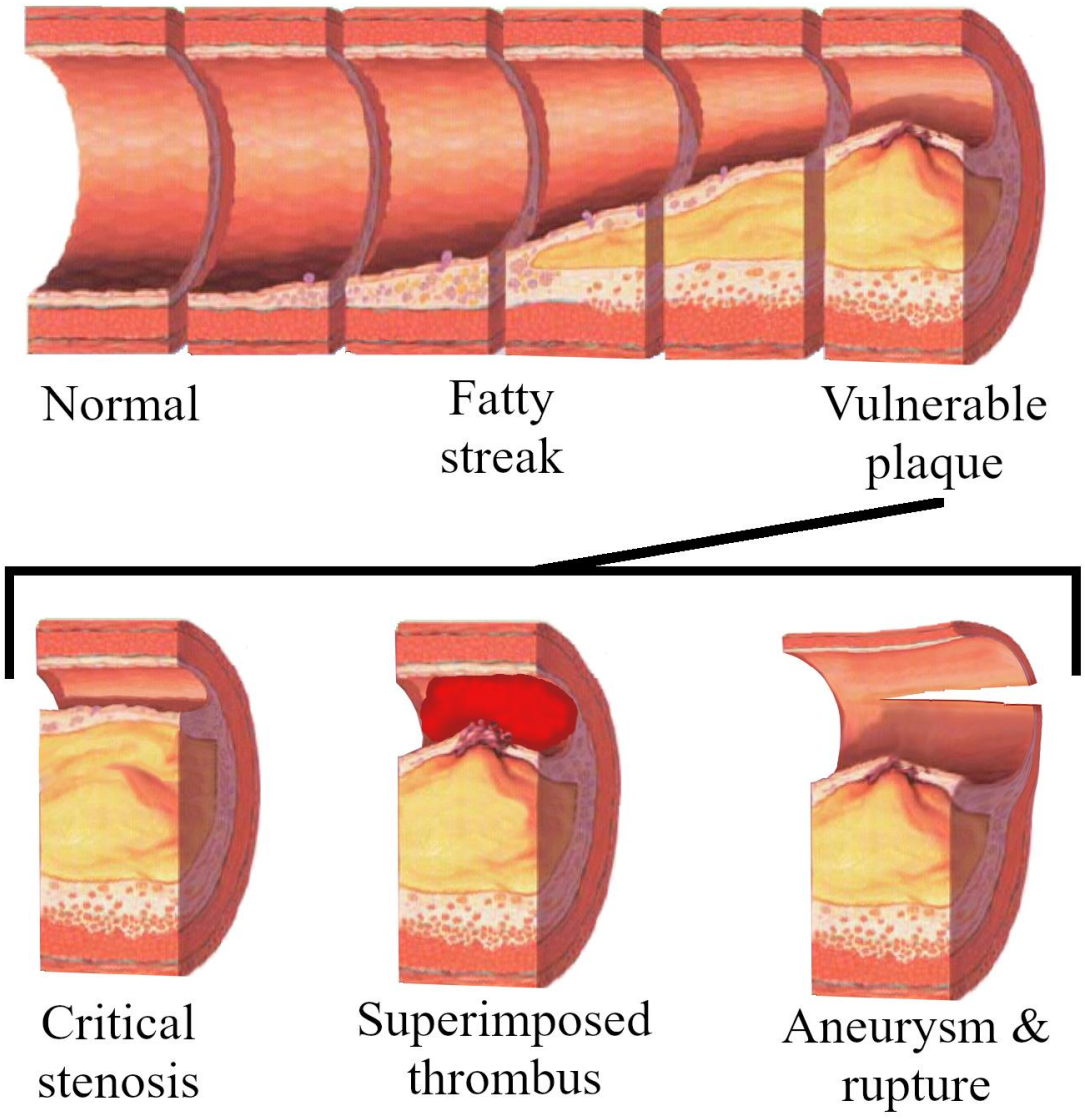

Figure 2.9: Diagram showing progression of atherosclerosis in an artery, including three examples of the most critical outcomes. (Created by Npatchett, reproduced under CC-BY 4.0 https://creativecommons.org/licenses/by-sa/4.0/deed.en, layout edited to be more linear)

A common location for plaque formation is on the outer walls of the left main coronary artery (LMCA) bifurcation where it splits into the left anterior descending (LAD) and left circumflex artery (LCx). An *in vivo* study of 140 patients analysing atherosclerotic plaque locations using intravascular ultrasound (IVUS) revealed the most typical presentations of atherosclerosis in the LAD-LCx bifurcation shown as percentages in Figure 2.10.

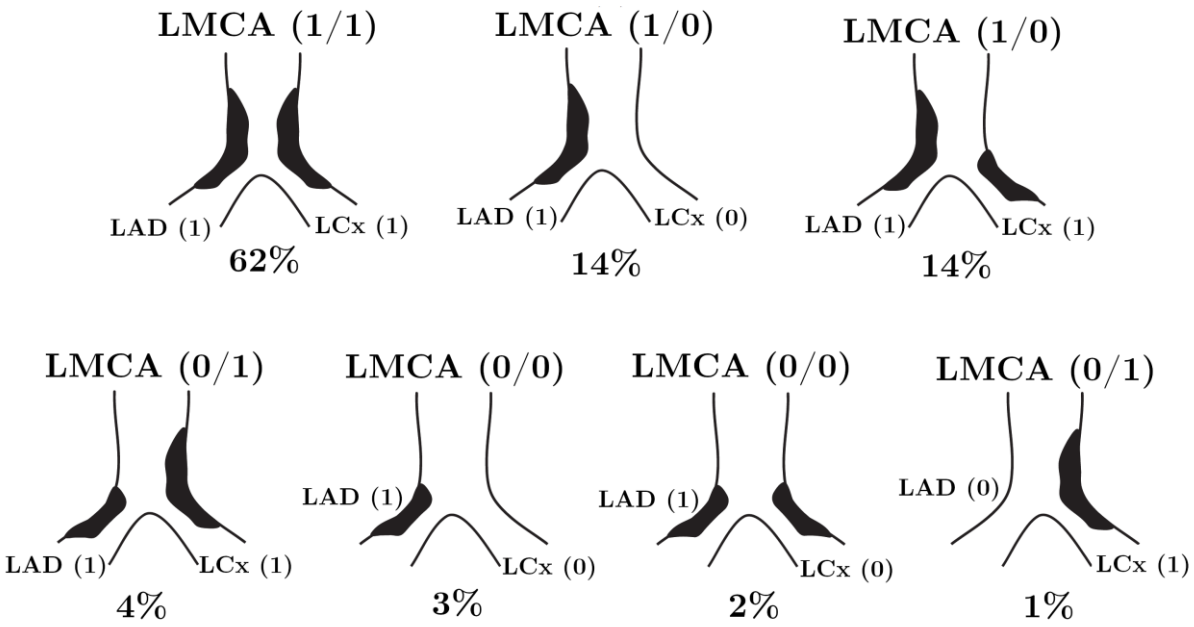

Figure 2.10: IVUS classification for LMCA plaque distribution. Continuous involvement from the distal LMCA into the proximal LAD artery is present in 90%. (Reprinted from Circulation: Cardiovascular Interventions, Vol 3 – Issue 2, Oviedo *et al.* (Oviedo *et al.*, 2010), *Intravascular ultrasound classification of plaque distribution in left main coronary artery bifurcations: where is the plaque really located?,* © 2010, with permission from Wolters Kluwer Health)

2.4.1.1 Importance of wall shear stress

Atherosclerosis is predominantly found in regions with low/reduced WSS (Wootton and Ku, 1999; Chiu and Chien, 2011), which can be found in: arterial bifurcations (such as the LCA in Figure 2.11), arterial curvature or distal to stenosis (Papaioannou *et al.*, 2006; Taylor and Figueroa, 2009; Oviedo *et al.*, 2010). The detailed effects of WSS on the healthy function of the endothelium has been extensively reviewed elsewhere (Chatzizisis *et al.*, 2007), with the main conclusions being that a healthy physiological WSS magnitude varying between 1.2 – 7 Pa during the cardiac cycle has been shown to be atheroprotective (Gimbrone *et al.*, 2001). With regions of time-averaged wall shear stress (TAWSS) below approximately 1 - 1.2 Pa being linked with the onset and progression of atherosclerosis (Stone, Coskun, Kinlay, *et al.*, 2003; Malek and Alper, 2007).

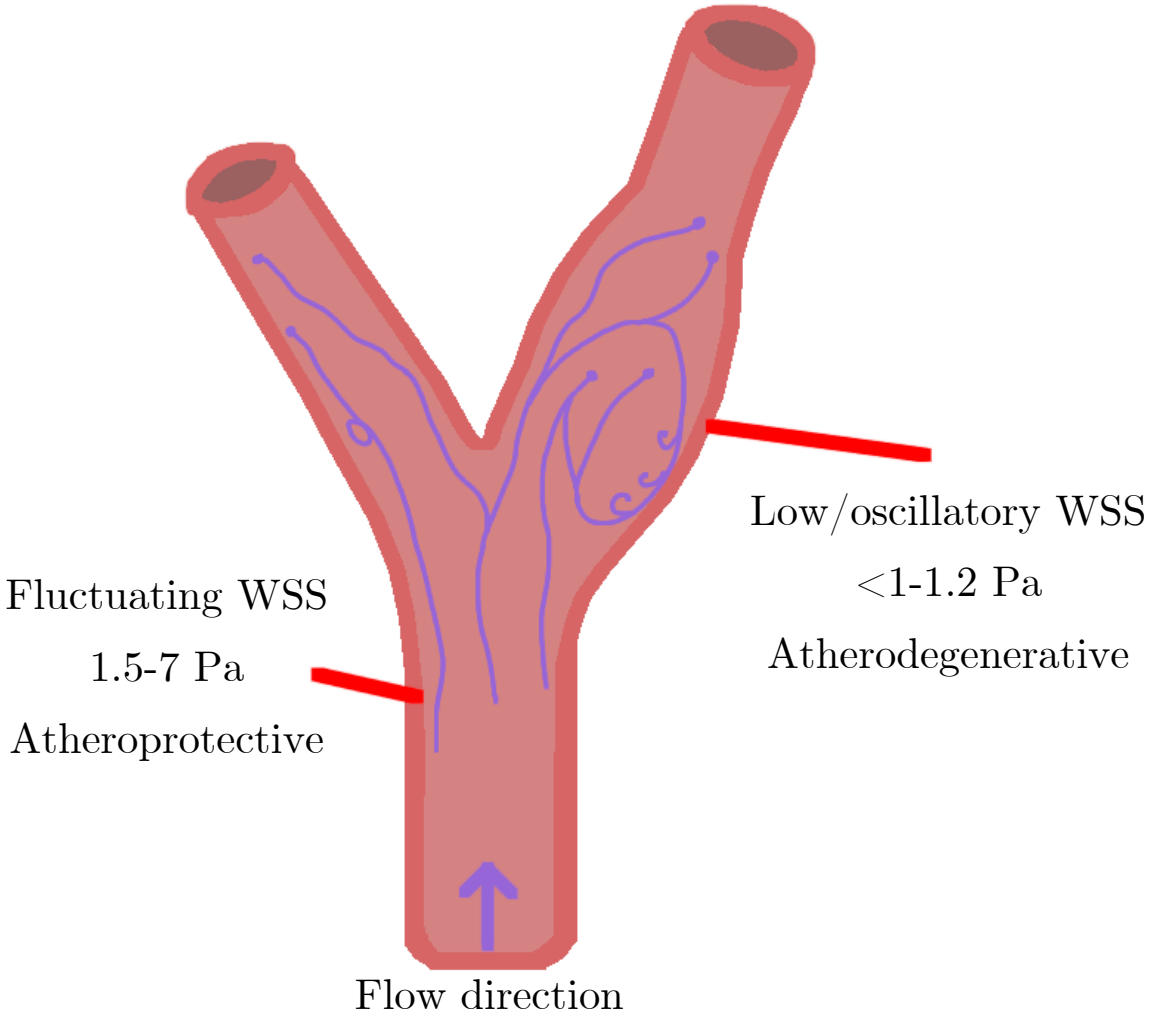

Figure 2.11: Diagram showing blood flow streamlines and recirculation patterns in a vessel representing a typical coronary bifurcation as shown in Figure 2.10, labelled to show associated regions of WSS magnitudes

Crucially it is the low-shear environment associated with the stagnant/recirculation zones which is not only atherodegenerative, but also the most relevant to the disturbed haemodynamics and rheology of blood. Indeed these two effects are unlikely to be a coincidence, with the disruption to healthy physiological blood flow catalysing the onset and progression of atherosclerosis with increased residence times of LDL (Stangeby and Ethier, 2002; Himburg *et al.*, 2004).

In addition to the magnitude of WSS affecting atherosclerosis, the other important consideration is its direction/oscillation. In regions of recirculation where the flow direction oscillates across the cardiac cycle, not only are TAWSS values pathologically low (De Keulenaer *et al.*, 1998; Cunningham and Gotlieb, 2005), but oscillatory flow also increases the adhesion of leucocytes to the endothelium (Chappell *et al.*, 1998) causing inflammation.

2.4.2 Atherothrombosis

Atherothrombosis is a critical complication of atherosclerosis, where the surface of the plaque/lesion accumulates a superimposed thrombus (Figure 2.9) formed from: smooth muscle cells, fibrinogen and aggregated platelets (Viles-Gonzalez, Fuster and Badimon, 2004; Davi and Patrono, 2007). The accumulation of this superimposed thrombus (Figure 2.9) is weakly attached to the surface of the plaque, and if dislodged by pathological effects such as: increased WSS, high shear rates and flexion it can cause a thrombus embolism which is often fatal (Falk, Shah and Fuster, 1995; Badimon, Padró and Vilahur, 2012).

2.5 Chronic kidney disease

2.5.1 Pathology

Chronic kidney disease (CKD) is a long-term condition describing the gradual or total loss of kidney function (Renal failure). The kidneys are responsible for filtering the blood and removing excess water/waste products. Approximately 10% of adults in the UK suffer from CKD, with a further 10% of those requiring medical intervention in the form of haemodialysis or transplant (UK, 2020). Kidney function can be measured using the glomerular filtration rate (GFR) measured in mL/min, further classified in Table 2.2.

Table 2.2: Categorisation of kidney function by GFR

Stage	Description	GFR (mL/min)
1	Signs of kidney damage (e.g., protein in urine) but normal GFR	>90
2	Kidney damage with mild decrease in GFR	60-89
3a	Moderate decrease in GFR	45-59
3b	Moderate decrease in GFR	30-44
4	Severe reduction in GFR	15-29
5	Kidney failure	<15

Many studies have established the links between CKD and the increased incidence of CVD (Menon, Gul and Sarnak, 2005; Liu *et al.*, 2014). Cardiovascular mortality was found to be 2× and 3× more likely in patients with Stage 3 and 4 CKD respectively, compared to patients with healthy kidney function (Matsushita *et al.*, 2010). The decrease in GFR and hence increase in toxic waste products within the blood is associated with: increased stenosis (Nakano *et al.*, 2010), coronary calcification (Chonchol *et al.*, 2008), and fatal MI with a significant increase in morbidity below 15 mL/min (Herzog *et al.*, 2011).

2.5.2 Treatment

The most common interventions for CKD is the use of either haemodialysis (HD) catheters, or an arteriovenous fistula (AVF). Whilst AVF are often recommended as the first choice (Santoro *et al.*, 2014), there is still a large preference for HD catheters, with 18% and 44% of US and Canadian CKD patients receiving HD, respectively (Fissell *et al.*, 2013). Reason's for prevalent use of HD over AVF are (Hayes *et al.*, 2012; Shroff, 2019):

- AVF takes time to form (Often months), and therefore acute HD or interim treatment must be performed with HD catheters;
- AVF can be painful, and therefore HD catheters are often used for younger patients.

The basic function of a HD catheter is to remove blood from the body, filter it externally, and then resupply it. The HD catheter is commonly inserted into the jugular vein in the neck where it extends through to the superior vena cava (SVC) and into the right atrium (RA) of the heart (Figure 2.12). Long term or chronic use HD catheters are 'Tunnelled' referring to the permanent fixture (port) placed under the skin allowing for convenient access during dialysis procedures.

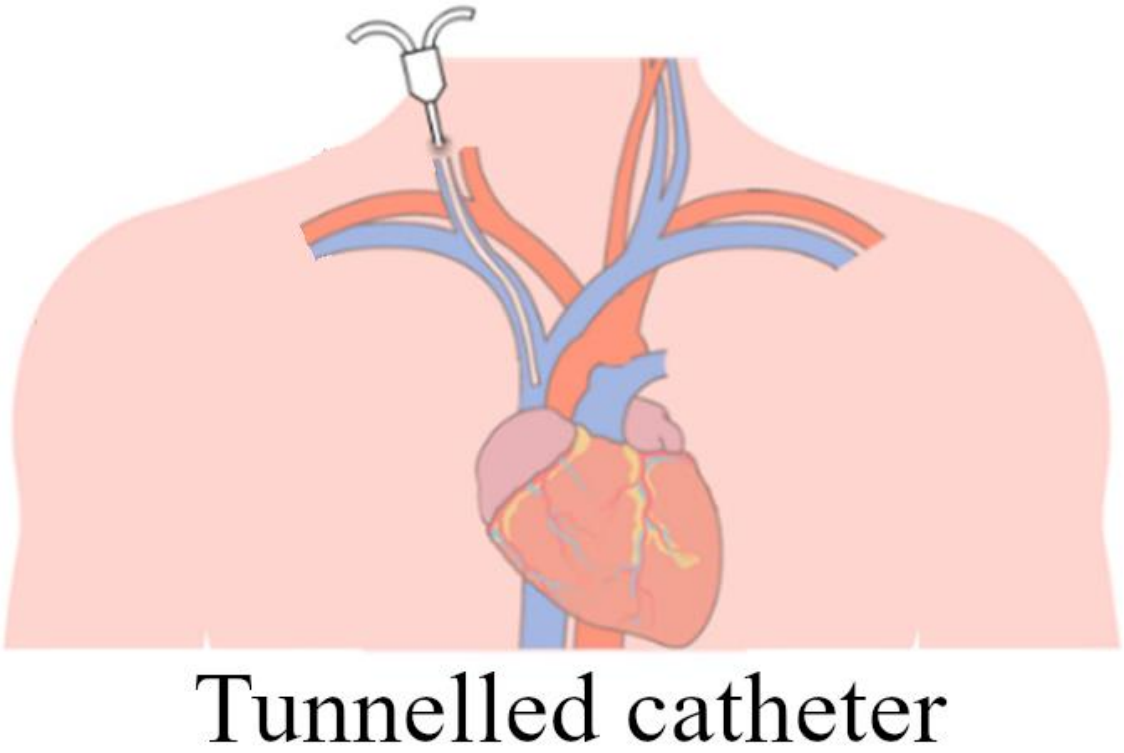

Figure 2.12: Diagram showing insertion of tunnelled HD catheter (Adapted from (Mathew *et al.*, 2019))

A typical HD catheter consists of a circular tube (approximately 5 mm in diameter) of silicone/polyurethane, separated by a thin septum along its centre to create two separate, semi-circular lumens (Mathew *et al.*, 2019). The 'arterial' lumen carries blood away from the heart to the dialysis machine, and the 'venous' lumen returns filtered

blood to the heart. There are a wide range of HD catheter tip designs available on the market, all trying to maximise the objective performance of the catheter. Some of the key design considerations for the optimal performance and patency of chronic HD catheters are listed in Table 2.3, with examples of three prevalent tip design styles shown in Figure 2.13.

Table 2.3: HD catheter design specifications and associated reasons

Specification	Description
High blood flow rate	Higher blood flow rates lower the time spent receiving dialysis, with dysfunctional flow rates categorised as $<250-300$ mL/min (Moist, Hemmelgarn and Lok, 2006).
Low recirculation	Recirculation refers to the re-filtration of previously dialysed blood. This is inefficient, increases time spent receiving dialysis and could result in failing to meet the guideline for rate of dialysis (Kousoula *et al.*, 2019).
Prevent clotting	Biofilm/thrombus formation occurs on the catheter surface, with the use of surface coatings or anticoagulants (heparin) used to reduce this (Mathew *et al.*, 2019).
Reduce fibrin formation	Fibrin formation occurs on the surface of the tip and can occlude side-holes, reducing flow rates and requiring removal/reinsertion. Higher shear rates are associated with increased fibrin formation (Lucas *et al.*, 2014).

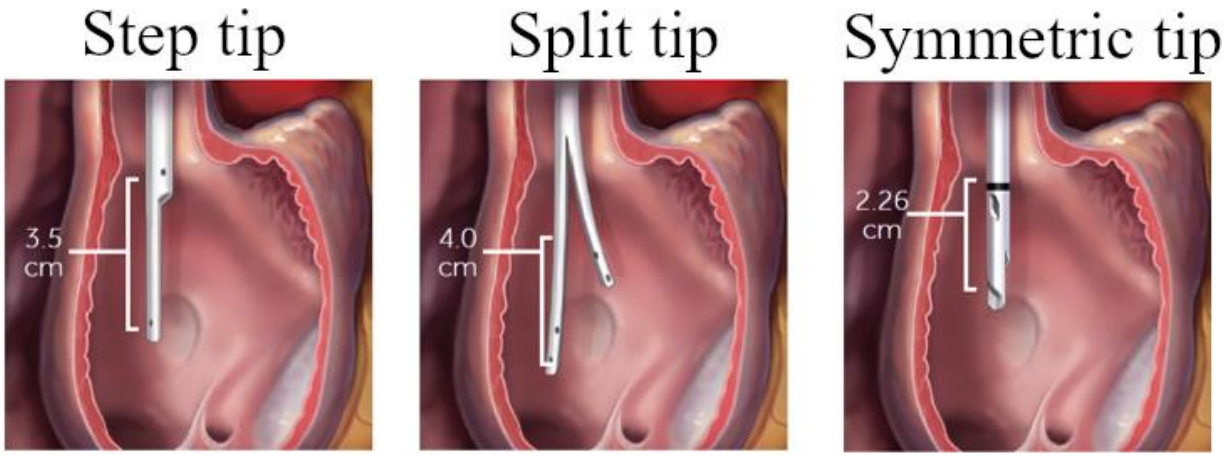

Figure 2.13: Diagram of three common HD catheter tip designs within the right atrium (Adapted from *Palindrome™ Precision Chronic Dialysis Catheter Family*, with permission from Medtronic Inc.)

2.5.3 Catheter malfunctions

Chronic HD catheters are susceptible to a wide range of complications that result in premature removal and reinsertion, with a review of common complications by Miller *et al.* (Miller, MacRae, *et al.*, 2016). The predominant complication is bloodstream infections at a rate of 1-5 incidences per 1000 catheter days (Miller, Clark, *et al.*, 2016), caused by bacterial contamination either during insertion or via the tunnelled port used to connect the catheter to the dialysis machine. Whilst these conditions are severe, solutions are mostly operator based, involving improved sterilisation techniques and preventative antibiotic creams (Lok *et al.*, 2020).

As approximately one third of HD catheter removals are due to insufficient blood flow rates (Miller, MacRae, *et al.*, 2016), there is significant scope to alter tip design in an attempt to increase both the flow rate and patency of HD catheter tips. The

accumulation of fibrin around the tip of the catheter begins to form within 24 hours after insertion and can occlude the hole openings of the catheter as seen in Figure 2.14.

Figure 2.14: Fibrin sheath formation resulting in complete occlusion of the catheter tip (Courtesy of (Miller, MacRae, *et al.*, 2016)), Reproduced under CC-BY-NC https://creativecommons.org/licenses/by-nc/2.0/)

This fibrin growth and formation is affected by the shear rate of the blood, platelet concentration/activation and additional factors such as the surface texture of the catheter tip (Lucas *et al.*, 2014). Increased shear stress is linked to platelet activation, with subsequent adhesion/aggregation of fibrin and other leucocytes forming thrombi which if dislodged can lead to serious complications (Gross and Wang, 1981).

Analysis of *in vivo* formed fibrin using scanning electron microscopy (SEM) has shown increased build-up in the high shear regions around side-holes in HD catheter tips (Figure 2.15A), with the contrast in surface texture resulting from cutting/grinding the tip geometry during manufacture shown below in Figure 2.15B.

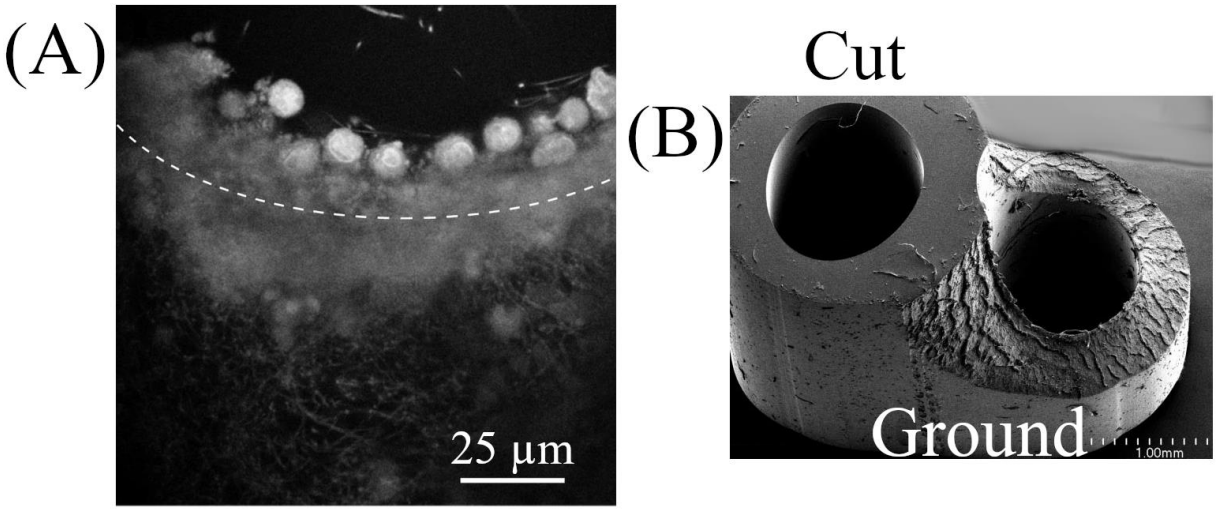

Figure 2.15: (A) – SEM image of *in vivo* fibrin formation around circular catheter side hole (dotted line) in high shear region. Dark grey regions are thicker formation, with white dots being white blood cells. (Reproduced from '*Blood Flow in Hemodialysis Catheters: A Numerical Simulation and Microscopic Analysis of In Vivo-Formed Fibrin'* by Lucas *et al.* in Artificial Organs 2014, Licensed from John Wiley and Sons) (B) – Optical microscopy image of surface texture on HD catheter from cutting and grinding (Courtesy of Twardowski *et al.*)

As there are a wide range of available design solutions for HD catheter tips, multiple randomised control trials and computational models have been unable to conclusively identify an optimal solution, or even clarify which design features are beneficial (Trerotola *et al.*, 2002; O'Dwyer *et al.*, 2005; Vesely and Ravenscroft, 2016; Lok *et al.*, 2020).

2.6 Computational fluid dynamics

2.6.1 Overview

Computational fluid dynamics (CFD) is a numerical technique which refers to the study and analysis of fluid flows. The experimental and theoretical study of fluid mechanics has allowed for detailed mathematical descriptions governing the behaviour of fluids. However, these equations are often a complex system of nonlinear partial differential equations (PDE) with no analytical solution (Fefferman, 2000). With the modern increases in computational power and advances in numerical approximation techniques, CFD can be used to accurately estimate the behaviour of fluids, and hence has a wide range of engineering applications including flow cavitation, mass transfer and external aerodynamics (Ekaterinaris and Platzer, 1998; Kunz *et al.*, 2000; Berning and Djilali, 2003).

Within the field of biomedical engineering, CFD is especially useful as it allows for the detailed study of physiological phenomena which would otherwise be inaccessible through *in vivo* measurements and scans. Whilst medical imaging can be used to provide clinically useful diagnostic data, it is limited to measuring directly observable parameters such as flow velocity or pressure – whereas CFD can be used for a much more comprehensive evaluation of the fluid behaviour (Gallo *et al.*, 2012). A summary of papers showing a range of cardiovascular scenarios where CFD has currently been

applied to is provided for reference in Table 2.4, all of which assume a smooth artery wall.

Table 2.4: Summary of cardiovascular papers showing the range of benefits from CFD models

Pathology	Application of CFD
Aneurysms	Identifying early risk factors through assessing haemodynamics and modelling risk of rupture from patient-specific models (Humphrey and Taylor, 2008).
Arterial stents	Evaluating effect of stents on the endothelial surface, and investigating how biomechanical processes lead to deterioration (Van Der Heiden *et al.*, 2013).
Drug delivery	Investing effects of particle sizes/shapes in drug delivery to the arterial surface, and the role haemodynamics can play (Ta *et al.*, 2017).
Valve dysfunction	Impact of mitral valve incompetence on regurgitation and how to design more effective artificial valves (Yoganathan, He and Jones, 2004).
Ventricle malformation	Evaluating surgical outcomes of the Fontan procedure, investigating optimal strategy depending on patient size/type of malformation (Degroff, 2008).

2.6.2 Assessing atherosclerosis with CFD

As atherosclerosis is one of the most common types of CVD it has been studied extensively both *in vivo* and *in silico*. Modern CFD models can be used to increase clinical understanding in the onset of atherosclerosis by examining the mechanisms of LDL accumulation within the intima (Ethier, 2002; Olgac, Kurtcuoglu and Poulikakos, 2008) (Fatty streak) and even for predicting likely locations of plaque growth from

patient scans (Rikhtegar *et al.*, 2012; Lee *et al.*, 2019). These predictions are based upon correlating haemodynamic parameters to the size/shape/location of *in vivo* plaque formation, with the most important parameters defined below in Table 2.5.

Table 2.5: Mathematical definitions of haemodynamic parameters associated with atherosclerosis

Parameter	Definition	Description
Wall shear stress (WSS)	$\tau_w = \mu \left.\frac{\partial u_t}{\partial n}\right\|_{wall}$	Instantaneous shear stress exerted by the blood flowing over the lumen wall.
Time-averaged wall shear stress (TAWSS)	$\bar{\tau}_w = \frac{1}{T}\int_0^T \lvert\vec{\tau}_w\rvert \, dt$	Time-averaged value of WSS, where T is the length of the cardiac cycle.
Oscillatory shear index (OSI)	$\theta_i = \frac{1}{2}\left(1 - \frac{\left\lvert\int_0^T \tau_w \, dt\right\rvert}{\int_0^T \lvert\tau_w\rvert \, dt}\right)$	Dimensionless parameter to indicate how much the flow is oscillating during the cardiac cycle. Value of 0 indicates unidirectional flow, and 0.5 indicates highly oscillatory flow (He and Ku, 1996).
Relative residence time (RRT)	$t_r = \frac{k}{(1-2\theta_i)\bar{\tau}_w}$	Relative measure used to indicate regions of flow stagnation in the near-wall region. k is an arbitrary constant set to $k = 1$ (Himburg *et al.*, 2004).

The classification of material properties and composition of plaques has allowed for CFD simulations to more accurately model plaque rupture due to haemodynamic forces (Faghihi *et al.*, 2014; Karimi, Navidbakhsh and Razaghi, 2014). The advantage of CFD studies here is that a comprehensive assessment of the size/shape and critical stenosis percentage can be performed to establish which plaques are most susceptible to rupture (Tang *et al.*, 2005; Samady *et al.*, 2011).

Whilst currently these predictive models are purely used as research/proof-of-concept, with increasing computational power and model automation (Nguyen *et al.*, 2015), there is potential for patient-specific CFD models to be used to aid clinical decision making in the future (Kung *et al.*, 2013). In more severe cases of atherosclerosis, CFD can be used to assess the impact of stenosis on haemodynamics and investigate which factors are relevant to the most critical outcomes (Feldman and Stone, 2000). This can then be used to evaluate current treatment guidelines, to ensure the last resort surgical/medical interventions (angioplasty, bypass, grafts or stents) are taken at the correct time.

2.6.2.1 Importance of surface roughness

Early identification of atherosclerotic plaques/lesions allows for immediate preventative measures to be taken, reducing the risk of progression to a more serious burden, a strategy which has been more eloquently summarised by others as *'Prevention is better than cure'*. As discussed previously, the first detectable presentation of atherosclerosis is increased accumulation of LDL in the intimal layer of the artery, with the resulting increase in intimal thickness being measured *in vivo* for diagnostic purposes using ultrasound (McCrindle *et al.*, 2007).

Crucially, this increased accumulation of LDL has been shown to be preceded by an increase in surface roughness of the lumen (Schmidt-Trucksäss *et al.*, 2003). As the magnitude of arterial lumen surface roughness is in the micro scale, limitations on ultrasound resolution make a thorough assessment for diagnostic purpose challenging.

An example of surface roughness on an *ex vivo* sample of porcine coronary artery created using optical microscopy (50× magnification, 323 × 323 µm) is shown for reference below in Figure 2.16.

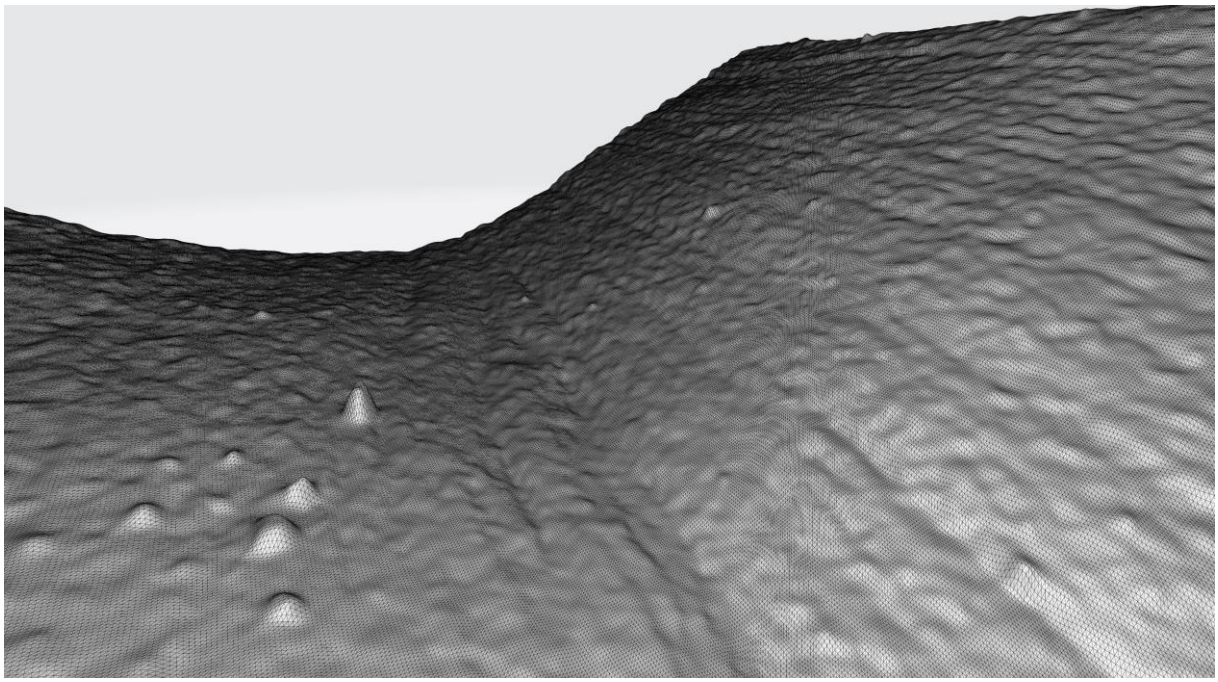

Figure 2.16: Representative surface roughness on segment of porcine coronary artery obtained from stereoscopic reconstruction of optical microscopy images using a triangle mesh in MATLAB (Spikes are imaging artefacts, their causes are explained by Burton *et al.* (Burton *et al.*, 2019)).

Current CFD models all neglect the role of lumen surface roughness in the formation/progression of atherosclerosis, partly due to a lack of precise measurements and the inherent difficulties in accurate multi-scale modelling. It is unclear how the role of surface roughness will alter the haemodynamics/rheology of blood in this region, including the transport of oxygen/nutrients to the endothelium, effectiveness of drug delivery as well as increasing the diffusion of LDL into the endothelium during the fatty-streak formation (Olgac *et al.*, 2009; Ta *et al.*, 2017).

2.6.2.2 Bifurcation haemodynamics

As discussed previously, bifurcations are prone to atherosclerosis due to the natural low-shear environment occurring on the outer walls. Previous CFD studies have investigated many aspects of the haemodynamics of bifurcations in an attempt to classify how different anatomical features impact atherosclerosis. The branch angle of the bifurcation has been thought to significantly impact the low-shear distributions, however, a study by Chiastra *et al.* showed these contributions were negligible compared to the curvature/torsion of the vessel (Chiastra *et al.*, 2017). These effects were further quantified by De Nisco *et al.* who demonstrated that vessel torsion is responsible for generating a helical flow pattern which has atheroprotective qualities (De Nisco *et al.*, 2019). Interestingly, there is some evidence that features (ridges) on the surface of the coronary artery follow a helical pattern, swirling along its length as shown in Figure 2.17 (Burton, Freij and Espino, 2017) (similar to a rifled gun barrel); although it is unclear if this is responsible for/caused by the helical flow pattern (chicken and egg scenario).

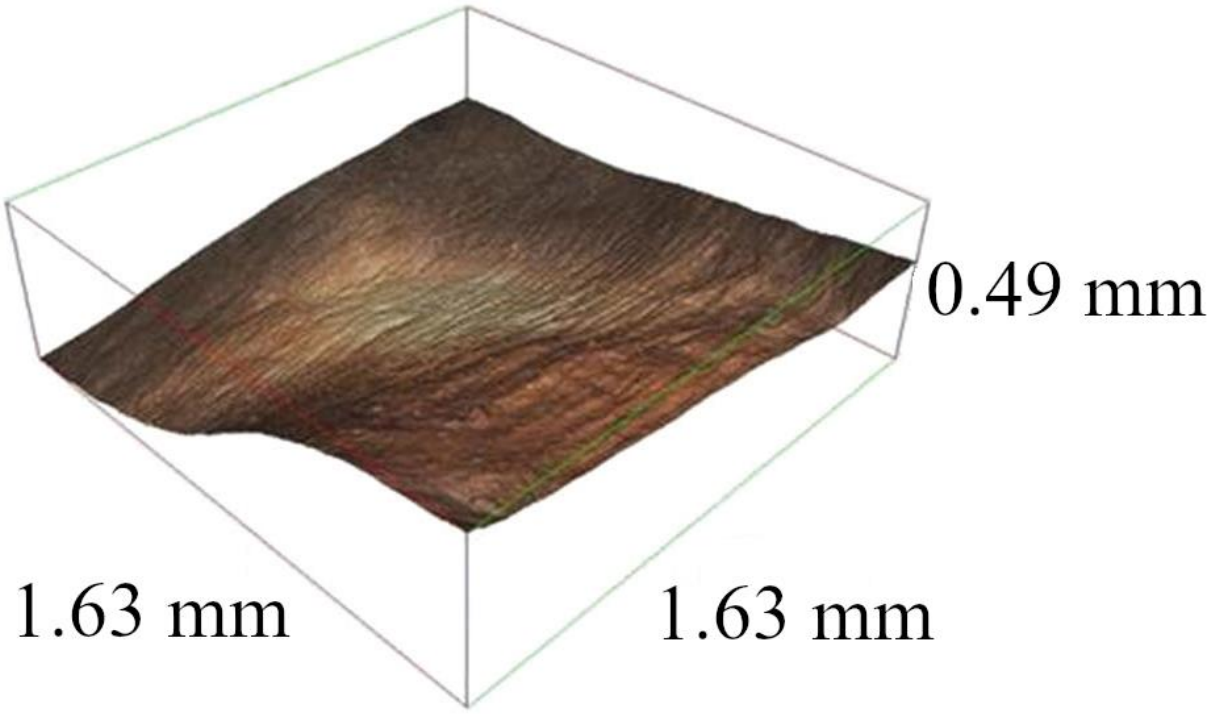

Figure 2.17: Helical ridges along the length of porcine coronary arteries from (Burton, Freij and Espino, 2017), reproduced under CC-BY 4.0 https://creativecommons.org/licenses/by-sa/4.0/deed.en

In stenosed bifurcations, the combination of elevated shear stress at the throat of the stenosis and increased residence times in the low-shear environment create the ideal conditions for shear-induced platelet activation and subsequent adhesion (Atherothrombosis) (Davi and Patrono, 2007). Massai *et al.'s* study on the carotid bifurcation showed platelets in the near-wall region experiencing significantly elevated shear stress and increased residence times, with helical flow minimising activation through increased platelet transport away from the walls (Massai *et al.*, 2012).

Finally, the importance of the rheology of blood and non-Newtonian effects are more significant in bifurcations due to the range of shear-rates and residence times that can occur (Soulis *et al.*, 2008). Key areas where non-Newtonian rheology are important

were highlighted by Kabinejadian *et al.* as the flow dividing wall and the outer/distal walls, which are the most common sites for atherosclerotic plaque formation (Kabinejadian and Ghista, 2012).

2.6.3 Rheology and haemodynamics

Any improvements that can be made to modelling the rheology of blood will improve all other cardiovascular CFD models, as these techniques can be implemented relatively easily once evaluated. There are a wide range of approaches to mathematical descriptions of blood's rheology, varying from a simple single-phase Newtonian viscosity to complex multiphase models with non-Newtonian RBC behaviour. With typical shear rates in healthy arteries approaching the Newtonian limit, and residence times thought to be insufficient for RBC aggregation to occur, single-phase Newtonian models are seemingly most common for cardiovascular CFD models (Galidi *et al.*, 2008; Arzani, 2018).

Whilst comparisons between Newtonian and non-Newtonian single-phase models have shown small differences in healthy cases (Johnston *et al.*, 2006), it is the disturbed haemodynamic environment arising in pathologic conditions where the non-Newtonian rheology is most important (Caro *et al.*, 2011b). Specifically in these regions the multiphase behaviour of blood is crucial; rouleaux formation, increased sedimentation of RBC, platelet adhesion and increased plasma concentration all play significant roles in the deterioration of the endothelium and assessment of shear stress-based parameters. Increased plasma viscosity has been linked to coronary heart disease

(Junker *et al.*, 1998), and abnormal haematocrit is symptomatic of several CVD which further shows the importance of multiphase modelling in pathological cardiovascular applications in particular (Somer and Meiselman, 1993).

2.7 Fundamental theory

2.7.1 Incompressible Navier-Stokes

By considering an infinitesimally small volume of fluid and applying the laws of continuum mechanics, the fundamental equations governing the flow of fluids can be defined, namely the mass continuity and the conservation of momentum. In a fluid of constant density, for mass to be conserved, the flow into and out of an infinitesimal volume must remain constant and hence gives rise to the mass continuity equation below in Equation 2.2.

$$\nabla \cdot U = 0 \qquad (2.2)$$

where U is the vector velocity field and ∇ is the differential 'del' operator, used to represent the gradient/divergence of scalar/vector field, respectively. Often the contribution of external 'body forces' such as those due to gravity are ignored due to their negligible contributions. Using a similar approach considering the balance of forces within a differential volume, applying Newtons 2nd law the conservation of momentum is defined below in Equation 2.3.

$$\underbrace{\frac{\partial \boldsymbol{u}}{\partial t}}_{unsteady} + \underbrace{(\boldsymbol{u}\cdot\nabla)\boldsymbol{u}}_{convection} - \underbrace{\nu\nabla^2\boldsymbol{u}}_{diffusion} = -\nabla p^* \qquad (2.3)$$

where $\boldsymbol{u}$ is the velocity vector, ν is the kinematic viscosity and p^* is the hydraulic pressure (Equations 2.4 & 2.5 respectively).

$$\nu = \frac{\mu}{\rho} \qquad (2.4)$$

$$p^* = \frac{p}{\rho} \qquad (2.5)$$

Together these equations form the backbone of CFD analysis, and can be modified/extended to include additional effects such as temperature, species transport and mass exchange. These equations are challenging to solve numerically as there is a non-linear term (convection) in the momentum conservation equation, there is no computable equation for pressure and any velocity field values must simultaneously satisfy the momentum equation and the restriction of mass continuity.

2.7.2 Finite-volume method

To obtain a numerical approximation of fluid flow within some geometry/volume, it first must be decomposed into a computational mesh. The mesh is a discrete way of representing our continuous fluid domain, allowing for the solution of the governing equations above at a finite number of individual points. The basic concept behind a finite-volume (FV) mesh is shown below for a 3D case in Figure 2.18.

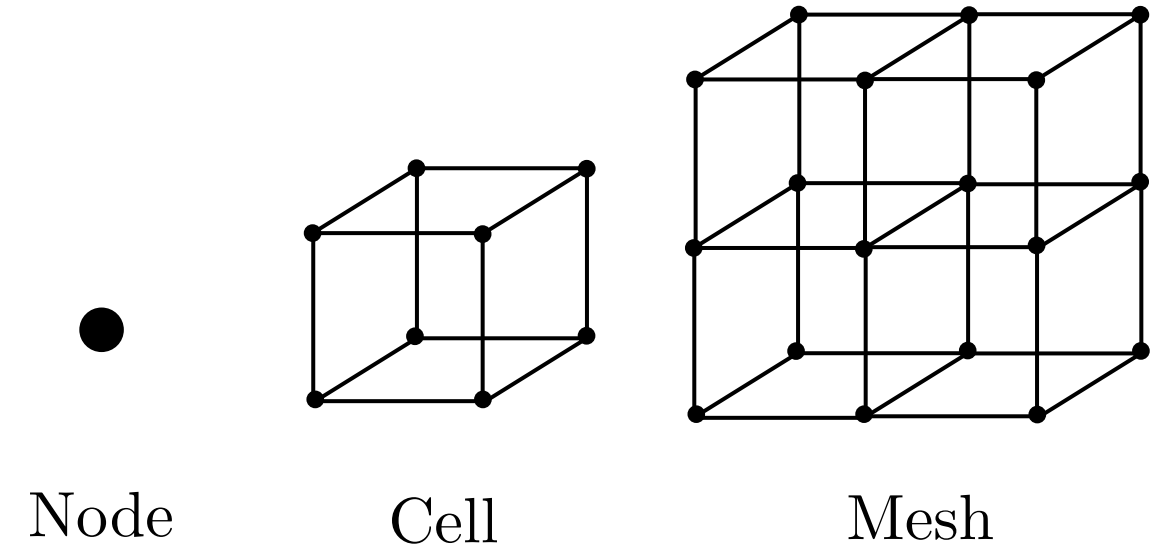

Figure 2.18: Basic components of a mesh used to discretise a 3D fluid domain

The purpose of the FV method is to discretise the Navier-Stokes (NS) equations into a system of algebraic equations which can be written in general matrix form and solved using a numerical scheme such as SIMPLE (Semi-Implicit Method for Pressure Linked Equations) or PISO (Pressure-Implicit with Splitting of Operators), which are discussed later. It is a cell-centred approach where flow variables such as velocity, temperature and pressure are stored within the centroid of each cell (P) as shown in Figure 2.19. Flow variables at the boundaries of the domain can be expressed either as magnitudes at points on the surface (Dirichlet) or as the normal derivative (Neumann).

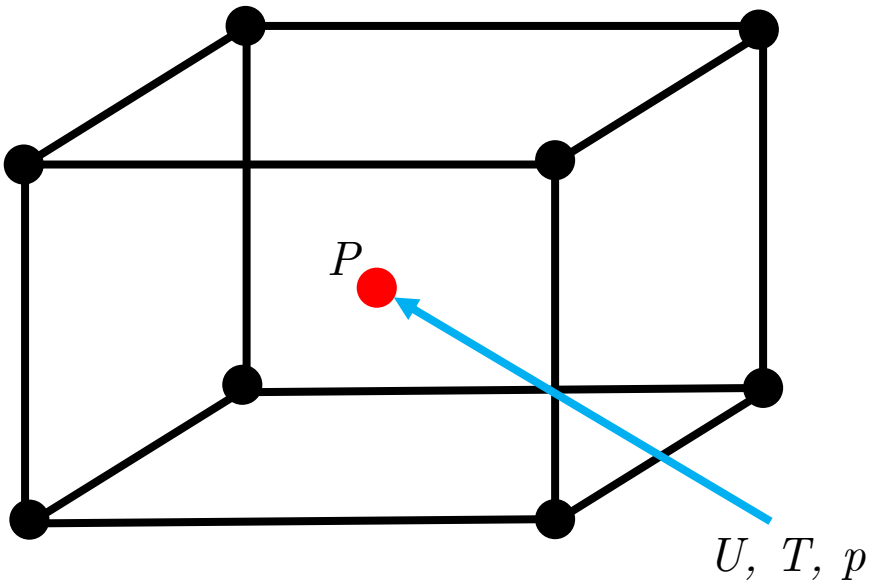

Figure 2.19: Centroid of cell in FV method where flow variables are stored

The first step in the discretisation process is to integrate the momentum equation term by term across the cell volume (Equation 2.6).

$$\int_V \frac{\partial \boldsymbol{u}}{\partial t}\, dV + \int_V (\boldsymbol{u}\cdot\nabla)\boldsymbol{u}\, dV - \int_V \mu\nabla^2\boldsymbol{u}\, dV + \int_V \nabla p^*\, dV = 0 \qquad (2.6)$$

The unsteady term does not vary across the volume and is easily computed (Equation 2.7).

$$\int_V \frac{\partial \boldsymbol{u}}{\partial t}\, dV = \frac{\partial \boldsymbol{u}}{\partial t} V \qquad (2.7)$$

The convection, diffusion and pressure gradient terms are more complex and require the divergence theorem to solve. For example, the convection term represents how the volume flux exiting each face of the volume 'convects' the velocity field in each direction. By applying the divergence theorem (Equation 2.8) to the convective term, it can be expressed as a surface integral (Equation 2.9).

$$\int_V \nabla \cdot \boldsymbol{F}\, dV = \int_S \boldsymbol{F} \cdot \hat{n}\, dS \qquad (2.8)$$

where F is a general vector, S is the area of each surface of the volume and $\hat{n}$ is the unit normal vector between the cell centroid, P, and the face.

$$\int_V (\boldsymbol{u} \cdot \nabla)\boldsymbol{u}\, dV = \int_S [\boldsymbol{u}(\boldsymbol{u} \cdot \hat{n})]\, dS \qquad (2.9)$$

Note that the inner term $(\boldsymbol{u} \cdot \hat{n})$ simply represents the volume flow rate out of the surface. This expression can be further simplified (Equation 2.10), as the cell has a finite number of faces (M), visualised in Figure 2.20.

$$\int_S [\boldsymbol{u}(\boldsymbol{u} \cdot \hat{n})]\, dS = \sum_{i=1}^{M} \int_S [\boldsymbol{u}_i(\boldsymbol{u}_i \cdot \hat{n}_i)]\, dS_i \qquad (2.10)$$

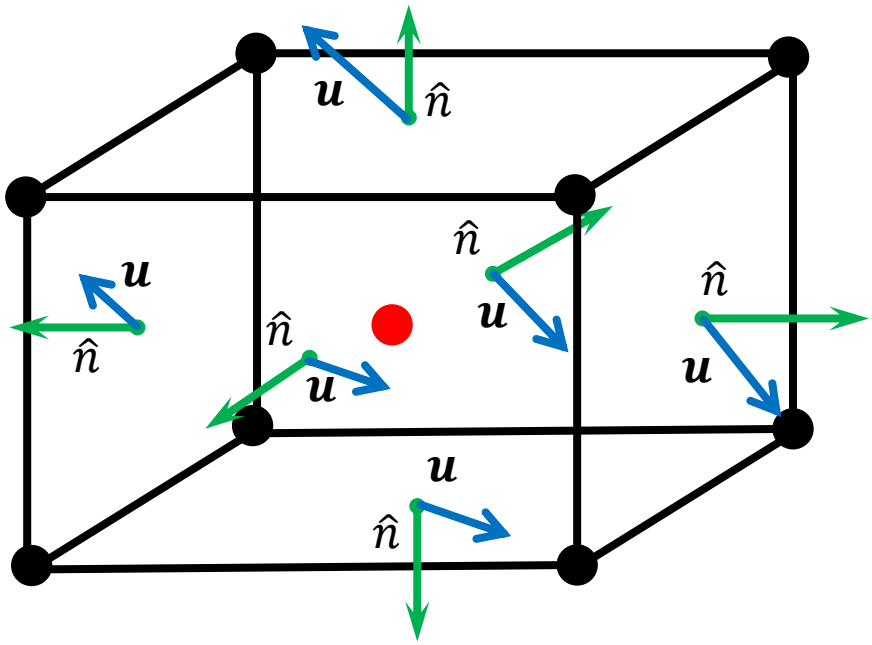

Figure 2.20: Volume flux out of the cell, viewed as the flux from each surface

The main approximation of the FV approach is now instead of integrating the velocity across this surface, it is instead assumed to vary linearly and hence the velocity at just the face centre is used in Equation 2.11.

$$\sum_{i=1}^{M} \int_{S} [\boldsymbol{u_i}(\boldsymbol{u_i} \cdot \hat{n}_i)]\, dS_i \approx \sum_{i=1}^{M} \boldsymbol{u_{fi}}(\boldsymbol{u_{fi}} \cdot \hat{n}_{fi}) S_i \qquad (2.11)$$

Note that $\boldsymbol{u_{fi}}$ corresponds to the face centred velocity vector on each face of the cell. The final result in Equation 2.11 is an unknown quantity ($\boldsymbol{u_{fi}}$) multiplied by scalar coefficients which can be generalised into a matrix. Using a similar approach, the advection term of the continuity equation can also be written in this manner (Equation 2.12).

$$\int_{V} \nu \nabla^2 \boldsymbol{u}\, dV \approx \sum_{i=1}^{M} \left[\nu(\nabla \boldsymbol{u_{fi}}) \cdot \hat{n}_{fi}\right] S_i \qquad (2.12)$$

Recalling that the FV approach is a cell-centred method, where velocity values are stored/computed at the centroid of the cell, the face-centred velocity values in Equations 2.11 & 2.12 are unknown and require definition. The clear way to obtain these face-centred values is through interpolation between the cell centroids of the current and neighbouring cell, P and N, respectively (Figure 2.21). There are a variety of interpolation schemes available in CFD solvers, with the common approach used in this thesis being linear interpolation, as it is generally more accurate than alternatives like upwind differencing, despite being more unstable. This increased accuracy is

beneficial for multiphase models, where increased instability is mitigated by reducing the mesh size and timestep.

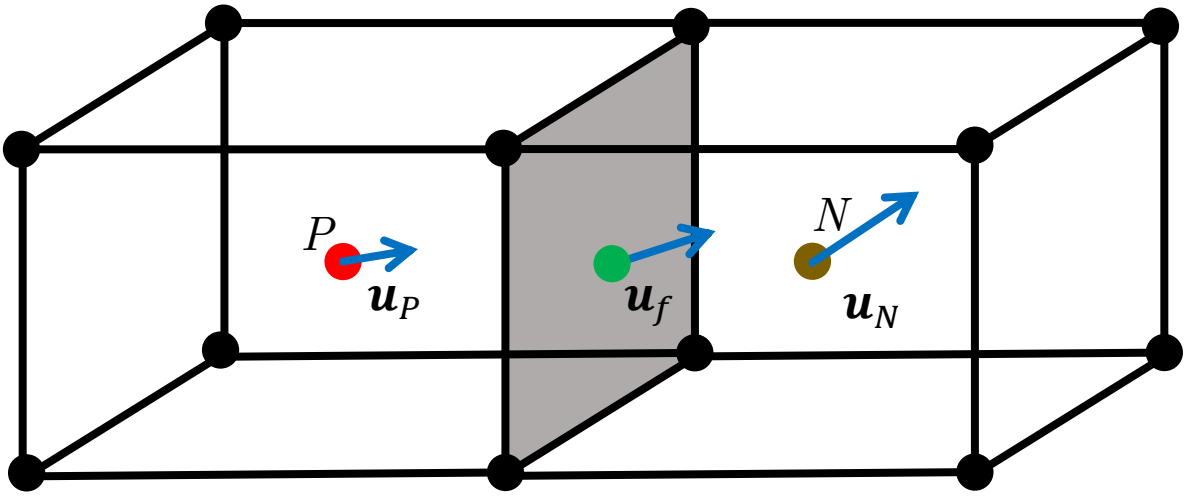

Figure 2.21: Face centred velocity between two neighbouring cells, calculated by linear interpolation

2.7.3 The SIMPLE algorithm

Once the FV method has been used to discretise the NS equations into a linear system of algebraic equations, the Semi-Implicit Method for Pressure Linked Equations (SIMPLE) algorithm can be used to obtain the velocity/pressure values for each cell. The SIMPLE algorithm was chosen over alternatives like PISO, as it computationally more efficient and faster to iterate, which is advantageous for larger meshes with transient conditions. This method uses boundary condition data to form initial guesses of the flow field and then iteratively solves the NS equations for velocity/pressure until residual error satisfies the convergence criteria. The FV method discussed previously

has been used to discretise the momentum equation into the general matrix form shown in Equation 2.13.

$$\boldsymbol{MU} = -\nabla p \tag{2.13}$$

where M is a matrix of known coefficients arising from the FV discretisation, $\boldsymbol{U}$ is the unknown vector velocity field and $\nabla \boldsymbol{p}$ is the unknown pressure gradient. Directly inverting $\boldsymbol{M}$ is highly inefficient, and so it is first separated into its diagonal and off diagonal components and re-written in Equations 2.14 and 2.15.

$$\boldsymbol{H} = \boldsymbol{AU} - \boldsymbol{MU} \tag{2.14}$$

$$\boldsymbol{AU} - \boldsymbol{H} = -\nabla p \tag{2.15}$$

Where $\boldsymbol{A}$ is simply the diagonal of $\boldsymbol{M}$, and $\boldsymbol{H}$ is the remaining (known) coefficients from previous iterations/initial conditions. Now Equation 2.15 can be easily inverted to yield a direct expression for the velocity field in Equation 2.16.

$$\boldsymbol{U} = \boldsymbol{A^{-1}H} - \boldsymbol{A^{-1}}\nabla p \tag{2.16}$$

Now a direct expression for the velocity field has been obtained, it can be substituted into the original mass continuity equation and hence define a Poisson expression for the pressure field in Equation 2.17.

$$\nabla \cdot (\boldsymbol{A^{-1}}\nabla p) = \nabla \cdot (\boldsymbol{A^{-1}H}) \tag{2.17}$$

Once this system of equations describing the velocity field from the momentum conservation equation, and the pressure field from the mass continuity equation have been defined, the SIMPLE algorithm is used iteratively to correct the initial guesses to

the velocity/pressure fields based upon boundary conditions/previous iterations. A schematic showing the SIMPLE algorithm process is shown below in Figure 2.22.

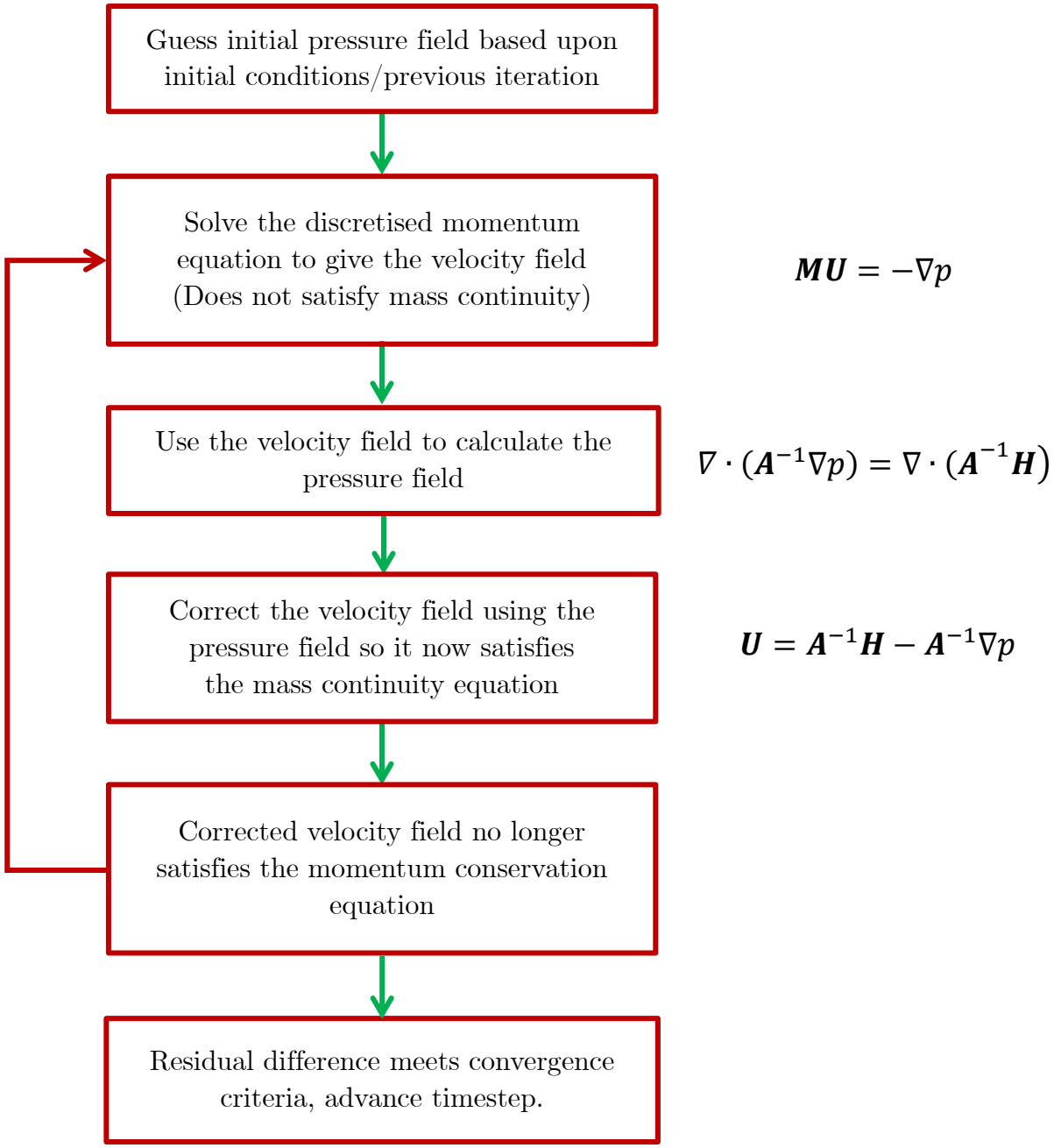

Figure 2.22: Flow chart showing the computational steps involved in the SIMPLE algorithm

2.7.4 Summary

This background chapter has presented the crucial foundations of both the anatomy and computational methods used in novel scenarios in this thesis. The important role haemodynamics plays in the healthy function of the cardiovascular system has been described, including the importance of parameters such as WSS and phenomena such as rouleaux formation in the onset/progression of CVD. The need for and benefit of computational methods within the field of biomedical engineering has been described, with the fundamental tools and governing equations described, ready to be expanded in subsequent chapters. Three broad themes the presented work discusses are;

- How does coronary artery surface roughness affect haemodynamics?
- Are multiphase rheology models useful in CVD simulations?
- Do haemodialysis catheter side-holes improve performance?

The following chapter will explore the development, implementation and assessment of micro-scale surface roughness in a coronary artery model. Insights into modelling the rheology of blood in this multi-scale environment, as well as evaluating the parameters commonly associated with CVD in this novel, realistically rough surfaced environment will be discussed in detail.

STATEMENT OF CONTRIBUTIONS I

The following chapter includes novel research which has been previously published in a peer-reviewed scientific journal, with myself as the principal author. It was published as gold standard open access, with a full CC-BY 4.0 copyright license (https://creativecommons.org/licenses/by/4.0/) allowing for the reproduction and alteration included within this thesis. Below are the details of the publication, and a statement of the contributions from each author.

Owen DG, Schenkel T, Shepherd DET, Espino DM. (2020) *Assessment of surface roughness and blood rheology on local coronary haemodynamics: a multi-scale computational fluid dynamics study*. J. R. Soc. Interface 17: 20200327. http://doi.org/10.1098/rsif.2020.0327

Owen DG: Conceptualisation, creation/development of models, data analysis and drafting of manuscript.

Schenkel T: Provided data for rheological models and revised manuscript.

Shepherd DET : Conceptualisation, coordination, and revised manuscript.

Espino DM: Conceptualisation, coordination, and revised manuscript.

3 | SURFACE ROUGHNESS

3.1 Introduction

Recent advances in computational fluid dynamics (CFD) have allowed for detailed study into coronary haemodynamics (Chaichana, Sun and Jewkes, 2011; Javadzadegan *et al.*, 2017), in particular the relationship between atherosclerosis and flow parameters such as wall shear stress (WSS) (Ku, D N ; Giddens, D P ; Zarins, C K ; Glagov, 1985; Asakura and Karino, 1990; Stone, Coskun, Kinlay, *et al.*, 2003; Malek and Alper, 2007).

A detailed overview on the use of patient-specific models by Taylor and Figueroa (Taylor and Figueroa, 2009) highlighted many clinical applications (Taylor and Steinman, 2010; Kabinejadian and Ghista, 2012; Sankaran *et al.*, 2012; Kung *et al.*, 2013; Guerciotti *et al.*, 2017), with the most relevant to this study being predictions in the progression of atherosclerosis (Knight *et al.*, 2010; Lee *et al.*, 2019), arterial fibrin clots (Yesudasan and Averett, 2019) and thrombus formation (Cito, Mazzeo and Badimon, 2013), as well the effect of arterial stenosis on blood flow (Eshtehardi *et al.*, 2012; Karimi *et al.*, 2013; Gholipour *et al.*, 2018). The lumen wall is assumed smooth for all coronary models to date.

Studies into the roughness of the coronary lumen have shown that its texture plays a role in the early formation of atherosclerosis (Schmidt-Trucksäss *et al.*, 2003; Cinthio, Hasegawa and Kanai, 2011; Niu *et al.*, 2013), with an increase in roughness resulting

from endothelial damage (Kitamura, Hasegawa and Kanai, 2012). Accurate estimation of *in vivo* lumen roughness using ultrasound may be useful clinically for diagnostic purposes, however this is challenging, with limitations on resolution as ultrasonic beam intervals are around 100 µm, with endothelial cells around 10-20 µm thick (Kitamura, Hasegawa and Kanai, 2012). Further, other imaging methods and geometry processing techniques under current clinical use are unable to capture the surface roughness of coronary arteries. However, the surface roughness (Ra) of porcine coronary arteries have recently been characterised *ex vivo* using optical microscopy (Burton, Freij and Espino, 2017; Burton, Williams and Espino, 2017; Burton and Espino, 2019), Atomic Force Microscopy (AFM) and Scanning Electron Microscopy (SEM) (Burton *et al.*, 2019).

Blood is a heterogeneous, thixotropic fluid which presents challenges to its accurate simulation using CFD. It is comprised of red blood cells (RBC) and other cells (e.g. monocytes, leucocytes etc) suspended within a plasma continuum (Gidaspow, 1994). A comprehensive review of computational approaches to blood modelling is provided by Bessonov *et al.* (Bessonov *et al.*, 2016). One approach taken to simulate blood is to model it using a single-phase rheological model. Single-phase models treat blood as a homogeneous fluid, with either a constant (Newtonian) viscosity or a shear-dependant viscosity (non-Newtonian). Non-Newtonian blood viscosity models enable the shear-thinning behaviour of blood to be modelled, however, blood is treated as a single constituent fluid. This neglects the contribution of the cellular phases (RBC, platelets,

white blood cells, etc.) suspended within the plasma, which at lower shear rates often aggregate causing rouleaux formation (Flormann *et al.*, 2017) and greatly increase the viscosity of the mixture (Yilmaz and Gundogdu, 2009).

Multiphase models, instead, can be used to simulate blood as a dilute suspension of RBC within a plasma continuum. Thus, the flow of RBC can be distinguished from that of the surrounding plasma. These multiphase models often use an Eulerian-Eulerian approach which has previously been used in other simulations (Ding, Sha and Lyczkowski, 1995; Jung *et al.*, 2006; Jung and Hassanein, 2008; Kim, VandeVord and Lee, 2008; Srivastava and Srivastava, 2009; Yilmaz, Kutlar and Gundogdu, 2011) to investigate cardiovascular pathologies, evolving theory developed by Gidaspow (Gidaspow, 1994) with an assessment of drag/lift/mass modelling of RBC for cardiovascular modelling by Yilmaz *et al.* (Yilmaz and Gundogdu, 2009).

An advantage of the multiphase models is their ability to capture local variations in haematocrit (RBC concentration) arising from fluid dynamics and can then apply this to the viscosity of the blood, compared to the assumed uniform distribution of the single-phase models. No current single or multiphase CFD models of blood flow through coronary arteries simulate surface roughness. Therefore, it is unknown how predictions from these models vary with surface topology.

The current study aims to investigate, for the first time, how a realistically rough walled segment of the coronary artery impacts on the well-established haemodynamic parameters used to assess coronary health and how roughness might impact the onset

and progression of atherosclerosis. A comparison of common approaches to blood rheology has been performed to assess their capability of modelling flow features at a micro-scale. Briefly, three approaches to modelling blood rheology are compared:

1) A constant viscosity Newtonian blood model;
2) non-Newtonian single-phase models, Carreau (Lee and Steinman, 2007), Carreau-Yasuda (Cho and Kensey, 1991), and generalised power law (Ballyk, Steinman and Ethier, 1994)
3) Multiphase models, Quemada-Das (Das, Johnson and Popel, 1998) and MKM5 (Hund, Kameneva and Antaki, 2017).

The models are compared using transient simulations of blood flow through a simplified macro-scale coronary artery, with comparisons focusing on how flow over a smooth segment of the artery differs to flow over a segment which includes micro-scale roughness.

3.2 Methods

3.2.1 Geometry

3.2.1.1 Artery Segmentation

This model considers an idealised, short cylindrical section of the left anterior descending (LAD) coronary artery with a constant diameter of 3.5 mm chosen based upon *in vivo* data (Leung, Stadius and Alderman, 1991; Dodge *et al.*, 1992; Zhang *et al.*, 2011). The artery wall is predominantly smooth, with the only roughness located on a segment of arc length 0.8 mm (26.2°) along the length of the artery. It is constructed from ten, 0.8 mm long segments giving a total length of 8 mm. Ten segments were sufficient for the roughness to impact on the local haemodynamics without being overly computationally intensive. For best comparisons between the rough and smooth walls within the same model, an identical smooth segment is computationally defined directly opposite the rough wall (Figure 3.1), with all results being evaluated over a 4 mm length starting 2.4 mm from the inlet.

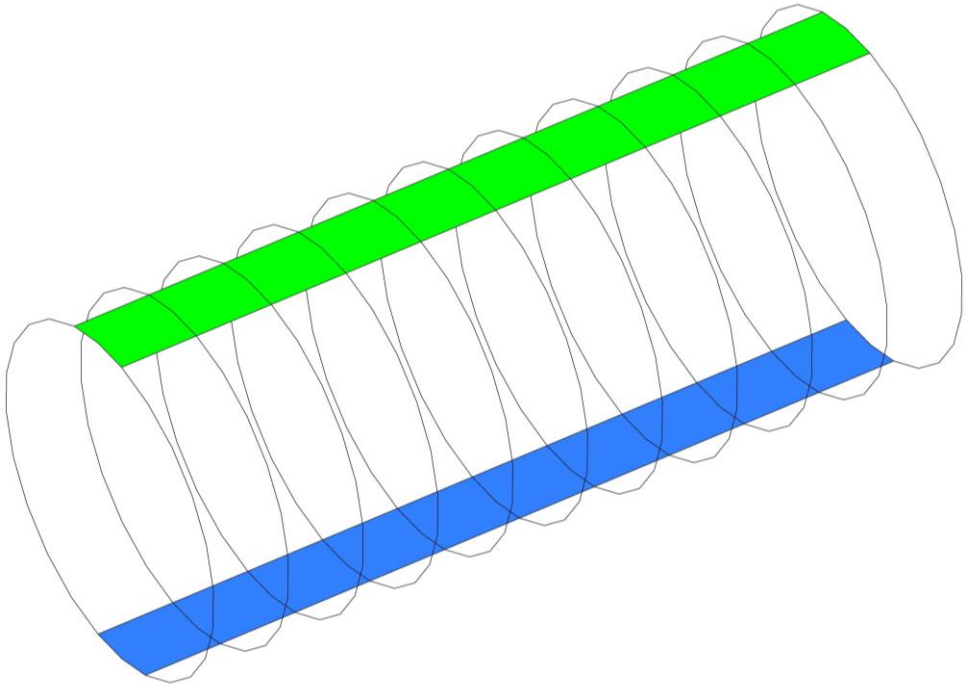

Figure 3.1: Partially rough coronary artery consisting of 10 × 0.8 mm long segments, with identical rough (Green) and smooth (Blue) sections defined opposite.

3.2.1.2 Rough surface generation

The surface roughness of the porcine coronary LAD artery in the circumferential and longitudinal directions have been reported as $Ra_C = 1.04 \pm 0.45\ \mu m$ and $Ra_L = 0.89 \pm 0.27\ \mu m$ respectively, with no variation along the length of the artery (Burton, Freij and Espino, 2017). To generate the rough surface, representative profiles of surface height (Figure 3.2A & 3.2B) in each direction were segmented into 16 × 0.05 mm sections and fitted to cubic B-splines. The circumferential profile was applied along a 0.8 mm section of the arterial circumference, with the longitudinal profile running perpendicularly (along the length of the artery). By extruding these two profiles along each other, an idealised three-dimensional rough surface can be created and then

repeated to form the rough section of the artery. A comparison between the surface generated using the height profiles from literature (Burton, Williams and Espino, 2017) and a representative sample of the porcine artery surface from optical microscopy data is shown in Figure 3.2C & 3.2D.

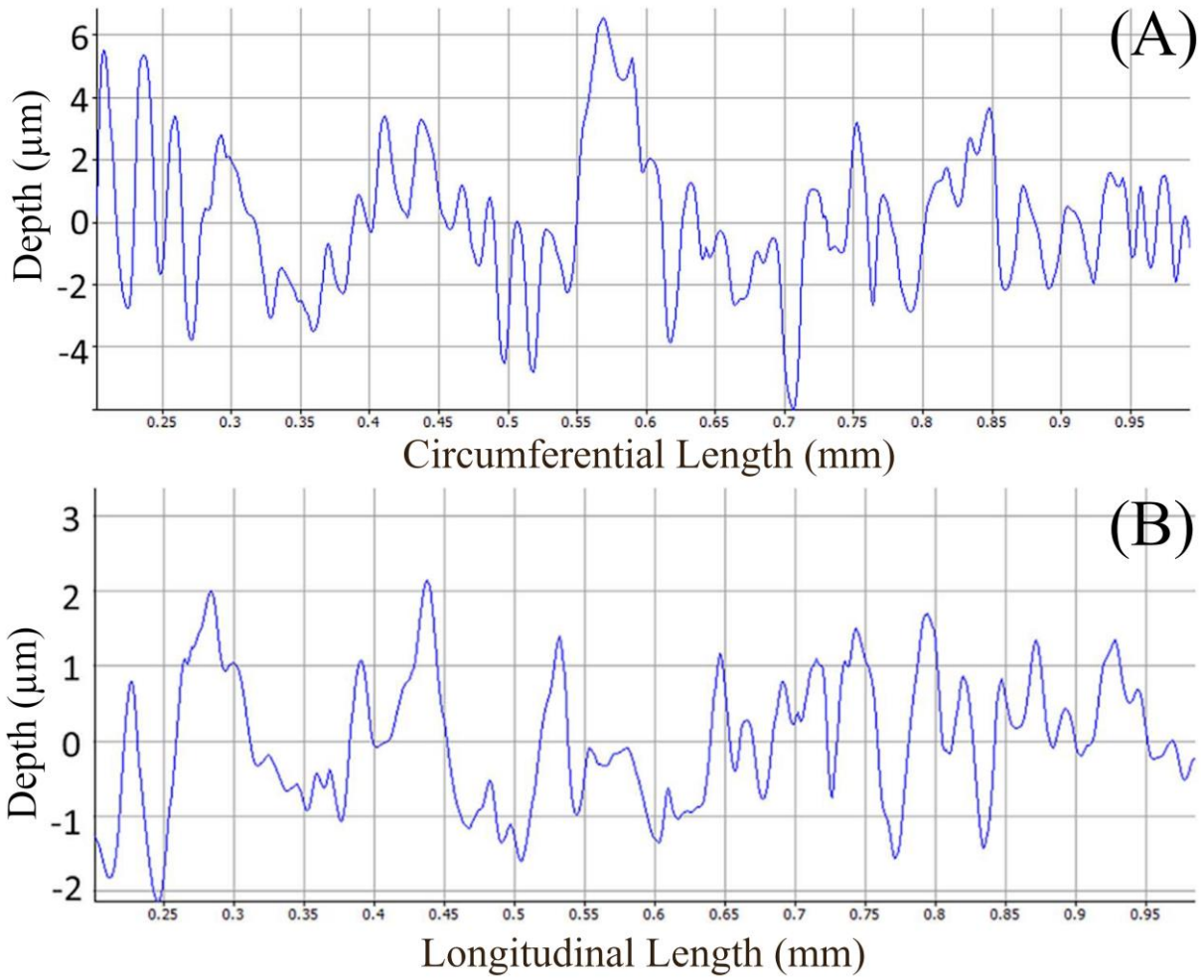

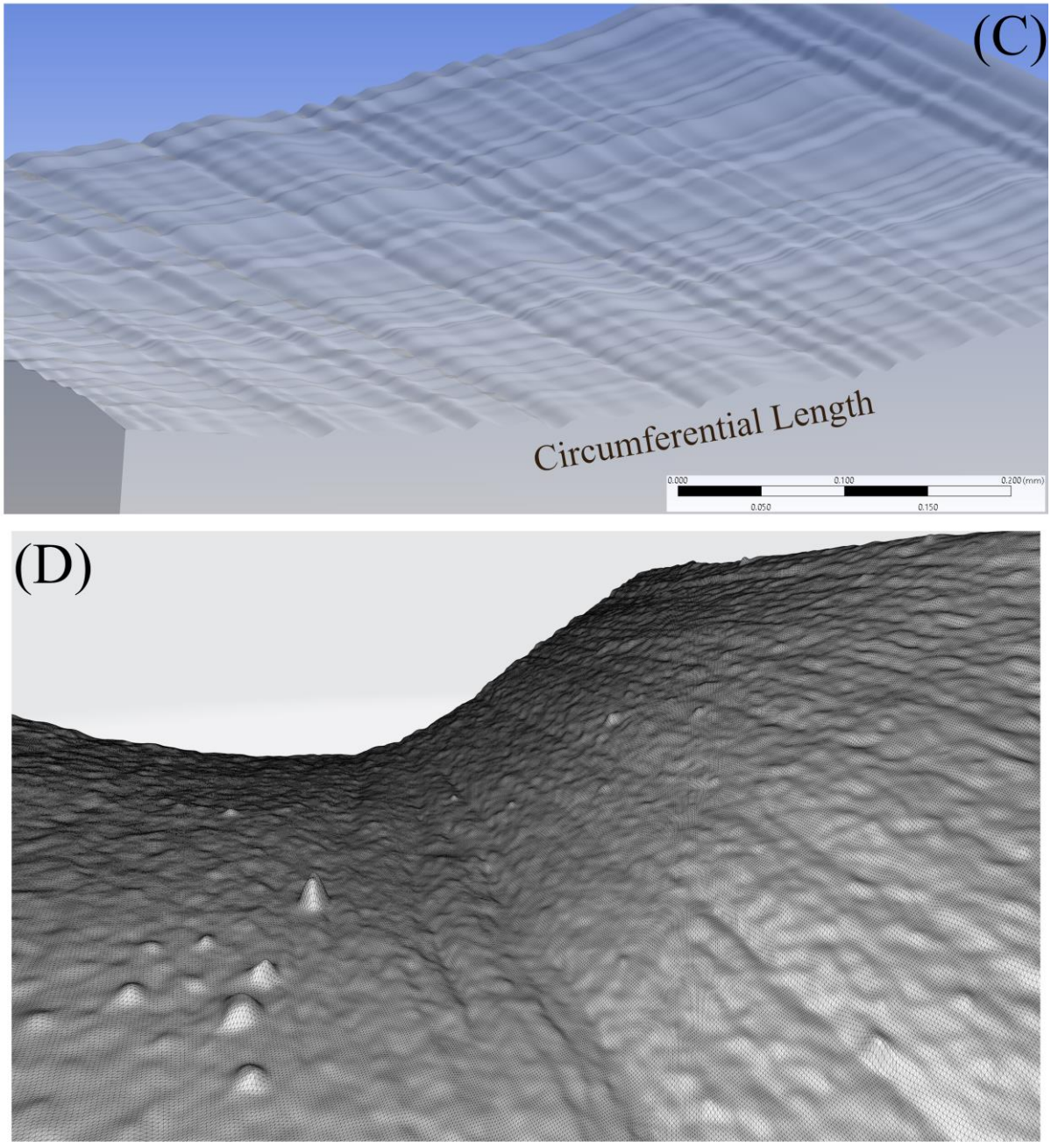

Figure 3.2: (A,B) – Circumferential and Longitudinal height profiles respectively, (C) – Rough surface on 0.8 mm artery segment, (D) – Representative surface roughness taken from optical microscopy (Spikes are imaging artefacts, their causes are explained by Burton *et al.* (Burton *et al.*, 2019))

3.2.2 Mesh

A detailed mesh is required to capture the smooth variation in surface texture. This was achieved using a combination of both tetrahedral and prism elements varying in size due to curvature, with elements having a minimum edge length of 0.2 µm and 18 inflation layers around the lumen surface. This was chosen so that the near-wall haemodynamics on the rough artery were computed over several elements. To ensure a mesh independent solution, simulations were performed on a shortened model (5 segments) at six equally spaced increasing levels of mesh refinement. The area-averaged WSS over the rough surface was calculated for each mesh refinement level, until the percentage difference between each refinement was below 0.5%. This resulted in the full artery mesh having 65 million elements (Figure 3.3) with an average orthogonal quality and skewness (Shewchuk, 2002) of 0.77 and 0.22, respectively.

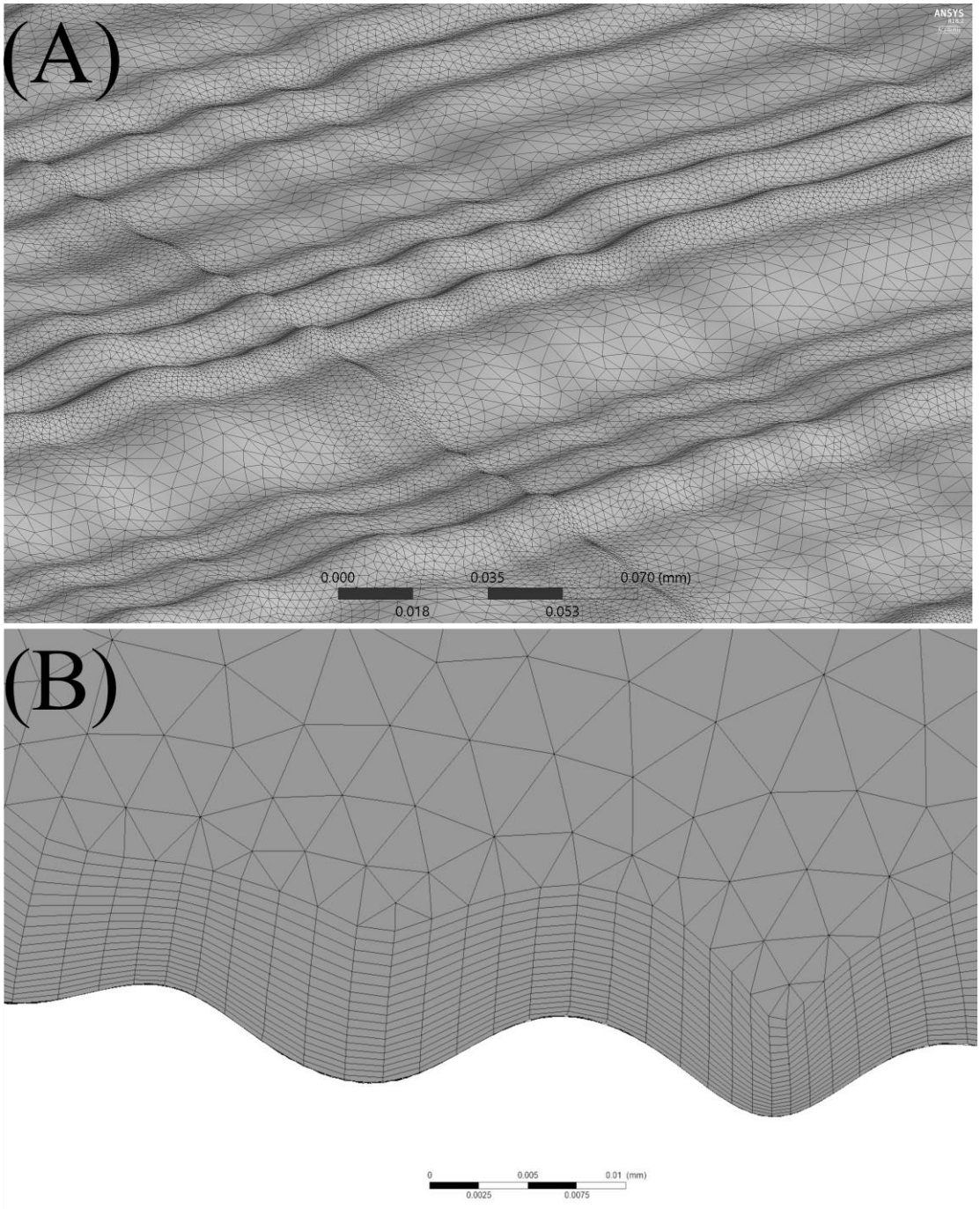

Figure 3.3: (A) - Variation of mesh size on a portion of the rough surface, (B) – Cross section of mesh showing inflation around circumferential roughness

3.2.3 Rheological models

Blood exhibits both Newtonian and non-Newtonian properties which can be described by fitting experimental viscometer data (Rand and Lacombe, 1964; Chien *et al.*, 1966; Brooks, Goodwin and Seaman, 1970; Copley, Huang and King, 1973) to constituent viscous definitions which can be functions of the volume fraction of the RBC (haematocrit) or, more typically, just the shear rate of the fluid (Equation 3.1). This study will examine 6 models which have been extensively used in cardiovascular simulations (Johnston *et al.*, 2004), with the effective model viscosity under varying shear given in Figure 3.4 and the accompanying model definitions in Table 3.1.

$$\dot{\gamma} = \sqrt{2D_{ij} \cdot D_{ij}} \qquad (3.1)$$

where $\dot{\gamma}$ is the shear rate of the fluid, D is the strain rate tensor with $i, j = 1,2,3$ as the inner products.

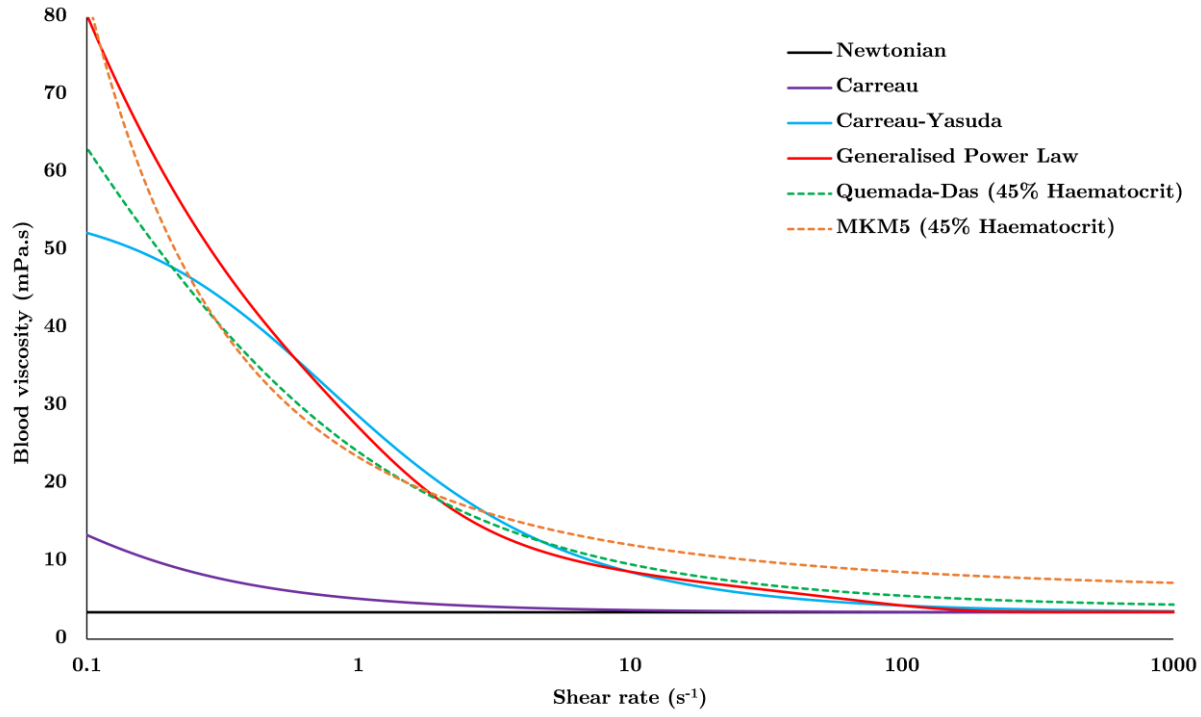

Figure 3.4: Variation in model viscosity for varying shear rate

Table 3.1: Rheological model definitions and parameters

Model	Viscosity definition (Pa.s)	Parameters
Newtonian (Yilmaz and Gundogdu, 2008)	$\mu = 0.00345$	-
Carreau (Lee and Steinman, 2007)	$\mu = \mu_\infty + (\mu_0 - \mu_\infty)[1 + (\lambda\dot{\gamma})^2]^{\frac{n-1}{2}}$	$\mu_\infty = 0.00345,\ n = 0.25$ $\mu_0 = 0.025,\quad \lambda = 25$
Carreau-Yasuda (Cho and Kensey, 1991)	$\mu = \mu_\infty + (\mu_0 - \mu_\infty)[1 + (\lambda\dot{\gamma})^p]^{\frac{n-1}{p}}$	$\mu_\infty = 0.00345,\ n = 0.22$ $\mu_0 = 0.056,\quad p = 1.25$ $\lambda = 1.902$

Table 3.1: Rheological model definitions and parameters (continued)

Model	Viscosity definition (Pa.s)	Parameters
Generalised Power-Law (Ballyk, Steinman and Ethier, 1994)	$\mu = k(\dot{\gamma})\lvert\dot{\gamma}\rvert^{n(\dot{\gamma})-1}$ $k(\dot{\gamma}) = \mu_\infty + \Delta\mu \cdot \exp\left[-\left(1+\frac{\lvert\dot{\gamma}\rvert}{a}\right)\exp\left(\frac{-b}{\dot{\gamma}}\right)\right]$ $n(\dot{\gamma}) = n_\infty - \Delta n \cdot \exp\left[-\left(1+\frac{\lvert\dot{\gamma}\rvert}{c}\right)\exp\left(\frac{-d}{\dot{\gamma}}\right)\right]$	$\mu_\infty = 0.0033, \Delta\mu = 0.25$ $n_\infty = 1, \quad \Delta n = 0.45$ $a = c = 50, b = 3, d = 4$
Quemada-Das (Das, Johnson and Popel, 1998)	$\mu = \mu_p\left[1-\frac{k\emptyset_{rbc}}{2}\right]^{-2}$ $k = \frac{k_0 + k_\infty\sqrt{\frac{\dot{\gamma}}{\gamma_c}}}{1+\sqrt{\frac{\dot{\gamma}}{\gamma_c}}}$ $k_0 = a_0 + \frac{2}{a_1 + \emptyset_{rbc}}$ $k_\infty = e^{b_0 + b_1\emptyset_{rbc} + b_2{\emptyset_{rbc}}^2 + b_3{\emptyset_{rbc}}^3}$ $\gamma_c = e^{c_0 + c_1\emptyset_{rbc} + c_2{\emptyset_{rbc}}^2 + c_3{\emptyset_{rbc}}^3}$	$\mu_p = 0.00123$ $a_0 = 0.06106$ $a_1 = 0.04777$ $b_0 = 1.80096$ $b_1 = -3.66602$ $b_2 = 2.57412$ $b_3 = 0.02346$ $c_0 = -7.01332$ $c_1 = 34.38771$ $c_2 = -39.80154$ $c_3 = 13.99167$ *Not valid for* $k\emptyset_{rbc} = 2$*, yet this occurs when* $0 > \emptyset_{rbc} > 1$
Modified Krieger Model 5 Parameters (Hund, Kameneva and Antaki, 2017) (MKM5)	$\mu = \mu_p\left[1-\frac{\emptyset_{rbc}}{\emptyset_{rbc,crit}}\right]^{-n}$ $n = \begin{cases} n_\infty & if \quad \emptyset_{rbc} < 0.2 \\ n_\infty + n_{st} & if \quad \emptyset_{rbc} > 0.2 \end{cases}$ $n_\infty = be^{-c\emptyset_{rbc}},\ n_{st} = \beta{\gamma'}^{-\nu}$ $\gamma' = 1 + (\lambda\dot{\gamma})^{\nu_g}$	$\mu_p = 0.00123$ $\emptyset_{rbc,crit} = 0.95$ $b = 8.78084$ $c = 2.82354$ $\beta = 16.27775$ $\nu = 0.14275$ $\lambda = 1252.64407$ $\nu_g = 2$

In Table 3.1, μ_p is the viscosity of plasma, $\emptyset_{rbc}$ is the haematocrit (phase volume fraction) and $\emptyset_{rbc,crit}$ is the critical haematocrit for which the RBC no longer behave as a fluid. The Newtonian model assumes a constant viscosity, both Carreau models use

a simplistic asymptotic polynomial shear thinning definition and the generalised power-law model combines the Casson (Fung, 1993) and Carreau models with a simple power-law. The final two models (Quemada-Das and MKM5) are based upon multiphase mixture theory where RBCs viscosity varies with both local shear forces and haematocrit (Krieger and Dougherty, 1959). The MKM5 model parameters have been revised (Schenkel and Halliday, 2020) based upon a curve fitting to the Brooks *et al.* (Brooks, Goodwin and Seaman, 1970) experimental data. As both multiphase models above describe the viscosity of whole blood, to determine the intrinsic viscosity of the RBCs themselves, Equation 3.2 below is used;

$$\mu_{rbc} = \frac{\mu_{blood} - (1 - \emptyset_{rbc})\mu_p}{\emptyset_{rbc}} \qquad (3.2)$$

where μ_{blood} is the definition of viscosity in the Quemada-Das and MKM5 models as shown in Table 3.1.

3.3 Numerical methods

3.3.1 Governing equations

3.3.1.1 Single-phase fluid

The commercial finite-volume (FV) solver Fluent (Ansys v19.2, Ansys Inc, Pennsylvania, USA) was used to solve the Navier-Stokes equations governing the behaviour of a 3D incompressible fluid (Equations 3.3 & 3.4) for all four of the single-phase models (Newtonian, Carreau, Carreau-Yasuda and generalised power law).

$$\frac{\partial u_i}{\partial x_i} = 0 \tag{3.3}$$

$$\frac{\partial u_i}{\partial t} + u_j \frac{\partial u_i}{\partial x_j} = \frac{\partial}{\partial x_j}\left(\mu \frac{\partial u_i}{\partial x_j}\right) - \frac{1}{\rho}\frac{\partial p}{\partial x_i} \tag{3.4}$$

where u_i is the velocity vector in the i direction, p is the fluid pressure, ρ is the density of the fluid, x is the coordinate in i or j direction and μ is the fluid viscosity and t is time. The viscous definitions for these models is given in Table 3.1, with the density of blood (Caballero and Laín, 2015; Vijayaratnam *et al.*, 2015; Ahmadi and Ansari, 2019) set as $\rho = 1060$ kgm^{-3}. All of the rheological models in Table 3.1 were coded using C, and were compiled as User Defined Functions (UDFs) to be hooked to the FV solver within Fluent, as definitions of fluid properties. The equations use the variables directly from the solver, and the limits of haematocrit in multiphase models are applied within the UDFs, which is detailed in the Appendix.

3.3.1.2 Multiphase fluid

A Eulerian-Eulerian multiphase mixture model pre-built in Fluent was implemented, which was modified using the UDFs in the Appendix to define the interactions of two fluids: A Newtonian continuum (Plasma) with a non-Newtonian particulate suspension (RBC) whose viscosity depends on local shear and haematocrit. With RBC accounting for >99% of the cellular volume fraction (Picart *et al.*, 1998) other particulates are not considered here. The fundamental laws governing phase volume fraction, continuity of mass/momentum for primary/secondary phases $p, q = plasma, rbc$ are given respectively in Equations 3.5-3.7.

$$\sum_{n=1}^{2} \emptyset_n = 1 \tag{3.5}$$

$$\frac{\partial}{\partial t}(\emptyset_q \rho_q) + \nabla \cdot (\emptyset_q \rho_q \vec{v}_q) = 0 \tag{3.6}$$

$$\frac{\partial}{\partial t}(\emptyset_q \rho_q \vec{v}_q) + \nabla \cdot (\emptyset_q \rho_q \vec{v}_q \vec{v}_q) = -\emptyset_q \nabla \mathrm{p} + \nabla \cdot \bar{\bar{\tau}}_q + \sum_{p,q=1}^{2} K_{pq}(\vec{v}_p - \vec{v}_q) + \vec{F}_{ext} \tag{3.7}$$

where ρ is density, $\vec{v}$ is velocity, p is pressure (shared by all phases), $\bar{\bar{\tau}}$ is the stress-strain tensor, K_{pq} is the interphase momentum exchange coefficient and $\vec{F}_{ext}$ are the external forces. The viscous definitions in Table 3.1 coupled with phase definitions for the density of plasma (Brooks, Goodwin and Seaman, 1970) and RBC (Ponder, 1948) being $\rho_p = 1003$ kgm^{-3} and $\rho_q = 1096$ kgm^{-3} respectively leaves only definitions of $\vec{F}_{ext}$ and K_{pq} to be described. The main consideration is the exchange of momentum between the two phases which is closely coupled to the viscous drag experienced by the

RBC. This relationship can be derived from the particulate phases interfacial-area (ANSYS, 2019a), and drag force given by the Schiller-Naumann (Schiller and Naumann, 1935) model for spheres in Equation 3.8 & 3.9:

$$K_{pq} = \frac{3}{4} C_D \frac{\rho_p \emptyset_q (1 - \emptyset_q) |\vec{v}_p - \vec{v}_q|}{d_q} \tag{3.8}$$

$$C_D = \begin{cases} \frac{24(1 + 0.15Re^{0.687})}{Re} & if\ Re \leq 1000 \\ 0.44 & if\ Re > 1000 \end{cases} \tag{3.9}$$

where d_q is the diameter of the RBC (Bessonov *et al.*, 2016; Ta *et al.*, 2017) chosen to be 8 µm, C_D is the drag coefficient for the RBC and Re is the relative Reynolds number which is defined in Equation 3.10:

$$Re = \frac{\rho_p |\vec{v}_p - \vec{v}_q| d_q}{\mu_p} \tag{3.10}$$

In addition to this, a 'virtual mass' force is included which concerns the change in inertia of the plasma during relative RBC acceleration (Drew, Lahey and Roco, 1993) which is defined in Equation 3.11:

$$\vec{F}_{vm} = 0.5 \emptyset_q \rho_p \left(\frac{d_p \vec{v}_p}{dt} - \frac{d_q \vec{v}_q}{dt} \right) \tag{3.11}$$

where the term $\frac{d_p}{dt}$ represents the phase material time derivative in Equation 3.12:

$$\frac{d_p(\emptyset)}{dt} = \frac{\partial(\emptyset)}{dt} + (\vec{v}_p \cdot \nabla)\emptyset \tag{3.12}$$

The lift force is not included in this model as it is not appropriate for models with such a high concentration of small diameter particles (small relative to the diameter of the artery), and is more applicable to larger dispersed flows in which highly separable flow occurs (Yilmaz and Gundogdu, 2009).

3.3.2 Boundary conditions

3.3.2.1 Inlet and outlet

The pulsatile variation of velocity over time, $V(t)$, was applied to the inlet using a Fourier fitted series ($R^2 = 0.998$) based upon velocity data for the LAD (Bénard, 2005).

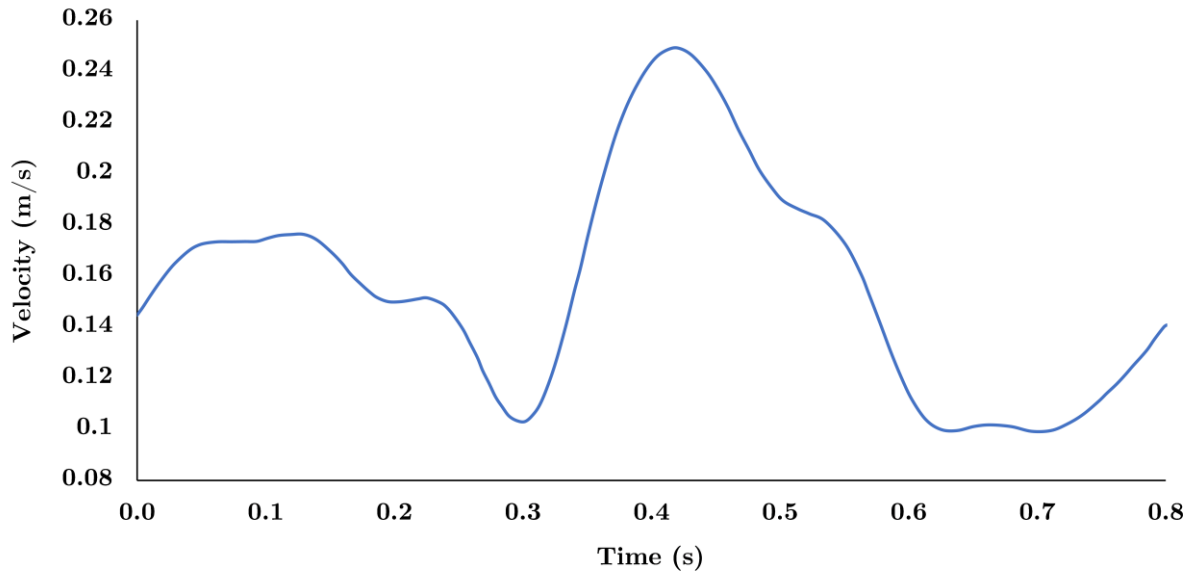

Figure 3.5: Variation of velocity for inlet to coronary artery

A simplified pulsatile model (Equation 3.13) has been used to describe the fully developed laminar flow occurring at the inlet as recommended by Chabi *et al.* for modelling micro-scale features around stents (Chabi *et al.*, 2015).

$$u(r,t) = 2V(t)\left[1 - \left(\frac{r^2}{R^2}\right)\right] \quad (3.13)$$

where $V(t)$ is the variation of velocity shown in Figure 3.5, r is the radial position and R is the maximum radius of the artery (adjusted for the increase in diameter due to the roughness). Due to the short length of the artery, a transient outlet boundary condition was not employed, instead, the outlet had a constant 75 mmHg (10 kPa) reference pressure applied based upon *in vivo* measurements (Poppas *et al.*, 1997) which have been implemented in similar coronary models (Jung *et al.*, 2006; Huang, Lyczkowski and Gidaspow, 2009; Yilmaz, Kutlar and Gundogdu, 2011).

3.3.2.2 Multiphase haematocrit

An initial uniform haematocrit distribution of 45% is assumed at the inlet based upon the healthy adult range (Pal, 2003) of 0.47 ± 0.07 with other similar studies also using this uniform distribution (Jung *et al.*, 2006; Kim, VandeVord and Lee, 2008; Yilmaz, Kutlar and Gundogdu, 2011; Buradi and Mahalingam, 2018). This uniform distribution is assumed due to a lack of *in vivo* data, however, to improve upon this uniform assumption, the distribution of haematocrit (after diffusion/transport/shear effects) at the outlet is copied periodically every 0.1 s to be the inlet condition in an attempt to reach a more physiological distribution.

3.3.3 Haemodynamic parameters

To assess the impact of surface roughness, and evaluate the effects of viscosity on the near-wall haemodynamics the following parameters were defined, as follows (Equations 3.14-3.19):

$$\tau_w = \mu \frac{\partial u_t}{\partial n}\bigg|_{wall} \tag{3.14}$$

where τ_w is WSS, u_t is the tangential wall velocity and n is the unit vector perpendicular to the wall.

$$\bar{\tau}_w = \frac{1}{T}\int_0^T |\vec{\tau}_w|\, dt \tag{3.15}$$

where $\bar{\tau}_w$ is the time-averaged wall shear stress (TAWSS) over the length of the cardiac cycle, T.

$$\bar{\tau}_{aaw} = \frac{1}{A}\sum_{i=1}^{n} \bar{\tau}_w |A_i| \tag{3.16}$$

where $\bar{\tau}_{aaw}$ is the area-averaged TAWSS (AATAWSS) which provides an overall magnitude for each rough/smooth segment defined previously.

$$\theta_i = \frac{1}{2}\left(1 - \frac{\left|\int_0^T \tau_w\, dt\right|}{\int_0^T |\tau_w|\, dt}\right) \tag{3.17}$$

where θ_i is the oscillatory shear index (OSI), a dimensionless parameter introduced by He & Ku (He and Ku, 1996) where values close to 0.5 indicate flow oscillation, and values near 0 indicate no flow reversal.

$$t_r = \frac{k}{(1 - 2\theta_i)\bar{\tau}_w} \tag{3.18}$$

where t_r is the relative residence time (RRT), which provides a measure of the time fluid spends in an arbitrary near-wall region first introduced by Himburg *et al.* (Himburg *et al.*, 2004). The proportionality constant k arises from the near-wall assumption and is set as $k = 1$.

$$I_L = \frac{\mu}{\mu_N} \tag{3.19}$$

where I_L is the local non-Newtonian importance factor (NNIF) first introduced by Ballyk *et al.* (Ballyk, Steinman and Ethier, 1994) where values outside of unity indicate the presence of non-Newtonian effects. The Newtonian viscosity of blood is set as that of the Newtonian model in Table 3.1 as $\mu_N = 3.45\ \text{mPa.s}$. The two multiphase models (Quemada-Das and MKM5) allow for the interactions between constituent parts of blood and due to their separate material definitions, each phase has its own associated variables such as: velocity, shear, viscosity and volume fraction. To calculate the same haemodynamic parameters above (Equations 3.14-3.19) for the multiphase models, the volume fraction of each phase is considered so the properties in a given cell are weighted between the two phases as given by Equation 3.20.

$$A_m = \emptyset_{rbc} A_{rbc} + \emptyset_{plasma} A_{plasma} \tag{3.20}$$

where A denotes any physical property of the phase/mixture.

3.3.4 Solver settings

The governing equations were solved iteratively using the discrete form of the SIMPLE algorithm for the pressure-velocity coupling (Phase-coupled for the multiphase models (Vasquez and Ivanov, 2000)), with a first order time discretisation. Computation was performed as a distributed process across multiple cores on high performance computing (HPC) nodes, with optimised efficiency through a customised message passing interface (MPI). Solution parameters and machine specifications for the solutions are listed below in Table 3.2. A smaller time-step was chosen for the multi-phase models to avoid initial instabilities due to the non-linearity of the RBC viscosity models. The models were solved for a total simulation time of 4.6 s corresponding to 7 cardiac cycles, with the multiphase model chosen to have a smaller time-step for improved phase interactions.

Table 3.2: Convergence parameters and solution information for the single and multiphase models

Phase	Cardiac Cycles	Time-step (s)	Minimum Continuity Residual	HPC Machines	Clock-Time (hours)
Single	7	0.005	10^{-5}	300 Intel Xeon ES-2640 v4 processors with 2TB DDR4 RAM	24
Multi		0.001			300

3.4 Results

3.4.1 Single-phase

The haemodynamic parameters defined above (Equations 3.14-3.19) were evaluated across the 7th cardiac cycle once the convergence criteria in Table 3.2 were reached, with results for the opposing rough/smooth segments of the artery (Figure 3.1) shown in Table 3.3.

Table 3.3: Haemodynamic parameters on the rough (R) and smooth (S) segments of the artery for all single-phase models

Parameter	Newtonian		Carreau		Carreau-Yasuda		Generalised Power Law	
	R	*S*	*R*	*S*	*R*	*S*	*R*	*S*
AATAWSS (Pa)	1.30	1.31	1.41	1.42	1.42	1.44	1.34	1.34
Max WSS (Pa)	6.50	2.68	5.58	3.40	6.29	3.26	6.51	3.00
Min WSS (Pa)	0.027	0.460	0.052	0.168	0.060	0.391	0.059	0.409
Max RRT (Pa^{-1})	34.4	0.7	12.0	0.8	14.4	0.7	15.5	0.7
Max OSI	0.012	$3.4x10^{-5}$	0.012	$4.8x10^{-5}$	0.012	$3.7\ x10^{-5}$	0.012	$3.6\ x10^{-5}$
Max NNIF	1	1	2.5	1.4	2	1.3	2.8	1.3
Max Shear (s^{-1})	1826	773	1504	925	1718	899	1800	851
Min Shear (s^{-1})	9.69	125.89	7.52	36.97	6.85	90.62	7.13	92.84

The AATAWSS for the rough/smooth segments differs by <1% in each single-phase model, despite the much wider range of instantaneous WSS for the rough segment. Given the two segments lie on the same artery, the average magnitudes of WSS are expected to be similar. The two Carreau type models have the most similar predictions of WSS, with the generalised power law more closely agreeing with the Newtonian model. All single-phase models predict the same distribution of haemodynamic parameters in Table 3.3, with only the magnitudes and ranges differing between each model.

The TAWSS on the rough segment varies by more than double that of the smooth, with 'peaks' and 'valleys' of the roughness experiencing a TAWSS of around 3.7 Pa and 0.08 Pa respectively for all single-phase models, with the distribution for the generalised power Law shown in Figure 3.6A.

Both the maximum OSI and RRT are significantly greater over the rough surface than the smooth surface, with the largest RRT occurring in the Newtonian model being more than double the closest non-Newtonian model. Overall, the magnitude of the OSI is negligible which is to be expected given the straight cylindrical nature of this artery segment, with a uniform distribution on the smooth segment and a seemingly random pattern of OSI on the rough segment, with concentrations around peaks in the circumferential roughness shown for the Carreau model in Figure 3.6B. The RRT distribution is uniform over the smooth segment in all single-phase models, with a magnitude ≈10× smaller than the rough segment. Maximum RRT occurs

unsurprisingly in the 'valleys' of the roughness as the velocity in these areas approaches zero, coupled with the lowest shear rates of between 7-10 s^{-1} resulting in an increased viscosity and minimal blood washout, with the distribution shown for the Newtonian model shown in Figure 3.6C.

The non-Newtonian effects are much more pronounced on the rough arterial segments, with the generalised power law model predicting a peak $I_L = 2.8$ despite the lack of complex geometry features such as plaques, bifurcations or curvature. This range of NNIF is explained by the wide range of shear rates occurring over the rough segment. The largest range of shear rates on the rough and smooth surfaces occurs with the Newtonian and Carreau models respectively, however, the generalised power law has the greatest combined range of shear rates, and thus the greatest NNIF value. The distribution of NNIF is uniform across the smooth segment, with a similar magnitude over the majority of the rough surface, except for the valleys of the roughness where the NNIF reaches its maximum due to the low-shear conditions. The NNIF distribution is shown for the Carreau-Yasuda model in Figure 3.6D.

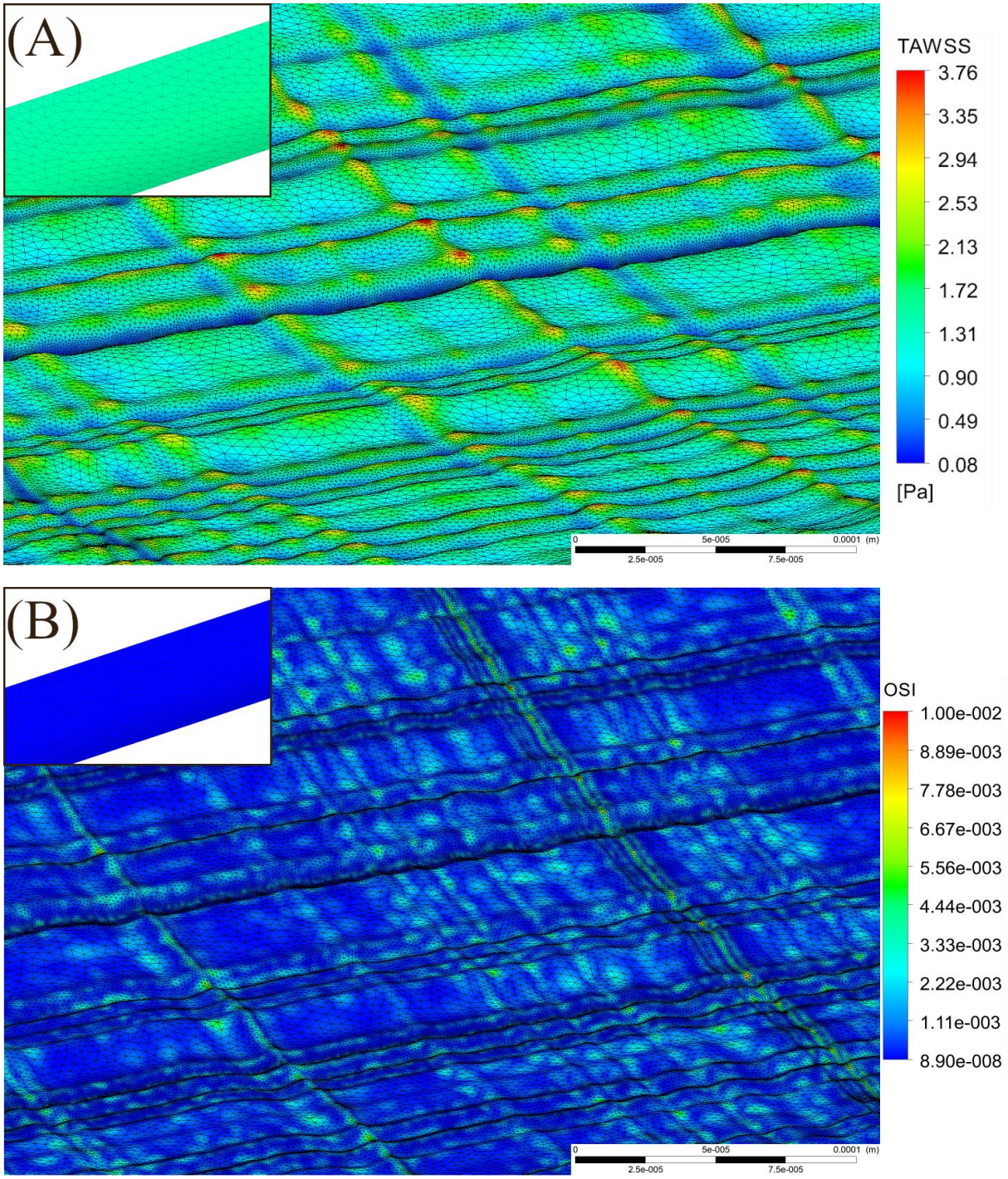

Figure 3.6: Contours of (A) – Time Averaged Wall Shear Stress (TAWSS - Generalised Power Law), (B) – Oscillatory Shear Index (OSI - Carreau) for the rough surfaced coronary artery segments with the distributions for the corresponding smooth segments inlaid as reference.

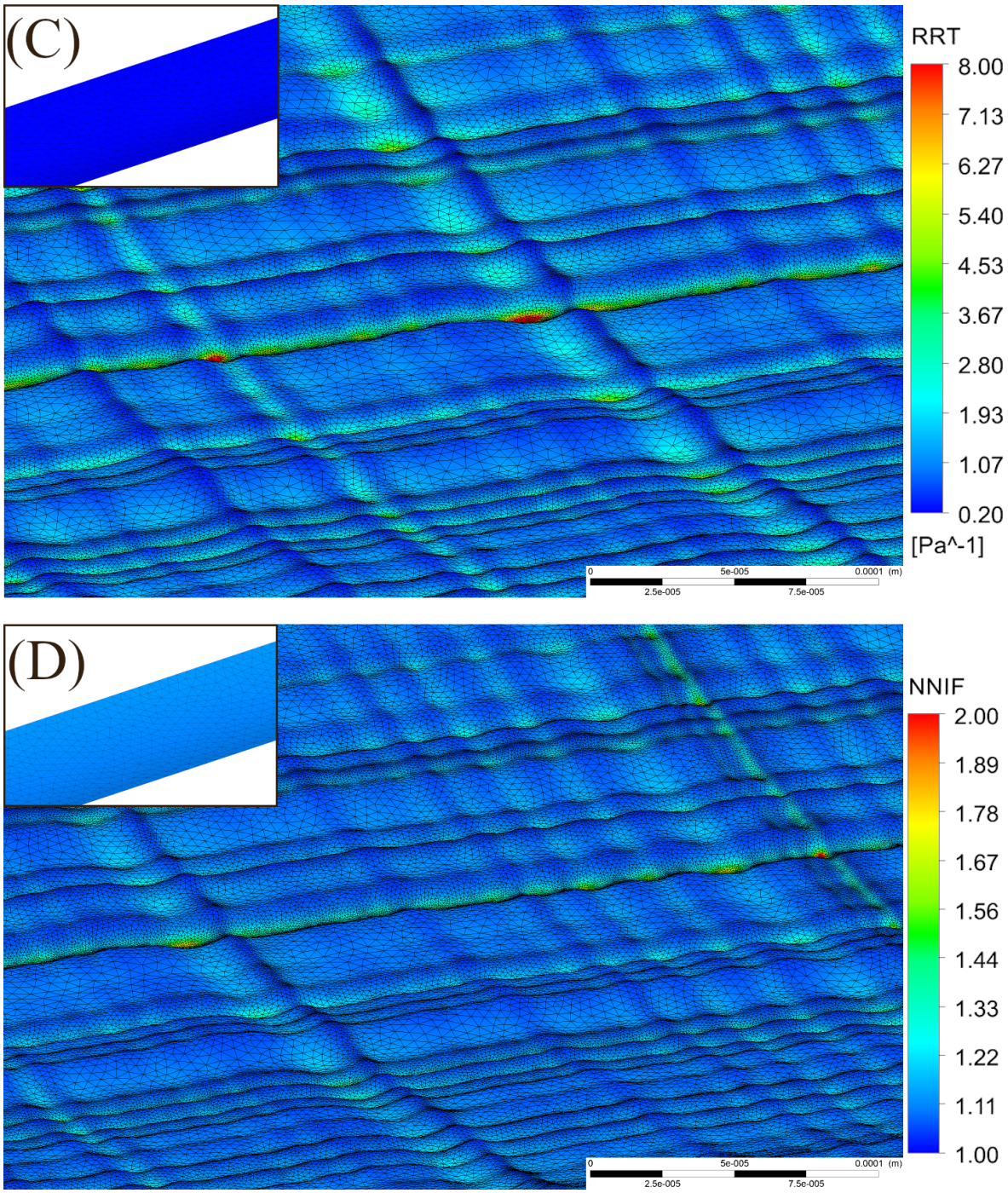

Figure 3.6: (C) – Relative Residence Time (RRT - Newtonian) and (D) – Non-Newtonian Importance Factor (NNIF - Carreau-Yasuda) for the rough surfaced coronary artery segments with the distributions for the corresponding smooth segments inlaid as reference.

3.4.2 Multiphase

All parameters in Table 3.4 below are calculated using the mixture relationship (Equation 3.20) for best comparisons between the single and multiphase models, with maximum/minimum values reported across the final cardiac cycle.

Table 3.4: Haemodynamic and multiphase parameters for the rough (R) and smooth (S) segments for both multiphase models

Parameter	Quemada-Das		Modified Krieger Model 5 Parameters (MKM5)	
	R	*S*	*R*	*S*
AATAWSS (Pa)	1.048	0.918	1.481	1.317
Max WSS (Pa)	243.6	1.57	157	1.85
Min WSS (Pa)	0.018	0.515	0.029	0.478
Max RRT (Pa^{-1})	72.9	1.1	14.6	0.8
Max OSI	3.6×10^{-1}	7.75×10^{-7}	2.25×10^{-1}	1.01×10^{-6}
Max NNIF	718.6	1.48	2.14×10^{5}	2.22
Max Shear (s^{-1})	3.65×10^{4}	721	3.58×10^{4}	862
Min Shear (s^{-1})	0.22	213	2.17	138
Max Haematocrit	0.968	0.467	0.980	0.469
Time Averaged Haematocrit	0.461	0.459	0.456	0.461
Time Averaged Mixture Viscosity (mPa.s)	5.184		7.515	

To compare the difference in AATAWSS on the rough/smooth segments the relative difference between the final magnitudes at the end of each cardiac cycle was calculated using Equation 3.21 and plotted below in Figure 3.7.

$$\bar{\tau}_{aaw,diff} = \frac{\left|\bar{\tau}_{aaw,r} - \bar{\tau}_{aaw,s}\right|}{\left|\bar{\tau}_{aaw,s}\right|} \tag{3.21}$$

Where the subscripts r and s indicate the rough and smooth segments, respectively.

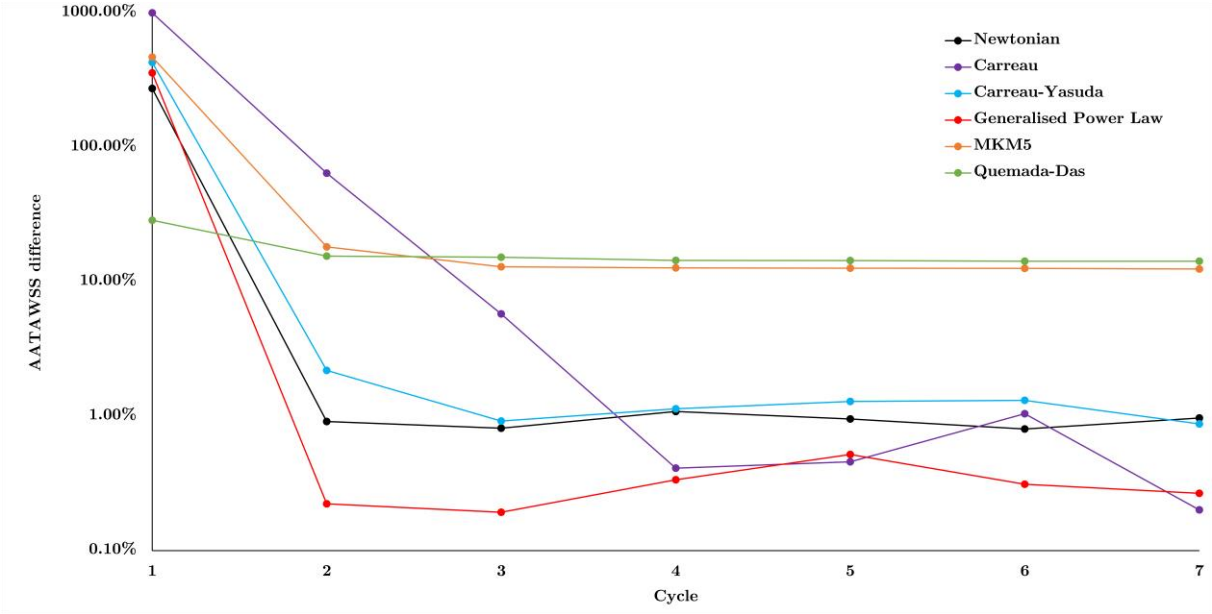

Figure 3.7: Difference in AATAWSS for the rough/smooth segments for each model

The difference in AATAWSS between the rough/smooth segments for both multiphase models is around 13%, compared to the <1% in the single-phase models. The MKM5 model's prediction of WSS parameters is most similar to the single-phase models, however, the inclusion of haematocrit in viscous calculations greatly increases the maximum WSS and NNIF for both multiphase models. The AATAWSS magnitudes for the Quemada-Das model are the lowest in this study for both the rough/smooth

segments, despite a stress distribution similar to the generalised power law model in Figure 3.6A.

The variation of WSS for the rough/smooth segments for all models is plotted in Figure 3.8 & 3.9. For the smooth segment, the variation in WSS is clearly proportional to the velocity of the flow, and for every model the WSS follows this trend, shown in Figure 3.5. The rough segment shows less of a change in WSS during the cycle, with a much more consistent average, maximum and minimum WSS over the surface, with the maxima occurring around the time of peak velocity.

The magnitudes of RRT and OSI are greater in both multiphase models for both the rough/smooth segments, with maximum OSI values approaching the 0.5 limit indicating regions of highly oscillatory shear stress. The wide variation in haematocrit shown over the surface in Figure 3.11 results in two extremes of viscous prediction and thus the extreme values of NNIF. Despite these extreme variations in local shear of the RBCs and haematocrit over the rough surface, the overall average magnitudes of AATAWSS, RRT, haematocrit and mixture viscosity remain unaffected, implying that these extremes are localised to very small regions.

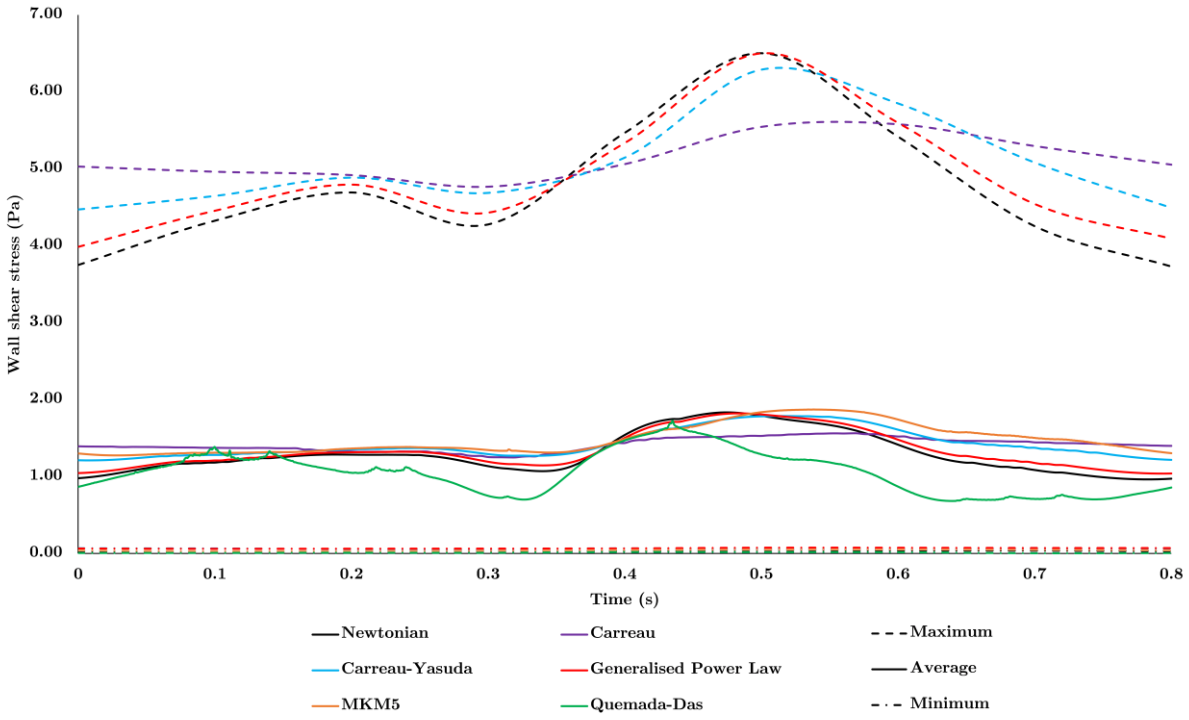

Figure 3.8: Variation of rough wall shear stress (WSS) with time, Maximum, average and minimum values of WSS on the rough segment for each model are presented (Max values for multiphase models not included due to magnitude)

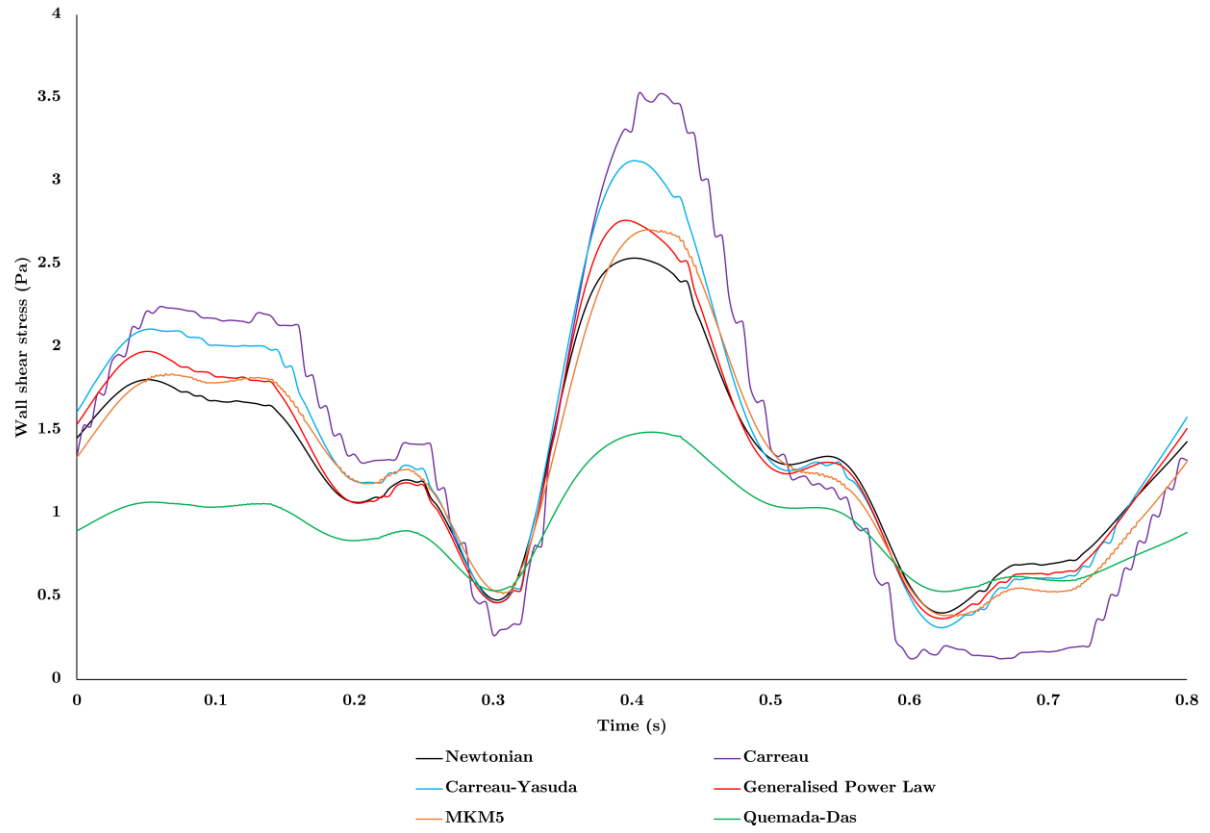

Figure 3.9: Variation of wall shear stress with time averaged over the smooth segment for each model are presented (Max and Min values not reported because of uniform nature of stress distribution)

The overall mixture viscosity predicted by the Quemada-Das model was around 30% lower than that of the MKM5 model which is expected given the shear graphs plotted for the inlet haematocrit in Figure 3.4, with the variation during the cardiac cycle shown in Figure 3.10.

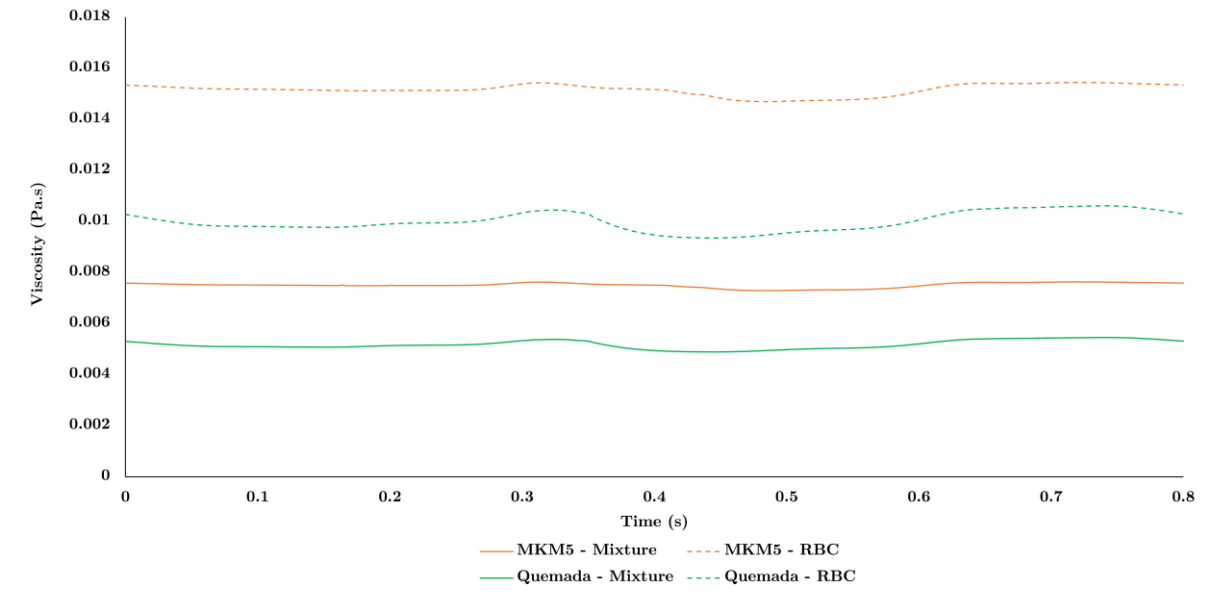

Figure 3.10: Variation of average viscosity with time. Variation of mixture and RBC viscosity during the cardiac cycle are presented

The haematocrit distribution over the smooth segment is uniform around 0.46 in both models, however, the rough segment varies significantly with peaks in haematocrit occurring with peaks in the roughness (Figure 3.11 & 3.12) similar to the OSI and TAWSS distribution of the single-phase models. Areas with extremes of haematocrit will also experience either high or low viscosity (Figure 3.4) which will in turn affect haemodynamic parameters such as NNIF and WSS. Variations in haematocrit over the rough surface after 5.6 s are further detailed in Figures 3.11 & 3.12, with blood flow from left to right of image, along the length of the artery.

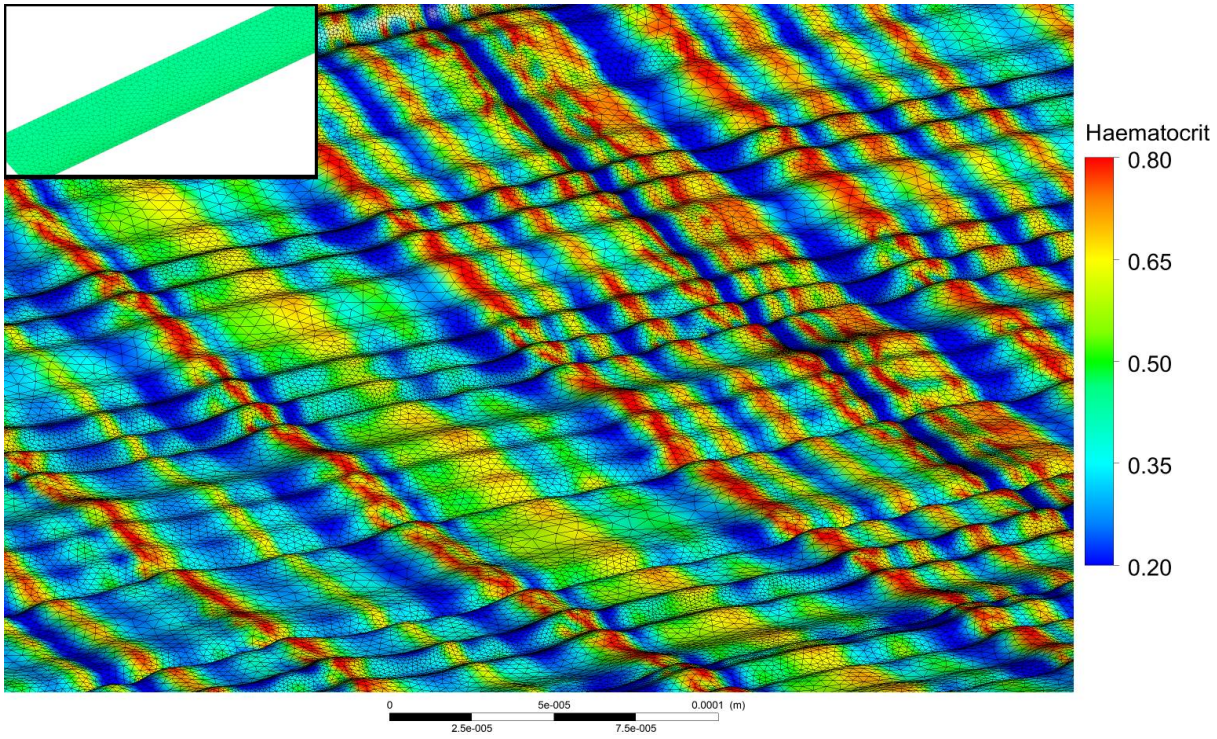

Figure 3.11: Haematocrit distribution over the rough segment (smooth inlaid) for the MKM5 model (After 6 cycles, t=5.6 s)

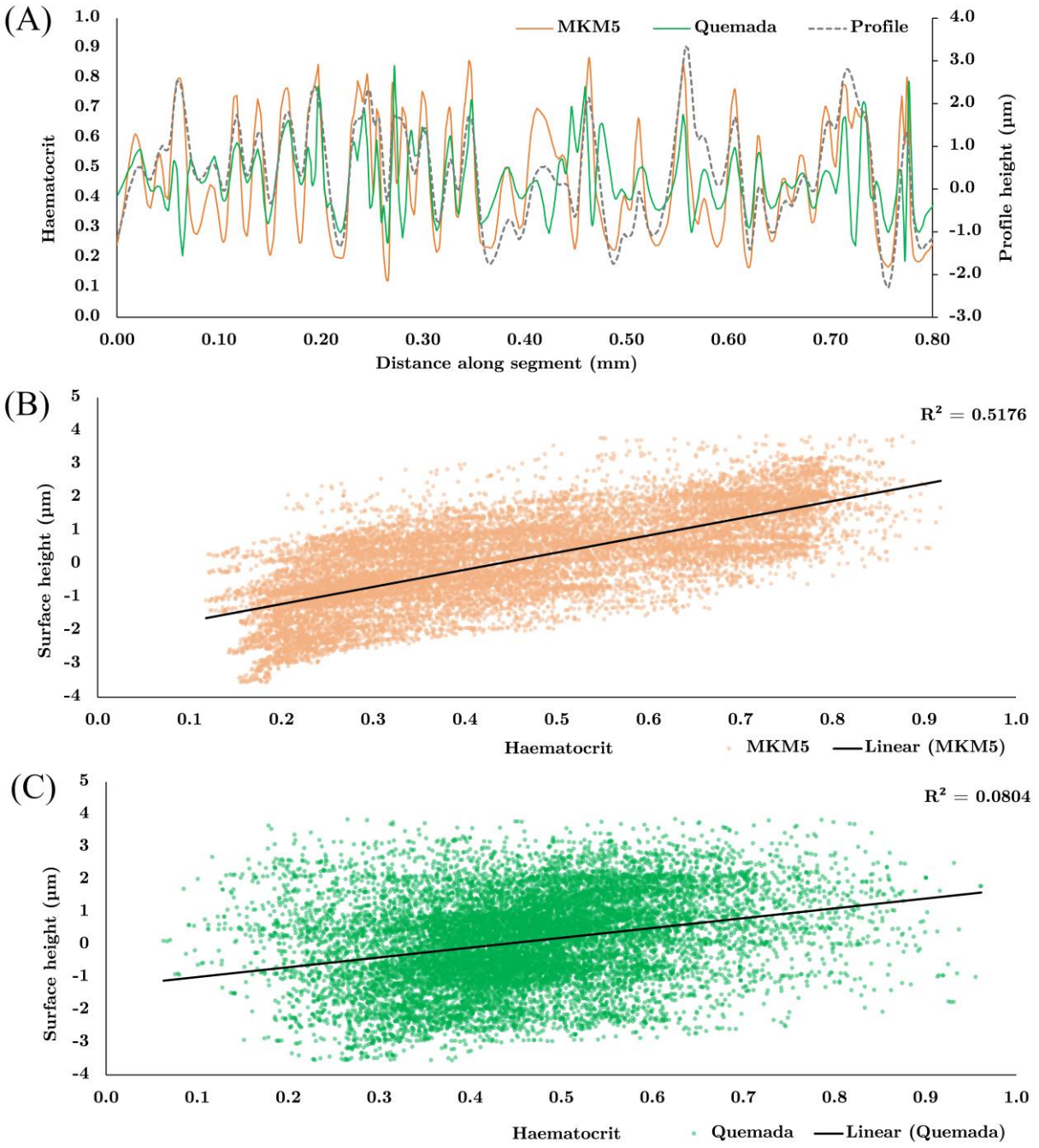

Figure 3.12: (A) – Variation of surface haematocrit and height along a rough segment (Data taken from 5 lines over the surface, parallel to flow direction), (B,C) – Scatter plots of surface height versus haematocrit for the MKM5 and Quemada models respectively ($p < 0.001$)

The impact of surface roughness on the haematocrit is clearly seen in Figure 3.12A, where large changes in surface height (e.g. -1 µm to 3 µm) result in a significant increase

in haematocrit for both multiphase models (0.2-0.8). As described in '3.3.2.2 Multiphase haematocrit', an initial uniform distribution of haematocrit (value of 0.45) was initially assumed at the inlet of the artery, with the subsequent transient blood flow resulting in small fluctuations due to effects of density, shear rate, etc.

The resulting distribution at the outlet was the copied to be the inlet condition at 0.1 s intervals to improve the accuracy of the boundary condition away from the uniform assumption. However, due to a lack of geometric features such as arterial curvature, tortuosity or bifurcations, there was minimal impact on the overall distribution of haematocrit. The resulting distributions taken at the end of the final cardiac cycle are shown in Figure 3.13.

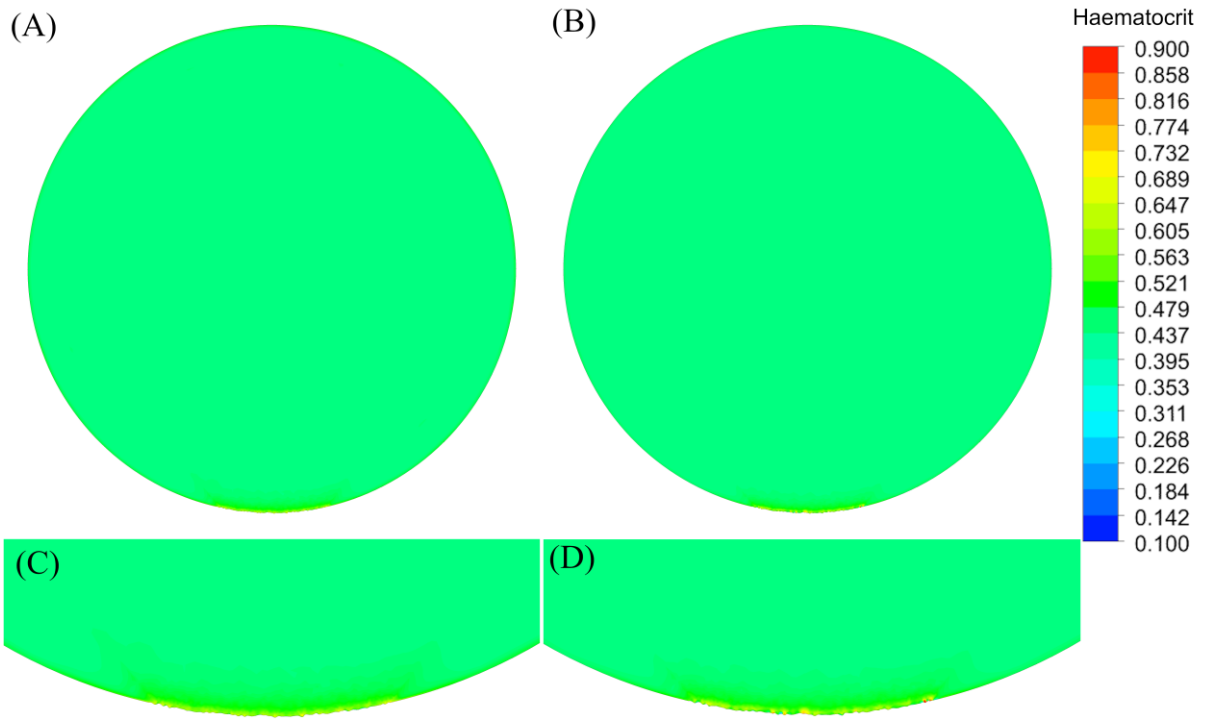

Figure 3.13: Haematocrit distribution at the outlet at the end of the 7th cardiac cycle for the (A,B) – MKM5 model and (C,D) – Quemada model

3.5 Discussion

3.5.1 Introduction

Simulations of blood flow in a coronary artery with a partially rough surface have been performed to investigate the effect of a realistic surface texture on conventional haemodynamic parameters. Overall, the rough surface had a greater variation in the parameters reported in Tables 3.3 & 3.4 in particular the WSS, RRT and shear rate, with values averaged across the entire rough/smooth segments being similar. The smooth walled assumption has been previously used in all cardiovascular models to date, which results in a uniform distribution of the haemodynamic parameters shown in Figure 3.6 compared to the variation seen for all parameters on the rough segment. As WSS is closely linked to the onset of atherosclerosis, an increase in lumen roughness will lead to larger regions with low WSS which will then become more susceptible to the onset of atherosclerotic lesions.

3.5.2 Rough surface effects

Near-wall haemodynamics are known to relate to the onset and progression of CVDs (Arzani *et al.*, 2017), with computational approaches typically focusing on Lagrangian particle tracking methods within this region (Longest, Kleinstreuer and Buchanan, 2004; Brault, Dumas and Lucor, 2016), or Eulerian models evaluating the WSS/Advection/Diffusion close to the wall (Arzani *et al.*, 2017; Chiastra *et al.*, 2017),

yet these do not include the endothelial surface texture. This simplification arises because the region of interest for coronary models is typically macroscopic, focussing on the effects of stenosis or bifurcations where the surface texture can be ignored.

For a straight cylindrical section of the coronary artery, the physiological WSS magnitude varies between (Malek and Alper, 2007) 1-7 Pa with a TAWSS magnitude of approximately (Chatzizisis *et al.*, 2007; Wentzel *et al.*, 2012) 1.5 Pa. According to a clinical *in vivo* study of 506 patients, an AATAWSS magnitude of 1-1.7 Pa can be considered moderate (Stone *et al.*, 2012), with all models predicting values between 1.3-1.48 Pa for both the rough/smooth segments except for the Quemada which was around 1 Pa. For further validation, an estimate of WSS assuming Poiseuille flow for this diameter is 1.39 Pa and, therefore, all single-phase models provide a physiological magnitude of both WSS and AATAWSS on both the rough/smooth segments.

The surface roughness of the coronary artery has been examined as a factor in the onset of atherosclerosis (Schmidt-Trucksäss *et al.*, 2003; Cinthio, Hasegawa and Kanai, 2011; Niu *et al.*, 2013), where the lumen roughness increases due to endothelial damage (Kitamura, Hasegawa and Kanai, 2012), and so models which focus on predicting likely sites where atherosclerosis may form (Stone, Coskun, Yeghiazarians, *et al.*, 2003; Rikhtegar *et al.*, 2012), or modelling the accumulation of lipids/monocytes (Iasiello *et al.*, 2016) in the artery may benefit from considering this locally in those regions. In addition, an *in vitro* study using human cultured endothelium of the carotid artery showed increased particulate adhesion in the presence of oscillating shear

stress(Chappell *et al.*, 1998). This is similar to the findings in this study (e.g. Figure 3.6B, 3.11 and 3.12A), where regions displaying peak OSI values appear to correspond to the highest haematocrit as RBC accumulate. Furthermore, the elevated WSS at these peaks would impact on other blood particulates such as platelets, where increased WSS and shear forces are pivotal in the activation and adhesion of platelets (Sorensen *et al.*, 1999).

While full-scale arterial models with this texture are still computationally unfeasible, the technique could be applied to local regions to study interactions with medical devices such as stents (Ladisa *et al.*, 2003; Wei, Chen and Li, 2019) or haemodialysis catheters (Knuttinen *et al.*, 2009; Lucas *et al.*, 2014). With coronary artery stents having a thickness of approximately (Vijayaratnam *et al.*, 2015) 100 µm, the variation in surface roughness for a diseased artery may impact on the local haemodynamics around the struts.

Whilst parameters averaged over the entire segments are comparable, the much wider range occurring over the undulations in the rough surface result in a maximum/minimum WSS of around 6.4 Pa and 0.05 Pa for all the rheological models. With regions of higher WSS thought to be atheroprotective (Traub and Berk, 1998; Papaioannou *et al.*, 2006), the AATAWSS for both segments is sufficiently high to indicate a healthy functioning artery (Malek and Alper, 2007), however, the 'valleys' of the roughness indicate regions with a low enough WSS where endothelial dysfunction may be a consideration even in this idealised geometry. These effects would likely be

exacerbated by arterial curvature/stenosis, especially as the surface roughness increases when the endothelium is damaged (Kitamura, Hasegawa and Kanai, 2012).

The size and shape of endothelial cells varies throughout the cardiovascular system, but are generally between 0.1 – 10µm thick (Félétou, 2011) compared to the circumferential roughness of around 1 µm. Therefore, the surface roughness will arise between the junction of adjacent cells, and along the length of individual cells, are they are not perfectly flat and deform during the fluctuations in wall shear stress (Roux *et al.*, 2020). As the roughness measurements were obtained *ex vivo*, and the CFD model has rigid walls, the deformation of individual cells is not accounted for. Whilst this study shows the first implementation of roughness in a CFD model, if *in vivo* roughness measurement techniques increase in resolution (Niu *et al.*, 2013), then the effects of varying endothelial size/shape during the cardiovascular cycle could be compared.

3.5.3 Rheological model effects

As the surface texture has yet to be modelled using CFD, a comparison of the most common approaches to blood rheology has also been performed, to assess their suitability for such multi-scale models. Since blood exhibits both Newtonian and non-Newtonian properties, the choice of rheological model describing this behaviour can greatly impact on the assessment of haemodynamic parameters (Cho and Kensey, 1991; Vijayaratnam *et al.*, 2015; Iasiello *et al.*, 2016), with the majority of models being

single-phase, whose viscosity only varies under shear, with fewer models considering phase interactions between plasma/RBC and the effects of haematocrit.

Previous comparisons between models for coronary arteries have shown that a Newtonian assumption consistently underestimates the magnitude of WSS (Cho and Kensey, 1991; Carty, Chatpun and Espino, 2016), and with the introduction of a non-Newtonian importance factor by Ballyk *et al.* (Ballyk, Steinman and Ethier, 1994), it has been shown that specific areas of the coronary artery (curvature/stenosis/bifurcations) experience significant regions of non-Newtonian flow (Soulis *et al.*, 2008; Caballero and Laín, 2015; Ahmadi and Ansari, 2019) and as such an appropriate model should be selected. Even with multiple comparisons between viscous models (Johnston *et al.*, 2004, 2006; Lee and Steinman, 2007; Jahangiri, Saghafian and Sadeghi, 2017), it is still challenging to determine which non-Newtonian model is most suitable for coronary models, and indeed likely depends on the focus of the study and the pathology in question.

All single-phase models show a large range of shear rates occurring over both the rough/smooth segments (Table 3.3), with the NNIF indicating again that even under normal physiological conditions blood exhibits significant non-Newtonian properties. At higher shear rates (>500 s^{-1}) all single-phase models predict a similar viscosity of around 3.45 mPa.s, yet it is at the lower shear rates (<100 s^{-1}) where predictions of viscosity diverge (Figure 3.4) impacting the NNIF as well as the conventional parameters used to assess atherosclerotic/stenotic regions. This low-shear behaviour is

crucial to modelling the rough surface accurately (Chien *et al.*, 1966; Cho and Kensey, 1991), yet physiologically accurate viscometer measurements for blood at low-shear are difficult due to inherent inaccuracies as well as blood's dependence on temperature and haematocrit (Brooks, Goodwin and Seaman, 1970; Cho and Kensey, 1991).

While the single-phase models might oversimplify the near-wall/low-shear haemodynamics occurring on the rough surface, a multiphase model which considers haematocrit and local RBC transport may improve upon this. The MKM5 multiphase model performs most similarly to the single-phase models, with all parameters for both the rough/smooth segments being in close agreement apart from Max WSS/OSI/Shear/NNIF on the rough segment. This is likely due to the instability of the multiphase models at extremes of haematocrit (Hund, Kameneva and Antaki, 2017). Above a certain haematocrit, blood ceases to behave as a fluid and the accumulation of RBC alters the local haemodynamics in these regions (Kim, VandeVord and Lee, 2008). This aggregation process is dependent on a range of biochemical factors (Wootton *et al.*, 2001; Hund, Kameneva and Antaki, 2017), and is not fully accounted for in the MKM5 model resulting in predictions of high haematocrit/shear (Figure 3.11 & Figure 3.12A) and hence much higher WSS/OSI/NNIF values in these regions. Whilst the link between surface roughness and haematocrit is clearly shown in Figure 3.12A, the large scatter distribution in Figures 3.12B/C indicate the influence of additional parameters in this near-wall region

which might include: low shear rate, flow stagnation and localised regions of high/low viscosity.

As plasma is less viscous than RBC, it exerts a lower WSS magnitude, hence, the presence of a RBC depleted region will promote poor endothelial function. As individual RBC are not simulated with this approach, additional effects due to the elastic deformation of RBC (Liu *et al.*, 2015; Secomb, 2017) may further modify these micro-scale near-wall haemodynamics as RBCs deform around the surface texture. Whilst this model combines the variation in lumen roughness with multiphase cellular transport, to further link the two scales, additional constraints on near-wall flow such as advection/diffusion at the endothelial surface or the aggregation/deformation of RBC would be desirable to better understand how RBC transport effects these shear-based parameters.

3.5.4 Limitations

Whilst all measures have been taken to ensure the accuracy of the presented model, the study has certain limitations/assumptions. The main limitation of the study was the use of a simple cylindrical shape, whilst based upon *in vivo* dimensions, the lack of any features such as arterial curvature/stenosis, bifurcations or methods to induce flow disturbance will compromise the development of natural recirculation/oscillations. Whilst this is detrimental to the physiological accuracy, the focus was the impact of

realistic surface roughness, and this geometry enabled controlled comparisons to be taken between the two surface types.

As the use of surface roughness in a 3D model has now been established, similar methodologies could be applied to more clinically relevant applications, such as increasing surface roughness as a precursor to arterial dysfunction, particle migration in the low-shear environments downstream of bifurcations and interactions between stents and a rough surfaced artery. Computation of maximum WSS values were performed pointwise, and whilst this provides sensible results for all single-phase models, the resulting max WSS values for the multiphase models were higher than expected for a physiological model. This arose due to extremes of haematocrit occurring in the near-wall region, in part potentially due to a lack of physical laws governing aggregation of RBC. One approach to reducing the multiphase WSS predictions would have been to average these values over a wider patch. However, for consistency between all models (and to avoid introducing an artefact to non-multiphase models), such a method was not used; additionally, such an approach would require the use of a parameter (e.g. patch area), the value of which would need to be arbitrarily chosen.

3.6 Conclusion

Comparisons of well-established haemodynamic parameters used in coronary artery models on both a smooth and realistically rough artery surface have shown that a rough surface results in a greater range of values, and averages over the rough/smooth

segments are in good agreement. The combination of macro-micro scales to evaluate coronary flow over these rough surfaces has highlighted how complex the near-wall haemodynamics can be, even in a geometrically and physiologically simple case. The different approaches to rheology applied to this surface show that the single-phase models provide a stable estimate of local haemodynamics as seen in other studies, yet oversimplify the complex behaviour occurring over the undulations at the lumen surface, particularly in the Newtonian case. The use of multiphase models attempts to further characterize the behaviour of blood in the low-shear/micro-scale roughness region, and whilst the MKM5 appears more suitable than the Quemada-Das, to truly encompass the behaviour of blood/particulates at this boundary requires considering additional phenomena such as advection/diffusion at the endothelium, RBC aggregation/deformation and the effects of fibrogen/plasma protein concentrations.

3.7 Progression

With the importance of non-Newtonian and multiphase blood rheology established in a rough-walled multiscale coronary simulation, the following chapter will expand upon these techniques in a more physiologically accurate coronary artery bifurcation. The increased number of geometrical features will lead to recirculation zones and present increased challenges to accurate modelling of the more complex haemodynamic environment.

STATEMENT OF CONTRIBUTIONS II

The following chapter includes novel research which has been previously published in a peer-reviewed scientific journal, with myself as the principal author. It was published as gold standard open access, with a full CC-BY 4.0 copyright license (https://creativecommons.org/licenses/by/4.0/) allowing for the reproduction and alteration included within this thesis. Below are the details of the publication, and a statement of the contributions from each author.

Owen DG, Diana C. de Oliveira, Emma K. Neale, Duncan E.T. Shepherd, Daniel M. Espino (2021) *Numerical modelling of blood rheology and platelet activation through a stenosed left coronary artery bifurcation.* PLoS ONE 16(11): e0259196

https://doi.org/10.1371/journal.pone.0259196

Owen DG: Conceptualisation, creation/development of models, data analysis and drafting of manuscript.

de Oliveira DC: Conceptualisation, data analysis, and revised manuscript.

Neale EK: Conceptualisation, revised manuscript.

Shepherd DET: Conceptualisation, coordination, and revised manuscript.

Espino DM: Conceptualisation, coordination, and revised manuscript.

4 | CORONARY BIFURCATION

4.1 Introduction

Cardiovascular diseases were responsible for an estimated 18.8 million deaths in 2017 (Roth *et al.*, 2018), with heart disease being the leading cause of death in the USA in the same year (Virani *et al.*, 2020). Of particular relevance to cardiovascular health are the coronary arteries, two major blood vessels which bifurcate into multiple smaller branches. The coronary arteries have been associated with several clinical pathologies, including atherosclerotic plaques/lesions (Malek and Alper, 2007; Dash, 2014), arterial stiffening (Weber *et al.*, 2004) and increased thrombosis (Collet *et al.*, 2006) (clot formation). Atherosclerosis is the development of fatty plaques within the artery wall, with their onset and progression associated with regions of low time-averaged wall shear stress (TAWSS) (Wentzel *et al.*, 2012) occurring around the branching of the artery (Louvard *et al.*, 2008) or distal to regions of stenosis (Chatzizisis *et al.*, 2007).

In addition to plaque rupture causing myocardial infarction or sudden death (Virani *et al.*, 2020), the altered haemodynamics arising from inflammatory plaque growth also impacts the behaviour and activation of platelets; catalysing plaque/fibrin growth through increased platelet adhesion (Davi and Patrono, 2007) and increased risk of thrombus formation (Badimon, Padró and Vilahur, 2012) (atherothrombosis), with a

detailed review of these phenomena provided by Davi and Patrono (Davi and Patrono, 2007).

Computational fluid dynamics (CFD) is a useful tool to study vascular pathologies and is capable of predicting the location and progression of coronary atherosclerotic plaques (Lee *et al.*, 2019), growth/rupture of aneurysms (Humphrey and Taylor, 2008) and microscopic thrombus growth (Yazdani *et al.*, 2017). The branching of the coronary arteries results in low-shear and stagnant/recirculation environments occurring on the outer walls (Chaichana, Sun and Jewkes, 2011), being common sites for plaque growth and hence stenosis to occur. The realistic simulation of blood flow in these regions is crucial for accurate haemodynamic predictions and hence the understanding of disease mechanisms.

As discussed in previous chapters, there are multiple fundamentally different approaches to blood rheology (Bessonov *et al.*, 2016), all based on fitting constituent equations to differing sets of experimental viscometer data (Brooks, Goodwin and Seaman, 1970). Blood is a multiphase fluid, comprised predominantly of a dilute suspension of red blood cells (RBC) within a plasma continuum (Gidaspow, 1994). Rheological properties depend on fluid shear rates, the concentration of RBC (Eckmann *et al.*, 2000) (hematocrit) and crucially the aggregation of individual RBC into a rouleaux, which is a key factor in non-Newtonian behaviour. Rouleaux formation requires prolonged exposure to low-shear rates (Galidi *et al.*, 2008) (<50 s^{-1}), and is inherently a microscopic phenomenon (Robertson, Sequeria and Kameneva, 2008). As

there are approximately 5×10^6 RBC per mm^3 of blood (Caro *et al.*, 2011a), it is impossible to simulate this phenomenon for large arteries with current computational power. Shear-rates in larger arteries are conventionally considered to be sufficiently high for rouleaux formation to be negligible, in which case a more simplistic approach is to assume blood to be a homogeneous single-phase fluid, with constant density and either a constant (Javadzadegan *et al.*, 2017) (Newtonian) or a shear-thinning (non-Newtonian) viscosity (Chaichana, Sun and Jewkes, 2012).

As a low-shear environment is commonly associated with disease, the extent to which this assumption oversimplifies crucial behaviour is contended (Arzani, 2018). As macroscale multiphase models do not simulate individual RBC, representing the rheological effects of aggregation and rouleaux formation is an ongoing challenge. However, the recent 5-parameter Modified Krieger Model (MKM5) is based upon the Krieger model for suspensions and attempts to incorporate the effect of aggregation on the viscosity of blood (Hund, Kameneva and Antaki, 2017).

Many of the studies that focus on the impact of different types of rheology in coronary artery haemodynamics employ healthy geometries, and assume blood to be a single-phase fluid (Johnston *et al.*, 2006; Lee and Steinman, 2007; Soulis *et al.*, 2008), with fewer studies assessing the effects of multiphase models in coronary haemodynamics (Jung *et al.*, 2006; Owen, Schenkel, *et al.*, 2020). Despite significant evidence on the non-Newtonian effects occurring around the coronary bifurcation, and the importance of haematocrit on the properties of blood, to date there is no conclusive study

comparing these effects on parameters associated with the progression of atherosclerosis, and the subsequent impact on atherothrombosis/platelet activation.

The present study aims to compare the impact of different rheological assumptions on a diseased left coronary bifurcation (at the level of the left anterior descending artery, LAD, and the left circumflex artery, LCx). In particular, the prediction of blood flow in the low-shear environment distal to the bifurcation/stenotic regions, including the aggregatory potential of RBC via low-shear residence time and variations in haematocrit. Furthermore, the effect of stenosis on the transport/activation of platelets will be considered for a multiphase model, using a novel Lagrangian platelet simulation to evaluate trajectories, residence times and level of activation. Based upon the previous analysis of rheological models in a realistically rough surfaced coronary in Chapter 3, this study will use a total of four rheological models: single-phase Newtonian (SN); single-phase Carreau (SC) multiphase Newtonian (MN); and multiphase MKM5. The Newtonian and Carreau models were kept as they are the most prevalent approaches to blood rheology in the literature (Johnston *et al.*, 2004, 2006; Skiadopoulos, Neofytou and Housiadas, 2017), and the MKM5 multiphase model was used in place of the Quemada-Das as it provided better predictions of *in-vivo* parameters in Chapter 3. A multiphase model, with Newtonian properties for RBC has been included for this study, to investigate if the non-Newtonian behaviour of whole blood can be approximated solely with a multiphase approach, as the MN model is much simpler to implement and more computationally efficient than the MKM5 model.

4.2 Methods

4.2.1 Geometry

4.2.1.1 Coronary bifurcation

The vessel geometry was constructed using a centreline profile from an *ex vivo* sample of healthy porcine left main coronary artery bifurcation (LAD-LCx) from Fresh Tissue Supplies, Horsham, UK. This was scaled to match human physiological dimensions (Dodge *et al.*, 1992) using SolidWorks (SolidWorks, Dassault Systèmes, Vèlizy-Villacublay, France), shown in Figure 4.1. The total length of the artery is 70 mm, with a branch angle of approximately 72°, an inlet diameter of 4.5 mm, and outlet diameters of the LAD and LCx branch being 3 mm and 2 mm, respectively. The reduction in circular lumen diameter was achieved via linear-interpolation between the inlet-outlet resulting in a gradual tapering. Surface roughness has not been implemented in this model, as the main focus is the effect of disturbed haemodynamics on the rheology of blood. To avoid any unwanted entrance/exit effects on the haemodynamics of the bifurcation, the inlets and outlets have been extended 15 mm using a constant diameter.

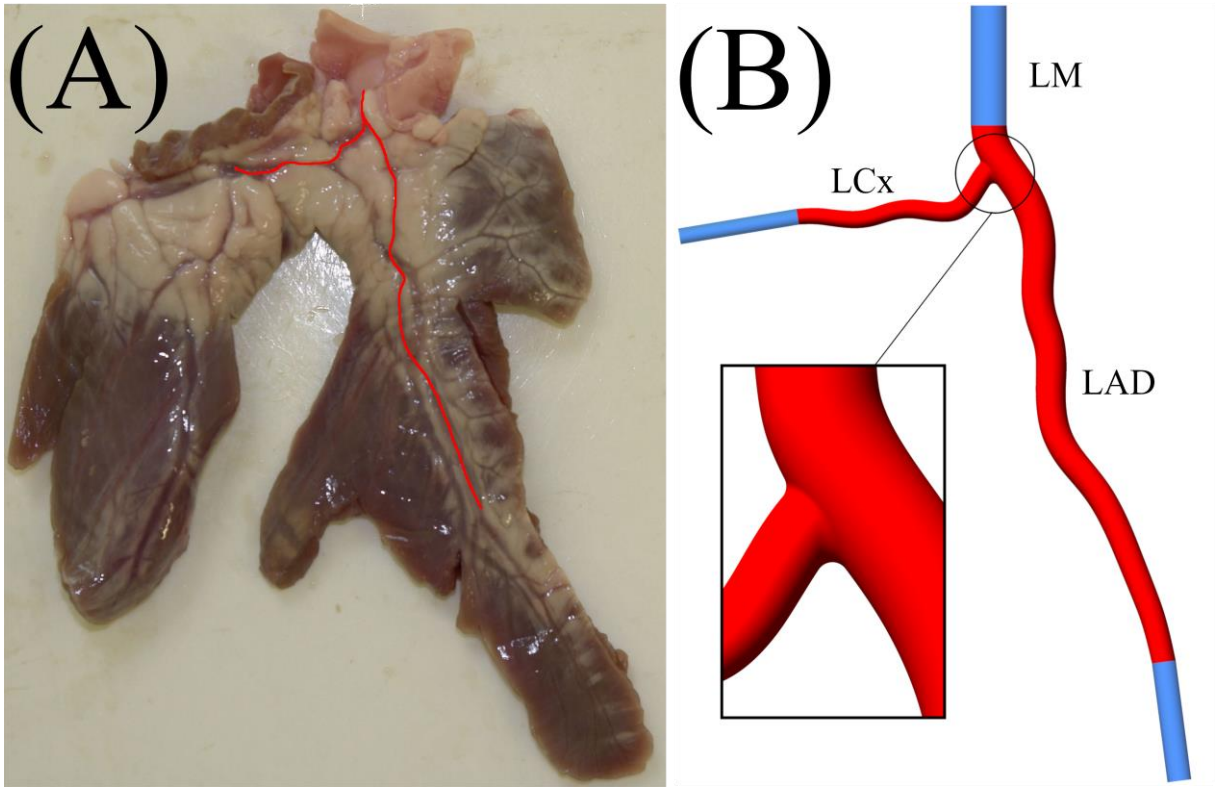

Figure 4.1: (A) – Porcine *ex vivo* heart segment, with coronary geometry marked in red. (B) Coronary artery bifurcation geometry including domain extensions shown in blue (LAD, left anterior descending artery; LCx, left circumflex artery; LM, left main coronary artery)

4.2.1.2 Diseased coronary bifurcation

A common coronary artery disease is the growth of atherosclerotic plaques within the lumen surface resulting in stenosis and a reduction in lumen diameter. Based upon an *in vivo* study of 140 patients, the most common occurring stenosis in coronary artery bifurcations is a continuous and diffuse plaque in both the LAD and LCx branches (Oviedo *et al.*, 2010). This results in a gradual tapering of the lumen approximately starting at the bifurcation and reduces in diameter along a cubic spline profile, to a minimum diameter occurring just distal to the bifurcation, which matches the

qualitative descriptions of Oviedo *et al.*, and other diseased CFD models (Gholipour, Ghayesh and Zander, 2018).

Stenosis can be defined as the reduction in lumen diameter due to plaque formation (Equation 4.1), with this study using a 50% stenosis.

$$S_p = \frac{D_{healthy} - D_{min}}{D_{healthy}} \qquad (4.1)$$

where S_p is the percentage stenosis, $D_{healthy}$ is the diameter before the plaque and D_{min} is the minimum arterial dimeter at the point of maximum stenosis. A comparison between the healthy/diseased arterial geometry is shown in Figure 4.2.

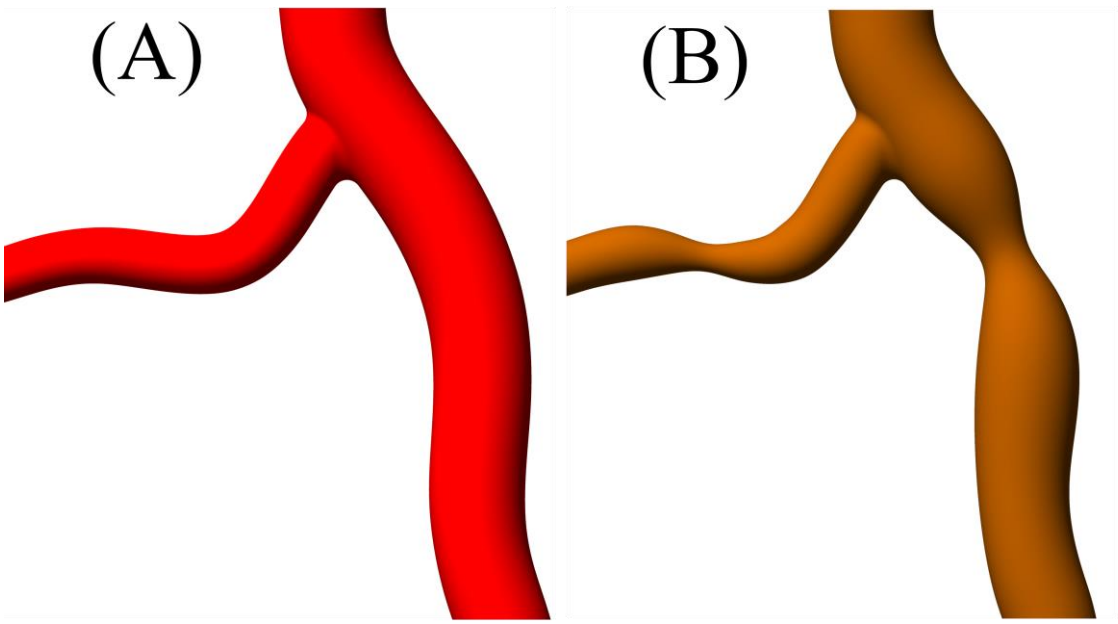

Figure 4.2: Comparison between (A) healthy and (B) diseased arterial bifurcation with stenosis

4.2.2 Rheological models

Whole blood exhibits significant non-Newtonian properties (Carty, Chatpun and Espino, 2016), with a viscosity that depends on shear rate (Restated as Equation 4.2) and haematocrit (red blood cell concentration) as well as a variety of other mechanical/biological factors (Bessonov *et al.*, 2016).

$$\dot{\gamma} = \sqrt{2D_{ij} \cdot D_{ij}} \qquad (4.2)$$

where $\dot{\gamma}$ is the shear rate of the fluid, D is the strain rate tensor with $i, j = 1,2,3$ as the inner products. This study examines four different rheological models, consisting of two single-phase models (which consider blood a single homogeneous fluid), and two multiphase models (which consider blood as a dilute suspension of RBC within a plasma continuum). Of the two single-phase models, one assumes blood to be Newtonian (Yilmaz and Gundogdu, 2008) with constant viscosity (Single Newtonian, SN), and the other uses a shear dependant Carreau (Lee and Steinman, 2007) viscosity definition (Single Carreau, SC).

Similarly for the two multiphase models, one uses a Newtonian approach, where the viscosity of each phase is constant (Multi Newtonian, MN) and the other uses a modified Krieger model with 5 parameters (Hund, Kameneva and Antaki, 2017) (MKM5) which allows RBC viscosity to vary with both shear forces and haematocrit. The viscosity of whole blood at varying physiological shear rates for each of the four

models is given in Figure 4.3. The accompanying mathematical definitions and coefficients for each model are provided in Table 4.1.

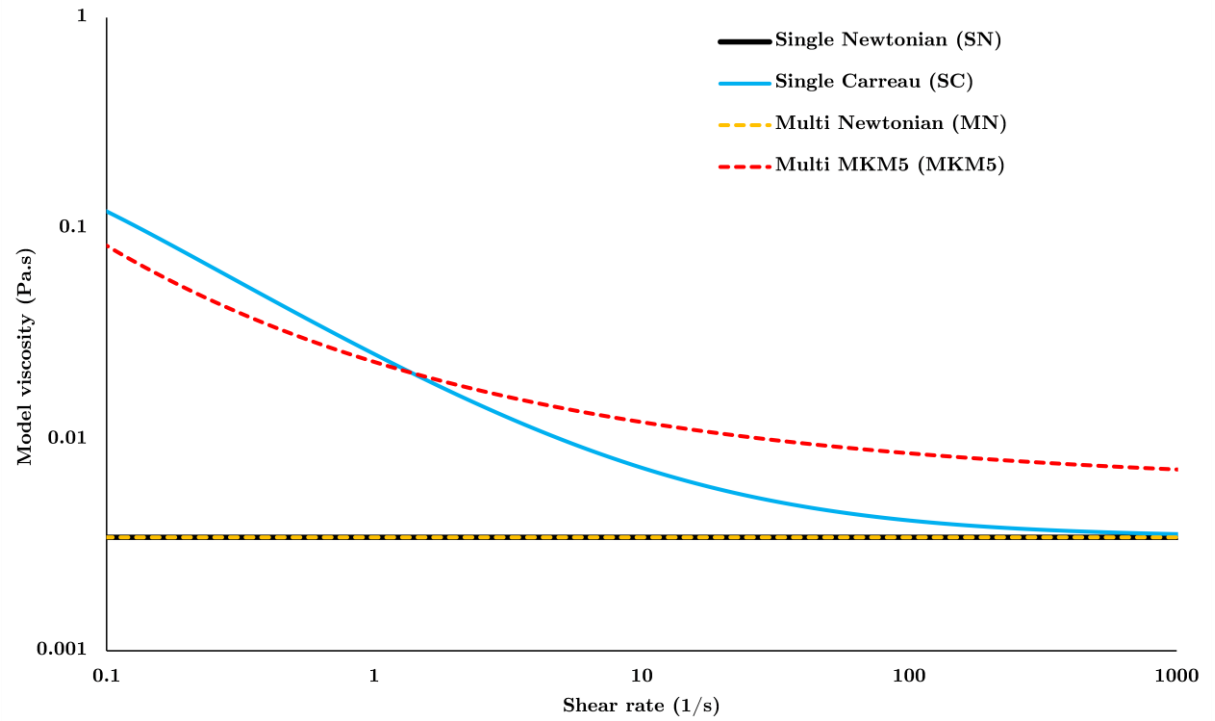

Figure 4.3: Apparent blood viscosity versus shear rate for the four rheological models (Multiphase models use a Haematocrit of 0.45)

Table 4.1: Definitions for the rheological models (some restated from previous chapter for convenience)

Model	Viscosity definition (Pa.s)	Parameters
Single-phase Newtonian (SN) (Yilmaz and Gundogdu, 2008)	$\mu = 0.00345$	-
Single-phase Carreau (SC) (Lee and Steinman, 2007)	$\mu = \mu_\infty + (\mu_0 - \mu_\infty)[1 + (\lambda\dot{\gamma})^2]^{\frac{n-1}{2}}$	$\mu_\infty = 0.00345,\ n = 0.25$ $\mu_0 = 0.25,\quad \lambda = 25$
Multiphase Newtonian (MN)	$\mu = \mu_{rbc}\emptyset_{rbc} + \mu_p(1 - \emptyset_{rbc})$	$\mu_{rbc} = 0.006163$ $\mu_p = 0.00123$
Multiphase Modified Krieger Model 5 Parameters (MKM5) (Owen, Schenkel, *et al.*, 2020)	$\mu = \mu_p\left[1 - \frac{\emptyset_{rbc}}{\emptyset_{rbc,crit}}\right]^{-n}$ $n = \begin{cases} n_\infty & if \quad \emptyset_{rbc} < 0.2 \\ n_\infty + n_{st} & if \quad \emptyset_{rbc} > 0.2 \end{cases}$ $n_\infty = be^{-c\emptyset_{rbc}},\ n_{st} = \beta\gamma'^{-\nu}$ $\gamma' = 1 + (\lambda\dot{\gamma})^{\nu_g}$	$\mu_p = 0.00123$ $\emptyset_{rbc,crit} = 0.95$ $b = 8.78084$ $c = 2.82354$ $\beta = 16.27775$ $\nu = 0.14275$ $\lambda = 1252.64407$ $\nu_g = 2$

In Table 4.1, μ_{rbc} is the viscosity of the RBC, μ_p is the viscosity of plasma, $\emptyset_{rbc}$ is the haematocrit and $\emptyset_{rbc,crit}$ is the critical haematocrit where the RBC no longer behave as a fluid. As the definitions in Table 4.1 are for the viscosities of whole blood, the viscous definitions required for the RBC in the MKM5 model can be inferred from a weighted average restated as Equation 4.3.

$$\mu_{rbc} = \frac{\mu_{blood} - (1 - \emptyset_{rbc})\mu_p}{\emptyset_{rbc}} \tag{4.3}$$

where μ_{blood} is the definition of MKM5 viscosity provided in Table 4.1. This equation was also used to calculate the Newtonian viscosity of the RBC based upon a haematocrit of 0.45 and a whole blood mixture viscosity of 3.45 mPa.s.

4.3 Numerical Methods

4.3.1 Governing equations

The governing equations for the continuity of mass and momentum for the single and multiphase models are restated briefly in Table 4.2 and are previously defined in 3.3.1 Governing equations. These equations were solved numerically using the commercial finite-volume solver Fluent (Ansys v20.1, Ansys Inc., Canonsburg, PA, USA). The single-phase models assumed blood to be incompressible with a density (Ahmadi and Ansari, 2019) of $\rho = 1060\,\mathrm{kg/m^3}$. The transport and phase interactions of the multiphase models were implemented using an Eulerian-Eulerian mixture model similar to other cardiovascular models (Yilmaz, Kutlar and Gundogdu, 2011), which considers RBC as a dilute suspension within a Newtonian plasma continuum, with a comprehensive overview of this technique described previously in Section 3.3.1.2 Multiphase equations.

Table 4.2: Conservation of mass and momentum for the single and multiphase models, with the volume fraction and external force (Virtual mass) definitions for the multiphase models

Single-phase equations	
$\frac{\partial u_i}{\partial x_i} = 0$	where u is the velocity, x is the spatial coordinate, t is time, μ is fluid viscosity, ρ is fluid density and p is pressure.
$\frac{\partial u_i}{\partial t} + u_j \frac{\partial u_i}{\partial x_j} = \frac{\partial}{\partial x_j}\left(\mu \frac{\partial u_i}{\partial x_j}\right) - \frac{1}{\rho}\frac{\partial p}{\partial x_i}$	
Multiphase equations	
$\sum_{n=1}^{2} \emptyset_n = 1$	where $\emptyset$ is the volume fraction of each phase, a, b are the primary/secondary phases (plasma/RBC) respectively, ρ_b is the density of phase b, $\vec{v}_b$ is the velocity of phase b, p is pressure (shared by all phases), $\bar{\bar{\tau}}_b$ is the stress-strain tensor of phase b, K_{ab} is the interphase momentum exchange coefficient and $\vec{F}_{ext}$ are the external forces.
$\frac{\partial}{\partial t}(\emptyset_b \rho_b) + \nabla \cdot (\emptyset_b \rho_b \vec{v}_b) = 0$	
$\frac{\partial}{\partial t}(\emptyset_b \rho_b \vec{v}_b) + \nabla \cdot (\emptyset_b \rho_b \vec{v}_b \vec{v}_b) = -\emptyset_b \nabla \mathrm{p} + \nabla \cdot \bar{\bar{\tau}}_b + \sum_{a,b=1}^{2} K_{ab}(\vec{v}_a - \vec{v}_b) + \vec{F}_{ext}$	
$\vec{F}_{vm} = 0.5 \emptyset_b \rho_a \left(\frac{d_a \vec{v}_a}{dt} - \frac{d_b \vec{v}_b}{dt}\right)$	

The momentum exchange coefficient between phases is derived from the RBC interfacial-area (ANSYS, 2019a), and the viscous drag they experience which is given by the Shiller-Naumann (Schiller and Naumann, 1935) model for spheres. The only external force considered was the virtual mass force, arising from the changing inertia of the plasma phase due to relative RBC acceleration. The lift due to shear is also not included due to limitations of numerical models at wide ranging Reynolds numbers/shear rates near the boundary (Yilmaz and Gundogdu, 2009) as well as only

being recommended for sub-micron particles (ANSYS, 2019b). In both multiphase models, the density of plasma (Brooks, Goodwin and Seaman, 1970) and RBCs (Ponder, 1948) were set as $\rho_a = 1003$ kg/m^3 and $\rho_b = 1096$ kg/m^3, respectively. The haematocrit distribution of the domain and inlet was set at a uniform 45% based upon physiological ranges (Pal, 2003), however, the exact *in vivo* distribution is unknown.

4.3.2 Platelet modelling

To further evaluate the haemodynamics of the coronary bifurcation, platelets were released into the domain and tracked over multiple cardiac cycles to evaluate their path lines and physical properties. The platelets were considered as 2 µm diameter rigid spheres (Basciano *et al.*, 2011) with density $\rho_p = 1040$ kgm^{-3}, and were assumed not to impact the blood transport (one way interaction with fluid phases). The platelets path line is calculated by equating particle inertia to the sum of forces upon the particle from Equation 4.4.

$$\frac{d\overrightarrow{u_p}}{dt} = F_D\left(\vec{u} - \overrightarrow{u_p}\right) + \vec{F} \qquad (4.4)$$

where $\vec{u}$ and $\overrightarrow{u_p}$ are the fluid and platelet velocity, respectively, F_D is the drag force (Equation 4.5) and $\vec{F}$ is the contribution of external forces. The drag equation assumes all platelets are spherical, with a fixed constant diameter. Ideally a mass-mean diameter would be applied, but the range of platelets diameters is not reported in the literature.

$$F_D = \frac{18\mu}{\rho_p {d_p}^2}\frac{C_D R_e}{24} \qquad (4.5)$$

where d_p is platelet diameter, R_e is the relative Reynolds number and C_D is the drag coefficient of the platelet defined in Equation 4.6, using coefficients over a range of Reynolds numbers determined by Morsi and Alexander (Morsi and Alexander, 1972).

$$C_D = \alpha_1 + \frac{\alpha_2}{R_e} + \frac{\alpha_3}{{R_e}^2} \tag{4.6}$$

Whilst the most significant force upon the platelets is viscous drag, other important forces when particle/fluid densities are similar are the pressure gradient and virtual mass forces (Equation 4.7 & 4.8) acting upon the platelet and are given, respectively, by:

$$\overrightarrow{F_p} = \frac{\rho}{\rho_p} \overrightarrow{u_p} \nabla \vec{u} \tag{4.7}$$

$$\overrightarrow{F_{vmp}} = \frac{\rho}{2\rho_p} \left(\overrightarrow{u_p} \nabla \vec{u} - \frac{d\overrightarrow{u_p}}{dt} \right) \tag{4.8}$$

Additional forces such as those due to buoyancy, Magnus force, and Brownian motion are not included as they were assumed negligible (Kleinstreuer and Feng, 2013). The time dependant shear history of the platelets was evaluated using the approach first presented by Bluestein *et al.* (Bluestein *et al.*, 1997), which determines a platelets level of activation (LOA) via the cumulative sum of the exposure time (Δt) to shear stresses within the blood (Equation 4.9) during n time steps.

$$A_L = \sum_n \mu \cdot \dot{\gamma} \cdot \Delta t \tag{4.9}$$

where A_L is the LOA of an individual platelet.

This relativistic measure can identify potential regions for the activation/aggregation of platelets, with an elevated LOA being defined as values $>66^{th}$ percentile from the total range. This level was set following methodology presented by De Nisco *et al.* (De Nisco *et al.*, 2019), as provides a model-specific value for disturbed haemodynamic parameters, which is useful for quantitative comparisons across rheological models.

Platelets were released in 8 separate groups from the physiological inlet at 0.1 s intervals to ensure results reflect the transient nature of coronary blood flow (Figure 4.5). Each mesh element seeds one platelet, for a total of 13,439 per release which approximates the normal human concentration (Dumont *et al.*, 2007). The platelets were released after 3 cardiac cycles (2.4 s) had been completed once physiological flow had developed and were tracked through the flow field for a total period of 4 s (up to 6.4 s) at which point 89% and 85% of platelets had left the domain in the healthy/diseased models respectively.

The platelet tracking model and Equation 4.9 were implemented into Fluent using a user defined function (UDF) which is detailed in the Appendix and operates as described below in Figure 4.4. In addition to tracking the LOA of platelets, they also function as tracers, which are used to identify regions where RBC experience a prolonged exposure to aggregatory levels of shear ($<50s^{-1}$).

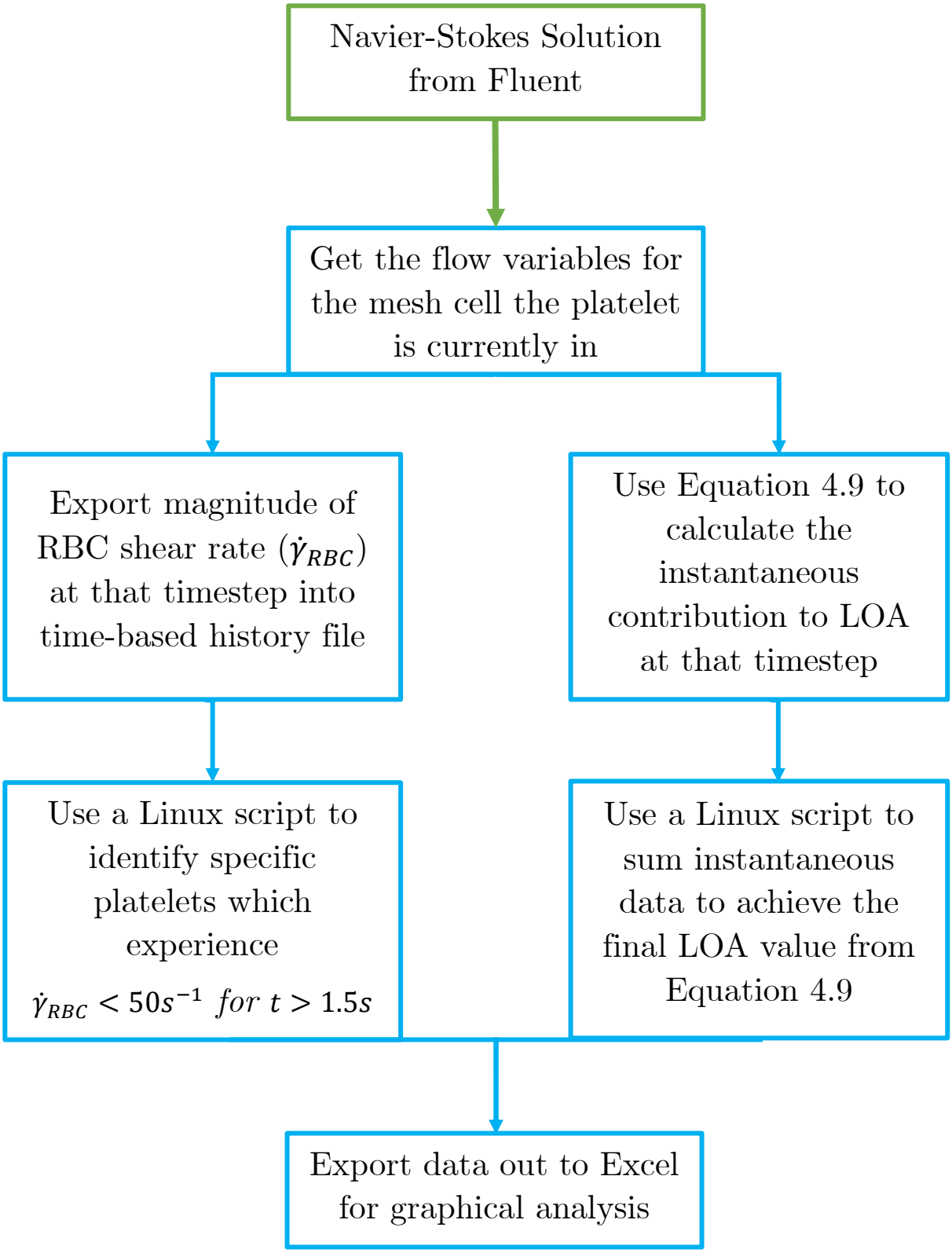

Figure 4.4: Flow chart of UDF to obtain platelet LOA and RBC aggregation data reported in results

4.3.3 Boundary conditions

A typical physiological left main coronary velocity waveform (Bénard, 2005) (Figure 4.5) was fitted to a Fourier series and scaled to match the model size, with a Reynolds number range from 277-691. The Womersley number was calculated to be 1.1 (For average model blood viscosity), and therefore a fully developed parabolic velocity profile was selected as an inlet condition.

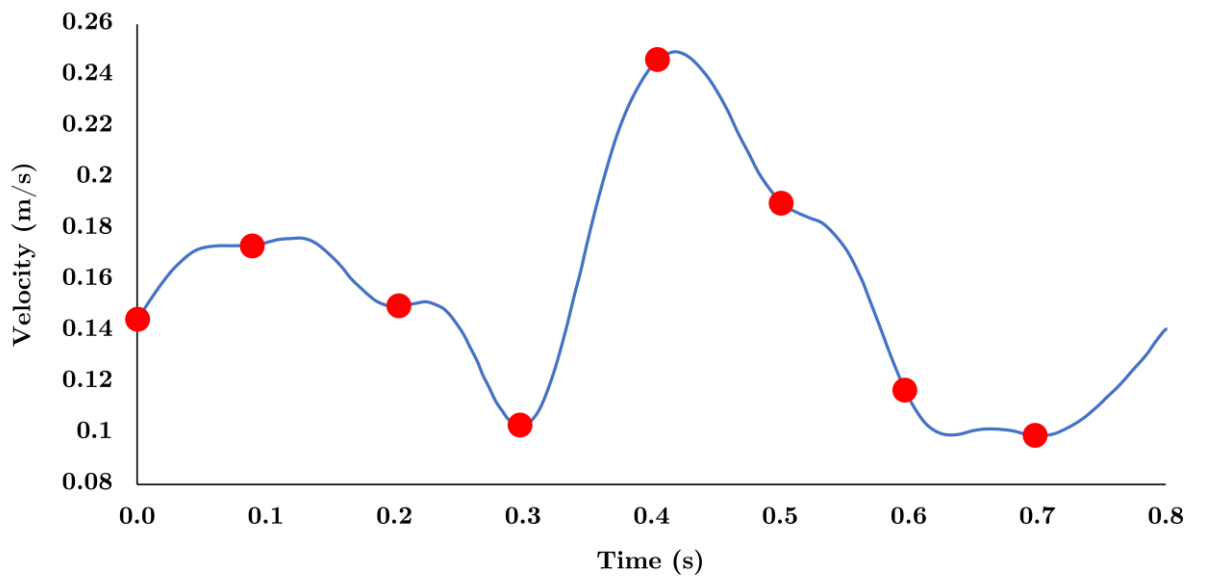

Figure 4.5: Variation of inlet velocity against time applied to the coronary artery, red dots indicate the 0.1 s intervals during which platelets were released into flow

A parabolic velocity profile describing developed laminar flow (Chabi *et al.*, 2015) was implemented to the waveform in Figure 4.5, restated as Equation 4.10.

$$u(r,t) = 2V(t)\left[1 - \left(\frac{r^2}{R^2}\right)\right] \qquad (4.10)$$

where $V(t)$ is the inlet velocity waveform, r is the radial position at the inlet and R is the maximum radius of the inlet (4.5 mm). A constant pressure of 120 mmHg (16 kPa) which approximates with mean systolic blood pressure (Davies *et al.*, 2006) was applied at the outlets.

4.3.4 Haemodynamic parameters

Table 4.3 outlines the key haemodynamic parameters for comparison arising from the different geometries and rheological models used.

Table 4.3: Haemodynamic parameter definitions (Some parameters are restated from previous chapters for convenience)

Parameter	Definition	Variables
$\bar{\omega}$	$\bar{\omega} = \frac{1}{V}\int_0^V \frac{1}{T}\int_0^T \lvert\omega\rvert dt\, dV$	where $\bar{\omega}$ is the volume average of the time-averaged vorticity and T is the length of the cardiac cycle
DVI	$DVI = \bar{\omega}_D - \bar{\omega}_H$	where DVI is the disturbed vorticity index, $\bar{\omega}_D$ and $\bar{\omega}_H$ are the volume-averages of the time-averaged vorticity for diseased and healthy cases, respectively
WSS	$\tau_w = \mu \frac{\partial u_t}{\partial n}\Big\rvert_{wall}$	where τ_w is wall shear stress (WSS), u_t is tangential wall velocity and n is unit vector perpendicular to the wall
TAWSS	$\bar{\tau}_w = \frac{1}{T}\int_0^T \lvert\tau_w\rvert\, dt$	where $\bar{\tau}_w$ is the time-averaged wall shear stress (TAWSS)
TANNIF	$\bar{I}_L = \frac{1}{T}\int_0^T \frac{\mu}{\mu_N}\, dt$	where $\bar{I}_L$ is the time-averaged local non-Newtonian importance factor (TANNIF) and μ_N is the Newtonian viscosity in Table 4.1

OSI	$\theta_i = \frac{1}{2}\left(1 - \frac{\left\lvert\int_0^T \tau_w \, dt\right\rvert}{\int_0^T \lvert\tau_w\rvert \, dt}\right)$	where θ_i is the oscillatory shear index (OSI)
RRT	$t_r = \frac{k}{(1-2\theta_i)\bar{\tau}_w}$	Where t_r is the relative residence time (RRT) and k is a proportionality constant and is set as $k = 1$

The DVI is a recently developed parameter, previously used in patient-specific stenotic artery models (Chu *et al.*, 2018), which aims to quantify flow disturbance. The TANNIF was first defined by Ballyk *et al.* (Ballyk, Steinman and Ethier, 1994), where regions of Newtonian flow have a value of 1, and non-Newtonian flow causes this value to diverge. The OSI (He and Ku, 1996) ranges from 0-0.5 where values close to 0.5 indicate highly oscillatory flow. The RRT is a measure for which higher values indicate regions of near-wall flow stagnation (Himburg *et al.*, 2004). Whilst TAWSS is inherently fluctuating and patient-specific, a pathologically low threshold was set as 1 Pa based upon the scientific consensus from *in vivo* and *in vitro* studies (Samady *et al.*, 2011; Stone *et al.*, 2012; Wentzel *et al.*, 2012). To comparatively evaluate model predictions of regions with high OSI and RRT, the percentage area greater than the value of the 66th percentile was computed for each model based upon the methodology of De Nisco *et al.* (De Nisco *et al.*, 2019) (OSI_{66} and RRT_{66} respectively).

4.3.5 Solver Settings

The solution to the above equations was obtained numerically via the discrete form of the SIMPLE algorithm for the pressure-velocity coupling, using a first order time

discretisation scheme. All models were solved in parallel, utilising 120 cores on high performance computing nodes. To generate the haemodynamic parameters, each model was solved for a total of 3 cardiac cycles (2.4 s), with a time step of 1 ms, and all haemodynamic results being evaluated over the final cardiac cycle. The platelet model was then solved for an additional 4 s of flow time. Convergence criteria per iteration was set at a mass continuity residual $<10^{-4}$, and velocity residuals $<10^{-6}$ with the single and multiphase models taking an average wall clock time of 7 and 24 hours, respectively.

4.3.6 Mesh convergence

To ensure a mesh independent solution is obtained, simulations of the diseased bifurcation were performed at 6 incrementally increasing mesh refinements. These were performed as a steady-state simulation, using the maximum inlet velocity of 0.5 m/s. A final meshing criterion was selected once the percentage difference of peak blood velocity and average WSS on the bifurcation flow divider were both below 2% for each mesh refinement. The results of the convergence study are shown in Figure 4.6, with the final mesh consisting of 5.4 million mostly tetrahedral elements, with a 0.25 mm thick prismatic layer of 10 elements around the lumen walls for an accurate boundary layer formulation (Figure 4.7). The mesh has minimum, average and maximum edge length of 0.001, 0.1 and 0.175 mm respectively, with an average element skewness and orthogonal quality of 0.20 and 0.80, respectively (Shewchuk, 2002).

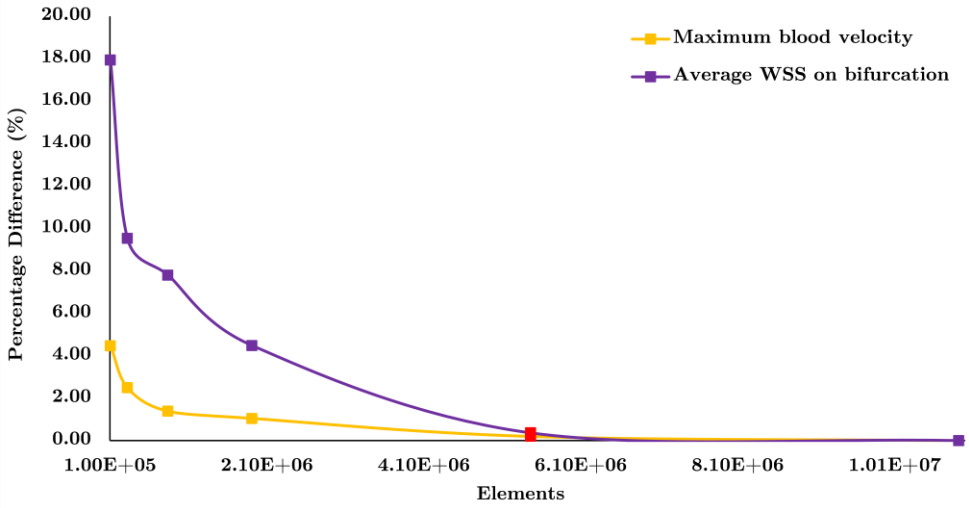

Figure 4.6: Percentage difference in peak velocity and bifurcation average wall shear stress for 6 mesh refinements (Red marker indicates final mesh used in study)

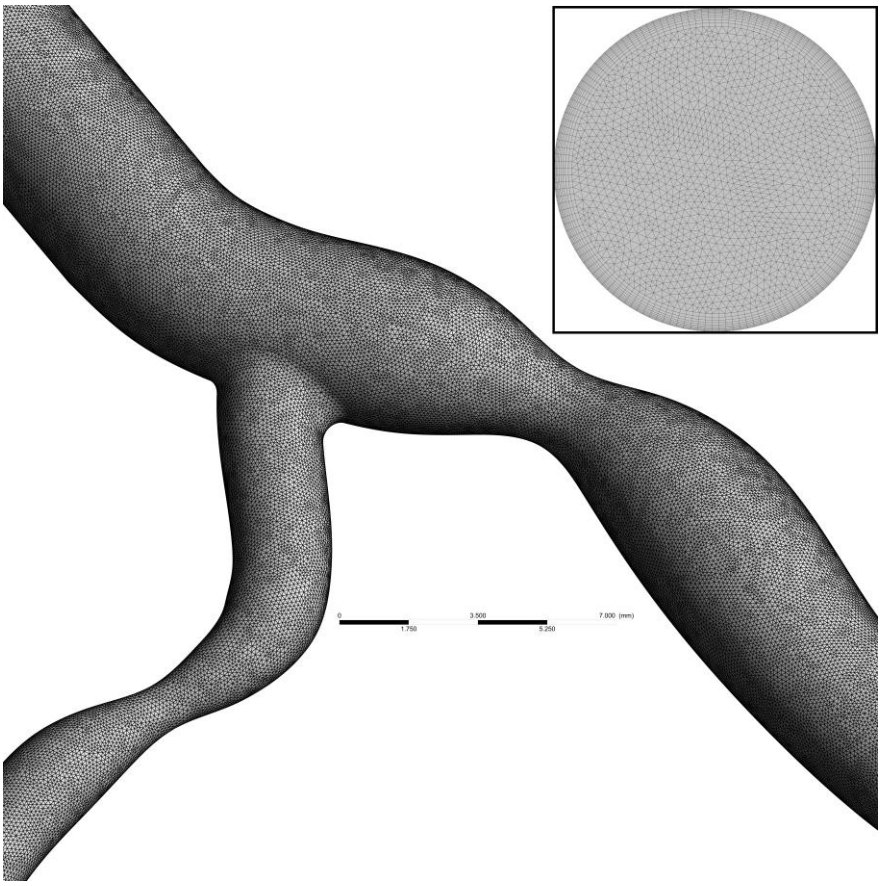

Figure 4.7: Mesh on surface of diseased coronary artery bifurcation and a cross section at inlet showing inflation layers near boundary

4.4 Results

4.4.1 Overview

The haemodynamics parameters defined in Table 4.3 were evaluated over the 3rd cardiac cycle for the healthy and diseased arteries and are reported in Table 4.4. The TAWSS area <1 Pa, represents the percentage area of the entire artery wall which is below the atherodegenerative threshold of 1 Pa.

Table 4.4: Parameters averaged over the final cardiac cycle for the healthy and stenosed geometries (TA = time averaged)

Parameter	Healthy				Diseased			
	SN	SC	MN	MKM5	SN	SC	MN	MKM5
$\bar{\boldsymbol{\omega}}$ (1/s)	234 ± 173	232 ± 173	227 ± 196	230 ± 179	275 ± 249	271 ± 248	259 ± 256	256 ± 227
DVI (mm^3/s)	-				4.15×10^5	3.90×10^5	3.22×10^5	2.58×10^5
TAWSS area <1 Pa	9.48%	5.89%	5.56%	0.05%	15.09%	13.34%	10.54%	3.79%
OSI_{66}	0.92%	0.87%	0.78%	0.61%	3.81%	3.62%	3.20%	2.09%
RRT_{66}	5.14%	3.47%	3.31%	0.01%	11.32%	10.11%	8.23%	5.55%
Max TANNIF	1.00	3.96	1.08	2.68	1.00	13.10	1.09	6.27
Max TA Haematocrit	-		0.508	0.595	-		0.515	0.613
Min TA Haematocrit			0.321	0.204			0.282	0.167

4.4.2 Shear stress parameters

All models show a consistent distribution of TAWSS around the bifurcation, with regions of low TAWSS localised on the outer walls, proximal to the bifurcation and distal to the stenosis (Figure 4.8). These effects are local to the bifurcation/stenosis, with the haemodynamic environment normalising downstream of the region shown in Figure 4.8, with all models predicting healthy TAWSS for the remainder of the artery (Figure 4.1). In the healthy artery, all models except the MKM5 show regions with pathologically low TAWSS <1 Pa. Single-phase models show consistently greater TAWSS, OSI_{66} and RRT_{66} values compared to the multiphase models, in particular the MKM5 model. Maximum values of TAWSS occur at the throat of the stenosis, with greatest values occurring in the LCx branch in all models. Despite allowing for RBC transport and phase interactions, the MN model performs most similarly to both single-phase approaches for TAWSS results.

The introduction of stenosis results in a moderate increase in areas with a pathologically low TAWSS for all models (+5.5% average), again with the MKM5's TAWSS results being smaller and localised closer to the stenosis (Figure 4.8). The SN model has the greatest results of all stress-based parameters throughout. Additionally, the TANNIF more than doubles for the SC and MKM5 models, indicating the presence of highly non-Newtonian flow in the diseased artery. Despite both the SC and MKM5 models both demonstrating non-Newtonian flow, the magnitude and distribution of TAWSS is

still different, showing the importance of haematocrit on rheology and near-wall haemodynamics.

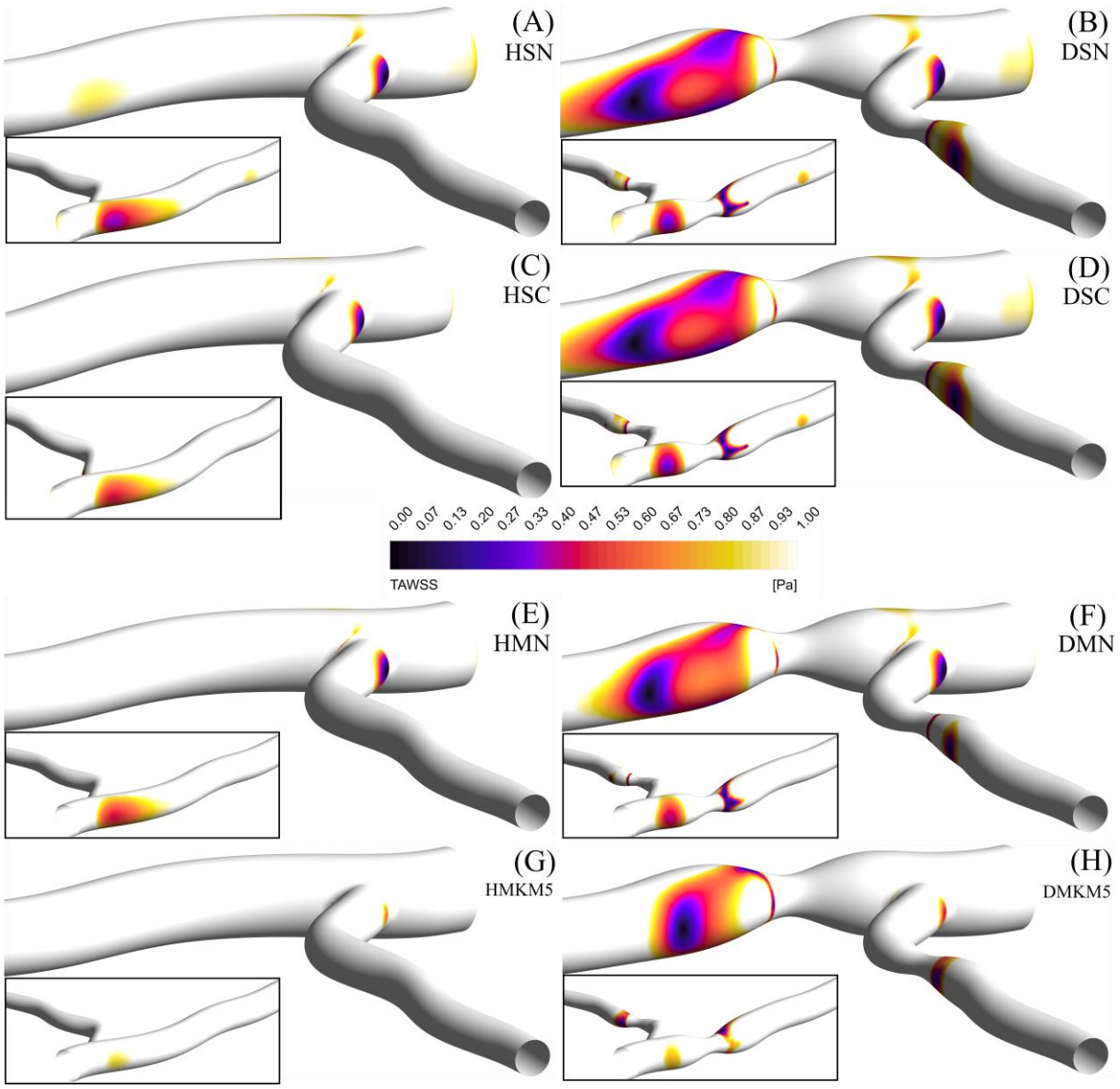

Figure 4.8: TAWSS contours of regions <1 Pa, for the left coronary bifurcation for the single Newtonian healthy (A) and diseased (B) cases, single Carreau healthy (C) and diseased (D) cases, multi Newtonian healthy (E) and diseased (F) cases, and the multi MKM5 healthy (G) and diseased (H) cases, with the reverse angle inlaid

4.4.3 Vorticity

Results in terms of vorticity were consistent across all rheological models, with the largest difference from the Newtonian model being 2.2% (MN) and 5.2% (MKM5) in healthy and diseased arteries, respectively. The regions of disturbed flow result in a wide range of vorticity values, and hence the large standard deviation in values across the cycle. The disruption to the flow caused by the stenosis increased the vorticial nature of the flow for all models, with an average increase of 15%. The reduction in lumen diameter and increased shear at the throat of the stenosis is shown to increase the vorticity of the flow distal to the throat of the stenosis, separating from the wall and spreading across the artery (Figure 4.9). Multiphase models predict a more localised disruption to the vorticity, closer to the throat of the stenosis, with the flow normalising much sooner than in the two single-phase approaches. Multiphase models yielded a smaller DVI than the single-phase, with the MN and MKM5 having a difference of 22.4% and 37.8% from the single-phase Newtonian, respectively.

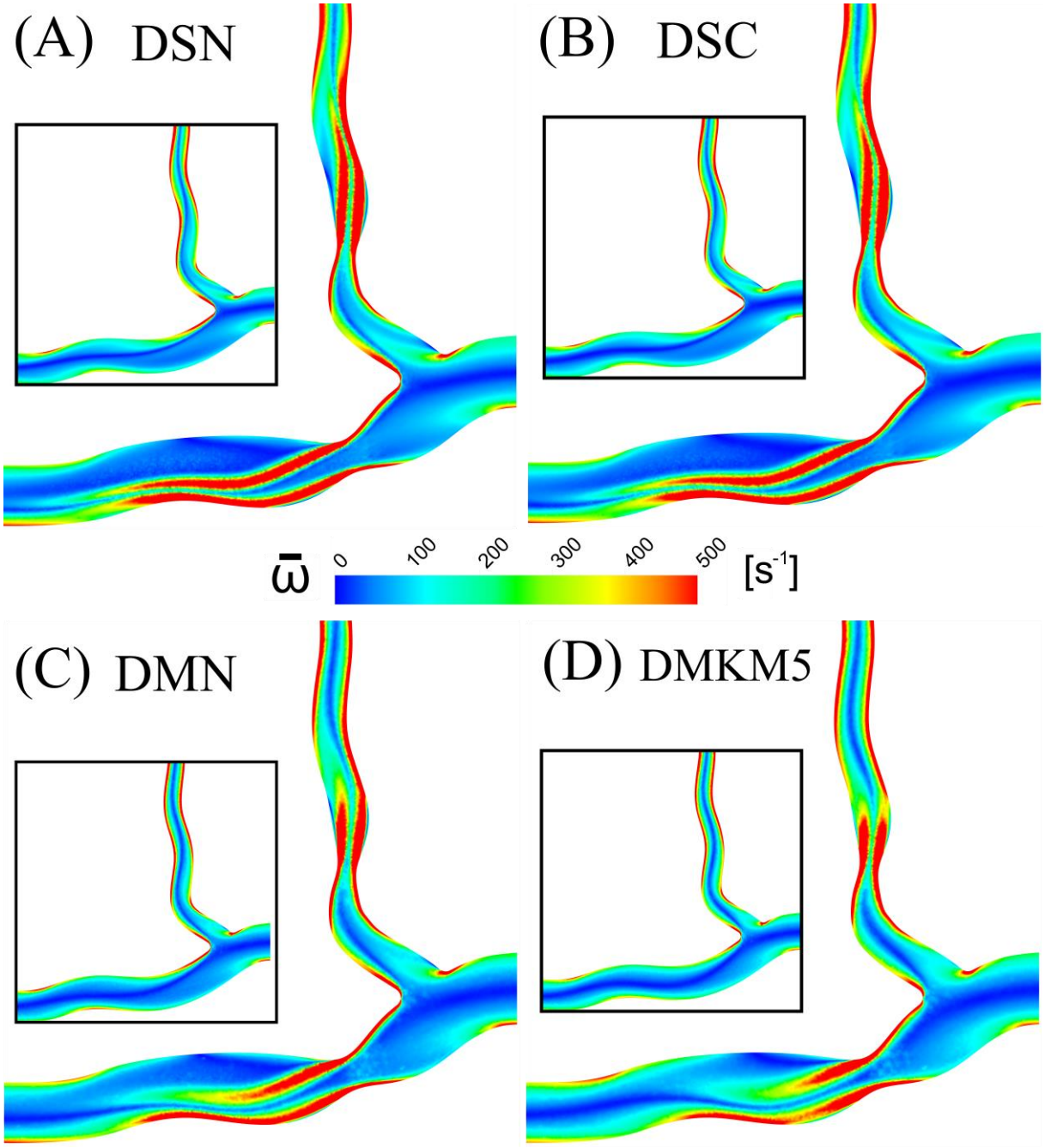

Figure 4.9: Mid-plane cross section of time averaged blood vorticity for the diseased artery: (A) Single-Newtonian, (B) Single-Carreau, (C) Multi-Newtonian and (D) Multi-MKM5 models. Results for the healthy artery are inlaid as reference

4.4.4 Haematocrit

To further analyse the differences between the two multiphase models, the distribution of haematocrit around the bifurcation in both the healthy and diseased cases is shown in Figure 4.10. Despite a uniform haematocrit inlet condition of 0.45 for both models, there is a significant difference in RBC concentration and hence phase transport between the two models. The MN model shows minimal deviation from the uniform distribution, even in the significantly disturbed flow occurring at the flow divider and the outer walls of the stenosis. The increased RBC transport arising in the MKM5 model predicts large regions of the artery with both increased and decreased haematocrit. As increased haematocrit will result in increased blood viscosity, these regions will experience elevated WSS and vice versa.

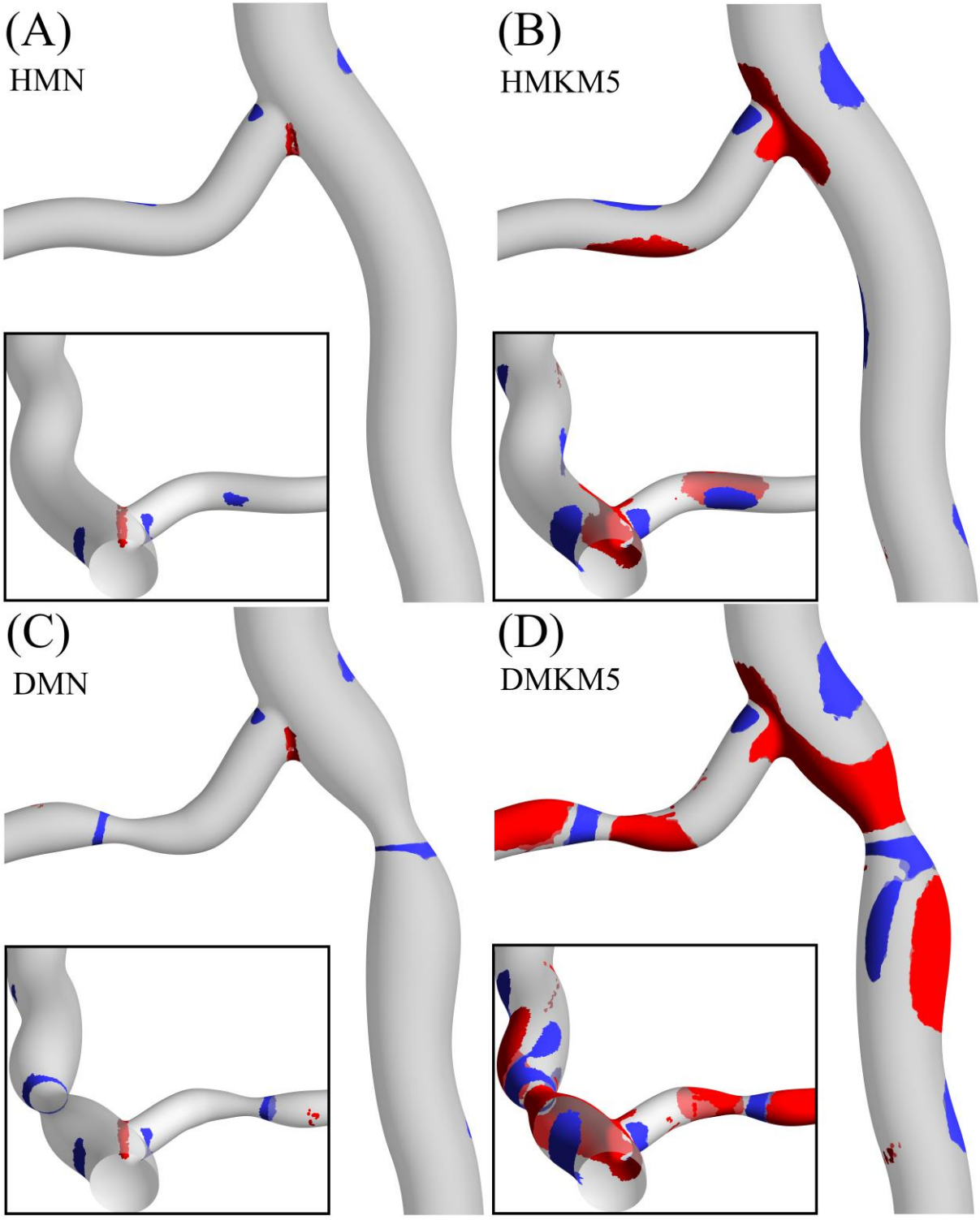

Figure 4.10: Red and blue iso-contours indicating regions of high (>0.5) and low (<0.4) TA haematocrit, respectively, for the healthy Multi-Newtonian (A) and Multi-MKM5 (B) models, and for the diseased Multi-Newtonian (C) and Multi-MKM5 (D) models, with reverse views inlaid

4.4.5 Platelet tracking

The platelet tracking model was implemented for the multiphase MKM5 model in the healthy and stenosed arteries, with results summarised in Table 4.5. The platelet residence time data has been used to extract regions in which the RBC shear rate is sufficiently low for aggregation (<50 s^{-1}) and calculate the exposure time of platelets which are continuously exposed to this low-shear environment. This exposure time was reset to 0, if a platelet experienced a shear rate >50 s^{-1} for longer than 0.1 s to account for the effects of disaggregation. Videos of platelet flow, residence time, LOA and aggregatory exposure time are available in the Supplementary Materials to this thesis and are highly recommended to contextualise the regions most prone to rouleaux/clot formation.

Table 4.5: Data from platelet tracking from the MKM5 model in the healthy/diseased artery

Parameter	Healthy	Diseased
Platelets released across 1 cardiac cycle	106,690	107,512
Mean LOA (Pa.s)	2.91	3.13
Median LOA (Pa.s)	1.67	1.75
Mean residence time of all platelets (s)	1.08	1.20
Mean residence time for platelets with an elevated LOA (s)	1.47	1.53
Mean exposure time of platelets to low-shear (<50 s^{-1}) aggregatory flow (s)	0.19	0.37

The diseased artery has consistently greater levels of activation (+7%) than the healthy artery, with a large increase in the residence time of platelets which experience an elevated LOA in both the healthy (+36%) and diseased (+28%) arteries. The distribution of LOA and residence time across all platelets released can be seen in Figure 4.11.

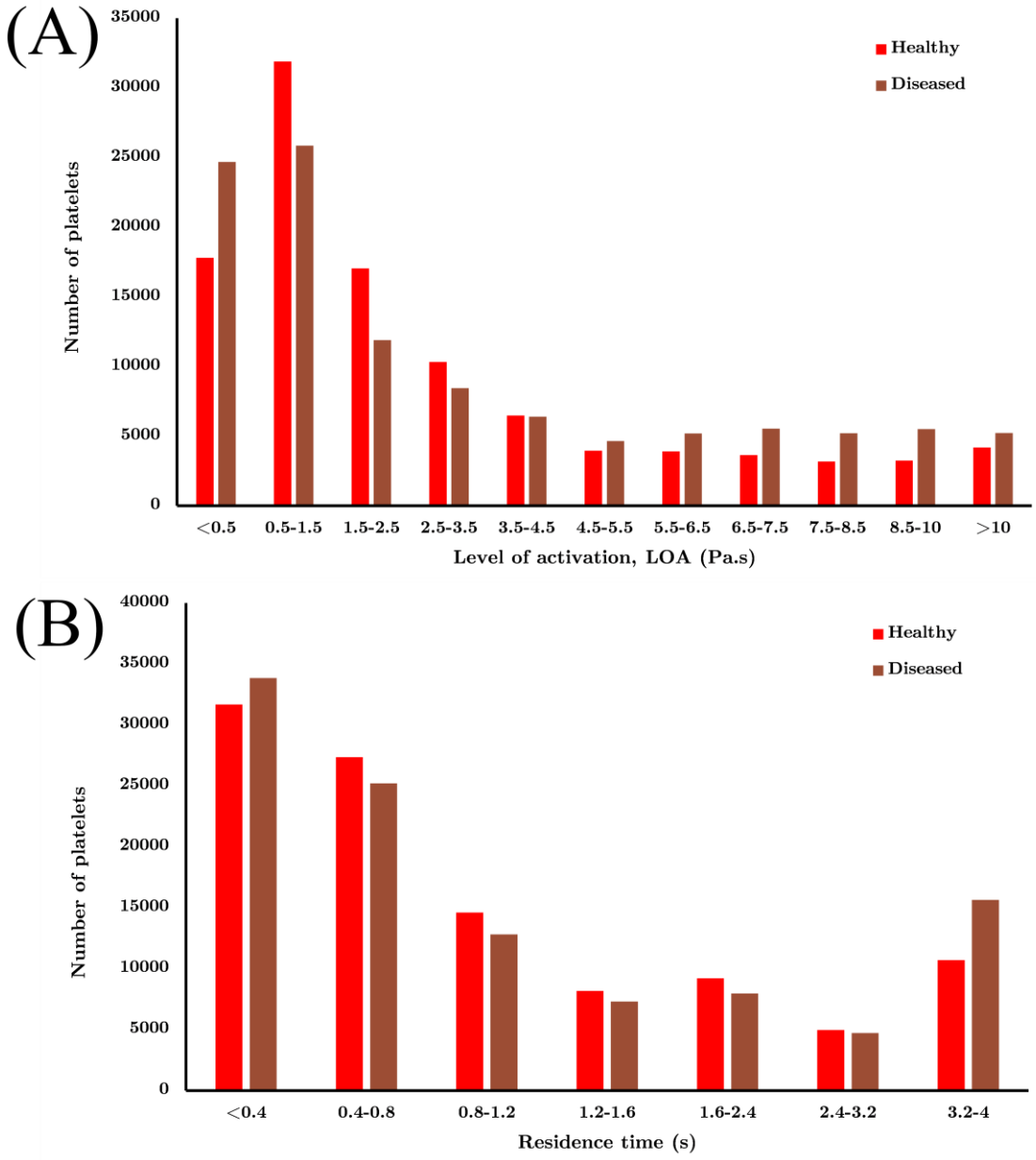

Figure 4.11: Bar charts showing distributions of LOA (A) and residence time (B) in both arteries

In both arteries approximately 55% of platelets have residence times below 1 cardiac cycle, with platelets seeded closest to the wall experiencing both the greatest residence times and LOA. Whilst platelets in the near-wall region have long RT in both arteries, the greater shear stress in the diseased artery results in consistently high LOA as seen in Figure 4.11A.

To evaluate the aggregatory potential of the low-shear environment around the bifurcation, the distributions of exposure time to sufficiently low RBC shear rates is shown in Figure 4.12. There is a distinct difference between the two arteries, with no platelets in the healthy artery exposed to aggregatory shear rates for greater than 0.7 s, compared to the maximum exposure of 2.9 s in the diseased artery occurring distal to the stenosis (Videos in Supplementary materials to thesis). The stenosis greatly increases the area of low-shear regions in the bifurcation which in turn increase the residence time of platelets and potentially RBC. The increased aggregatory potential in the diseased artery is highlighted in Fig 4.13B, showing localised recirculation of platelets in an ultra-low shear, high viscosity, high hematocrit, high residence time environment distal to the throat of the stenosis.

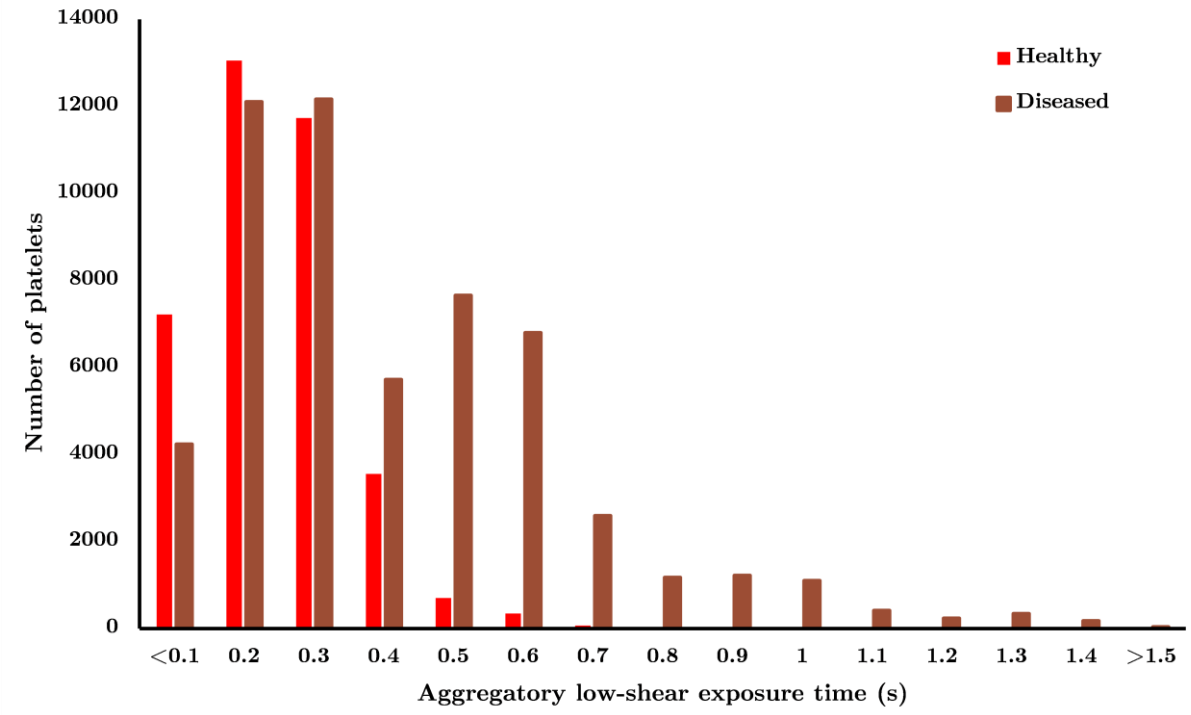

Figure 4.12: Bar chart showing the distribution of exposure time for the platelets which experienced a RBC shear rate <50 s^{-1}

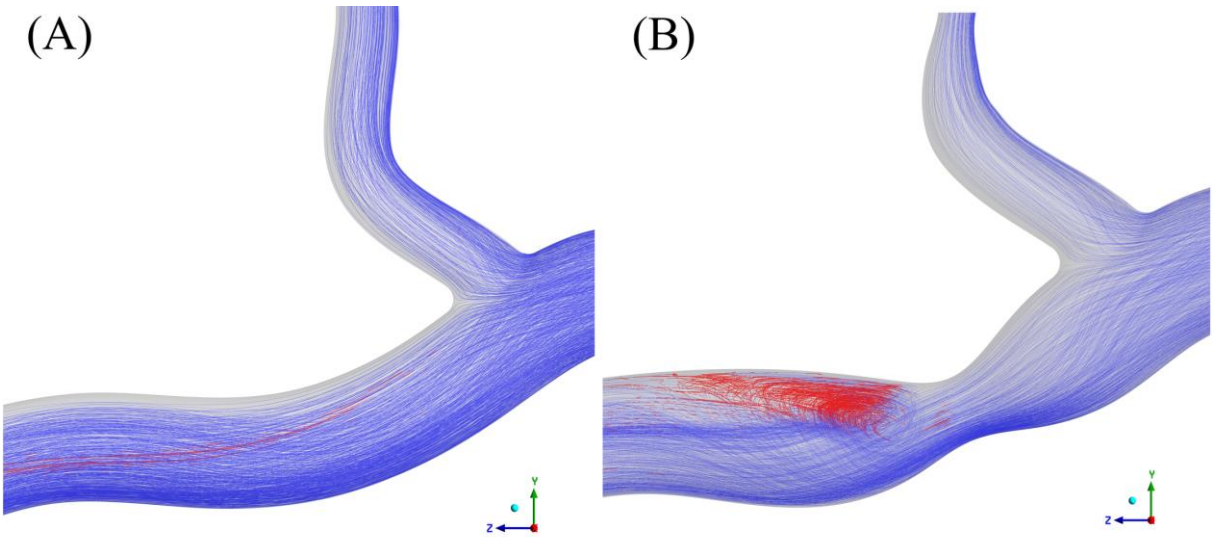

Figure 4.13: Platelet path lines for the healthy (A) and diseased (B) arteries, red indicates a low enough RBC shear rate for aggregation (<50 s^{-1})

4.5 Discussion

4.5.1 Introduction

This study presents for the first time, a Lagrangian platelet tracking model to assess the likely regions of platelet activation and hence indicate potential regions with an increased risk of clotting/thrombus formation alongside a comprehensive examination of the relation between blood rheology RBC aggregation/concentration and haemodynamics. Simulations of a porcine LAD/LCx stenotic bifurcation have shown the importance of non-Newtonian and multiphase rheological properties on accurate predictions of parameters associated with atherosclerosis, with initial insights into how shear stress activation of platelets catalyses atherothrombosis.

4.5.2 Rheology and WSS

The links between WSS and atherosclerosis in coronary arteries have been well documented both *in vivo* and *in silico*, with regions of low TAWSS being associated with: plaque growth (Taylor and Steinman, 2010), reduced lumen diameter (Stone *et al.*, 2012) and increased thrombus formation (Stone, Coskun, Yeghiazarians, *et al.*, 2003). An *in vitro* study of coronary artery bifurcations of comparable branch angles also showed significant areas of low-shear and stagnation on the outer walls of the bifurcation (Asakura and Karino, 1990) as seen in Figure 4.8. Additionally, an *in vivo* study of 506 patients with acute coronary syndrome confirmed the TAWSS patterns

in Figure 4.8, with peak stresses occurring at the throat of stenosis, and increased regions of low TAWSS occurring 3-6 mm distal of the stenosis (Stone *et al.*, 2012). The increased RBC transport to these regions of stagnation distal to expansion (Karino and Goldsmith, 1979) (Figure 4.10) is also associated with increased residence time of platelets (Figure 4.411) and atherogenic proteins which may further impair healthy endothelial function (Liepsch *et al.*, 1988).

Of the four rheological approaches used in this study, three are based upon the viscometer data from Chien *et al.* (Chien *et al.*, 1966), with the MKM5 model being fitted to the Brooks *et al.* (Brooks, Goodwin and Seaman, 1970) dataset. Discrepancies in the range of shear rates evaluated, haematocrit concentrations and temperature of blood combined with inherent limitations in measuring viscosity at the lowest shear rates (Brooks, Goodwin and Seaman, 1970) results in significant differences in predictions of blood viscosity across each model (Table 4.4). This significantly lower viscosity results in greater regions predicted to have a pathologically low TAWSS, with even the healthy bifurcation exhibiting large regions <1 Pa. Furthermore, single-phase models will never be able to predict the non-Newtonian effects arising from RBC aggregation which is a key factor in non-Newtonian descriptors. Additionally in the diseased case, whilst distributions of TAWSS are similar across all models, the atherodegenerative regions are localised much closer to the stenosis (<6 mm) as demonstrated in Stone *et al.'s in vivo* study (Stone *et al.*, 2012).

4.5.3 Vorticity

The vorticial nature of blood flow has been shown to impact cardiac function through multiple in vivo studies, with increased arterial vorticity arising in patients with right ventricular dysfunction (Hirtler *et al.*, 2016). Despite this link, coronary vorticity is thoroughly unexplored despite its potential as a non-invasive biomarker for assessing haemodynamic function (Fenster *et al.*, 2015). The present study has demonstrated that the introduction of stenosis significantly increases the vorticity of coronary blood flow by 11-18% (across all models), with regions of high vorticity extending directly from the throat of the stenosis into the low-shear environments associated with atherosclerosis (Binu and Sukesh Kumar, 2012). With DVI being correlated to the formation and geometry of atherosclerotic legions (Chu *et al.*, 2018), the 38% lower value predicted by the MKM5 model compared to the SN model clearly shows the significance that RBC/plasma interactions have on flow disturbance. Based on Chu *et al.'s* patient-specific CFD study of coronary arteries (Chu *et al.*, 2018), a lower DVI value may imply the growth of a more focal and severe lesion which correlates to the more localised TAWSS distribution of the MKM5 model immediately distal to the stenosis compared to the elongated SN distribution (Figure 4.8). Given these results and the variability in DVI with different rheology and phase models, it is therefore important to choose a sufficiently complex rheology/phase model which allows for a more accurate study of the severity of stenosis in coronary arteries.

4.5.4 Haematocrit and platelets

Despite both multiphase models utilising the same velocity and haematocrit boundary conditions, predictions in RBC transport and haematocrit vary extensively in both the healthy and stenosed arteries (Figure 4.10). The non-Newtonian behaviour of RBC in the MKM5 model is most significant in the near-wall region due to the wide range of shear rates and haematocrit occurring near the surface (Owen, Schenkel, *et al.*, 2020). These fluctuations in haematocrit close to the surface will not only impact WSS magnitudes due to increased viscosity, but also affect platelet transport (Wu, Aubry, *et al.*, 2017) which is strongly linked to interaction/collisions with RBC (AlMomani *et al.*, 2008), hence the limited RBC transport of the multiphase Newtonian model is a significant limitation in accurately modelling blood rheology.

Evaluating the behaviour of platelets and their association with thrombus/clot formation is relevant for vascular pathologies (Rayz *et al.*, 2008; Yazdani *et al.*, 2017) (e.g. stenosis/aneurysms) but also the function of medical devices (Gorbet and Sefton, 2004; Owen, Oliveira, *et al.*, 2020) (e.g. catheters/stents). Platelet transport/activation is a complex process influenced by both mechanical factors such as shear stress (Anand, Rajagopal and Rajagopal, 2003), but also through biochemical reactions with proteins/agonists within the blood itself (Sorensen *et al.*, 1999), with reviews of computational approaches by Anand & Rajagopal (Anand and Rajagopal, 2017) and Yesudasan *et al.* (Yesudasan and Averett, 2019).

The majority of platelet models focus on predicting thrombus formation and platelet behaviour through these biochemical interactions. However, the majority of these models focus on micro-scale flow (Govindarajan *et al.*, 2016; Wu, Jamiolkowski, *et al.*, 2017) which are poorly suited for the larger scale haemodynamics of this coronary bifurcation. Whilst the platelet model presented in this study lacks the biochemical activation potential of other models, its key benefit is linking the level of activation to prolonged residence times in specific 'at-risk' areas, to indicate likely regions for aggregation, sedimentation and clot formation in diseased arteries.

The seeding of platelets in the near-wall region shows platelets remaining around the bifurcation for multiple cardiac cycles in both arteries (Supplementary Materials to this thesis include animations of platelet flow). Importantly the elevated blood shear stress at the throat of the stenosis and subsequent distal low-shear stagnation increases the LOA and creates the ideal environment for adhesion and clot growth. Platelets have long been associated with atherosclerosis (Farstad, 1998), with *in vivo* studies showing their role in both the onset (Badimon, Padró and Vilahur, 2012) and progression (Collet *et al.*, 2006) of plaque growth.

Additionally, the non-Newtonian effects of RBC aggregation are shown to be relevant in the diseased artery, with exposure time to sufficiently low-shear rates exceeding the approximate time (>1.5 s) for rouleaux formation to occur (Robertson, Sequeria and Kameneva, 2008). The increased aggregation and sedimentation of erythrocytes distal to the stenosis is both symptomatic (Goldstone, Schmid-Schönbein and Wells, 1970)

and catalytic to the deterioration of the endothelium (Massberg *et al.*, 2002) and the development of atherothrombosis (Viles-Gonzalez, Fuster and Badimon, 2004).

4.5.5 Limitations

The presented study was designed for the assessment of disease and rheology, however, there are several limitations/assumptions which impact the physiological accuracy. The principal limitations are from the geometry as it lacks some of the additional complexity and individuality arising from patient-specific scans (Lee and Steinman, 2007; Rabbi, Laboni and Arafat, 2020), including the vessel torsion which is one factor in the development of atheroprotective helical flow (Liu *et al.*, 2009). However, the differences between two patient-specific healthy/diseased geometries would limit the assessment of causation which is the focus of this work. As applying boundary conditions of helical flow is not well documented, and whilst torsion is not directly associated with low WSS (De Nisco *et al.*, 2019), the lack of helical flow development may impact haemodynamic predictions but is consistent across all models and is unlikely to alter the main conclusions.

Only the main bifurcation branch was considered (LAD-LCx) as it is one of the most common locations for plaque growth (Oviedo *et al.*, 2010). However, neglecting the additional downstream branches may alter pressure gradients and hence result in overestimation of WSS (Wiwatanapataphee *et al.*, 2012). Despite this, the comparisons between rheological models are unbiased and unaffected. Additional differences in flow boundary conditions arising from the implantation of stenosis could not be implemented

in the model as adjusting the inlet condition without a suitable patient-specific profile would only further introduce errors/randomness and hence may limit the evaluation of the effects of vessel geometry on the rheology/platelet activation.

The Lagrangian method of platelet simulation which determined activation only due to time-averaged shear stresses neglects the contribution of biochemical interactions in platelet activation. This discrete approach was chosen due to the macro-scale focus of this geometry and the inability of micro-scale (including majority of biochemical approaches) models to assess the trajectory, residence time and shear history of individual platelets.

Due to the sheer number of RBC in full sized arteries (Caro *et al.*, 2011b), individual RBC are not simulated in a Eulerian-Eulerian model, and so the effects of RBC deformation on their rheology/sedimentation cannot fully be included. Despite this, the momentum exchange coefficient (K_{ab}) between RBC/plasma is a function of Reynold's number/drag coefficient which will partially account for changes in shape due to flow conditions. With this study indicating aggregatory potential even in large arteries, we hope to expand current multiphase, macroscale rheology models to incorporate these aggregatory behaviours by linking factors such as: residence time, low-shear exposure and hematocrit to experimental rheometer measurements of RBC aggregates.

There is potential for extending our model into a hybrid of both approaches, where platelets with high LOA act as a source term for additional species such as

fibrinogen/vWF or other agonists in the platelet activation cascade, however this was deemed outside the scope of the current work.

4.6 Conclusion

In this study, the choice of rheological model has been shown to strongly influence the assessment of coronary haemodynamic parameters. Single-phase models oversimplify crucial low-shear blood characteristics compared to the non-Newtonian multiphase model (MKM5) which provides a better representation of *in vivo* measurements. Whilst single-phase or Newtonian models may be acceptable for representing physiological undisturbed flow, the increased exposure time (>1.5 s) to aggregatory levels of low-shear in diseased arteries will impact crucial near-wall haemodynamics.

Moreover, the wide ranges of haematocrit (0.163 - 0.617) and elevated vorticity (+15%) occurring distal to stenosis could impair the healthy function of the endothelium via pathological regions of TAWSS and the disruption of advection/diffusion of proteins/nutrients due to altered rheological properties. Additionally, the thrombogenic potential of stenotic arteries has been further classified, with platelets located in the near-wall region experiencing the highest LOA, and subsequently experiencing lengthier residence times (+32% increase) in the low-shear, stagnant region distal to the stenosis.

4.7 Progression

In addition to developing simulations to increase understanding of cardiovascular haemodynamics, the platelet modelling techniques used in this chapter have potential for evaluating the performance of haemodialysis catheters. With the ability to monitor residence time and shear history of platelets, the relative performance of difference haemodialysis catheter designs can be compared and optimised to improve patency.

STATEMENT OF CONTRIBUTIONS III

The following chapter includes novel research which has been previously published in a peer-reviewed scientific journal, with myself as the principal author. It was published as gold standard open access, with a full CC-BY 4.0 copyright license (https://creativecommons.org/licenses/by/4.0/) allowing for the reproduction and alteration included within this thesis. Below are the details of the publication, and a statement of the contributions from each author.

Owen DG, de Oliveira DC, Qian S, Green NC, Shepherd DET, Espino DM (2020) *Impact of side-hole geometry on the performance of hemodialysis catheter tips: A computational fluid dynamics assessment*. PLoS ONE 15(8): e0236946. https://doi.org/10.1371/journal.pone.0236946

Owen DG: Conceptualisation, creation/development of models, data analysis and drafting of manuscript.

de Oliveira DC: Conceptualisation, methodology advice and revised manuscript.

Qian S: Conceptualisation and revised manuscript.

Green NC: Conceptualisation, coordination, and revised manuscript.

Shepherd DET: Conceptualisation, coordination, and revised manuscript.

Espino DM: Conceptualisation, coordination, and revised manuscript.

5 | HAEMODIALYSIS CATHETERS

5.1 Introduction

The most common interventions for chronic kidney disease (CKD) is the use of either haemodialysis (HD) catheters, or an arteriovenous fistula (AVF). Whilst AVF are often recommended as the first choice (Santoro *et al.*, 2014), there is still a large preference for HD catheters, with 18% and 44% of US and Canadian CKD patients receiving HD, respectively (Fissell *et al.*, 2013).

Haemodialysis is the process by which blood is removed via a dialysis catheter situated in the right atrium or superior vena cava (SVC), filtered externally, then resupplied back into the bloodstream through the same catheter. Chronic kidney disease affects an estimated 15% of adults in the USA (*Chronic Kidney Disease Surveillance System website*, 2020), with more than 726,000 receiving dialysis (*Chronic Kidney Disease in the United States*, 2019). As patients typically receive 15 hours of haemodialysis per week (*Haemodialysis Facts and Stats*, 2020), the optimal and efficient function of haemodialysis catheters is important for expedited blood filtration, with a wide variety of tip designs and features attempting to achieve this.

Typical problems affecting catheter performance are recirculation of dialysed blood (Knuttinen *et al.*, 2009), bio-film and fibrin formation (Bosma *et al.*, 2010), shear induced platelet activation (Nobili *et al.*, 2008) and regions of flow stagnation (Depner, 2003). One of the current leading tip designs is widely considered to be a symmetric style tip (Knuttinen *et al.*, 2009; Vesely and Ravenscroft, 2016); however, there are multiple different design concepts including the Palindrome (Medtronic, Dublin, Ireland), Vector-Flow (Tele-Flex, Pennsylvania, United Sates) and Glide-path (CR-Bard, New Jersey, United States). These designs include a variety of features with different geometry side-holes (circular, oval, trapezoidal) located in a variety of configurations (Vesely and Ravenscroft, 2016).

Comparisons of catheter performance have been performed both *in vitro* (Foust, 2004; Vesely and Ravenscroft, 2016) and *in silico* (Clark, Van Canneyt and Verdonck, 2012; Clark *et al.*, 2015) to identify favourable design features; however, due to the large variability in design between catheters, it is difficult to conclude if a design is optimal or how different features impact the flow into the catheter. In particular, whilst side-holes improve flow rates (Tal *et al.*, 2006) and reduce recirculation (Clark *et al.*, 2015), they have been associated with elevated susceptibility to clot formation and anchoring, increased rates of infection and leakage of heparin solution (Tal *et al.*, 2006; Barbour, Gow and Aliseda, 2018). A key factor in the design of catheter tips is the reduction of shear stress during inflow as elevated shear stress levels >10 Pa being a potential threshold for platelet activation and blood damage (Gross and Wang, 1981). As

outflowing blood from the catheter flows almost entirely through the main lumen opening, the majority of high-shear rate effects are localised to the inflowing side-holes. Therefore, careful evaluation of side-hole performance must be performed before incorporation into any design.

This study aims to investigate the impact of different side-hole configurations on the local haemodynamics and catheter performance through several computational fluid dynamic (CFD) studies. The variation of size, shape and number of side-holes will be assessed by comparing velocities and flow rates occurring at the tip, regions of high shear stress during inflow, and the effect on platelets, including their path-lines, residence time and shear history.

5.2 Catheter designs

5.2.1 Base symmetric design

The catheter design used for this analysis is similar to many commercially available designs: a generic, symmetric style tip with two semi-circular lumens (5 mm internal diameter) and an outer body diameter of 5.5 mm (16.5 Fr) (Vesely and Ravenscroft, 2016). All geometry was created using Ansys DesignModeller (Ansys Inc, Pennsylvania, United states). Catheter lumens are typically manufactured from extruded polyurethane, with tip features applied using drilling, skive tools and bonding (Wentling, 2004). The tip opening is achieved with a 10 mm radius skive cutting tool,

resulting in an ‘angled-cut’ profile and leaving a 0.5 mm septum separating the two lumens, as shown in Figure 5.1.

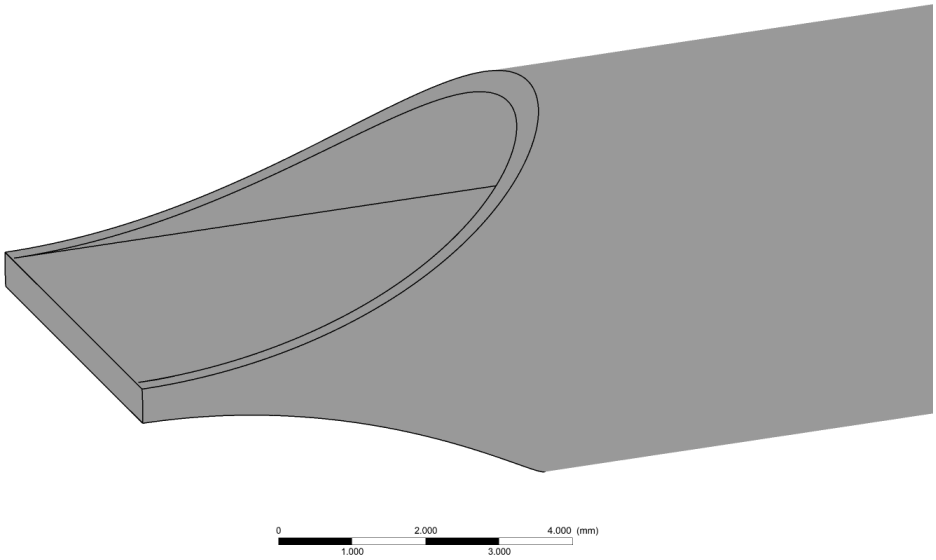

Figure 5.1: Base symmetric tip design showing the angle-cut profile of the sidewall, with the central septum separating the inflow and outflow lumens

5.2.2 Variations in design

The two shapes of side-hole considered are: a simple circular hole which could be drilled or punched into the catheter body resulting in a ‘straight-cut’ profile (Figure 5.2A), and a rounded oval shape achieved using the same skive tool for the tip opening resulting in a ‘angled-cut’ profile (Figure 5.2C). The size of these holes is reported in Table 5.1, with each hole positioned such that the smallest distance between the end of the hole and end of the tip is constant (16.5 mm) in all designs.

Table 5.1: Areas of the small, medium and large side-holes

Shape	Small Area (mm^2)	Medium Area (mm^2)	Large Area (mm^2)
Circular	7.06	9.62	12.57
Oval			

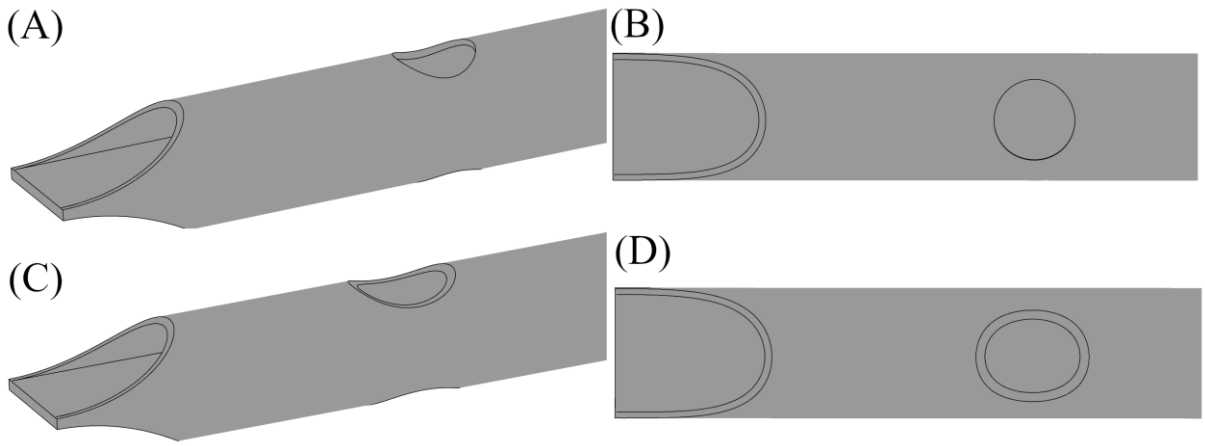

Figure 5.2: Medium size side-holes for the circular (A)-(B) and oval (C)-(D) shaped catheters

After analysing the impact of the shapes/areas described above on catheter performance, the best performing area will then be split into two equally sized holes and evaluated in a dual-hole configuration, as show in Figure 5.3. Dual-hole configurations are employed in multiple tip designs (Vesely and Ravenscroft, 2016), such as Equistream (CR-Bard, New Jersey, United States), Hemosplit XK (CR-Bard, New Jersey, United States) and the Ash Split (Medcomp, Pennsylvania, United States), as they can distribute flow evenly and reduce the impact on performance if one hole becomes occluded.

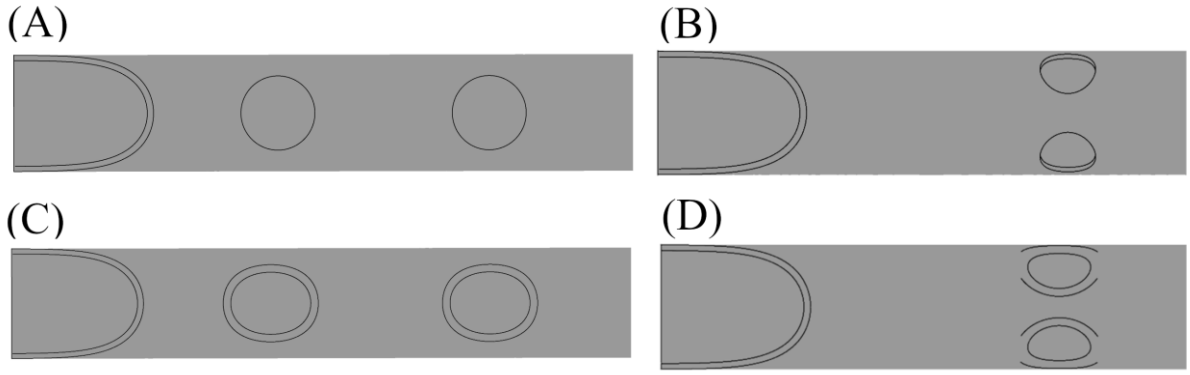

Figure 5.3: Linear (A,C) and Parallel (B,D) dual-hole configurations for the circular and oval holes

5.3 Numerical methods

5.3.1 Fluid domain

Similar to other CFD catheter studies (Mareels *et al.*, 2007; Clark, Van Canneyt and Verdonck, 2012; Clark *et al.*, 2015), the catheters are enclosed in a 20 mm diameter cylinder representing the superior vena cava (SVC) to allow for uniform comparisons on performance. The SVC model is 90 mm long, with a 60 mm length catheter inserted to allow sufficient distance for fully normalised inflow to the catheter to develop and no outlet effects to occur (Figure 5.4A). To compare inflow parameters across multiple designs, a cuboid 'tip-volume' is defined for the inflow lumen of each catheter design (Figure 5.4B) with an average volume of 350 ml. The tip volume has a width of 5 mm and a height of 2.5 mm to include the entire inflow lumen. It extends from the most distal point of the catheter up to a plane proximal to the side-hole where the inflow velocity has become stable/fully developed, with no further flow disturbances occurring

until the blood exits the catheter base. This focuses the comparisons between the different configurations on the most critical regions of inflowing blood.

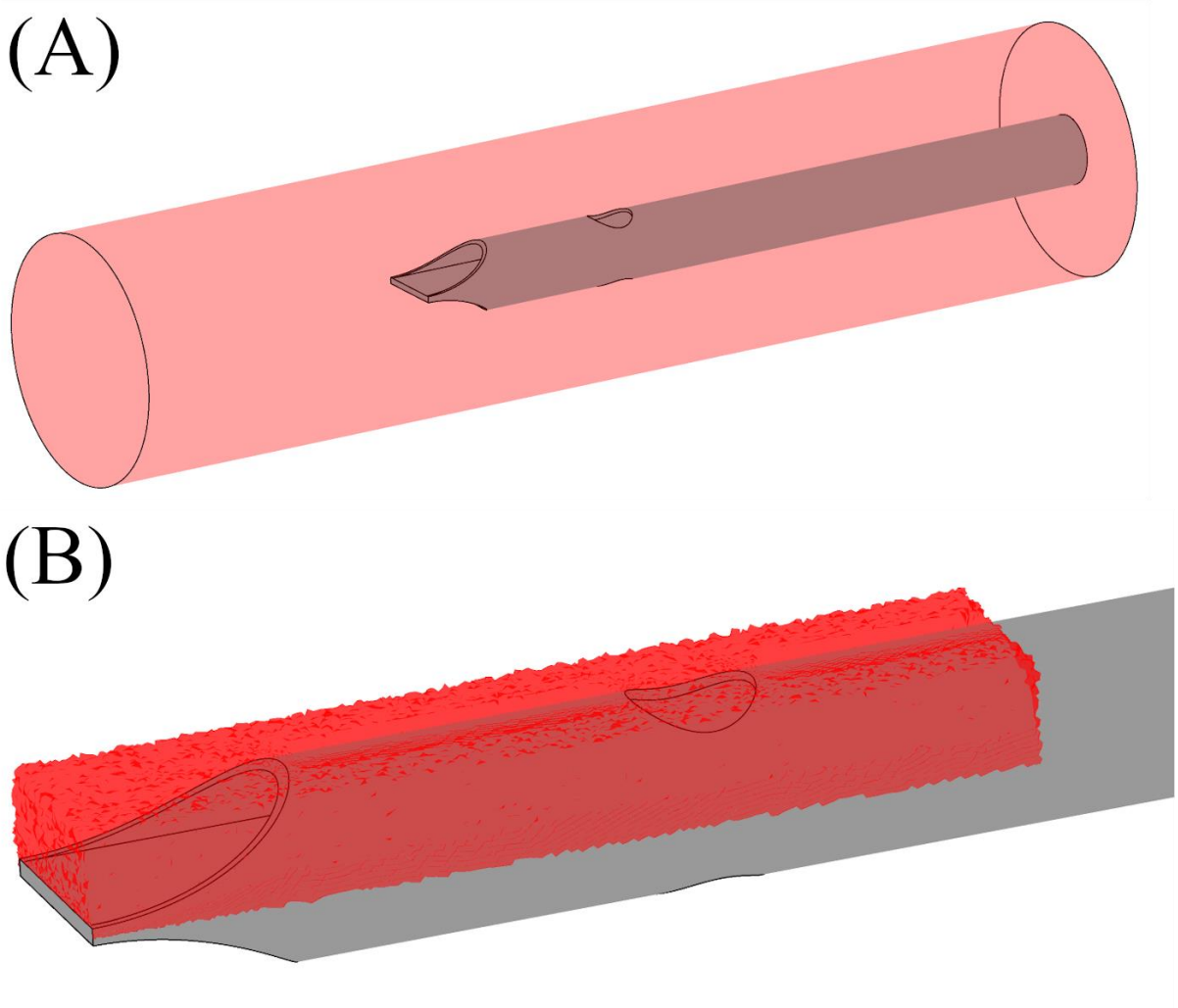

Figure 5.4: (A) SVC enclosure showing catheter placement, (B) Tip volume for medium sized circular hole

5.3.2 Mesh convergence

Simulations were performed on the medium sized circular hole tip design at six incrementally increasing mesh densities. The mesh used in the study was chosen once the percentage difference for maximum velocity and average shear rate in the tip was below 0.5%. This resulted in a 18 million element predominantly tetrahedral mesh, with 12 prismatic layers surrounding the inner/outer lumens of the catheter body. The average skewness and orthogonal quality of the mesh was 0.2 and 0.77, respectively (Shewchuk, 2002), with a cross section of the mesh shown in Figure 5.5A and the percentage differences for the varying mesh densities in Figure 5.5B.

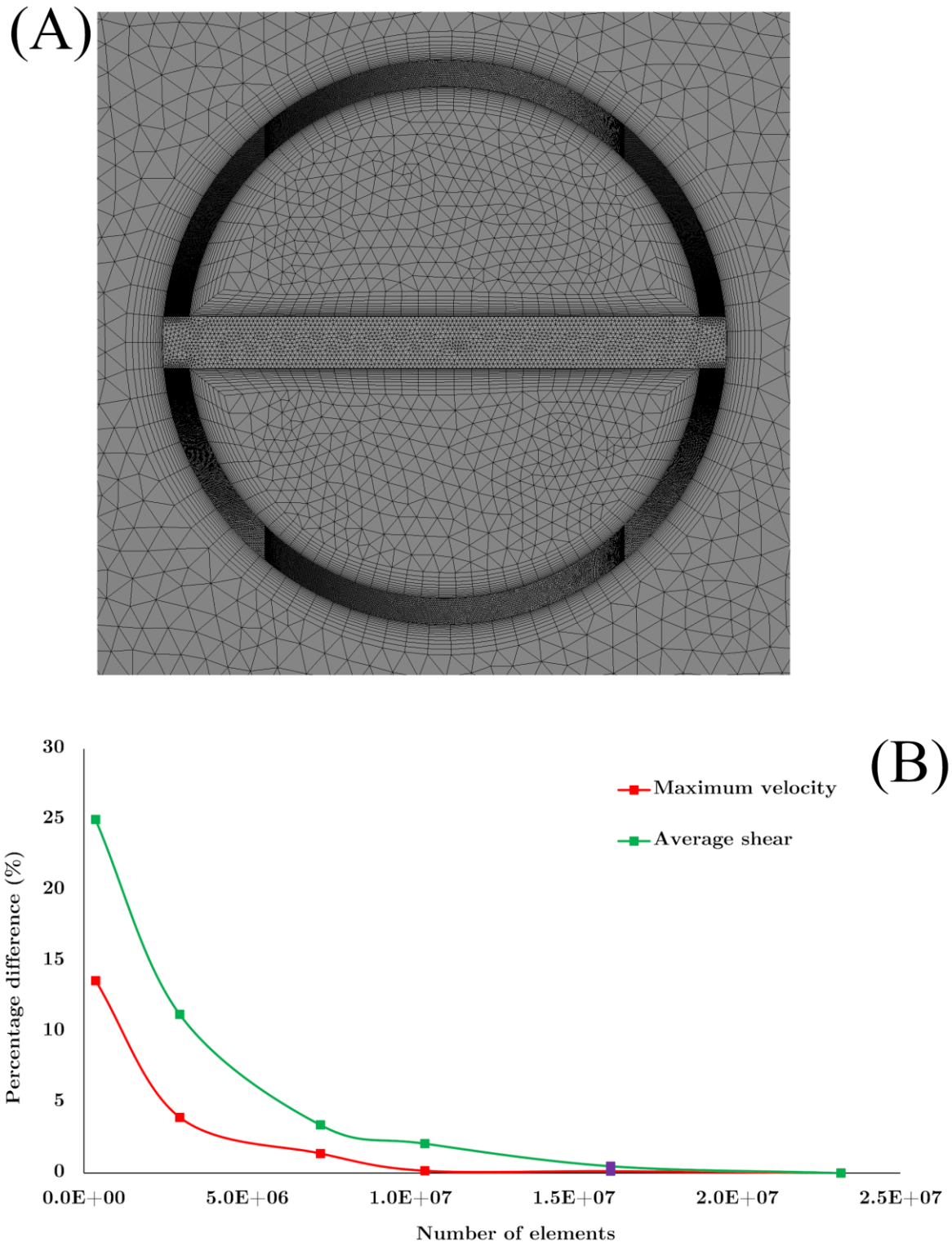

Figure 5.5: (A) Cross section of mesh, (B) Percentage difference with increasing elements for maximum tip velocity and average shear rate in tip (Purple marker indicates final mesh used in study)

5.3.3 Blood model

Blood is a non-Newtonian fluid (Carty, Chatpun and Espino, 2016), which exhibits shear-thinning behaviours at higher shear rates (Vijayaratnam *et al.*, 2015) (>100 s^{-1}). Blood can often be assumed Newtonian in specific physiological applications (Sorensen *et al.*, 1999), however, given the range of shear rates that occur during inflow a suitable non-Newtonian blood model should be selected. This study uses the asymptotic shear-thinning Carreau model from Chapters 3 & 4 (Lee and Steinman, 2007), which uses the definition of shear rate restated in Equation 5.1 & Equation 5.2.

$$\dot{\gamma} = \sqrt{2 * D_{ij} \cdot D_{ij}} \qquad (5.1)$$

where $\dot{\gamma}$ is the shear rate of the fluid, D is the strain rate tensor with $i, j = 1,2,3$ as the inner products.

$$\mu = \mu_\infty + (\mu_0 - \mu_\infty)[1 + (\lambda\dot{\gamma})^2]^{\frac{n-1}{2}} \qquad (5.2)$$

where μ is the viscosity of blood and $\mu_\infty = 0.00345\ Pa.s,\ n = 0.25,\ \mu_0 = 0.025\ Pa.s,$ $\lambda = 25\ s$. A multiphase approach was deemed unnecessary for this study, as the main factor in non-Newtonian rheology (continuous RBC exposure to low shear) are not present in the higher-shear environment around the inflow of blood to the catheter.

5.3.4 Platelet modelling

To further analyse the different designs, the path lines of platelets flowing through the side-holes is also considered. The methodology used is very similar to that described in

'4.3.2 Platelet modelling', and so is described briefly in this section. The platelets were generated on a tangential plane 1 mm above the surface of the catheter and are tracked through the flow field across steps of 0.5 µm. Localising platelet generation around the side-hole makes tracking more computationally efficient, as only platelets inflowing through the high-shear side-hole are tracked through the domain. Platelets are modelled as rigid spheres with a diameter (Basciano *et al.*, 2011) of 2 µm which experience drag modelled by the Schiller-Naumann model (Schiller and Naumann, 1935) (restated as Equation 5.3) and lift due to shear via the Saffman lift model (Li and Ahmadi, 1992) (restated as Equation 5.4). Examples of the theoretical considerations of these techniques applied to other blood consitiuents and lung particulates have been reviewed by Kleinstreuer and Feng (Kleinstreuer and Feng, 2013).

$$C_D = \begin{cases} \dfrac{24(1 + 0.15Re^{0.687})}{Re} & if\ Re \leq 1000 \\ 0.44 & if\ Re > 1000 \end{cases} \qquad (5.3)$$

$$\overrightarrow{F_L} = \frac{2Kv^{\frac{1}{2}}d_{ij}}{d_p(d_{lk}d_{kl})}\left(\vec{u} - \overrightarrow{u_p}\right) \qquad (5.4)$$

where Re is the Reynolds Number, K is a constant equal to 2.594, v is the kinematic viscosity, d_{ij} is the deformation tensor, d_p is the diameter of the platelet, $\vec{u}$ is the velocity of the fluid and $\overrightarrow{u_p}$ is the velocity of the platelet. This model allows for the calculation of path lines, shear forces and residence times for each individual platelet during inflow. These platelet tracking equations differ from the previous chapter (4.3.2), where the drag coefficient and inclusion of the lift force are used in this study more

suited to the much greater shear rates (>10000 s^{-1}) within the catheter (Ekanayake *et al.*, 2020).

To assess the potential damage occurring to the platelets, the platelet lysis index (PLI) (Equation 5.5) is used. This was first introduced by Giersiepen *et al.* (Giersiepen *et al.*, 1990) for mechanical heart valves and has been previously applied to haemodialysis catheters (Mareels *et al.*, 2007; Clark, Van Canneyt and Verdonck, 2012). The PLI indicates regions where platelets experience higher shear stress and longer residence times (as potential sites for adhesion and thrombus formation) based upon path lines.

$$PLI = A{t_p}^{0.77}{\tau_p}^{3.075} \qquad (5.5)$$

where A is a constant equal to 3.31x10^{-6}, t_p is the residence time of the platelet and τ_p is the shear stress acting on the platelet. Contrary to previous studies which used a velocity weighted average (Mareels *et al.*, 2007; Clark, Van Canneyt and Verdonck, 2012), in this study a value for the PLI is calculated at each step (0.5 µm) using Equation 5.5, which is then summated for each line and averaged over all steps to provide an overall PLI magnitude for each catheter to be used for comparisons between designs.

5.3.5 Boundary conditions

Blood flow through the SVC was a constant velocity of 0.3 m/s (From right to left in Figure 5.4) based upon peak values from Mareels *et al.* (Mareels *et al.*, 2007) as transient effects have been shown negligible in other comparative CFD catheter studies

(Mareels *et al.*, 2007). The flow at the catheter inlet was constant at 400 mL/min, with a negative pressure applied at the catheter outlet (Depner, 2003) with the average magnitude across all configurations being -1810 Pa, which was varied in magnitude until an outflow of -400 mL/min was achieved. The walls of the catheter and SVC had a no-slip condition, with the SVC outlet set to a constant gauge pressure of 0 Pa.

5.3.6 Solver settings

The governing equations for conservation of mass and momentum for a 3D incompressible fluid were solved numerically using the commercial finite-volume Ansys Fluent v19.2 (Ansys Inc, Pennsylvania, United States) SIMPLE solver. The flow was assumed laminar and steady-state, similar to other comparative CFD catheter studies (Clark, Van Canneyt and Verdonck, 2012; Clark *et al.*, 2015). Two criteria were used to assess convergence: a mass continuity residual magnitude $<10^{-5}$ and a outflow rate of 400 $\pm$ 1 mL/min. The models were solved using parallel processing on Linux based HPC architecture, with all models utilising 200 cores for 3 hours.

5.3 Results

5.3.1 Variation in side-hole area

Tip volume results from increasing the area of the side-holes are shown in Table 5.2, with the inclusion of the same symmetric tip without side-holes (Figure 5.1) as reference.

Table 5.2: Tip volume parameters for the varying sized circular/oval side-holes (Percentage shear stress >10 Pa is a volume-weighted measure within the tip volume)

Tip Design	Side-hole area	Inflow tip volume measurements			
		Max Velocity (m/s)	Average shear stress (Pa)	Percentage Shear stress >10 Pa	Side-hole flow (mL/min)
No hole	-	1.923	5.16	13.75%	-
Circular	Small	1.684	3.70	7.94%	308
	Medium	1.804	3.30	7.53%	363
	Large	1.794	3.30	7.52%	363
Oval	Small	1.866	3.80	8.37%	319
	Medium	1.942	3.43	8.08%	382
	Large	1.982	3.42	7.58%	438

From Table 5.2, it is clear that the addition of side-holes to catheters can reduce the maximum velocity of inflowing blood (-0.239 m/s for small circular hole), as well as

reducing both the average shear stress in the tip and the percentage shear stress above 10 Pa, a potential threshold for platelet activation and blood damage (Gross and Wang, 1981).

It can be observed that side-hole area positively correlates with maximum velocity of blood in the tip and total flow (mL/min) through the hole, but negatively correlates with both of the stress related parameters. However, it should be noted that the increase from small to medium area is much greater than from the medium to large areas. As flow patterns through the side-holes were consistent across almost all configurations, velocity contours along the centreline for a representative sample of the tip designs are shown in Figure 5.6.

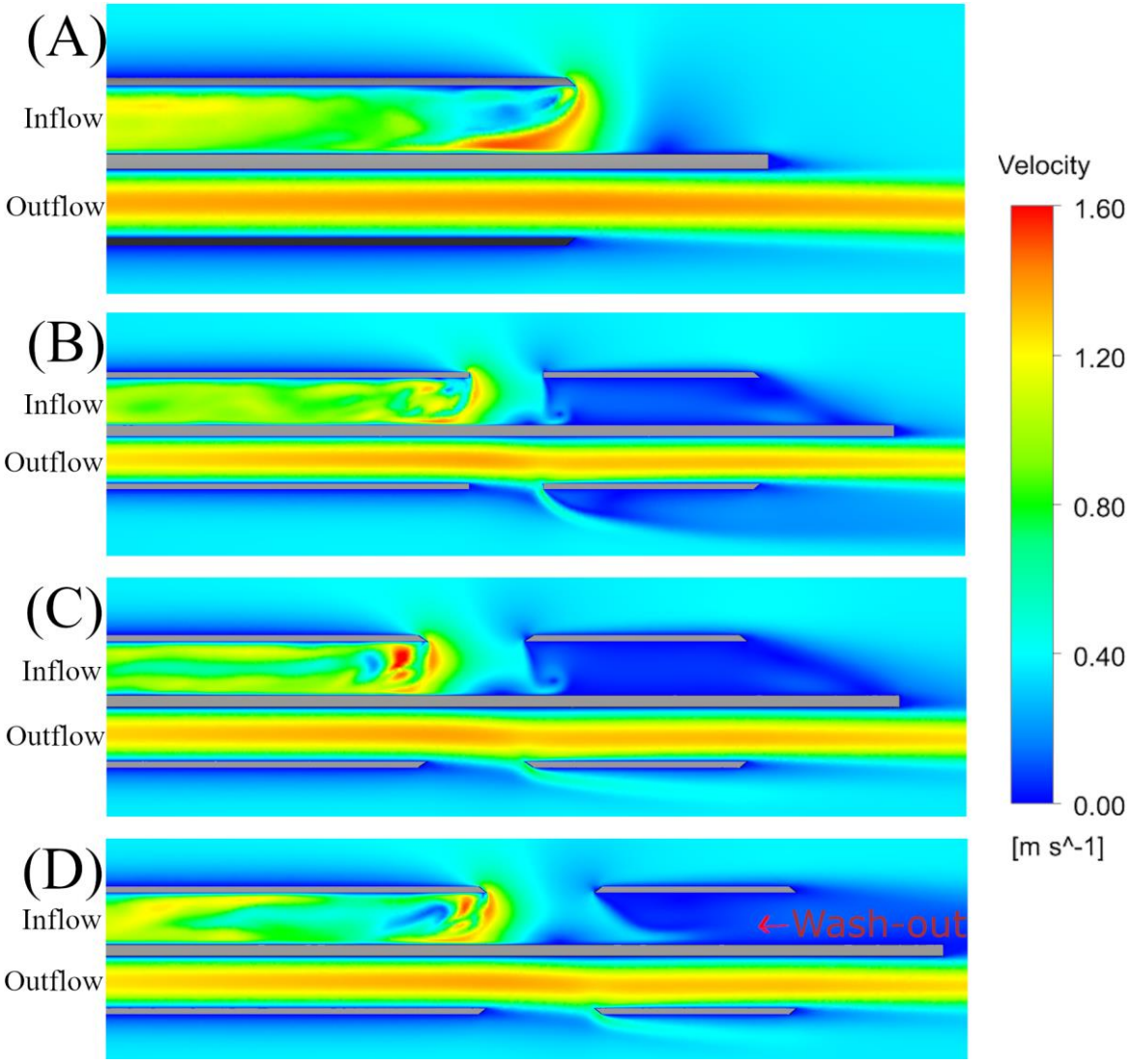

Figure 5.6: Velocity contours for the no-hole (A), Medium circular (B), Medium Oval (C) and Large oval (D)

Velocity contours for the two medium-sized side-holes are similar; however, the 'angled-cut' of the oval hole results in a slightly more unstable flow structure which leads to a higher maximum velocity. The vortex formed by the blood changing direction within the catheter lumen (in the redundant distal section of the tip) was present in all catheter models except for the large oval side-hole (Figure 5.6D). In the majority of the catheters, the pressure gradient is sufficient to capture all inflow from the side-

holes and some smaller additional inflow from the distal tip resulting in a combined flow of 400 mL/min. In the large oval shaped side-hole, this pressure gradient is insufficient to capture all the flow through the side-hole, and instead the additional 38 mL/min 'washes-out' upstream of the side-hole, calculated via the volume flux on a plane inside the lumen, distal to the side-hole (Figure 5.6D). This likely occurs as the circular hole concentrates a greater proportion of the inflow at the most proximal point to the base of the catheter compared to the more gradual curvature of the oval shape.

Whilst this study predominantly focuses on the inflow to the catheter, as this component experiences the most critical flow conditions for both performance and blood damage, the inclusion of side-holes can also be seen to impact the outflow. Comparing outflow from Figure 5.6A to the other catheter designs, it can be inferred that side-holes increase shear stress of outflowing blood as without side-holes there is zero impedance to the blood exiting the catheter, whereas all designs which include side-holes apply additional shear to this outflowing blood as it is redirected out the side-hole. In particular, the angle of outflow in the 'straight-cut' circular side-hole is much greater than the 'angled-cut' of the oval shape side-hole which redirects the outflow more gradually.

The contours in Figure 5.7 show that the main region where shear stress is >10 Pa occurs predominantly along the centreline of the catheter where the majority of inflow is occurring, hence blood in this region experiences the highest shear rate. This distribution was found across all sizes of side-holes. Both shapes of side-hole have two

clear regions where the shear stress is <10 Pa, which occurs in places where blood experiences a more gradual redirection, such as the vortex mentioned previously. Whilst the shape of the side-hole has minimal effect overall on the shear stress within the tip volume (<4% difference in average shear stress for medium size), a much larger region where shear stress in >10 Pa can be seen on the exterior of the circular hole. Results for the simulation of platelet inflow are tabulated in Table 5.3.

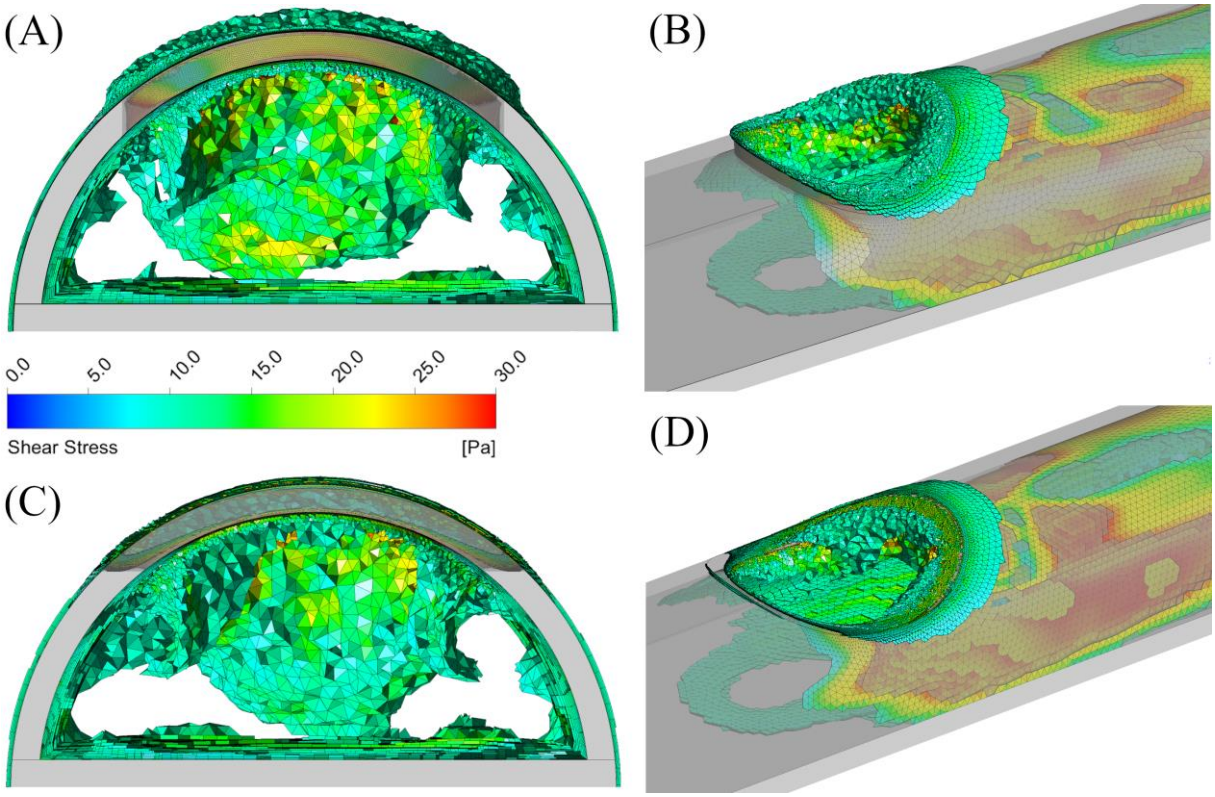

Figure 5.7: Regions inside the tip volume where blood shear stress is >10 Pa for the medium sized circular (A)-(B) and medium sized oval side-holes (C)-(D)

Table 5.3: Platelet parameters for the varying sized circular/oval side-holes

Tip Design	Side-hole size	Inflow platelet model				
		Average residence time (s)	PLI	Average shear stress (Pa)	Percentage Shear stress >10 Pa	Average shear (s^{-1})
Circular	Small	0.0081	0.0126	8.85	32.04%	2449
	Medium	0.0103	0.0249	8.05	27.23%	2222
	Large	0.0103	0.0505	8.01	26.84%	2212
Oval	Small	0.0085	0.0039	8.82	26.86%	2444
	Medium	0.0110	0.0183	8.62	25.59%	2390
	Large	0.0184	0.0340	7.30	24.88%	2017

The results from the platelet modelling are consistent with the tip volume assessment, indicating a reduction in both shear and shear stress acting on the platelets with an increasing side-hole area. Increased side-hole area is shown to increase platelet residence time and also increases the PLI magnitude for both shaped side-holes, with oval shaped holes having the lowest PLI magnitudes. The platelet inflow is visualised in Figure 5.8.

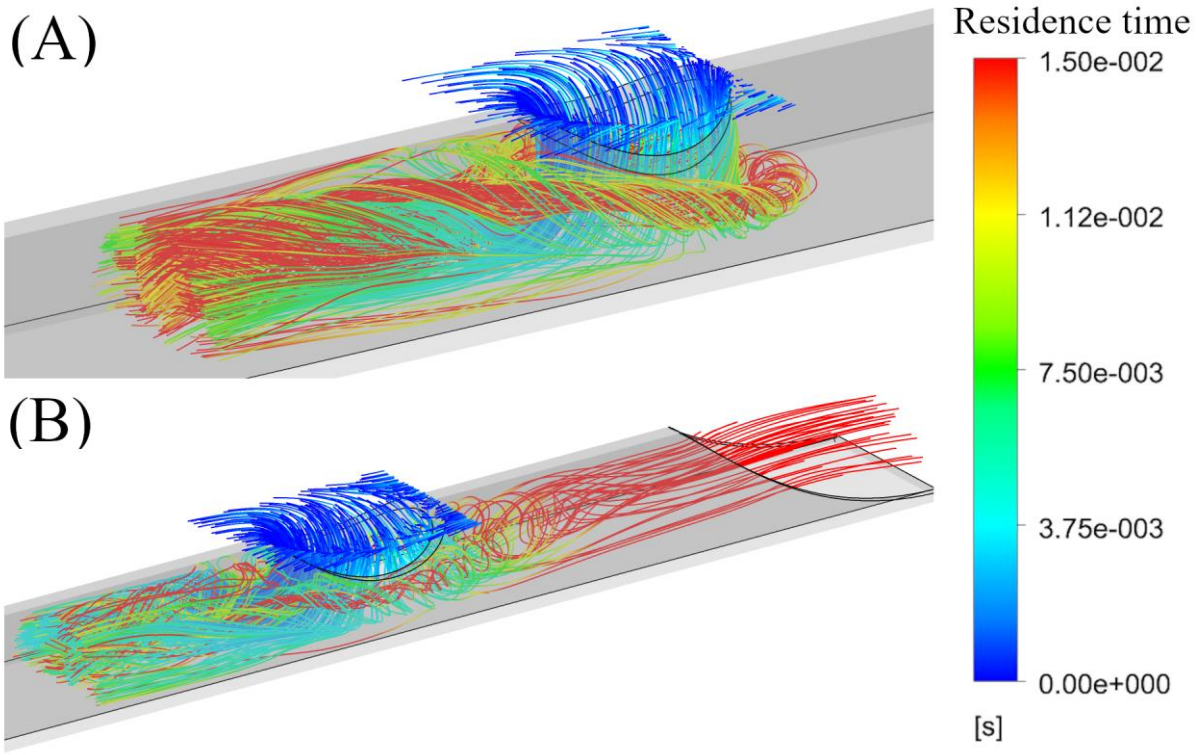

Figure 5.8: Residence time of platelets for the medium circular (A) and the large oval (B) side-holes

Whilst the majority of platelet inflow is immediately carried downstream, increasing the side-hole area causes increased residence time. Platelets with the greatest residence time can be seen circulating within the lumen (Figure 5.8A), in regions of low velocity and shear before the pressure gradient is sufficient to remove them downstream. In the case of the large oval-shaped side-hole, some flow leaks through the rest of the tip as not all the flow through the side-hole travels out through the base, resulting in platelet residence times of up to 0.2 s.

5.3.2 Dual-hole configurations

Based upon the above analysis, the medium sized area (9.62 mm^2) was chosen to be split into two equal sized side-holes. The same tip volume used for the previous analysis was used to analyse the dual-hole configurations (Figure 5.3) and to generate the same parameters in Table 5.4.

Table 5.4: Tip volume parameters for the dual side-hole configurations

Tip Design	Dual side-hole style	Inflow tip volume measurements			
		Max Velocity (m/s)	Average shear stress (Pa)	Percentage Shear stress >10 Pa	Total side-hole flow (mL/min)
Circular	Linear	1.77	3.67	8.58%	356
	Parallel	1.65	3.23	7.13%	363
Oval	Linear	1.84	4.15	10.1%	361
	Parallel	1.91	3.51	8.22%	376

As the linear configuration functions as two separate holes, the flow is split unevenly across each hole resulting in lower flow rates than the parallel configuration. This results in greater shear stress parameters as compared to the parallel configuration. Both dual-hole configurations lower the maximum velocity occurring in the tip when compared to the single medium hole with the same area (Table 5.2). However, the parallel configuration performs in a similar manner to the single medium-sized hole in shear parameters. As shown in Figure 5.9, there is a build-up of high shear stress around

the exterior of the side-holes, which occludes a greater portion of the hole area given the reduction in size than a single side-hole.

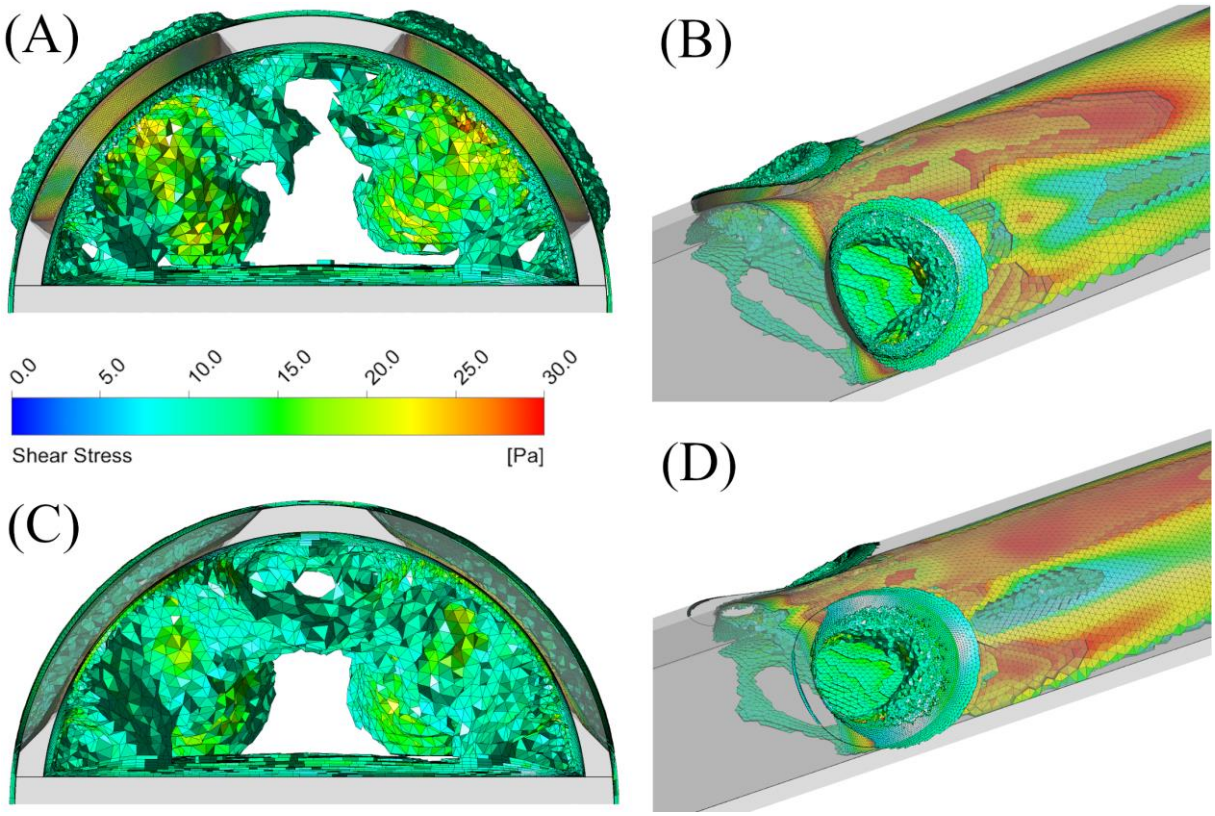

Figure 5.9: Regions inside the tip volume where shear stress >10 Pa for the dual-hole parallel circular (A)-(B) and oval (C)-(D) configurations

The same platelet tracking model was also used to analyse the dual-hole configuration tips, with planes generated tangential to the surface of the catheter, 1 mm above each side-hole with the results tabulated in Table 5.5.

Table 5.5. Platelet parameters for the dual side-hole configurations

Tip Design	Dual side-hole style	Inflow platelet model				
		Average residence time (s)	PLI	Average shear stress (Pa)	Percentage Shear stress >10 Pa	Average shear (s^{-1})
Circular	Linear	0.0126	0.0038	8.03	22.74	2219
	Parallel	0.0100	0.0089	7.63	17.03	2054
Oval	Linear	0.0159	0.0402	8.25	24.84	2282
	Parallel	0.0114	0.0108	8.48	23.47	2348

The dual side-hole configurations experience similar residence times to the single hole tips, but with a much lower magnitude of PLI as a result of the reduction in high shear stress regions >10 Pa. The parallel arrangement has lower residence times than the linear configuration as the inflow is split equally, allowing for undisturbed inflow from both holes. In the linear configuration, the inflow from the second hole is obstructed as it flows down the lumen by the inflow from the first hole and can be seen in Figure 5.10.

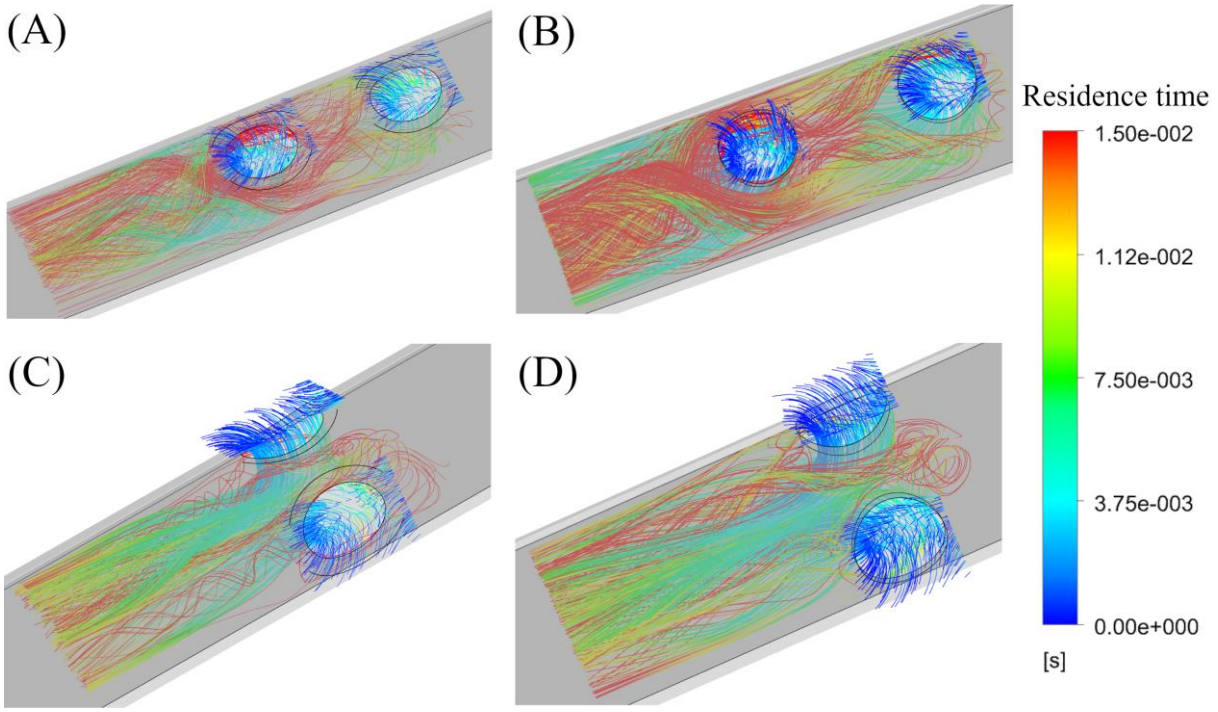

Figure 5.10: Residence times of inflowing platelets for the: Linear oval (A), Linear circular (B), Parallel oval (C) and Parallel circular (D)

Both linear configurations exhibit an uneven flow distribution, where the most proximal hole accounts for >66% of the total side-hole inflow, whereas the parallel configurations split the inflow evenly, as shown in Figure 5.11. This low flow rate in the most distal side-hole results in more uniform low velocity distribution across the hole opening, whereas the side-holes which experience the higher flow rates of 180+ mL/min show regions of high velocity around the apex.

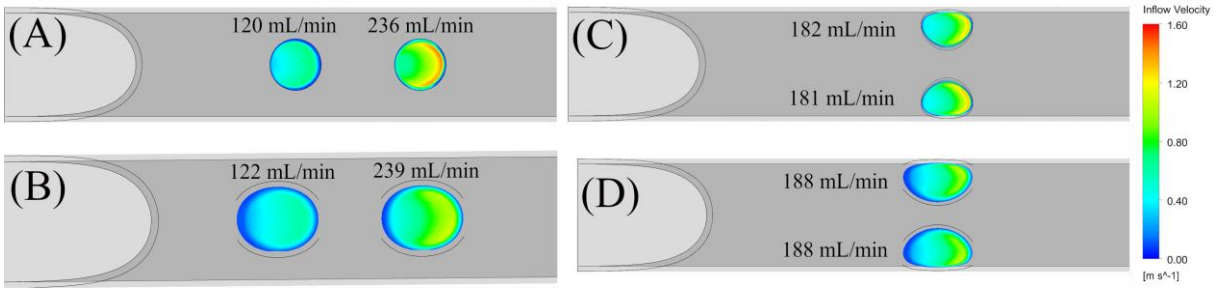

Figure 5.11: Velocity contours and flow rates for the Linear circular (A), Linear oval (B), Parallel circular (C) and parallel oval (D)

5.4 Discussion

This study aimed to investigate the impact of different side-hole configurations on the local haemodynamics and performance of haemodialysis catheter tips. Simulations of multiple tip geometries were performed to critically assess the effects of side-hole geometry, area and number on the haemodynamics of inflowing blood on a simple symmetric tip representative of other designs currently in use. The inflow was assessed across a consistent volume from the tip of the catheter until the inflow was stable and normalised, comparing velocities, flow rates and regions of high shear stress. In addition, the path lines of platelets were also calculated to identify regions of high residence time and shear history which are combined in the platelet lysis index for each catheter tip design.

The inclusion of a side-hole in all the configurations tested improved the objective catheter performance (Table 5.1), with clear reductions in shear stress within the catheter lumen. The medium sized side-hole (9.62 mm^2) performed the best, with

increasing area decreasing the shear stress-based parameters as the larger area allowed for a more gradual redirection of inflow. However, if the side-hole became too large the inflow could 'wash-out' slowly through the tip (Figure 5.6D, 5.7B). It is unclear if this would be a benefit or drawback to function, as 'wash-out' could potentially be preventing platelet adhesion and thrombus formation as blood is kept moving, or alternatively, it may promote adhesion, as blood containing platelets activated by high-shear inflow through the side-hole are spending increased time around the catheter walls thereby increasing chances of adhesion instead of all side-hole inflow exiting the catheter. However, to date this has not been studied either *in vivo* or *in silico* and would require additional testing or a more sophisticated model capable of predicting clot or fibrin growth seeded in these regions.

Performance of the circular and oval-shaped side-holes was similar in most aspects with the largest difference being the larger regions where shear stress >10 Pa around the exterior of the circular holes. With this being used a threshold for platelet activation/blood damage, these areas would be the first to show signs of fibrin formation as shown by Lucas *et al.* (Lucas *et al.*, 2014) which match the regions shown in Figure 5.6 & 5.8. The higher average shear rate of the circular holes is resultant from the increased curvature, as well as the oval shape having an 'angled-cut' for a more gradual redirection of inflow indicating the oval shape as being more viable long term. With circular side-holes typically being drilled/punched (Wentling, 2004), any imperfections/roughness will be ideal seed points for clotting/fibrin formation especially

in the presence of high shear (Twardowski and Moore, 2001). The use of laser cut side-holes as opposed to punched/drilled holes may be useful in reducing these seed points.

The best dual-hole configuration is clearly the parallel setup, with the lowest average shear stress, residence time and percentage shear stress <10 Pa. As the linear configuration concentrates the majority of inflow through the most proximal hole (Figure 5.11), the distal hole experiences a much lower flow rate, and if the catheter were to have additional holes, the flow is likely to become stagnant (Lin *et al.*, 2003) allowing for increased residence time for platelets which should be avoided.

Increasing the number of side-holes may allow for the continued function of the catheter in the event one hole becomes occluded. However, the reduction in side-hole area to achieve this results in a more significant portion having elevated shear stress <10 Pa, both on the exterior of the hole and inside the lumen. This larger region of elevated shear stress around the two much smaller holes implies the slow growth of fibrin formation (Lucas *et al.*, 2013, 2014) may impact on these designs much quicker, as a greater proportion of each hole becomes blocked much faster than a single, larger side-hole.

Side-holes are included in many different styles of catheter tips, with associated benefits of increasing flow rates and spatial separation of inflow/outflow, hence reducing recirculation. Yet these benefits are offset by practical considerations; side-hole catheters have been prone to higher rates of infection and reduced effectiveness of heparin for clot removal and dysfunction from occluded side-holes (Twardowski and

Moore, 2001; Tal *et al.*, 2006). However, the scale to which side-holes increases infection rates in the wide variety of designs on the market is not well understood, requiring a comprehensive *in vivo* study (Tal *et al.*, 2006). Side-holes should only be considered beneficial if any adverse effects on catheter patency are minimal enough to be offset by the increases in flow rate.

Whilst the methodology presented has been used extensively for analysing comparative catheter performance (Clark, Van Canneyt and Verdonck, 2012; Lucas *et al.*, 2014; Clark *et al.*, 2015), a limitation of this study is the lack of accompanying *in vitro* or *in vivo* validation. Data on *in vitro* catheter performance is quite limited, with studies often using the same assumptions as CFD models of constant flow rate or an enclosed cylindrical SVC (Lin *et al.*, 2003; Mareels *et al.*, 2007; Barbour, Gow and Aliseda, 2018). Whilst additional experimental testing is required, CFD studies can be used to highlight issues which *in vitro* studies can focus upon such as flow stagnation and increased residence times. An *in vitro* validation of these techniques was performed by Mareels *et al.* (Mareels *et al.*, 2007) and where possible the present study has reported similar parameters (Residence time, PLI, Average shear/stress) over similar ranges for easier comparisons. In previous comparative CFD catheter studies an overall PLI magnitude was calculated using the entrance velocity of the platelets as a weighting factor (Mareels *et al.*, 2007; Clark, Van Canneyt and Verdonck, 2012), however, as this velocity is intrinsically linked to residence time, and is not included in the original Giersiepen *et al.* methodology (Giersiepen *et al.*, 1990), nor Goubergrits *et al.*

implementation (Goubergrits and Affeld, 2004), the overall magnitude was taken as the average of the PLI magnitude summated for each platelet path line.

Whilst this analysis was performed steady-state, as transient boundary conditions in the SVC have not been shown to significantly alter the inflowing haemodynamics (Mareels *et al.*, 2007), the model could be improved if some transient effects were accounted for. The majority of transient effects arise from the larger variations of blood flow velocity and recirculation occurring inside the right atrium (RA), where the flow is much more energetic than in the SVC. As the haemodynamics of these larger atria are still challenging to simulate, only recently have feasibility studies validated numerical simulations of RA blood flow with HD catheter insertion (Oliveira *et al.*, 2021).

5.5 Conclusion

The inclusion of side-holes on a symmetric tip catheter have been shown to increase the overall performance by increasing flow rates and decreasing shear stress. The side-hole size/shape requires careful consideration, with larger side-holes ($>$9.62 mm^2) reducing shear stress for inflow, however, too large an area results in 'wash-out' which if unaccounted for could greatly increase the likelihood of platelet adhesion. An oval shaped hole appears preferable to a circular hole, as the gradual redirection of inflowing blood experiences lower average shear and has a decreased chance of hole occlusion via fibrin formation. The inclusion of multiple side-holes is best when both holes are

parallel, yet the combination of two smaller side-holes is less desirable than a single, larger hole, as any occlusion of the smaller side-holes will impact performance more severely. Whilst side-holes may improve catheter performance, this should not come at the cost of reduced longevity *in vivo* and the determination of optimal design should be weighed against this. The ideal catheter would maximise the flow rate whilst minimising the chances of clotting/fibrin formation which can be achieved through optimising both the tip design and manufacturing processes.

6 | GENERAL DISCUSSION

6.1 Summation

The aim of this thesis was to develop insightful cardiovascular CFD simulations which explore novel haemodynamic environments to increase our understanding of human physiology, how diseases progress and to improve the design of medical devices. Each chapter of the presented work provides a significant contribution to this aim, with acquired insight and techniques both being incorporated as the research progressed. The key objectives undertaken to meet the overall aim of this thesis were completed as follows:

- Defining a methodology for implementing realistic microscopic coronary artery surface roughness into conventional macroscopic CFD models.
- Comparison of conventional rheological models in this novel multi-scale environment including the first cardiovascular applications of the MKM5 model based upon the Krieger model for suspensions.
- Assessing the impact of stenosed bifurcations on disturbed haemodynamics with a focus on the level of platelet activation and the likelihood of RBC aggregation/rouleaux formation.
- Evaluation of side-hole geometry on the performance and patency of haemodialysis catheter design, including recommendations for optimal performance.

Chapter 3 demonstrated a successful method for implementing newly acquired artery surface roughness data into the previously 'smooth' walled coronary models. With surface roughness increasing during the onset of atherosclerosis (Kitamura, Hasegawa and Kanai, 2012), the impact of this roughness on haemodynamic parameters commonly associated with CVD have been quantified. Despite large fluctuations in values of stress-based parameters, haematocrit and shear rate, the average results between rough/smooth segments of coronary artery were similar. The 'valleys' of the roughness experience much greater residence times, pathologically low shear stress and varying haematocrit resulting in an atherodegenerative environment. Single-phase Newtonian models oversimplify the complex near-wall behaviour, however, at such small scales the current multiphase models require further constraints to account for aggregation of RBC within the valleys of the roughness.

Chapter 4 expands upon the rheological models investigated in the previous chapter by using a novel platelet tracking technique which allowed for quantifying RBC residence time to investigate aggregatory potential but also identifying the potential for platelet activation during atherothrombosis in a stenosed left coronary artery bifurcation. Previously a Newtonian assumption has been justified due to the high shear rates and low residence times of RBC in larger arteries (Johnston *et al.*, 2006). However, this chapter shows that even in large coronary arteries that disturbed haemodynamic environments (distal to stenosis, bifurcations, aneurysms or strong curvature) can exhibit multiphase non-Newtonian behaviour due to continued exposure to low-shear

on timescales similar to those required for aggregation/rouleaux formation. The introduction of stenosis clearly showed increased levels of platelet activation, with greatly increased residence times in the low-shear environment as they recirculated around the plaque (Videos in Supplementary Materials to this thesis). These conditions would be ideal for adhesion to the endothelium and as such could catalyse the deterioration of the plaque into atherothrombotic rupture.

Chapter 5 applied the platelet modelling techniques and understanding of the non-Newtonian properties of blood into a comprehensive assessment of haemodialysis catheter side-holes. With a large variety of shapes, sizes, positions and number of side-holes commercially available, evaluating the effects side-holes have on clinically relevant factors allowed for design recommendations to improve flow performance and long-term patency. Overall, side-holes were shown to increase performance, with angle-cut oval holes being preferable to straight-cut circular holes. In general, multiple holes should be avoided (due to low-flow/redundancy), with careful consideration of manufacturing techniques to ensure the surface roughness of the material is not a seeding point for bacteria/fibrin growth which could infect/occlude the holes and require reinsertion.

The themes and ideas presented in this thesis span from purely theoretical techniques of blood modelling to direct applications of improving medical device design through CFD simulations. Regardless of cardiovascular application, the choice of rheological model (and its inherent limitations) should be carefully considered during setup and

contextualised when analysing results. In a field governed by necessary assumptions, limitations and approximations, the question is not if a result is 'correct', merely if it is useful.

6.2 Future work

As the increase in surface roughness is challenging to measure *in vivo* diagnostically (Niu *et al.*, 2013), simulating the progressive increase in surface roughness and its effects on haemodynamics would be of great interest to further explore atherodegenerative pathways. Perhaps the most enticing applications of this roughness implementation could be applied to improving the design of coronary artery stents, as their main function is an interaction with the coronary artery surface, and they are extensively studied computationally (Duraiswamy *et al.*, 2007). Understanding that since in-stent restenosis is linked to both the WSS and shear stress within blood (Keller *et al.*, 2014), including the surface features which mimic real arteries combined with a more complete representation of the rheology of blood may allow for improvements in design.

Another advancement which would significantly improve not only multiphase models, but the standard of cardiovascular CFD modelling in general would be accounting for aggregation in multiphase model behaviour. This would require both new formulations of viscous definitions, with a component depending on the residence time of RBC, but also detailed *ex vivo* experiments to acquire data on the viscous properties of rouleaux. A key limitation to current rheology models is utilising simplistic rheometer data, which

could be much more accurate and further categorise the behaviour of blood under low-shear and aggregatory conditions. Regrettably, the main benefit of cardiovascular CFD models is also one of its main limitations. The ability to measure, investigate and assess parameters which are inaccessible through medical imaging (haematocrit, platelet tracking etc) allows for exciting new areas of study – but become challenging to validate in clinical environments.

There is significant scope to improve the computational study of haemodialysis catheters, to better replicate *in vivo* conditions. Whilst our work has explored including a realistic right atrium to assess recirculation and optimal positioning, another element which is poorly understood is the mechanical deformation of the catheter and how it affects performance. The chaotic and fluctuating blood flow around the catheter, combined with varying negative pressures required to remove blood result in deformation of the tip. Studies which allow for complex fluid structure interaction could provide better estimates of flow performance, as well as increasing our understanding of fibrin/clot formation in a dynamic environment. With advances in approaches to predictive fibrin clot modelling (Yesudasan and Averett, 2019), coupling this bio-physical process to macroscopic flow features in haemodialysis catheters would not only be a significant step forward in understanding how bio-fouling of medical devices occurs, but lead to increased patency and reduced mortality in patients worldwide.

REFERENCES

Ahmadi, M. and Ansari, R. (2019) 'Computational simulation of an artery narrowed by plaque using 3D FSI method: influence of the plaque angle, non-Newtonian properties of the blood flow and the hyperelastic artery models', *Biomedical Physics & Engineering Express*, 5(4), p. 045037. doi: 10.1088/2057-1976/ab323f.

Alberti, K. G. M. M. *et al.* (2009) 'Harmonizing the metabolic syndrome: A joint interim statement of the international diabetes federation task force on epidemiology and prevention; National heart, lung, and blood institute; American heart association; World heart federation; International ', *Circulation*, 120(16), pp. 1640–1645. doi: 10.1161/CIRCULATIONAHA.109.192644.

AlMomani, T. *et al.* (2008) 'Micro-scale dynamic simulation of erythrocyte-platelet interaction in blood flow', *Annals of Biomedical Engineering*, 36(6), pp. 905–920. doi: 10.1007/s10439-008-9478-z.

Anand, M. and Rajagopal, K. R. (2017) 'A short review of advances in the modelling of blood rheology and clot formation', *Fluids*, 2(3), pp. 1–9. doi: 10.3390/fluids2030035.

Anand, M., Rajagopal, K. and Rajagopal, K. R. (2003) 'A model incorporating some of the mechanical and biochemical factors underlying clot formation and dissolution in flowing blood', *Journal of Theoretical Medicine*, 5(3–4), pp. 183–218. doi: 10.1080/10273660412331317415.

Anderson, H. V. *et al.* (2000) 'Coronary artery flow velocity is related to lumen area and regional left ventricular mass', *Circulation*, 102(1), pp. 48–54. doi: 10.1161/01.CIR.102.1.48.

ANSYS (2019a) *Ansys Fluent 19.2 Theory Guide - Interfacial Area*. Available at: https://ansyshelp.ansys.com/account/secured?returnurl=/Views/Secured/corp/v192/flu_th/flu_th_sec_eulermp_theory_inter_area_conc.html (Accessed: 1 April 2020).

ANSYS (2019b) *Ansys Fluent 19.2 Theory Guide - Saffman Lift Force, 2019*. Available at: https://ansyshelp.ansys.com/account/secured?returnurl=/Views/Secured/corp/v192/flu_th/flu_th_sec_eulermp_lift.html (Accessed: 1 April 2020).

Arzani, A. *et al.* (2017) 'Wall shear stress exposure time: a Lagrangian measure of near-wall stagnation and concentration in cardiovascular flows', *Biomechanics and Modeling in Mechanobiology*, 16(3), pp. 787–803. doi: 10.1007/s10237-016-0853-7.

Arzani, A. (2018) 'Accounting for residence-time in blood rheology models: Do we really need non-Newtonian blood flow modelling in large arteries?', *Journal of the Royal*

Society Interface, 15(146). doi: 10.1098/rsif.2018.0486.

Asakura, T. and Karino, T. (1990) 'Flow patterns and spatial distributions of atherosclerotic lesions in human coronary arteries', *Circulation Research*, 66(4), pp. 1045–1066. doi: 10.1161/01.RES.66.4.1045.

Avram, R. *et al.* (2019) 'Real-world heart rate norms in the Health eHeart study', *npj Digital Medicine*, 2(1). doi: 10.1038/s41746-019-0134-9.

Badimon, L., Padró, T. and Vilahur, G. (2012) 'Atherosclerosis, platelets and thrombosis in acute ischaemic heart disease', *European Heart Journal: Acute Cardiovascular Care*, 1(1), pp. 60–74. doi: 10.1177/2048872612441582.

Ballyk, P. D., Steinman, D. A. and Ethier, C. R. (1994) 'Simulation of Non-Newitonian Blood Flow in an end to side anastomosis', *Biorheology*, 31(5), pp. 565–586.

Barbour, M. C., Gow, K. W. and Aliseda, A. (2018) 'Convectively Dominated Heparin Leakage From Multiple Catheter Designs: An In Vitro Experimental Study', *ASAIO journal (American Society for Artificial Internal Organs : 1992)*, 64(5), pp. e94–e104. doi: 10.1097/MAT.0000000000000776.

Basciano, C. *et al.* (2011) 'A relation between near-wall particle-hemodynamics and onset of thrombus formation in abdominal aortic aneurysms', *Annals of Biomedical Engineering*, 39(7), pp. 2010–2026. doi: 10.1007/s10439-011-0285-6.

Bénard, N. (2005) *Analyse de l'écoulement physiologique dans un stent coronarien : Application à la caractérisation des zones de resténose pariétale.* Université de Poitiers.

Bentzon, J. F. *et al.* (2014) 'Mechanisms of plaque formation and rupture', *Circulation Research*, 114(12), pp. 1852–1866. doi: 10.1161/CIRCRESAHA.114.302721.

Berenson, G. S. *et al.* (1998) 'Association between multiple cardiovascular risk factors and atherosclerosis in children and young adults', *European Journal of Pediatrics*, 157(11), pp. 947–948. doi: 10.1056/nejm199810083391514.

Berning, T. and Djilali, N. (2003) 'A 3D, Multiphase, Multicomponent Model of the Cathode and Anode of a PEM Fuel Cell', *Journal of The Electrochemical Society*, 150(12), p. A1589. doi: 10.1149/1.1621412.

Bessonov, N. *et al.* (2016) 'Methods of Blood Flow Modelling', *Mathematical Modelling of Natural Phenomena*, 11(1), pp. 1–25. doi: 10.1051/mmnp/201611101.

BHF (2019) 'UK Factsheet', *British Heart Foundation*, (April), pp. 1–21.

Binu, L. S. and Sukesh Kumar, A. (2012) 'Simulation of left main coronary bifurcation lesions using 3D computational fluid dynamics model and its comparison with 2D', in *Lecture Notes in Engineering and Computer Science*, pp. 631–636.

Bishop, J. J. *et al.* (2001) 'Rheological effects of red blood cell aggregation in the venous

network: A review of recent studies', *Biorheology*, 38(2–3), pp. 263–274.

Bluestein, D. *et al.* (1997) 'Fluid mechanics of arterial stenosis: Relationship to the development of mural thrombus', *Annals of Biomedical Engineering*, 25(2), pp. 344–356. doi: 10.1007/BF02648048.

Bosma, J. W. *et al.* (2010) 'Reduction of biofilm formation with trisodium citrate in haemodialysis catheters: A randomized controlled trial', *Nephrology Dialysis Transplantation*, 25(4), pp. 1213–1217. doi: 10.1093/ndt/gfp651.

Brault, A., Dumas, L. and Lucor, D. (2016) 'A multiscale SPH particle model of the near-wall dynamics of leukocytes in flow', (September 2013), pp. 83–102. doi: 10.1002/cnm.

Brooks, D. E., Goodwin, J. W. and Seaman, G. V. F. (1970) 'Interactions among erythrocytes under shear', *Journal of Applied Physiology*, 28(2).

Buradi, A. and Mahalingam, A. (2018) 'Effect of stenosis severity on wall shear stress based hemodynamic descriptors using multiphase mixture theory', *Journal of Applied Fluid Mechanics*, 11(6), pp. 1497–1509. doi: 10.18869/acadpub.jafm.73.249.29062.

Burton, H. E. *et al.* (2019) 'Multiscale three-dimensional surface reconstruction and surface roughness of porcine left anterior descending coronary arteries', *Royal Society Open Science*, 6(9). doi: 10.1098/rsos.190915.

Burton, H. E. and Espino, D. M. (2019) 'The effect of mechanical overloading on surface roughness of the coronary arteries', *Applied Bionics and Biomechanics*, 2019, pp. 7–9. doi: 10.1155/2019/2784172.

Burton, H. E., Freij, J. M. and Espino, D. M. (2017) 'Dynamic Viscoelasticity and Surface Properties of Porcine Left Anterior Descending Coronary Arteries', *Cardiovascular Engineering and Technology*, 8(1), pp. 41–56. doi: 10.1007/s13239-016-0288-4.

Burton, H. E., Williams, R. L. and Espino, D. M. (2017) 'Effects of freezing, fixation and dehydration on surface roughness properties of porcine left anterior descending coronary arteries', *Micron*, 101(June), pp. 78–86. doi: 10.1016/j.micron.2017.06.009.

Caballero, A. D. and Laín, S. (2015) 'Numerical simulation of non-Newtonian blood flow dynamics in human thoracic aorta', *Computer Methods in Biomechanics and Biomedical Engineering*, 18(11), pp. 1200–1216. doi: 10.1080/10255842.2014.887698.

Cadroy, Y. and Hanson, S. R. (1990) 'Effects of red blood cell concentration on hemostasis and thrombus formation in a primate model', *Blood*, 75(11), pp. 2185–2193. doi: 10.1182/blood.v75.11.2185.2185.

Caro, C. G. *et al.* (2011a) *The mechanics of the circulation, second edition*, *The Mechanics of the Circulation, Second Edition*. doi: 10.1017/CBO9781139013406.

Caro, C. G. *et al.* (2011b) *The Mechanics of the Circulation (2nd ed.)*. 2nd edn. Cambridge: Cambridge University Press. doi: 10.1017/CBO9781139013406.

Caro, C. G., Fitz-Gerald, J. M. and Schroter, R. C. (1971) 'Atheroma and arterial wall shear. Observation, correlation and proposal of a shear dependent mass transfer mechanism for atherogenesis.', *Proceedings of the Royal Society of London. Series B. Biological sciences*, 177(46), pp. 109–159. doi: 10.1098/rspb.1971.0019.

Carty, G., Chatpun, S. and Espino, D. M. (2016) 'Modeling Blood Flow Through Intracranial Aneurysms: A Comparison of Newtonian and Non-Newtonian Viscosity', *Journal of Medical and Biological Engineering*, 36(3), pp. 396–409. doi: 10.1007/s40846-016-0142-z.

Chabi, F. *et al.* (2015) 'Critical evaluation of three hemodynamic models for the numerical simulation of intra-stent flows', *Journal of Biomechanics*, 48(10), pp. 1769–1776. doi: 10.1016/j.jbiomech.2015.05.011.

Chaichana, T., Sun, Z. and Jewkes, J. (2011) 'Computation of hemodynamics in the left coronary artery with variable angulations', *Journal of Biomechanics*, 44(10), pp. 1869–1878. doi: 10.1016/j.jbiomech.2011.04.033.

Chaichana, T., Sun, Z. and Jewkes, J. (2012) 'Computational fluid dynamics analysis of the effect of plaques in the left coronary artery', *Computational and Mathematical Methods in Medicine*, 2012. doi: 10.1155/2012/504367.

Chappell, D. C. *et al.* (1998) 'Expression in Cultured Human Endothelium', *Circulation research*, 82, pp. 532–539.

Chatzizisis, Y. S. *et al.* (2007) 'Role of Endothelial Shear Stress in the Natural History of Coronary Atherosclerosis and Vascular Remodeling. Molecular, Cellular, and Vascular Behavior', *Journal of the American College of Cardiology*, 49(25), pp. 2379–2393. doi: 10.1016/j.jacc.2007.02.059.

Chiastra, C. *et al.* (2017) 'Healthy and diseased coronary bifurcation geometries influence near-wall and intravascular flow: A computational exploration of the hemodynamic risk', *Journal of Biomechanics*, 58, pp. 79–88. doi: 10.1016/j.jbiomech.2017.04.016.

Chien, S. *et al.* (1966) 'Effects of hematocrit and plasma proteins on human blood rheology at low shear rates.', *Journal of applied physiology*, 21(1), pp. 81–87. doi: 10.1152/jappl.1966.21.1.81.

Chiu, J. J. and Chien, S. (2011) 'Effects of disturbed flow on vascular endothelium: Pathophysiological basis and clinical perspectives', *Physiological Reviews*, 91(1), pp. 327–387. doi: 10.1152/physrev.00047.2009.

Cho, Y. I. and Kensey, K. R. (1991) 'Effects of the non-Newtonian viscosity of blood on flows in a diseased arterial vessel. Part 1: Steady flows', *Biorheology*, 28(3–4), pp.

241–262. doi: 10.3233/BIR-1991-283-415.

Chonchol, M. *et al.* (2008) 'Chronic kidney disease is associated with angiographic coronary artery disease', *American Journal of Nephrology*, 28(2), pp. 354–360. doi: 10.1159/000111829.

Chronic Kidney Disease in the United States (2019) *Centre for diease control and prevention*. Available at: https://www.cdc.gov/kidneydisease/pdf/2019_National-Chronic-Kidney-Disease-Fact-Sheet.pdf (Accessed: 10 February 2020).

Chronic Kidney Disease Surveillance System website (2020) *Centre for Disease control and prevention*. Available at: https://www.cdc.gov/kidneydisease/publications-resources/2019-national-facts.html (Accessed: 10 February 2020).

Chu, M. *et al.* (2018) 'Quantification of disturbed coronary flow by disturbed vorticity index and relation with fractional flow reserve', *Atherosclerosis*, 273, pp. 136–144. doi: 10.1016/j.atherosclerosis.2018.02.023.

Cinthio, M., Hasegawa, H. and Kanai, H. (2011) 'Initial phantom validation of minute roughness measurement using phase tracking for arterial wall diagnosis non-invasively in vivo', *IEEE Transactions on Ultrasonics, Ferroelectrics, and Frequency Control*. doi: 10.1109/TUFFC.2011.1879.

Cito, S., Mazzeo, M. D. and Badimon, L. (2013) 'A review of macroscopic thrombus modeling methods', *Thrombosis Research*, 131(2), pp. 116–124. doi: 10.1016/j.thromres.2012.11.020.

Clark, T. W. I. *et al.* (2015) 'Comparison of symmetric hemodialysis catheters using computational fluid dynamics', *Journal of Vascular and Interventional Radiology*, 26(2), pp. 252–259. doi: 10.1016/j.jvir.2014.11.004.

Clark, T. W. I., Van Canneyt, K. and Verdonck, P. (2012) 'Computational flow dynamics and preclinical assessment of a novel hemodialysis catheter', *Seminars in Dialysis*, 25(5), pp. 574–581. doi: 10.1111/j.1525-139X.2012.01052.x.

Collet, J. P. *et al.* (2006) 'Altered fibrin architecture is associated with hypofibrinolysis and premature coronary atherothrombosis', *Arteriosclerosis, Thrombosis, and Vascular Biology*, 26(11), pp. 2567–2573. doi: 10.1161/01.ATV.0000241589.52950.4c.

Copley, A. L., Huang, C. R. and King, R. G. (1973) 'Rheogoniometric studies of whole human blood at shear rates from 1000 to 0.0009 sec-1. I. Experimental findings.', *Biorheology*. doi: 10.3233/BIR-1973-10103.

Cunningham, K. S. and Gotlieb, A. I. (2005) 'The role of shear stress in the pathogenesis of atherosclerosis', *Laboratory Investigation*, 85(1), pp. 9–23. doi: 10.1038/labinvest.3700215.

Das, B., Johnson, P. C. and Popel, A. S. (1998) 'Effect of nonaxisymmetric hematocrit

distribution on non-Newtonian blood flow in small tubes', *Biorheology*, 35(1), pp. 69–87. doi: 10.1016/S0006-355X(98)00018-3.

Dash, D. (2014) 'Recent perspective on coronary artery bifurcation interventions', *Heart Asia*, pp. 18–25. doi: 10.1136/heartasia-2013-010451.

Davi, G. and Patrono, C. (2007) 'Platelet activation and atherothrombosis', *New England Journal of Medicine*, 357(24), pp. 2482–2494. doi: 10.1056/NEJMc080056.

Davies, J. E. *et al.* (2006) 'Evidence of a Dominant Backward-Propagating " Suction " Wave Responsible for Diastolic Coronary Filling in Humans , Attenuated in Left Ventricular Hypertrophy', pp. 59–61. doi: 10.1161/CIRCULATIONAHA.105.603050.

Degroff, C. G. (2008) 'Modeling the Fontan circulation: Where we are and where we need to go', *Pediatric Cardiology*, 29(1), pp. 3–12. doi: 10.1007/s00246-007-9104-0.

Depner, T. A. (2003) 'Catheter Performance', *Seminars in Dialysis*. doi: 10.1046/j.1525-139x.2001.00106.x.

Desk, R., Williams, L. and Health, K. (1992) 'AJIA Medical / Scientific Statement Special Report A Definition of the Intima of Human Arteries and of Its Atherosclerosis-Prone Regions', *Circulation*.

Ding, J., Sha, W. T. and Lyczkowski, R. W. (1995) 'Modeling of concentrated liquid-solids flow in pipes displaying shear-thinning phenomena', *Chemical Engineering Communications*, 138(1), pp. 145–155. doi: 10.1080/00986449508936386.

Dodge, J. T. *et al.* (1992) 'Lumen diameter of normal human coronary arteries: Influence of age, sex, anatomic variation, and left ventricular hypertrophy or dilation', *Circulation*, 86(1), pp. 232–246. doi: 10.1161/01.CIR.86.1.232.

Drew, D. A., Lahey, R. T. and Roco, M. . (1993) 'Particulate two-phase flow', in *Particulate two-phase flow*. Butterworth-Heinemann.

Dumont, K. *et al.* (2007) 'Comparison of the hemodynamic and thrombogenic performance of two bileaflet mechanical heart valves using a CFD/FSI model', *Journal of Biomechanical Engineering*, 129(4), pp. 558–565. doi: 10.1115/1.2746378.

Duraiswamy, N. *et al.* (2007) 'Stented artery flow patterns and their effects on the artery wall', *Annual Review of Fluid Mechanics*, 39, pp. 357–382. doi: 10.1146/annurev.fluid.39.050905.110300.

Eckmann, D. M. *et al.* (2000) 'Hematocrit, volume expander, temperature, and shear rate effects on blood viscosity', *Anesthesia and Analgesia*, 91(3), pp. 539–545. doi: 10.1213/00000539-200009000-00007.

Ekanayake, N. I. K. *et al.* (2020) 'Lift and drag forces acting on a particle moving with zero slip in a linear shear flow near a wall', *Journal of Fluid Mechanics*. doi: 10.1017/jfm.2020.662.

Ekaterinaris, J. A. and Platzer, M. F. (1998) 'Computational prediction of airfoil dynamic stall', *Progress in Aerospace Sciences*, 33(11–12), pp. 759–846. doi: 10.1016/S0376-0421(97)00012-2.

Eshtehardi, P. *et al.* (2012) 'Association of Coronary Wall Shear Stress With Atherosclerotic Plaque Burden, Composition, and Distribution in Patients With Coronary Artery Disease', *Journal of the American Heart Association*, 1(4), pp. e002543–e002543. doi: 10.1161/JAHA.112.002543.

Ethier, C. R. (2002) 'Computational modeling of mass transfer and links to atherosclerosis', *Annals of Biomedical Engineering*, 30(4), pp. 461–471. doi: 10.1114/1.1468890.

Faghihi, S. *et al.* (2014) 'Study of Plaque Vulnerability in Coronary Artery Using Mooney–Rivlin Model: a Combination of Finite Element and Experimental Method', *Biomedical Engineering: Applications, Basis and Communications*, 26(01), p. 1450013. doi: 10.4015/s1016237214500136.

Fahraeus, R. (1929) 'THE SUSPENSION STABILITY OF BLOOD', *Physiological Reviews*, IX(2), pp. 399–431. Available at: https://doi.org/10.1152/physrev.1929.9.3.399.

Falk, E., Shah, P. K. and Fuster, V. (1995) 'Coronary plaque disruption', *Circulation*. doi: 10.1161/01.CIR.92.3.657.

Farstad, M. (1998) 'The role of blood platelets in coronary atherosclerosis and thrombosis', *Scandinavian Journal of Clinical and Laboratory Investigation*, 58(1), pp. 1–10. doi: 10.1080/00365519850186779.

Fefferman, C. L. (2000) *Existence and smoothness of the Navier-Stokes equation*, *The millennium prize problems*.

Feldman, C. L. and Stone, P. H. (2000) 'Intravascular hemodynamic factors responsible for progression of coronary atherosclerosis and development of vulnerable plaque', *Current Opinion in Cardiology*, 15(6), pp. 430–440. doi: 10.1097/00001573-200011000-00010.

Félétou, M. (2011) 'The Endothelium, Part I: Multiple Functions of the Endothelial Cells -- Focus on Endothelium-Derived Vasoactive Mediators', in *Morgan and Claypool Life Sciences Journal*.

Fenster, B. E. *et al.* (2015) 'Vorticity is a marker of right ventricular diastolic dysfunction', *American Journal of Physiology - Heart and Circulatory Physiology*, 309(6), pp. H1087–H1093. doi: 10.1152/ajpheart.00278.2015.

Fissell, R. B. *et al.* (2013) 'Hemodialysis patient preference for type of vascular access: Variation and predictors across countries in the DOPPS', *Journal of Vascular Access*, 14(3), pp. 264–272. doi: 10.5301/jva.5000140.

Flormann, D. *et al.* (2017) 'The buckling instability of aggregating red blood cells', *Scientific Reports*, 7(1), pp. 1–10. doi: 10.1038/s41598-017-07634-6.

Foust, J. (2004) *Blood flow simulation past a catheter positioned in the SVC-IVC-RA junction: steady and unsteady flow considerations*. Lehigh University.

Fung, Y. . (1993) *Biomechanics: Mechanical Properties of Living Tissues*. 2nd edn. Berlin: Springer.

Galidi, G. P. *et al.* (2008) *Hemodynamical Flows: Modeling, Analysis and Simulation*.

Gallo, D. *et al.* (2012) 'On the use of in vivo measured flow rates as boundary conditions for image-based hemodynamic models of the human aorta: Implications for indicators of abnormal flow', *Annals of Biomedical Engineering*, 40(3), pp. 729–741. doi: 10.1007/s10439-011-0431-1.

Gholipour, A. *et al.* (2018) 'Three-dimensional biomechanics of coronary arteries', *International Journal of Engineering Science*, 130, pp. 93–114. doi: 10.1016/j.ijengsci.2018.03.002.

Gholipour, A., Ghayesh, M. H. and Zander, A. (2018) 'Nonlinear biomechanics of bifurcated atherosclerotic coronary arteries', *International Journal of Engineering Science*, 133, pp. 60–83. doi: 10.1016/j.ijengsci.2018.08.003.

Gidaspow, D. (1994) 'Continuum and kinetic theory descriptions', in *Multiphase flow and fluidization*.

Giersiepen, M. *et al.* (1990) 'Estimation of shear stress-related blood damage in heart valve prostheses - in vitro comparison of 25 aortic valves', *International Journal of Artificial Organs*, 13(5), pp. 300–306. doi: 10.1177/039139889001300507.

Gimbrone, M. A. *et al.* (2001) 'Endothelial Dysfunction, Haemodynamic Forces and Atherogensis', p. 11. doi: 10.1111/j.1749-6632.2000.tb06318.x.

Gogia, S. and Neelamegham, S. (2015) 'Role of fluid shear stress in regulating VWF structure, function and related blood disorders', *Biorheology*, 52(5–6), pp. 319–335. doi: 10.3233/BIR-15061.

Goldstone, J., Schmid-Schönbein, H. and Wells, R. (1970) 'The rheology of red blood cell aggregates', *Microvascular Research*, 2(3), pp. 273–286. doi: 10.1016/0026-2862(70)90018-X.

Gorbet, M. B. and Sefton, M. V. (2004) 'Biomaterial-associated thrombosis: Roles of coagulation factors, complement, platelets and leukocytes', *Biomaterials*, 25(26), pp. 5681–5703. doi: 10.1016/j.biomaterials.2004.01.023.

Goubergrits, L. and Affeld, K. (2004) 'Numerical estimation of blood damage in artificial organs', *Artificial Organs*, 28(5), pp. 499–507. doi: 10.1111/j.1525-1594.2004.07265.x.

Govindarajan, V. *et al.* (2016) 'Computational Study of Thrombus Formation and Clotting Factor Effects under Venous Flow Conditions', *Biophysical Journal*, 110(8), pp. 1869–1885. doi: 10.1016/j.bpj.2016.03.010.

Gross, D. R. and Wang, N. H. C. (1981) 'Response of Platelets to Shear Stress: A Review', in *The Rheology of Blood Vessels and Associated Tissues*. Alphen aan den Rijn: Sijthoff & Noordhoff, pp. 160–183.

Guerciotti, B. *et al.* (2017) 'Computational study of the risk of restenosis in coronary bypasses', *Biomechanics and Modeling in Mechanobiology*. doi: 10.1007/s10237-016-0818-x.

Haemodialysis Facts and Stats (2020) *Kidney Care UK*. Available at: https://www.kidneycareuk.org/news-and-campaigns/facts-and-stats/ (Accessed: 10 February 2019).

Hall, J. and Guyton, A. (2020) *Textbook of Medical Physiology*. 14th edn. Saunders.

Hayes, W. N. *et al.* (2012) 'Vascular access: Choice and complications in European paediatric haemodialysis units', *Pediatric Nephrology*, 27(6), pp. 999–1004. doi: 10.1007/s00467-011-2079-3.

He, X. and Ku, D. N. (1996) 'Pulsatile flow in the human left coronary artery bifurcation: Average conditions', *Journal of Biomechanical Engineering*, 118(1), pp. 74–82. doi: 10.1115/1.2795948.

Van Der Heiden, K. *et al.* (2013) 'The effects of stenting on shear stress: Relevance to endothelial injury and repair', *Cardiovascular Research*, 99(2), pp. 269–275. doi: 10.1093/cvr/cvt090.

Hellums, J. D. *et al.* (1987) 'Studies on the Mechanisms of Shear-Induced Platelet Activation', *Cerebral Ischemia and Hemorheology*, pp. 80–89. doi: 10.1007/978-3-642-71787-1_8.

Herzog, C. A. *et al.* (2011) 'Cardiovascular disease in chronic kidney disease. A clinical update from Kidney Disease: Improving Global Outcomes (KDIGO)', *Kidney International*, 80(6), pp. 572–586. doi: 10.1038/ki.2011.223.

Himburg, H. A. *et al.* (2004) 'Spatial comparison between wall shear stress measures and porcine arterial endothelial permeability', *American Journal of Physiology - Heart and Circulatory Physiology*, 286(5 55-5), pp. 1916–1922. doi: 10.1152/ajpheart.00897.2003.

Hirtler, D. *et al.* (2016) 'Assessment of intracardiac flow and vorticity in the right heart of patients after repair of tetralogy of Fallot by flow-sensitive 4D MRI', *European Radiology*, 26(10), pp. 3598–3607. doi: 10.1007/s00330-015-4186-1.

Holzapfel, G. A. *et al.* (2005) 'Determination of layer-specific mechanical properties of

human coronary arteries with nonatherosclerotic intimal thickening and related constitutive modeling', *American Journal of Physiology - Heart and Circulatory Physiology*, 289(5 58-5), pp. 2048–2058. doi: 10.1152/ajpheart.00934.2004.

Howard, G. *et al.* (1998) 'Cigarette smoking and progression of atherosclerosis: The atherosclerosis risk in communities (ARIC) study', *Journal of the American Medical Association*, 279(2), pp. 119–124. doi: 10.1001/jama.279.2.119.

Huang, J., Lyczkowski, R. W. and Gidaspow, D. (2009) 'Pulsatile flow in a coronary artery using multiphase kinetic theory', *Journal of Biomechanics*, 42(6), pp. 743–754. doi: 10.1016/j.jbiomech.2009.01.038.

Humphrey, J. D. and Taylor, C. A. (2008) 'Intracranial and abdominal aortic aneurysms: Similarities, differences, and need for a new class of computational models', *Annual Review of Biomedical Engineering*. doi: 10.1146/annurev.bioeng.10.061807.160439.

Hund, S., Kameneva, M. and Antaki, J. (2017) 'A Quasi-Mechanistic Mathematical Representation for Blood Viscosity', *Fluids*, 2(1), p. 10. doi: 10.3390/fluids2010010.

Iasiello, M. *et al.* (2016) 'Analysis of non-Newtonian effects on Low-Density Lipoprotein accumulation in an artery', *Journal of Biomechanics*, 49(9), pp. 1437–1446. doi: 10.1016/j.jbiomech.2016.03.017.

Jahangiri, M., Saghafian, M. and Sadeghi, M. R. (2017) 'Numerical simulation of non-Newtonian models effect on hemodynamic factors of pulsatile blood flow in elastic stenosed artery', *Journal of Mechanical Science and Technology*, 31(2), pp. 1003–1013. doi: 10.1007/s12206-017-0153-x.

Javadzadegan, A. *et al.* (2017) 'Haemodynamic assessment of human coronary arteries is affected by degree of freedom of artery movement', *Computer Methods in Biomechanics and Biomedical Engineering*, 20(3), pp. 260–272. doi: 10.1080/10255842.2016.1215439.

Johnston, B. M. *et al.* (2004) 'Non-Newtonian blood flow in human right coronary arteries: Steady state simulations', *Journal of Biomechanics*, 37(5), pp. 709–720. doi: 10.1016/j.jbiomech.2003.09.016.

Johnston, B. M. *et al.* (2006) 'Non-Newtonian blood flow in human right coronary arteries: Transient simulations', *Journal of Biomechanics*, 39(6), pp. 1116–1128. doi: 10.1016/j.jbiomech.2005.01.034.

Jung, J. *et al.* (2006) 'Multiphase hemodynamic simulation of pulsatile flow in a coronary artery', *Journal of Biomechanics*, 39(11), pp. 2064–2073. doi: 10.1016/j.jbiomech.2005.06.023.

Jung, J. and Hassanein, A. (2008) 'Three-phase CFD analytical modeling of blood flow', *Medical Engineering and Physics*, 30(1), pp. 91–103. doi:

10.1016/j.medengphy.2006.12.004.

Junker, R. *et al.* (1998) 'Relationship Between Plasma Viscosity and the Severity of Coronary Heart Disease', *Arteriosclerosis, Thrombosis, and Vascular Biology*, (18), p. 87. doi: https://doi.org/10.1161/01.ATV.18.6.870.

Kabinejadian, F. and Ghista, D. N. (2012) 'Compliant model of a coupled sequential coronary arterial bypass graft: Effects of vessel wall elasticity and non-Newtonian rheology on blood flow regime and hemodynamic parameters distribution', *Medical Engineering and Physics*. doi: 10.1016/j.medengphy.2011.10.001.

Karimi, A. *et al.* (2013) 'A finite element investigation on plaque vulnerability in realistic healthy and atherosclerotic human coronary arteries', *Proceedings of the Institution of Mechanical Engineers, Part H: Journal of Engineering in Medicine*, 227(2), pp. 148–161. doi: 10.1177/0954411912461239.

Karimi, A., Navidbakhsh, M. and Razaghi, R. (2014) 'Plaque and arterial vulnerability investigation in a three-layer atherosclerotic human coronary artery using computational fluid-structure interaction method', *Journal of Applied Physics*, 116(6). doi: 10.1063/1.4893368.

Karino, T. and Goldsmith, H. L. (1979) 'Adhesion of human platelets to collagen on the walls distal to a tubular expansion', *Microvascular Research*, 17(3), pp. 238–262. doi: 10.1016/S0026-2862(79)80002-3.

Kassab, G. S. and Fung, Y. C. B. (1995) 'The pattern of coronary arteriolar bifurcations and the uniform shear hypothesis', *Annals of Biomedical Engineering*, 23(1), pp. 13–20. doi: 10.1007/BF02368296.

Keller, B. K. *et al.* (2014) 'Contribution of Mechanical and Fluid Stresses to the Magnitude of In-stent Restenosis at the Level of Individual Stent Struts', *Cardiovascular Engineering and Technology*, 5(2), pp. 164–175. doi: 10.1007/s13239-014-0181-y.

De Keulenaer, G. W. *et al.* (1998) 'Oscillatory and steady laminar shear stress differentially affect human endothelial redox state: Role of a superoxide-producing NADH oxidase', *Circulation Research*, 82(10), pp. 1094–1101. doi: 10.1161/01.RES.82.10.1094.

Kim, Y. H., VandeVord, P. J. and Lee, J. S. (2008) 'Multiphase non-Newtonian effects on pulsatile hemodynamics in a coronary artery', *International Journal for Numerical Methods in Fluids*, 58(7), pp. 803–825. doi: 10.1002/fld.1768.

Kitamura, K., Hasegawa, H. and Kanai, H. (2012) 'Accurate estimation of carotid luminal surface roughness using ultrasonic radio-frequency echo', *Japanese Journal of Applied Physics*, 51(7 PART2), pp. 1–12. doi: 10.1143/JJAP.51.07GF08.

Kleinstreuer, C. and Feng, Y. (2013) 'Computational analysis of non-spherical particle

transport and deposition in shear flow with application to lung aerosol dynamics - A review', *Journal of Biomechanical Engineering*, 135(2). doi: 10.1115/1.4023236.

Knight, J. *et al.* (2010) 'Choosing the optimal wall shear parameter for the prediction of plaque location-A patient-specific computational study in human right coronary arteries', *Atherosclerosis*, 211(2), pp. 445–450. doi: 10.1016/j.atherosclerosis.2010.03.001.

Knuttinen, M. G. *et al.* (2009) 'A review of evolving dialysis catheter technologies', *Seminars in Interventional Radiology*, 26(2), pp. 106–114. doi: 10.1055/s-0029-1222453.

Kousoula, V. *et al.* (2019) 'Reversed connection of cuffed, tunneled, dual-lumen catheters with increased blood flow rate maintains the adequacy of delivered dialysis despite the higher access recirculation', *International Urology and Nephrology*, 51(10), pp. 1841–1847. doi: 10.1007/s11255-019-02268-1.

Krieger, I. M. and Dougherty, T. J. (1959) 'A Mechanism for Non-Newtonian Flow in Suspensions of Rigid Spheres', *Transactions of the Society of Rheology*, 3(1), pp. 137–152. doi: 10.1122/1.548848.

Ku, D N ; Giddens, D P ; Zarins, C K ; Glagov, S. (1985) 'Pulsatile Flow and Atherosclerosis in the Human Carotid Bifurcation', *Arteriosclerosis*.

Kung, E. *et al.* (2013) 'Predictive modeling of the virtual Hemi-Fontan operation for second stage single ventricle palliation: Two patient-specific cases', *Journal of Biomechanics*, 46(2), pp. 423–429. doi: 10.1016/j.jbiomech.2012.10.023.

Kunz, R. F. *et al.* (2000) 'A preconditioned Navier-Stokes method for two-phase flows with application to cavitation prediction', *Computers and Fluids*, 29(8), pp. 849–875. doi: 10.1016/S0045-7930(99)00039-0.

Ladisa, J. F. *et al.* (2003) 'Three-dimensional computational fluid dynamics modeling of alterations in coronary wall shear stress produced by stent implantation', *Annals of Biomedical Engineering*, 31(8), pp. 972–980. doi: 10.1114/1.1588654.

Langille, B. L. and O'Donnell, F. (1986) 'Reductions in arterial diameter produced by chronic decreases in blood flow are endothelium-dependent', *Science*, 231(4736), pp. 405–407. doi: 10.1126/science.3941904.

Lee, K. E. *et al.* (2019) 'Prediction of Plaque Progression in Coronary Arteries Based on a Novel Hemodynamic Index Calculated From Virtual Stenosis Method', *Frontiers in Physiology*, 10(May), pp. 1–7. doi: 10.3389/fphys.2019.00400.

Lee, S. W. and Steinman, D. A. (2007) 'On the relative importance of rheology for image-based CFD models of the carotid bifurcation', *Journal of Biomechanical Engineering*, 129(2), pp. 273–278. doi: 10.1115/1.2540836.

Leung, W. H., Stadius, M. L. and Alderman, E. L. (1991) 'Determinants of normal

coronary artery dimensions in humans', *Circulation*. doi: 10.1161/01.CIR.84.6.2294.

Li, A. and Ahmadi, G. (1992) 'Dispersion and deposition of spherical particles from point sources in a turbulent channel flow', *Aerosol Science and Technology*. doi: 10.1080/02786829208959550.

Liepsch, D. W. *et al.* (1988) 'Correlation of laser-Doppler-velocity measurements and endothelial cell shape in a stenosed dog aorta.', *Advances in experimental medicine and biology*, 242, pp. 43–50. doi: 10.1007/978-1-4684-8935-4_6.

Lin, J. *et al.* (2003) 'Computational and experimental study of proximal flow in ventricular catheters: Technical note', *Journal of Neurosurgery*, 99(2), pp. 426–431. doi: 10.3171/jns.2003.99.2.0426.

Liu, H. *et al.* (2015) 'Multi-scale modeling of hemodynamics in the cardiovascular system', *Acta Mechanica Sinica/Lixue Xuebao*, 31(4), pp. 446–464. doi: 10.1007/s10409-015-0416-7.

Liu, M. *et al.* (2014) 'Cardiovascular disease and its relationship with chronic kidney disease', *European review for medical and pharmacological sciences*, 18(19), pp. 2918–2926.

Liu, X. *et al.* (2009) 'A numerical study on the flow of blood and the transport of LDL in the human aorta: The physiological significance of the helical flow in the aortic arch', *American Journal of Physiology - Heart and Circulatory Physiology*, 297(1), pp. 163–171. doi: 10.1152/ajpheart.00266.2009.

Lok, C. E. *et al.* (2020) 'KDOQI Clinical Practice Guideline for Vascular Access: 2019 Update', *American Journal of Kidney Diseases*, 75(4), pp. S1–S164. doi: 10.1053/j.ajkd.2019.12.001.

Longest, P. W., Kleinstreuer, C. and Buchanan, J. R. (2004) 'Efficient computation of micro-particle dynamics including wall effects', *Computers and Fluids*, 33(4), pp. 577–601. doi: 10.1016/j.compfluid.2003.06.002.

Louvard, Y. *et al.* (2008) 'Classification of coronary artery bifurcation lesions and treatments: Time for a consensus!', *Catheterization and Cardiovascular Interventions*, pp. 175–183. doi: 10.1002/ccd.21314.

Lucas, T. C. *et al.* (2013) 'Hemodialysis catheter thrombi: Visualization and quantification of microstructures and cellular composition', *Journal of Vascular Access*, 14(3), pp. 257–263. doi: 10.5301/jva.5000142.

Lucas, T. C. *et al.* (2014) 'Blood Flow in Hemodialysis Catheters: A Numerical Simulation and Microscopic Analysis of In Vivo-Formed Fibrin', *Artificial Organs*, 38(7), pp. 556–565. doi: 10.1111/aor.12243.

Malek, A. M. and Alper, S. L. (2007) 'Hemodynamic Shear Stress and Its Role in

Atherosclerosis', 282(21), pp. 2035–2042.

Mareels, G. *et al.* (2007) 'Particle Image Velocimetry-validated, computational fluid dynamics-based design to reduce shear stress and residence time in central venous hemodialysis catheters', *ASAIO Journal*, 53(4), pp. 438–446. doi: 10.1097/MAT.0b013e3180683b7c.

Massai, D. *et al.* (2012) 'Shear-induced platelet activation and its relationship with blood flow topology in a numerical model of stenosed carotid bifurcation', *European Journal of Mechanics, B/Fluids*, 35, pp. 92–101. doi: 10.1016/j.euromechflu.2012.03.011.

Massberg, S. *et al.* (2002) 'A critical role of platelet adhesion in the initiation of atherosclerotic lesion formation', *Journal of Experimental Medicine*, 196(7), pp. 887–896. doi: 10.1084/jem.20012044.

Mathew, E. *et al.* (2019) 'Fused deposition modelling as a potential tool for antimicrobial dialysis catheters manufacturing: New trends vs. conventional approaches', *Coatings*, 9(8). doi: 10.3390/coatings9080515.

Matsushita, K. *et al.* (2010) 'Association of estimated glomerular filtration rate and albuminuria with all-cause and cardiovascular mortality in general population cohorts: a collaborative meta-analysis', *The Lancet*, 375(9731), pp. 2073–2081. doi: 10.1016/S0140-6736(10)60674-5.

Mattace-Raso, F. U. S. *et al.* (2010) 'Determinants of pulse wave velocity in healthy people and in the presence of cardiovascular risk factors: "Establishing normal and reference values"', *European Heart Journal*, 31(19), pp. 2338–2350. doi: 10.1093/eurheartj/ehq165.

Maxwell, M. J. *et al.* (2007) 'Identification of a 2-stage platelet aggregation process mediating shear-dependent thrombus formation', *Blood*, 109(2), pp. 566–576. doi: 10.1182/blood-2006-07-028282.

Mayer-Davis, E. J. *et al.* (1998) 'Intensity and amount of physical activity in relation to insulin sensitivity the Insulin Resistance Atherosclerosis Study', *Journal of the American Medical Association*, 279(9), pp. 669–674. doi: 10.1001/jama.279.9.669.

McCrindle, B. W. *et al.* (2007) 'Drug therapy of high-risk lipid abnormalities in children and adolescents: A scientific statement from the American Heart Association atherosclerosis, hypertension, and obesity in youth committee, council of cardiovascular disease in the young, with the c', *Circulation*, 115(14), pp. 1948–1967. doi: 10.1161/CIRCULATIONAHA.107.181946.

Menon, V., Gul, A. and Sarnak, M. J. (2005) 'Cardiovascular risk factors in chronic kidney disease', *Kidney International*, 68(4), pp. 1413–1418. doi: 10.1111/j.1523-1755.2005.00551.x.

Miller, L. M., Clark, E., *et al.* (2016) 'Hemodialysis tunneled catheter-related infections', *Canadian Journal of Kidney Health and Disease*, 3(1). doi: 10.1177/2054358116669129.

Miller, L. M., MacRae, J. M., *et al.* (2016) 'Hemodialysis tunneled catheter noninfectious complications', *Canadian Journal of Kidney Health and Disease*, 3(1). doi: 10.1177/2054358116669130.

Moist, L. M., Hemmelgarn, B. R. and Lok, C. E. (2006) 'Relationship between blood flow in central venous catheters and hemodialysis adequacy.', *Clinical journal of the American Society of Nephrology : CJASN*, 1(5), pp. 965–971. doi: 10.2215/CJN.01090306.

Morsi, S. A. and Alexander, A. J. (1972) 'An investigation of particle trajectories in two-phase flow systems', *Journal of Fluid Mechanics*, 55(2), pp. 193–208. doi: 10.1017/S0022112072001806.

Murray, C. D. (1931) 'THE PHYSIOLOGICAL PRINCIPLE OF MINIMUMI WORK. I. THE VASCULAR SYSTEM AND THFE COST OF BLOOD VOLUME', *Journal of General Physiology*, 14(4), p. 445. doi: 10.1085/jgp.14.4.445.

Mustard, J. F. and Packham, M. A. (1974) 'The role of blood and platelets in atherosclerosis and the complications of atherosclerosis', *Thrombosis and Hemostasis*.

Nakano, T. *et al.* (2010) 'Association of Kidney Function With Coronary Atherosclerosis and Calcification in Autopsy Samples From Japanese Elders: The Hisayama Study', *American Journal of Kidney Diseases*, 55(1), pp. 21–30. doi: 10.1053/j.ajkd.2009.06.034.

Nguyen, V. T. *et al.* (2015) 'A Patient-Specific Computational Fluid Dynamic Model for Hemodynamic Analysis of Left Ventricle Diastolic Dysfunctions', *Cardiovascular Engineering and Technology*, 6(4), pp. 412–429. doi: 10.1007/s13239-015-0244-8.

De Nisco, G. *et al.* (2019) 'The Atheroprotective Nature of Helical Flow in Coronary Arteries', *Annals of Biomedical Engineering*, 47(2), pp. 425–438. doi: 10.1007/s10439-018-02169-x.

Niu, L. *et al.* (2013) 'Surface Roughness Detection of Arteries via Texture Analysis of Ultrasound Images for Early Diagnosis of Atherosclerosis', *PLoS ONE*, 8(10). doi: 10.1371/journal.pone.0076880.

Nobili, M. *et al.* (2008) 'Platelet activation due to hemodynamic shear stresses: Damage accumulation model and comparison to in vitro measurements', *ASAIO Journal*, 54(1), pp. 64–72. doi: 10.1097/MAT.0b013e31815d6898.

Nording, H. M., Seizer, P. and Langer, H. F. (2015) 'Platelets in inflammation and atherogenesis', *Frontiers in Immunology*, 6(MAR), pp. 3378–3384. doi: 10.3389/fimmu.2015.00098.

O'Dwyer, H. *et al.* (2005) 'A prospective comparison of two types of tunneled hemodialysis catheters: The ash split versus the PermCath', *CardioVascular and Interventional Radiology*, 28(1), pp. 23–29. doi: 10.1007/s00270-003-0230-7.

Olgac, U. *et al.* (2009) 'Patient-specific three-dimensional simulation of LDL accumulation in a human left coronary artery in its healthy and atherosclerotic states', *American Journal of Physiology - Heart and Circulatory Physiology*, 296(6). doi: 10.1152/ajpheart.01182.2008.

Olgac, U., Kurtcuoglu, V. and Poulikakos, D. (2008) 'Computational modeling of coupled blood-wall mass transport of LDL: Effects of local wall shear stress', *American Journal of Physiology - Heart and Circulatory Physiology*, 294(2), pp. 909–919. doi: 10.1152/ajpheart.01082.2007.

Oliveira, D. C. De *et al.* (2021) 'Computational fluid dynamics of the right atrium : Assessment of modelling criteria for the evaluation of dialysis catheters', (Ivc), pp. 1–26. doi: 10.1371/journal.pone.0247438.

Oviedo, C. *et al.* (2010) 'Intravascular ultrasound classification of plaque distribution in left main coronary artery bifurcations where is the plaque really located?', *Circulation: Cardiovascular Interventions*, 3(2), pp. 105–112. doi: 10.1161/CIRCINTERVENTIONS.109.906016.

Owen, D. G., Schenkel, T., *et al.* (2020) 'Assessment of surface roughness and blood rheology on local coronary haemodynamics: a multi-scale computational fluid dynamics study', *Royal Society Journal Interface*, 17(169).

Owen, D. G., Oliveira, D. C. De, *et al.* (2020) 'Impact of side-hole geometry on the performance of hemodialysis catheter tips : A computational fluid dynamics assessment', *PLoS ONE*, pp. 1–16. doi: 10.1371/journal.pone.0236946.

Pal, R. (2003) 'Rheology of concentrated suspensions of deformable elastic particles such as human erythrocytes', *Journal of Biomechanics*, 36(7), pp. 981–989. doi: 10.1016/S0021-9290(03)00067-8.

Papaioannou, T. G. *et al.* (2006) 'Assessment of vascular wall shear stress and implications for atherosclerotic disease', *International Journal of Cardiology*, 113(1), pp. 12–18. doi: 10.1016/j.ijcard.2006.03.035.

Picart, C. *et al.* (1998) 'Human blood shear yield stress and its hematocrit dependence', *Journal of Rheology*, 42(1), pp. 1–12. doi: 10.1122/1.550883.

Ponder, E. (1948) *Hemolysis and related Phenomena*. New York: Grune & Stratton.

Poppas, A. *et al.* (1997) 'Serial assessment of the cardiovascular system in normal pregnancy: Role of arterial compliance and pulsatile arterial load', *Circulation*. doi: 10.1161/01.CIR.95.10.2407.

Rabbi, M. F., Laboni, F. S. and Arafat, M. T. (2020) 'Computational analysis of the coronary artery hemodynamics with different anatomical variations', *Informatics in Medicine Unlocked*, 19(100314). doi: 10.1016/j.imu.2020.100314.

Rand, P. W. and Lacombe, E. (1964) 'Hemodilution, tonicity and blood viscosity', *The Journal of clinical investigation*, 43(11), pp. 2214–2226. doi: 10.1172/JCI105095.

Rayz, V. L. *et al.* (2008) 'Numerical modeling of the flow in intracranial aneurysms: Prediction of regions prone to thrombus formation', *Annals of Biomedical Engineering*, 36(11), pp. 1793–1804. doi: 10.1007/s10439-008-9561-5.

Rikhtegar, F. *et al.* (2012) 'Choosing the optimal wall shear parameter for the prediction of plaque location-A patient-specific computational study in human left coronary arteries', *Atherosclerosis*, 221(2), pp. 432–437. doi: 10.1016/j.atherosclerosis.2012.01.018.

Roberts, W. C. (1989) 'Qualitative and quantitative comparison of amounts of narrowing by atherosclerotic plaques in the major epicardial coronary arteries at necropsy in sudden coronary death, transmural acute myocardial infarction, transmural healed myocardial infarction and ', *The American Journal of Cardiology*, 64, pp. 324–328.

Robertson, A. M., Sequeria, A. and Kameneva, M. V. (2008) 'Hemorheology', in *Hemodynamical Flows: Modeling, analysis and simulation*, pp. 63–120.

Roth, G. A. *et al.* (2018) 'Global, regional, and national age-sex-specific mortality for 282 causes of death in 195 countries and territories, 1980–2017: a systematic analysis for the Global Burden of Disease Study 2017', *The Lancet*, 392(10159), pp. 1736–1788. doi: 10.1016/S0140-6736(18)32203-7.

Roux, E. *et al.* (2020) 'Fluid Shear Stress Sensing by the Endothelial Layer', *Frontiers in Physiology*, 11(July), pp. 1–17. doi: 10.3389/fphys.2020.00861.

Ruggeri, Z. M. *et al.* (2006) 'Activation-independent platelet adhesion and aggregation under elevated shear stress', *Blood*, 108(6), pp. 1903–1910. doi: 10.1182/blood-2006-04-011551.

Samady, H. *et al.* (2011) 'Coronary artery wall shear stress is associated with progression and transformation of atherosclerotic plaque and arterial remodeling in patients with coronary artery disease', *Circulation*, 124(7), pp. 779–788. doi: 10.1161/CIRCULATIONAHA.111.021824.

Sankaran, S. *et al.* (2012) 'Patient-specific multiscale modeling of blood flow for coronary artery bypass graft surgery', *Annals of Biomedical Engineering*, 40, pp. 2228–2242. doi: 10.1007/s10439-012-0579-3.

Santoro, D. *et al.* (2014) 'Vascular access for hemodialysis: Current perspectives', *International Journal of Nephrology and Renovascular Disease*, 7, pp. 281–294. doi:

10.2147/IJNRD.S46643.

Schenkel, T. and Halliday, I. (2020) 'Continuum Scale Non Newtonian Particle Transport Model for Haemorheology -- Implementation and Validation', pp. 1–12. Available at: http://arxiv.org/abs/2004.12380.

Schiller, L. and Naumann, Z. (1935) *A drag coefficient correlation*, *Z.Ver.Deutsch.Ing.*

Schmid-Schönbein, H. *et al.* (1975) 'Microrheology and light transmission of blood - III. The velocity of red cell aggregate formation', *Pflügers Archiv European Journal of Physiology*, 354(4), pp. 299–317. doi: 10.1007/BF00587849.

Schmidt-Trucksäss, A. *et al.* (2003) 'Quantitative measurement of carotid intima-media roughness - Effect of age and manifest coronary artery disease', *Atherosclerosis*, 166(1), pp. 57–65. doi: 10.1016/S0021-9150(02)00245-9.

Secomb, T. W. (2017) 'Blood Flow in the Microcirculation', *Annu. Rev. Fluid Mech*, 49(August), pp. 443–61. doi: 10.1146/annurev-fluid-010816-060302.

Shewchuk, J. R. (2002) 'What is a Good Linear Element ? Interpolation , Conditioning , and Quality Measures', *Eleventh International Meshing Roundtable*, pp. 115–126. doi: 10.1.1.68.8538.

Shroff, R. (2019) *Access for paediatric dialysis*, *The European Rare Kidney Disease Reference Network*. Available at: https://www.erknet.org/fileadmin/files/user_upload/Access_for_paediatric_dialysis_-_SHROFF_-_ERKNet_Webinar_-_7.1.2019.pdf (Accessed: 6 February 2022).

Simmonds, M. J. *et al.* (2018) *Blood-device interaction*, *Mechanical Circulatory and Respiratory Support*. Elsevier Inc. doi: 10.1016/B978-0-12-810491-0.00019-9.

Skiadopoulos, A., Neofytou, P. and Housiadas, C. (2017) 'Comparison of blood rheological models in patient specific cardiovascular system simulations', *Journal of Hydrodynamics*, 29(2), pp. 293–304. doi: 10.1016/S1001-6058(16)60739-4.

Skorczewski, T., Erickson, L. C. and Fogelson, A. L. (2013) 'Platelet motion near a vessel wall or thrombus surface in two-dimensional whole blood simulations', *Biophysical Journal*, 104(8), pp. 1764–1772. doi: 10.1016/j.bpj.2013.01.061.

Somer, T. and Meiselman, H. J. (1993) 'Disorders of blood viscosity', *Annals of Medicine*, 25(1), pp. 31–39. doi: 10.3109/07853899309147854.

Sorensen, E. N. *et al.* (1999) 'Computational Simulation of Platelet Deposition and Activation: I. Model Development and Properties', *Annals of Biomedical Engineering*, 27(4), pp. 436–448. doi: 10.1114/1.200.

Soulis, J. V. *et al.* (2008) 'Non-Newtonian models for molecular viscosity and wall shear stress in a 3D reconstructed human left coronary artery', *Medical Engineering and Physics*, 30(1), pp. 9–19. doi: 10.1016/j.medengphy.2007.02.001.

Srivastava, V. P. and Srivastava, R. (2009) 'Particulate suspension blood flow through a narrow catheterized artery', *Computers and Mathematics with Applications*, 58(2), pp. 227–238. doi: 10.1016/j.camwa.2009.01.041.

Stangeby, D. K. and Ethier, C. R. (2002) 'Computational analysis of coupled blood-wall arterial LDL transport', *Journal of Biomechanical Engineering*, 124(1), pp. 1–8. doi: 10.1115/1.1427041.

Stary, H. *et al.* (1994) 'AHA Medical / Scientific Statement Special Report A Definition of Initial , Fatty Streak , and Intermediate Lesions of Atherosclerosis', *Circulation*, 89, pp. 2462–2478.

Stary, H. C. *et al.* (1995) 'A definition of advanced types of atherosclerotic lesions and a histological classification of atherosclerosis: A report from the Committee on Vascular Lesions of the Council on Arteriosclerosis, American Heart Association', *Arteriosclerosis, Thrombosis, and Vascular Biology*, 15(9), pp. 1512–1531. doi: 10.1161/01.ATV.15.9.1512.

Stone, G. W. *et al.* (2011) 'A Prospective Natural-History Study of Coronary Atherosclerosis', *New England Journal of Medicine*, 364(3), pp. 226–235. doi: 10.1056/nejmoa1002358.

Stone, P. H., Coskun, A. U., Kinlay, S., *et al.* (2003) 'Effect of endothelial shear stress on the progression of coronary artery disease, vascular remodeling, and in-stent restenosis in humans: In vivo 6-month follow-up study', *Circulation*, 108(4), pp. 438–444. doi: 10.1161/01.CIR.0000080882.35274.AD.

Stone, P. H., Coskun, A. U., Yeghiazarians, Y., *et al.* (2003) 'Prediction of sites of coronary atherosclerosis progression: In vivo profiling of endothelial shear stress, lumen, and outer vessel wall characteristics to predict vascular behavior', *Current Opinion in Cardiology*, 18(6), pp. 458–470. doi: 10.1097/00001573-200311000-00007.

Stone, P. H. *et al.* (2012) 'Prediction of progression of coronary artery disease and clinical outcomes using vascular profiling of endothelial shear stress and arterial plaque characteristics: The PREDICTION study', *Circulation*, 126(2), pp. 172–181. doi: 10.1161/CIRCULATIONAHA.112.096438.

Swirski, F. K. and Nahrendorf, M. (2013) 'Leukocyte Behavior in Atherosclerosis, Myocardial Infarction, and Heart Failure', *Atherosclerosis*, 161(January), pp. 161–166.

Ta, H. T. *et al.* (2017) 'The effects of particle size , shape , density and flow characteristics on particle margination to vascular walls in cardiovascular diseases, Expert Opinion on Drug Delivery', *Expert Opinion on Drug Delivery*, 15(1), pp. 33–45. doi: 10.1080/17425247.2017.1316262.

Tal, M. G. *et al.* (2006) 'Comparison of side hole versus non side hole high flow hemodialysis catheters', *Hemodialysis International*, 10(1), pp. 63–67. doi:

10.1111/j.1542-4758.2006.01176.x.

Tall, A. R. and Yvan-Charvet, L. (2015) 'Cholesterol, inflammation and innate immunity', *Nature Reviews Immunology*, 15(2), pp. 104–116. doi: 10.1038/nri3793.

Tang, D. *et al.* (2005) 'Local maximal stress hypothesis and computational plaque vulnerability index for atherosclerotic plaque assessment', *Annals of Biomedical Engineering*, 33(12 SPEC. ISS.), pp. 1789–1801. doi: 10.1007/s10439-005-8267-1.

Tansey, E. A. *et al.* (2019) 'Understanding basic vein physiology and venous blood pressure through simple physical assessments', *Advances in Physiology Education*, 43(3), pp. 423–429. doi: 10.1152/ADVAN.00182.2018.

Taylor, C. A. and Figueroa, C. A. (2009) 'Patient-Specific Modeling of Cardiovascular Mechanics', *Annual Review of Biomedical Engineering*, 11(1), pp. 109–134. doi: 10.1146/annurev.bioeng.10.061807.160521.

Taylor, C. A. and Steinman, D. A. (2010) 'Image-based modeling of blood flow and vessel wall dynamics: Applications, methods and future directions: Sixth international bio-fluid mechanics symposium and workshop, March 28-30, 2008 Pasadena, California', *Annals of Biomedical Engineering*, 38(3), pp. 1188–1203. doi: 10.1007/s10439-010-9901-0.

Traub, O. and Berk, B. C. (1998) 'Laminar shear stress: Mechanisms by which endothelial cells transduce an atheroprotective force', *Arteriosclerosis, Thrombosis, and Vascular Biology*, pp. 677–685. doi: 10.1161/01.ATV.18.5.677.

Trerotola, S. O. *et al.* (2002) 'Randomized comparison of split tip versus step tip high-flow hemodialysis catheters', *Kidney International*, 62(1), pp. 282–289. doi: 10.1046/j.1523-1755.2002.00416.x.

Turitto, V. T. and Weiss, H. J. (1980) 'Red blood cells: Their dual role in thrombus formation', *Science*, 207(4430), pp. 541–543. doi: 10.1126/science.7352265.

Twardowski, Z. J. and Moore, H. L. (2001) 'Side holes at the tip of chronic hemodialysis catheters are harmful', *Journal of Vascular Access*, 2(1), pp. 8–16. doi: 10.1177/112972980100200103.

UK, K. C. (2020) *Chronic Kidney Disease in the UK*. Available at: https://www.kidneycareuk.org/about-kidney-health/conditions/ckd/%0A (Accessed: 21 April 2021).

Vasquez, S. A. and Ivanov, V. A. (2000) 'A phase coupled method for solving multiphase problems on unstructured meshes', *American Society of Mechanical Engineers, Fluids Engineering Division (Publication) FED*, pp. 743–748.

Vesely, T. M. and Ravenscroft, A. (2016) 'Hemodialysis catheter tip design: Observations on fluid flow and recirculation', *Journal of Vascular Access*, 17(1), pp.

29–39. doi: 10.5301/jva.5000463.

Vijayaratnam, P. R. S. *et al.* (2015) 'The impact of blood rheology on drug transport in stented arteries: Steady simulations', *PLoS ONE*, 10(6), pp. 1–19. doi: 10.1371/journal.pone.0128178.

Viles-Gonzalez, J. F., Fuster, V. and Badimon, J. J. (2004) 'Atherothrombosis: A widespread disease with unpredictable and life-threatening consequences', *European Heart Journal*, 25(14), pp. 1197–1207. doi: 10.1016/j.ehj.2004.03.011.

Virani, S. S. *et al.* (2020) 'Heart disease and stroke statistics—2020 update: A report from the American Heart Association', *Circulation*, 141(9), pp. 139–596. doi: 10.1161/CIR.0000000000000757.

Wagner, C., Steffen, P. and Svetina, S. (2013) 'Aggregation of red blood cells: From rouleaux to clot formation', *Comptes Rendus Physique*, 14(6), pp. 459–469. doi: 10.1016/j.crhy.2013.04.004.

Weber, T. *et al.* (2004) 'Arterial Stiffness, Wave Reflections, and the Risk of Coronary Artery Disease', *Circulation*, 109(2), pp. 184–189. doi: 10.1161/01.CIR.0000105767.94169.E3.

Wei, L., Chen, Q. and Li, Z. (2019) 'Influences of plaque eccentricity and composition on the stent–plaque–artery interaction during stent implantation', *Biomechanics and Modeling in Mechanobiology*, 18(1), pp. 45–56. doi: 10.1007/s10237-018-1066-z.

Wentling, A. G. (2004) 'Hemodialysis catheters: Materials, design and manufacturing', *Contributions to Nephrology*, 142, pp. 112–127. doi: 10.1159/000074869.

Wentzel, J. J. *et al.* (2012) 'Endothelial shear stress in the evolution of coronary atherosclerotic plaque and vascular remodelling: Current understanding and remaining questions', *Cardiovascular Research*, 96(2), pp. 234–243. doi: 10.1093/cvr/cvs217.

Wilkins, E. *et al.* (2017) 'European Cardiovascular Disease Statistics 2017', *European Heart Network*, pp. 94–100. Available at: www.ehnheart.org.

Wiwatanapataphee, B. *et al.* (2012) 'Effect of branchings on blood flow in the system of human coronary arteries', *Mathematical Biosciences and Engineering*, 9(1), pp. 199–214. doi: 10.3934/mbe.2012.9.199.

Wohner, N. *et al.* (2011) 'Lytic resistance of fibrin containing red blood cells', *Arteriosclerosis, Thrombosis, and Vascular Biology*, 31(10), pp. 2306–2313. doi: 10.1161/ATVBAHA.111.229088.

Wootton, D. M. *et al.* (2001) 'A mechanistic model of acute platelet accumulation in thrombogenic stenoses', *Annals of Biomedical Engineering*, 29(4), pp. 321–329. doi: 10.1114/1.1359449.

Wootton, D. M. and Ku, D. N. (1999) 'Fluid mechanics of vascular systems, diseases,

and thrombosis', *Annual Review of Biomedical Engineering*, (1), pp. 299–329. doi: 10.1146/annurev.bioeng.1.1.299.

World Health Organisation - CVD Facts (2017). Available at: http://www.who.int/mediacentre/factsheets/fs310/en/.

Wu, W. T., Jamiolkowski, M. A., *et al.* (2017) 'Multi-Constituent Simulation of Thrombus Deposition', *Scientific Reports*, 7(February), pp. 1–16. doi: 10.1038/srep42720.

Wu, W. T., Aubry, N., *et al.* (2017) 'Transport of platelets induced by red blood cells based on mixture theory', *International Journal of Engineering Science*, 118, pp. 16–27. doi: 10.1016/j.ijengsci.2017.05.002.

Yazdani, A. *et al.* (2017) 'A General Shear-Dependent Model for Thrombus Formation', *PLoS Computational Biology*, 13(1), pp. 1–24. doi: 10.1371/journal.pcbi.1005291.

Yesudasan, S. and Averett, R. D. (2019) 'Recent advances in computational modeling of fibrin clot formation: A review', *Computational Biology and Chemistry*, 83(November), p. 107148. doi: 10.1016/j.compbiolchem.2019.107148.

Yilmaz, F. and Gundogdu, M. Y. (2008) 'A critical review on blood flow in large arteries; relevance to blood rheology, viscosity models and physiologic conditions', *Korea-Australia Rheology Journal*, 20(November), pp. 197–211. doi: 10.1.1.462.7926.

Yilmaz, F. and Gundogdu, M. Y. (2009) 'Analysis of conventional drag and lift models for multiphase CFD modeling of blood flow', *Korea-Australia Rheology Journal*, 21(3), pp. 161–173.

Yilmaz, F., Kutlar, A. I. and Gundogdu, M. Y. (2011) 'Analysis of drag effects on pulsatile blood flow in a right coronary artery by using Eulerian multiphase model', *Korea Australia Rheology Journal*, 23(2), pp. 89–103. doi: 10.1007/s13367-011-0012-8.

Yoganathan, A. P., He, Z. and Jones, S. C. (2004) 'Fluid mechanics of heart valves', *Annual Review of Biomedical Engineering*, 6, pp. 331–362. doi: 10.1146/annurev.bioeng.6.040803.140111.

Zhang, L. ren *et al.* (2011) 'Coronary artery lumen diameter and bifurcation angle derived from CT coronary angiographic image in healthy people', *Zhonghua xin xue guan bing za zhi*, 39(12), pp. 1117–1123.

Zhu, H. *et al.* (2009) 'Cataloguing the geometry of the human coronary arteries: A potential tool for predicting risk of coronary artery disease', *International Journal of Cardiology*, 135(1), pp. 43–52. doi: 10.1016/j.ijcard.2008.03.087.

APPENDIX A | CODES AND SCRIPTS

Rheological Model

The following code was used to implement the MKM5 rheology model (Chapters 3 & 4) into Ansys Fluent. It is written in C, and uses various macros and operations defined within the user defined functions (UDF) manual provided with the Ansys Fluent Software. This code is best compiled, using Visual-Studio (if running on Windows) or can be compiled automatically if using Linux. Green text is comments to aid understanding of my (often incoherent) code.

```
/* UDF for viscosity of RBC phase in an Eulerian-Eulerian MKM5 Rheology model
(Numerical constants reported in publications) */

#include "udf.h"
#include "math.h"

DEFINE_PROPERTY(rbc_viscosity,c,thread)
{
int rbc_domain_index = 1;
int interior_zone_ID = 1;

Domain *mixture_domain = Get_Domain(1); /* Identify Mixure domain */
Domain *rbc_domain = DOMAIN_SUB_DOMAIN(mixture_domain,rbc_domain_index); /* Define
rbc_domain within the mixture domain */

Thread *mixture_thread = Lookup_Thread(rbc_domain,interior_zone_ID); /* Identify
mixture thread, and our subsequent phase_specific threads */
Thread *rbc_thread = THREAD_SUB_THREAD(mixture_thread,rbc_domain_index);
Thread **pt;
pt = THREAD_SUB_THREADS(rbc_thread);

real rbcvisco, rbc_phi, rbc_shear, ninf, inner, krieg_mix, prod, dimshear, nst, nsum;
/* Declare our variables used in the rheology model*/
rbcvisco=0.01445; /* Set value to be used during initialisation */
```

```
mp_thread_loop_c(rbc_thread, mixture_domain, pt) /* Loop over all cells within our
rbc_thread, within the mixture domain */
{
    rbc_phi = C_VOF(c, pt[1]); /* Volume fraction of RBC (0 is primary phase, 1 is 2nd
phase and so on) */
    rbc_shear = C_STRAIN_RATE_MAG(c, pt[1]); /* Shear rate of RBC phase */

    if (rbc_phi <= 0.01) /* Set lower bound for haematocrit to avoid initial non-
linear instabiltites (Value never reached in normal flow) */
    {
        rbc_phi = 0.01;
        ninf = ((-8.780739943551884) * (exp(-2.823542271766962 * rbc_phi)));
        inner = (1 - ((rbc_phi) / (0.98)));
        krieg_mix = ((0.00123) * (pow(inner, ninf)));
        rbcvisco = (((krieg_mix)-(0.00123) * (1 - rbc_phi)) / (rbc_phi));
    }

    if (rbc_phi > 0.05 && rbc_phi <= 0.2) /* Model without shear thinning exponent */
    {
        ninf = ((-8.780739943551884) * (exp(-2.823542271766962 * rbc_phi)));
        inner = (1 - ((rbc_phi) / (0.98)));
        krieg_mix = ((0.00123) * (pow(inner, ninf)));
        rbcvisco = (((krieg_mix)-(0.00123) * (1 - rbc_phi)) / (rbc_phi));
    }

    if (rbc_phi > 0.2 && rbc_phi <= 0.95) /* Model with shear thinning exponenent */
    {
        ninf = ((-8.780739943551884) * (exp(-2.823542271766962 * rbc_phi)));
        inner = (1 - ((rbc_phi) / (0.98)));
        prod = (1252.6440693060042 * rbc_shear);
        dimshear = (1 + pow(prod, 2.0));
        nst = (-16.277748270259284 * (pow(dimshear, -0.14274532071176718)));
        nsum = (ninf + nst);
        krieg_mix = ((0.00123) * (pow(inner, nsum)));
        rbcvisco = (((krieg_mix)-(0.00123) * (1 - rbc_phi)) / (rbc_phi));
    }

    else if (rbc_phi > 0.95) /* Set upper bound for haematocrit beound which RBC no
longer behave as a fluid */
    {
        rbc_phi = 0.95;
        ninf = ((-8.780739943551884) * (exp(-2.823542271766962 * rbc_phi)));
        inner = (1 - ((rbc_phi) / (0.98)));
        prod = (1252.6440693060042 * rbc_shear);
        dimshear = (1 + pow(prod, 2.0));
        nst = (-16.277748270259284 * (pow(dimshear, -0.14274532071176718)));
        nsum = (ninf + nst);
        krieg_mix = ((0.00123) * (pow(inner, nsum)));
        rbcvisco = (((krieg_mix)-(0.00123) * (1 - rbc_phi)) / (rbc_phi));
    }
}
return rbcvisco;
}
```

Velocity Profiles

The following code was used to implement the variation of velocity at the inlet for the coronary artery models featured in Chapters 3 & 4.

```
/* Fully developed transient coronary velocity waveform for 3.5 mm diameter artery
(Radius increased to account for roughness)  */

#include "udf.h"

DEFINE_PROFILE(CoronaryVelocityWaveform, thread, position)
{
real a0 = 0.1563; /* Constants acquired from FFT curve fitting in MATLAB*/
real a1 = -0.03047;
real b1 = 0.008136;
real a2 = 0.02537;
real b2 = 0.03907;
real a3 = -0.01189;
real b3 = -0.007487;
real a4 = 0.01033;
real b4 = 0.002253;
real a5 = -0.009741;
real b5 = 0.003973;
real a6 = 0.005918;
real b6 = -0.001254;
real a7 = 0.001991;
real b7 = 0.001075;
real a8 = -0.00389;
real b8 = 0.000374;
real w = 7.833;
real x;
real y;
real z[ND_ND];
real t = CURRENT_TIME;
face_t f;

begin_f_loop(f, thread) /* Loop over all faces (elements) on inlet - Blood flow is in
z direction */
        {
        F_CENTROID(z,f,thread); /* Store the centroid (x,y), of the face we are in */
        x = z[0];
        y = z[1];
        F_PROFILE(f, thread, position) = (2*(a0 + a1*cos(t*w) + b1*sin(t*w) + /*
Calculate the magnitude of velocity for the current face based upon our FFT waveform,
and the position on the inlet - Giving the parabolic effect*/
               a2*cos(2*t*w) + b2*sin(2*t*w) + a3*cos(3*t*w) + b3*sin(3*t*w) +
               a4*cos(4*t*w) + b4*sin(4*t*w) + a5*cos(5*t*w) + b5*sin(5*t*w) +
               a6*cos(6*t*w) + b6*sin(6*t*w) + a7*cos(7*t*w) + b7*sin(7*t*w) +
               a8*cos(8*t*w) + b8*sin(8*t*w))*(1-(y*y+x*x)/(0.0000009761)));
        }
end_f_loop(f, thread)
}
```

Platelet Activation

The following code was used to determine the level of activation for platelets in Chapter 4. The UDF also reports the current RBC shear rate the platelets experience, as a way to track the potential for aggregation.

```
/* UDF to define the level of activation (LOA) of a platelet, as well as extract RBC
shear/residence time data for Aggregation calcs. Results are written to files which
are analysed using scripts */
#include "udf.h"
#include "mem.h"
#include "dpm.h"
#include "dpm_types.h"

DEFINE_DPM_SCALAR_UPDATE(activation_calc,cell,thread,initialize,p)
{
    cell_t c = P_CELL(p); /* Define cell particle is in */
    Thread *t = P_CELL_THREAD(p); /* Thread particle is in (General thread - not a
phase thread!) */
    Thread** pt;
    pt = THREAD_SUB_THREADS(t); /* Pointer to the phase thread within general thread -
[0] - Primary and [1] - Secondary*/


  if (initialize)
    {
      P_USER_REAL(p,0) = C_MU_EFF_MIXTURE(c,t,pt,0); /* Plasma Viscosity */
      P_USER_REAL(p,1) = C_MU_EFF_MIXTURE(c,t,pt,1); /* RBC Viscosity*/
      P_USER_REAL(p,2) = C_VOF(c,pt[0]); /* PLASMA VOF */
      P_USER_REAL(p,3) = C_VOF(c,pt[1]); /* RBC VOF */
      P_USER_REAL(p,4) = C_STRAIN_RATE_MAG(c,pt[0]); /* Plasma Strain */
      P_USER_REAL(p,5) = C_STRAIN_RATE_MAG(c,pt[1]);  /* RBC Strain */
      P_USER_REAL(p,6) = P_TIME(p); /* Particle time to calculate Delta T) */
      P_USER_REAL(p,7) = 0;  /* Initial Variable for Stress-Vof */
    }
  else
    {
      P_USER_REAL(p,0) = C_MU_EFF_MIXTURE(c,t,pt,0);
      P_USER_REAL(p,1) = C_MU_EFF_MIXTURE(c,t,pt,1);
      P_USER_REAL(p,2) = C_VOF(c,pt[0]);
      P_USER_REAL(p,3) = C_VOF(c,pt[1]);
      P_USER_REAL(p,4) = C_STRAIN_RATE_MAG(c,pt[0]);
      P_USER_REAL(p,5) = C_STRAIN_RATE_MAG(c,pt[1]);
      P_USER_REAL(p,6) = P_TIME(p);
      P_USER_REAL(p,7) =
(C_MU_EFF_MIXTURE(c,t,pt,0)*C_STRAIN_RATE_MAG(c,pt[0])*C_VOF(c,pt[0]) +
C_MU_EFF_MIXTURE(c,t,pt,1)*C_STRAIN_RATE_MAG(c,pt[1])*C_VOF(c,pt[1])); /* Shear stress
in blood */
     }
}
```

Platelet Data Export

The following code was used to print the values calculated previously, to a file which can then be analysed externally. It is important to retain platelet ID numbers as the particle track files generated from fluent '.xml', can be filtered to only show specific ID's – which can be very useful with some of our later manipulations.

```
/* Output our above variables to .csv or which files we prefer, to be analysed using
external scripts */
DEFINE_DPM_OUTPUT(activation_output,header,fp,p,t,plane)
{
if(header)
 {
 par_fprintf_head(fp,"P-ID Shear-Stress-VOF Particle-Time RBC-SHEAR-RATE \n "); /*
Outputs the ID of particle, shear stress, current time and RBC-shear for every
particle, at every particle time-step*/
 }
if(NULLP(p))
 return;
 par_fprintf(fp,"%d %" int64_fmt " %d %e %e %e \n",
 P_INJ_ID(P_INJECTION(p)),
 p->part_id,
 p->part_id,P_USER_REAL(p,7),P_USER_REAL(p,6),P_USER_REAL(p,5));
}
```

Platelet Tracking

The following code was used to selectively remove/terminate platelets in Chapter 5. This ensures platelets are only tracked in relevant areas to the simulations (Tip volume).

```
/* UDF to remove DPM particles (platelets here) based upon certain conditions (In our
case to enforce existence only within our catheter tip volume) */

#include "udf.h"
#include "math.h"

DEFINE_DPM_SCALAR_UPDATE(removal,cell,thread,initialize,p)
{
real pt, x, y, z, rad_pos; /* Declare variables */
pt=P_TIME(p);
x=P_POS(p)[0];
y=P_POS(p)[1];
z=P_POS(p)[2];
rad_pos=sqrt(y*y+x*x); /* Radial position useful as catheter is circular, centred
about origin*/

/* Platelets released everywhere on a plane, removed platelets to only leave ones
around the hole (Start of tip volume) */
if (z<0.03870 && pt<0.00000001)
        {
        MARK_PARTICLE(p, P_FL_REMOVED);
        }
if (z>0.04140 && pt<0.00000001)
        {
        MARK_PARTICLE(p, P_FL_REMOVED);
        }
if (x>0.0013 && pt<0.00000001)
        {
        MARK_PARTICLE(p, P_FL_REMOVED);
        }
if (x<-0.0013 && pt<0.00000001)
        {
        MARK_PARTICLE(p, P_FL_REMOVED);
        }
/* Remove particles which are on the outflow half (Inflow half is y<0)  */
if (y>0)
       {
        MARK_PARTICLE(p, P_FL_REMOVED);
        }
/* Remove particles which are outside catheter and past hole */
if (rad_pos>0.0024 & z>0.04140)
        {
        MARK_PARTICLE(p, P_FL_REMOVED);
        }
/* Remove particles which are past the end of the catheter */
if (z>0.06)
        {
```

```
        MARK_PARTICLE(p, P_FL_REMOVED);
        }

/* Remove particles which are inside inflow lumen and have normalised in flow field
(End of tip volume) */
if (rad_pos<0.00251 && y<0 && z<0.033)
       {
        MARK_PARTICLE(p, P_FL_REMOVED);
        }
}
```

Platelet Analysis

The following code was used as a shell script in Linux to sort and analyse the raw platelet data obtained in Chapter 4, using the UDF's in Appendix A. The script is used to calculate the total level of activation (LOA) for each platelet from the total time history and print it to a single column '.csv' file for plotting in Excel.

```
# remove header from ansys files
tail -n +3 interior-blood.dpm > noheader

# sort by particle ID and Time ( Expected input columns of the form: ID VOF_STRESS
TIME RBC_SHEAR)
sort -n -s -k1,1 -k3,3  noheader > id-time-sort

# Calculate instantaneous level of activation (LOA) using (Input: ID VOF_STRESS TIME
RBC_SHEAR) from above
awk -v OFS='' 'NR == 1 {
  next
}
{
  print $0, (NR > 2 && p1  == $1 ? ($3 - p3) * (p2) : "")
}
{
   p1 = $1
   p2 = $2
   p3 = $3
   p4 = $4
}' id-time-sort | column -t > instant-pas

# Add up LOA for each platelet
awk 'NR==1{print;next} {if ($1 in seen); else b[c++]=$1; seen[$1]=1; for
(i=2;i<=NF;i++) {a[$1][i]+=$i}} END{for (j=0;j<c;j++) {s=b[j]; for
(i=2;i<=NF;i++){s=s" "a[b[j]][i]}; print s}}' instant-pas | column -t > total-pas

# take ID and LOA and turn non-scientific format
awk '{printf("%.0f %.12f\n",$1,$5)}' total-pas > nonscience

# Calculate mean LOA of all platelets
awk '{ sum += $2 } END { if (NR > 0) print sum / NR }' nonscience > meanstress
cat meanstress


# Print LOA of each platelet (Additional analysis in EXCEL)
awk '{ print $2 }' nonscience > PAS-EXCEL.csv
```

Red Blood Cell Aggregation

The following code was used as a shell script in Linux to further analyse the platelet data in Chapter 4, allowing for the tracking of exposure time to sufficiently low-shear rates for RBC to potentially form aggregates.

```
# Platelets who experience low enough shear for aggregation at any point
awk '(NR>1) && ($4 <= 50 ) ' id-time-sort > lowshear

# Identify platelets who continuously experience this low shear ie gap between regions
< 0.05 s)
awk -v OFS='' 'NR == 1 {
  next
}
{
  print $0, (NR > 1 && p1  == $1  && ($3-p3) < 0.05 ? $3-p3 :"")
}
{
   p1 = $1
   p2 = $2
   p3 = $3
   p4 = $4
}' lowshear | column -t > dirty

# Print ID TIME SHEAR DT for platelets who continuously experience low shear
awk '{print $1, $3, $4, $5}' dirty | sed '/^[[:space:]]*$/d' > agg

# non science format the data
awk '{printf("%.0f %.10f\n",$1,$4)}' agg > nonscience

# Sum all columns
awk 'NR==1{print;next} {if ($1 in seen); else b[c++]=$1; seen[$1]=1; for
(i=2;i<=NF;i++) {a[$1][i]+=$i}} END{for (j=0;j<c;j++) {s=b[j]; for
(i=2;i<=NF;i++){s=s" "a[b[j]][i]}; print s}}' nonscience | column -t > sumdt

# Longest time in region
awk '{printf("%.0f %.10f\n",$1,$2)}' sumdt > nonscience1

# Sort by higest TOTAL exposure to low shear
sort -n -r -k2,2 nonscience1 > sort1

# Get rid of ones who experience it for an instant only.
awk '(NR>1) && ($2 >= 0.01 ) ' sort1 > exposure.csv

# Platelets with long enough exposure to aggregarte
awk '(NR>1) && ($2 >= 1.5 ) ' exposure.csv > aggregate.csv

# Platelet ID's of aggregated
awk -vORS=, '{ print $1 }' aggregate.csv > aggregated.txt

# ID's which have low shear exposure at all
awk -vORS=, '{ print $1 }' exposure.csv > total-low-shear.txt
```

Automating Model Setup

When using Fluent remotely through a Linux HPC interface, often it is simpler to create/edit models using a text user interface (TUI) instead of the frequently convoluted and inefficient graphical user interface (GUI). Any action taken in the Fluent GUI can be represented as a string of text commands. Not only is this more efficient when using remote applications but is highly scalable in reducing human operator time in model creation. The majority of models presented in this thesis were built first locally using a GUI, then slowly the relevant inputs required to build the model were translated into TUI commands, until the entire model could be generated effortlessly from any inputted Fluent mesh file. This allows for any changes in mesh/geometry without the need to laboriously recreate models, and allows for the simple creation of multiple similar models, e.g. different rheology models, boundary conditions or catheter geometries. The following TUI commands can be passed to Fluent when it is launched in Linux (Journal files), and the entire setup and solution of the healthy LCA bifurcation MKM5 model in Chapter 4 is trivially achieved. This only requires the correct 'healthy-smoothed.msh' input file (as well as the UDF's given above). It creates and defines material properties, applies relevant multiphase settings, defines functions for use in later CFD-Post analysis, defines our boundary conditions, sets convergence criteria and solves the model in increments of 400 time steps. The '.dat' files are complete solution data files and allow for the resumption of calculations in the event they were aborted.

```
/define/user-defined/compiled-functions/ compile libudf yes velocity.c mkm5.c "" ""
/define/user-defined/compiled-functions/ load "libudf"
/file/read-case healthy-smoothed.msh
/file/cff-files? no
/define/models/unsteady-1st-order yes
/define/models/viscous/ laminar? yes
/define/materials/change-create/ air plasma yes constant 1003 no no yes constant
0.00123 no no no yes
/define/materials/change-create/ plasma rbc yes constant 1060 no no yes user-defined
"rbc_visco::libudf" no no no no
/define/models/multiphase/model/ eulerian
/define/models/multiphase/number-of-phases/ 2
/define/models/multiphase/eulerian-parameters/ no no implicit no
/define/phases/phase-domain/ phase-1 plasma-phase yes plasma
/define/phases/phase-domain/ phase-2 rbc-phase yes rbc no no constant 8e-6
/define/phases/set-domain-properties/interaction-domain/forces/drag/ yes schiller-
naumann no
/define/phases/set-domain-properties/interaction-domain/forces/virtual-mass/ virtual-
mass? yes
/define/phases/set-domain-properties/interaction-domain/forces/virtual-mass/ vmass-
coeff yes constant 0.5
/define/phases/set-domain-properties/interaction-domain/interfacial-area/ interfacial-
area yes ia-symmetric
/define/custom-field-functions/define/ "rbc-strain-rate-func"
rbc_phase_strain_rate_mag
/define/custom-field-functions/define/ "rbc-viscosity-func" rbc_phase_viscosity_lam
/define/custom-field-functions/define/ "plasma-strain-rate-func"
plasma_phase_strain_rate_mag
/define/custom-field-functions/define/ "plasma-viscosity-func"
plasma_phase_viscosity_lam
/define/custom-field-functions/define/ "rbc-vof-func" rbc_phase_vof
/define/custom-field-functions/define/ "plasma-vof-func" plasma_phase_vof
/define/boundary-conditions/velocity-inlet/ inlet plasma-phase no no yes yes yes yes
udf "inletvelocity::libudf"
/define/boundary-conditions/velocity-inlet/ inlet rbc-phase no no yes yes yes yes udf
"inletvelocity::libudf" no 0.45
/define/boundary-conditions/pressure-outlet/ bigoutlet mixture no 15998.7 no yes no
/define/boundary-conditions/pressure-outlet/ smalloutlet mixture no 15998.7 no yes no
/solve/monitors/residual/convergence-criteria/ 0.0001 0.0001 0.0001 0.0001 0.0001
0.0001 0.0001 0.0001 quit
/solve/set/data-sampling/ yes 800 yes yes yes yes yes yes yes yes yes yes
wc multi-mkm5.cas
/solve/initialize/hyb-initialization/
/solve/set/time-step/ 0.001
/solve/dti 400 150
wd multi-mkm5-full-400.dat
/solve/dti 400 150
wd multi-mkm5-full-800.dat
/solve/dti 400 150
wd multi-mkm5-full-1200.dat
/solve/dti 400 150
wd multi-mkm5-full-1600.dat
/solve/dti 400 150
wd multi-mkm5-full-2000.dat
/solve/dti 400 150
wd multi-mkm5-full-2400.dat
exit
yes
```

Similar to the approach above, TUI commands can also be used to setup discrete phase model (DPM) injections as used to create/track the flow of platelets through the fluid domain as seen in Chapters 4 and 5. The following TUI commands create one injection of platelets into the diseased LCA bifurcation MKM5 model in Chapter 4. A plane at the physiological inlet is defined, with an injection of platelets applied to this plane. The relevant DPM settings are then applied, including the use of the above platelet UDFs. The '.dpm' file is where all of the platelet level of activation/aggregation data is stored, with the '.xml' file being used in CFD-Post to visualise data and create animations (Supplementary material to publication – which I highly recommend).

```
/define/user-defined/compiled-functions/ compile libudf yes activation.c velocity.c
mkm5.c "" ""
/define/user-defined/compiled-functions/ load "libudf"
rc diseased-multi-mkm5.cas
rd diseased-multi-full-mkm5-1600.dat
/file/cff-files? no
/surface/plane-point-n-normal/ release 0 0 0.015 0 0 1
/define/models/dpm/interaction/coupled-calculations? yes
/define/models/dpm/interaction/update-dpm-sources-every-flow-iteration? yes
/define/models/dpm/interaction/dpm-iteration-interval/ 5
/define/models/dpm/user-defined/ "none" "none" "activation_output::libudf"
"activation_calc::libudf" "none" 9
/define/models/dpm/unsteady-tracking/ yes no 1e-5 no
/define/models/dpm/numerics/tracking-parameters/ 12000000 yes 2e-6
/define/models/dpm/options/saffman-lift-force/ yes
/define/models/dpm/options/virtual-mass-force/ yes 0.5
/define/models/dpm/options/pressure-gradient-force/ yes
/define/injections/create-injection/ p1 no yes surface no release () yes yes no no no
no no no 2e-6 1.8 1.8000001 0.15 1e-20
/define/materials/change-create/ anthracite platelet yes constant 1040 no yes
/file/transient-export/particle-history-data/ p-exp-1 cfdpost diseased-p-track-1 p1 ()
user-value-3 user-value-7 user-value-8 user-value-5 particle-current-time particle-id
particle-velocity-mag particle-x-velocity particle-y-velocity particle-z-velocity () 1
0
/report/dpm-sample/ "p1" () "interior-blood" () () "activation_output::libudf" no no
/solve/set/time-step/ 0.001
/solve/dti 4000 50
/report/dpm-sample
exit
yes
```